Experimental study and modeling for the safety of Li-ion batteries

Ridha Omrani

THÈSE

Pour obtenir le grade de

DOCTEUR DE L'UNIVERSITÉ GRENOBLE ALPES

École doctorale : I-MEP2 - Ingénierie - Matériaux, Mécanique, Environnement, Energétique, Procédés, Production
Spécialité : 2MGE : Matériaux, Mécanique, Génie civil, Electrochimie
Unité de recherche : CEA Grenoble / LITEN

Etude expérimentale et modélisation pour la sécurité des batteries Li-ion

Experimental study and modeling for the safety of Li-ion batteries

Présentée par :

Ridha OMRANI

Direction de thèse :

Philippe AZAIS — Directeur de thèse
INGENIEUR HDR, Université Grenoble Alpes

Rapporteurs :

François TRAN VAN
PROFESSEUR DES UNIVERSITES, Université de Tours
Stéphane LARUELLE
PROFESSEUR DES UNIVERSITES, Université de Picardie Jules Verne

Thèse soutenue publiquement le **18 octobre 2022**, devant le jury composé de :

Philippe AZAIS INGENIEUR HDR, CEA centre de Grenoble	Directeur de thèse
Delphine RIU PROFESSEUR DES UNIVERSITES, Grenoble INP	Présidente
Christophe FORGEZ PROFESSEUR DES UNIVERSITES, Université de Technologie de Compiègne	Examinateur
François TRAN VAN PROFESSEUR DES UNIVERSITES, Université de Tours	Rapporteur
Stéphane LARUELLE PROFESSEUR DES UNIVERSITES, Université de Picardie Jules Verne	Rapporteur

Invités :

Sébastien Benjamin
INGENIEUR, SAFT

Remerciement

Je souhaite tout d'abord remercier les membres du jury d'avoir accepté d'évaluer ce travail de thèse, à savoir Mme Delphine Riu, M. François Tran-Van, M. Stéphane Laruelle, M. Christophe Forgez et M. Sébastien Benjamin.

Je tiens particulièrement à remercier mes encadrants pour m'avoir accompagné dans ce travail, pour leur soutien, leurs encouragements et leurs précieux conseils durant toute la période de la thèse. En particulier Philippe Azais, mon directeur de thèse, pour ses qualités humaines, sa forte implication scientifique ainsi que ses nombreux contacts, mais également Didier Buzon pour ses connaissances techniques approfondies, sa réactivité et ses remarques constructives. J'ai appris beaucoup durant ces trois ans de thèse grâce à vous et à l'autonomie que vous m'avez accordée.

Je souhaite remercier Mathias Gerard, Marion Chandesris et toutes les personnes du laboratoire de modélisation multi-échelle et suivi de performance, je me suis sentie chez moi grâce à votre accueil chaleureux.

Je souhaite remercier pareillement toutes les personnes du DEHT, DTNM, IRIG et IRAMIS qui ont participé à la réalisation des expériences au CEA Grenoble et à Saclay. Merci à Sylvie Génies, Michel Bardet, Eric De vito, Jean-François Colin, Benoit Chavillon, Vasily Tarnopolsky, Suzy Surble, Johnny Amiran, Thomas Pietri, Xavier Jacolin, Kamel Bachir Elezaar… C'est grâce à votre contribution que j'ai réussi à présenter ce travail.

J'ai une pensée particulière pour les camarades qui ont partagé mes journées au cours de ces années de thèse, Oumaima, Imen, Alex, Mathilde, Gael, Venkat, Panda, Joel-Louis, Quentin et Alexis. Merci pour votre amitié, pour les discussions et les moments que j'ai passés avec vous. Une pensée aussi pour Pierre, Pierre-François, Miguel et Youssef merci pour votre sympathie et bon courage aux futurs docteurs.

À mon père Mohsen, mes sœurs Khadija, Soulaima et Islem, je vous remercie pour votre amour inconditionnel. À Rabie, Ilyes, Achref et Chahinez merci pour votre soutien illimité.

Ma mère Hinda, que ton âme repose dans la paix éternelle, cette thèse est pour toi !

Abbreviations

EVs/PHEVs	*Electric Vehicles/Plug-in Hybrid Electric Vehicles*
FMECA	*Failure Mode, Effects and Criticality Analysis*
SOC	*states of charge*
HEV	*Hybrid Electric Vehicle*
PHEV	*Plug-in Hybrid Electric Vehicle*
BEV	*Battery Electric Vehicle*
IEA	*International energy agency*
ACEA	*European Automobile Manufacturers' Association*
CAAM	*China Association of Automobile Manufactures*
EAFO	*European Alternative Fuels Observatory*
CTP	*Cell-to-Pack design*
OEM	*Original Equipment Manufacturer*
LiPo	*lithium polymer*
SEI	*solid electrochemistry interphase*
IEC	*International Electrotechnical Commission*
TR	*Thermal runaway*
DSC	*differential scanning calorimeter*
ARC	*accelerated rate calorimetry*
C80	*Calvet calorimeter*
SH	*self-heating*
XPS	*X-ray photoelectron spectroscopy*
TOF-SIMS	*Time Of Flight - Secondary Ion Mass Spectrometry*
NMR MAS	*Nuclear magnetic resonance Magic angle spinning*
XRD	*X-Ray Diffraction*
EPO	*European Patent Office*
PEO	*polyethylene oxide*
PVD	*physical vapor deposition*
PEG	*Polyethylene glycol*
CMC	*Carboxymethyl cellulose*
INR	*lithium iron phosphate cylindrical cell*
AlOOH	*Aluminium hydroxide oxide*
PVDF	*Polyvinylidene fluoride*
PE	*Polyethylene*
ISC	*Internal Short Circuit*
LEDC	*lithium ethylene di-carbonate*
LMC	*lithium methyl carbonate*

Symbols & Subscripts

1D	*One dimension*
3D	*three dimensions*
Li_m	*Metallic lithium*
^7Li	lithium-7 isotope
wt.	*weight*
ELe	*electrolyte*
T_p	*Peak temperature*
$E_{a,x}$	*Activation energy of* x
A_x	pre-exponential factor of x
neg	*negative*
pos	*positive*
T	*Temperature*
V	*Volume*
H	*Specific enthalpy*
k	*Reaction rate*
n	*Reaction order*
M	*Molar mass*
C_p	*Heat capacity*
t	*Time*
ρ	*Density*
A	*Surface*

General introduction

Climate change is one of the biggest challenges of our times and requires the decarbonization of all sectors, with priority given to energy and transport. There is no longer a need to demonstrate that humans have a direct impact on greenhouse gas emissions, which is leading to the increase in the average temperature of our world (>+1 °C since the beginning of the pre-industrial era[1]) and important climate changes (in France, for example, we are already at +2 °C).

In countries with a very carbon-intensive energy mix, i.e., many countries in the world, the priority is to decarbonize electricity because it is generally based on numerous thermal power plants (gas, coal, fuel oil), which are therefore high CO_2 emitters. The solutions to replace these power plants are to use nuclear power, hydroelectricity, or intermittent renewable energy sources (wind, photovoltaic). These latter require an additional operating reserve for the balancing of load with demand, but they must also be decarbonized otherwise there is no interest. One of the possible solutions, for relatively short periods (< a few days), consists to use batteries. Since 2017, Li-ion batteries are the most used to maintain the stability of the energy grid.

The other main sector is transportation with nearly a fourth of greenhouse gas emissions. The solution is to substitute the thermal powertrain with a partial or total electric powertrain. Of course, this is only interesting if decarbonized electricity is used. This electrification is relatively recent with Li-ion batteries (compared to lead-acid batteries which are used for more than a century). This renewal is caused by the high energy density of these batteries, which offers an interesting autonomy (>100 km/day), a good integration in the vehicle (in mass and volume), and a cost that becomes acceptable. In the last decade, we have gone from 125.000 EVs/PHEVs selling worldwide in 2012 to 6.75M EVs/PHEVs by 2021 leading to say that transportation electrification is now a reality, at least in China and Europe.
At the same time, the energy density of the Li-ion battery system has greatly increased from ~90 Wh/kg @ system in 2011 to ~170 Wh/kg @ system in 2021. This transformation requires safety at different levels, given the sharp increase in the number of vehicles sold and the energy density at all scales: at the material scale, moving from LMO ($LiMn_2O_4$) to NMC811 ($LiNi_{0.8}Mn_{0.1}Co_{0.1}O_2$) cathodes between 2011 and 2021, and at the cell scale with almost 290 Wh/kg @ cell and 170 Wh/kg @ system.

[1] « The world's energy problem », Our World in Data, https://ourworldindata.org/worlds-energy-problem.

The main techno-economic challenges associated with the evolution of this technology and required for the widespread use of Li-ion batteries in traction applications are:

- To increase the energy density at the system level, the power density (to improve the charging speed), and lifetime for both cycling and calendar mode,
- To maintain the battery system performance as stable as possible with temperature to limit the need for bulky and expensive thermal management systems, which means increasing the power density without losing the energy density,
- To reduce the use and recycling cost, this last point is more recent but needs to be considered in the future especially because of the European limitations on the use of critical and/or strategic materials. Not only Lithium is concerned but also the other Li-ion battery materials that are under real geopolitical tension such as cobalt, nickel, and copper.

The Li-ion battery system must be as safe as possible under all conditions of use (a charge, discharge, low or high temperature, vibration, shock ...). The field experts have proposed an extensive "corpus" of standards to test the safety of the system. In addition, safety must be treated at all scales (from the material to the system) by identifying the technology limits to avoid a domino effect on the whole structure. Safety is based on several components: mechanical, thermal, electronic, and electrochemical control. However, the energy of the system is stored in the cell and its thermal runaway is one of the most constraining failure modes to be taken into account in the FMECA (Failure Mode, Effects and Criticality Analysis).

If it is known that the thermal runaway of Li-ion cells involves several violent reactions and generates a considerable amount of energy[2], a detailed understanding of its mechanisms as well as the ability of modeling remains a first-order scientific and industrial challenge. The most commonly considered approach to model the thermal runaway is to study each of these degradation reactions independently and cumulate the results to represent the overall reaction. This approach is relevant when the analysis is performed on a cell for which the manufacturing process and the internal composition are completely known but much more complex in the case of commercial cells already formed and for which the manufacturing process may regularly change. On the other hand, the consequences of thermal runaway are strongly related to the state of health of the Li-ion cell; the safety degrades especially during fast charging or low temperature charging due to lithium plating phenomena. Besides, the safety standards tests are proposed for fresh cells and aged cells are not considered: there is no guarantee that the result will be the same after aging. Then, it seems essential to take into account the impact of aging on the Li-ion cell safety behavior.

[2] Xuning Feng et al., « Investigating the Thermal Runaway Mechanisms of Lithium-Ion Batteries Based on Thermal Analysis Database », *Applied Energy* 246: 53-64, https://doi.org/10.1016/j.apenergy.2019.04.009.

In this thesis, our main objective is to improve the comprehension of the thermal runaway in a commercial cylindrical cell based on Ni-rich/Graphite chemistry (INR18650-32E) and to develop a thermal runaway model by integrating the new reactions induced by the aging of the cell at low temperature. The study relies on different characterization methods to consolidate and improve the methodology leading to the development of a relevant thermal runaway model.

The experimental analyses of the battery materials were multiplied using DSC, NMR, XRD, XPS, and TOF-SIMS characterization analyses. The tests were conducted under different states of charge (SOC), with different electrolyte chemistries, and using multiple samples and configurations (different materials present or missing).

To evaluate the impact of aging on the thermal safety of the cell, the study is conducted firstly on materials from a fresh cell and then compared to the behavior of materials from an aged cell at low temperature.

Based on the experimental results, a predictive runaway model was developed at the material and complete cell scale by integrating a molar balance of species and taking into account the impact of aging on the battery.

The investigation axes of this study will be detailed in this manuscript involving four chapters.

The first chapter is a presentation of the context and the state of the art of the thesis subject. Firstly, an overview of the lithium battery technology will be presented. The aging phenomenon will be addressed with particular attention to the impact that can cause on the safety behavior of the cell. Then, the thermal phenomenon of Li-ion batteries, its origin, and its consequences will be presented. Finally, the state of the art in the development of Li-ion battery modeling, especially thermal runaway modeling, will be presented. The research studies with a direct interest in the findings of this thesis will be cited and discussed in the following chapters.

In the second chapter, the established experimental methodology is described in detail. The DSC analysis results combined with different characterization techniques (XRD, XPS, and TOF-SIMS) used to characterize each degradation reaction are described. The thermal behavior results of the fresh cell materials and their mixtures (performed to physically discrete the exothermic reactions at the electrode scale) are presented and discussed. In the last part of this chapter, an evaluation of the studied thermal runaway exothermic reactions of the cell materials at the beginning of their life is proposed.

The third chapter is dedicated to the study of the impact of aging at low temperatures on the security behavior of the cell observed at a different level. The adopted aging protocol followed by an observation of the impact of low-temperature aging on the cell materials illustrated with ^{7}Li NMR MAS analysis will be presented. Then, a quantification study of the lithium plating

formed on aged graphite electrodes will be proposed. Then, the thermal behavior of the aged cell materials based on DSC analysis will be investigated against the behavior of fresh cell materials. Finally, an energy balance of the full cell will be presented based on the obtained results in chapters II and III.

The thermal runaway model development involving all the exothermic thermal degradation reactions of the fully charged INR18650-32E cell before and after cyclic-aging at -20 °C will be presented in the last chapter. The calibration of the chemical kinetic model including a species balance: kinetic parameters, specific enthalpies, and the degradation mechanism determination methodology, will be described and discussed. Then, simulations of abusive tests of the fully charged INR18650-32E cell before and after aging at -20 °C will be presented.

The last part of this manuscript presents the general conclusions derived from the different key points of this thesis, with the highlighting of future work perspectives.

Chapter I:

Overview & state of the art

Contents

List of tables

List of figures

Now, as the context of the thesis is presented, we will review in this chapter a selection of relevant studies in the literature around the safety of Li-ion batteries. Some reference studies relating to this thesis will be mentioned and discussed in chapters II, III, and IV.

In this chapter, an overview of the Li-ion battery technology and aging phenomena will be presented first. The thermal phenomenon of Li-ion batteries, its origin, and its consequences will be presented. Particular attention will be addressed to the impact of aging on the safety behavior of Li-ion batteries. Finally, the state of the art in the development of Li-ion battery modeling, especially materials thermal degradation and thermal runaway modeling for Li-ion batteries, will be presented.

1 Overview of lithium-ion batteries

1.1 The genesis of lithium-ion batteries

The technology of lithium-ion batteries was born during the oil crisis in the 1970s [1].
Stanley Whittingham studied the intercalation of lithium ions into titanium disulfide (TiS_2) and then invented the first metal sulfide cathode for lithium-ion batteries with a lithium metal electrode for the anode. In 1980, *John Goodenough* predicted that the cathode would have higher energy capacity by using a metal oxide instead of metal sulfide and he invented the LCO (lithium oxide cobalt, $LiCoO_2$) based cathode. In 1982, *Rachid Yazami* and *Philippe Touzain* succeeded the reversible intercalation of lithium into graphite carbon for the first time. In 1985, *Akira Yoshino* invented the complete Li-ion battery system using LCO/carbon electrodes with organic electrolytes. In 2019, the Nobel Prize in chemistry was awarded to *S.Whittingham, J.Goodenough, and A.Yoshino* for their work in developing Li-ion batteries [1].

Lithium-ion batteries were commercialized for the first time by Sony in 1991 and revolutionized the wireless communication field. Since the 2000s, they have been associated with the development of the market for wireless communication technologies such as phones and laptops. In 2003, the first lithium-ion battery-assisted bike was introduced in Europe. In 2008, the Tesla Roadster became the first recognized electric vehicle powered at 100% electricity using a lithium-ion battery pack [2].

Today, lithium-ion battery is the preferred technology for hybrid and battery electric vehicles (HEV - Hybrid Electric Vehicle, PHEV - Plug-in Hybrid Electric Vehicle, BEV - Battery Electric Vehicle) with high-energy requirements. According to the Global EV Outlook 2022 report, over 16.5 million electric cars (PHEV + BEV) were sold worldwide in 2021 [3].
More details are presented in Figure 1.

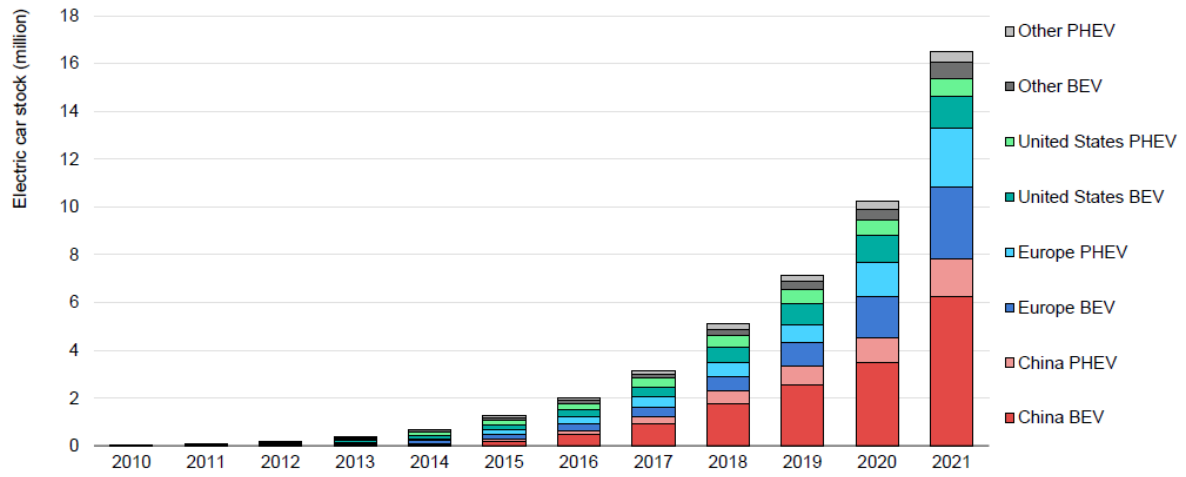

Figure 1: Global electric car stock 2010-2021, copied from [3]

Notes: BEV = battery electric vehicle; PHEV = plug-in hybrid electric vehicle. Electric car stock in this figure refers to passenger light-duty vehicles. “Other” includes Australia, Brazil, Canada, Chile, India, Japan, Korea, Malaysia, Mexico, New Zealand, South Africa, and Thailand. Europe in this figure includes the EU27, Norway, Iceland, Switzerland, and United Kingdom. Sources: IEA analysis based on country submissions, complemented by ACEA; CAAM; EAFO; EV Volumes; Mark lines [3]

All these electric vehicles include a lithium-ion battery pack. A battery pack is the assembly of several modules connected in series and/or in parallel depending on the intended application and each module contains a certain number of lithium-ion cells as presented in Figure 2 [4], [5]. In some pack designs, cells are assembled without any intermediate module definition (Cell-to-Pack design or CTP). The format, chemistry, and the number of cells used to build the pack depend on the manufacturer / OEM (Original Equipment Manufacturer).

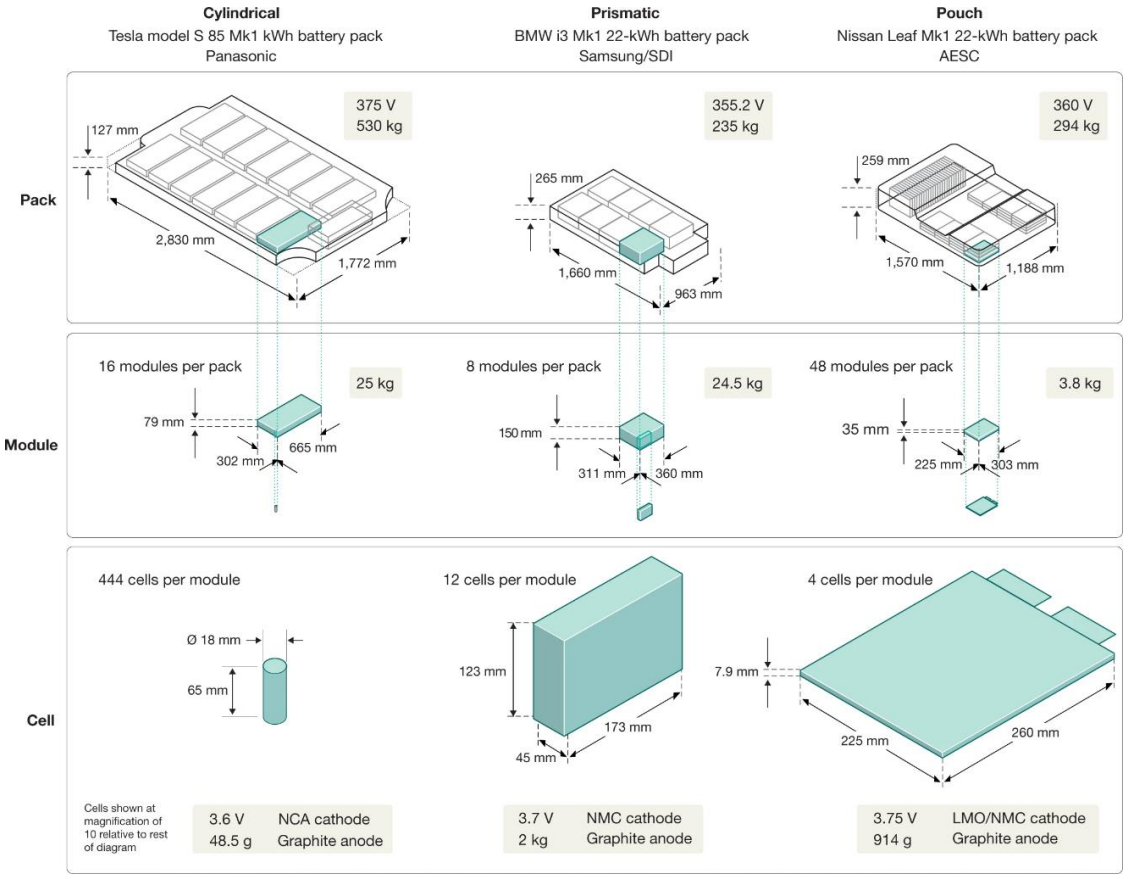

Figure 2: Examples of three different battery packs and modules (cylindrical, prismatic, and pouch cells) in use in current electric cars, reported from [5]

As illustrated in Figure 2, several formats of lithium-ion cells are commercially available. Cylindrical and prismatic cells are usually protected by a hard casing made of stainless steel, while pouch cells, also called LiPo (lithium polymer), are wrapped in a soft aluminized polymer casing. These cell formats are also available with different dimensions.

Another cell format is also available as presented in Figure 3, it is called «coin cell» and is generally used in small electronic devices or at a laboratory scale for Li-ion batteries research and development purposes.

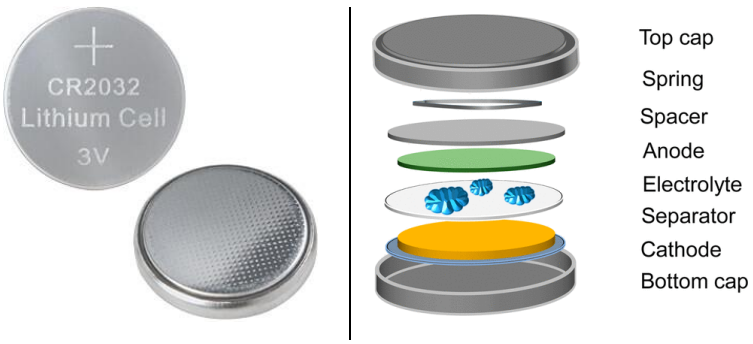

Figure 3: lithium coin cell battery assembly [6]

Whatever the format, a lithium-ion battery is mainly composed of two electrodes, a positive electrode and a negative electrode separated by a porous membrane (separator). An organic electrolyte ensures the internal transport of the ions in the system. The positive electrode is the host material; initially charged with lithium atoms.

In the cylindrical and prismatic cells shown in Figure 2, the electrodes and the separator are rolled together. In the pouch cell format, they are generally stacked on top of each other but in some cells, the electrodes are rolled and then crushed to make a flat format.

The battery is characterized usually by a nominal voltage (V) and a capacity (Ah) defined by the fabricant. The battery voltage is the difference between the voltage of positive and negative electrodes. The average voltage of lithium-ion batteries depends on electrode materials and it is typically 4.2 V when the cell is fully charged and 2.5 V when fully discharged; the nominal voltage is about 3.7 V.

The capacity of the battery, expressed in coulomb (C = A.s) or ampere-hour (Ah), indicates the number of electrical charges stored in the battery electrode materials. It is usually specific for each material by mass (Ah/kg) or by volume (Ah/cm^3). As an example, the capacity of graphite is 372 Ah/kg.

The capacity of the Li-ion battery depends on the material of the electrodes. Then, they are selected according to various criteria such as:

- The specific capacity i.e., the amount of electricity (or Li ions) per mass unit that can be stored in the electrode materials;
- The ionic and electronic conductivity of the electrode materials;
- The thermal, mechanical, and chemical stability of the electrode materials.

The electrolyte used in Li-ion battery should also satisfy some conditions:

- A good ionic conductivity to minimize the transport resistance of lithium ions;
- Thermal and chemical stability under different operating conditions;
- Low toxicity and low cost.

1.2 The structure of the lithium-ion battery

1.2.1 Negative and positive electrode materials

The materials and the chemistry of Li-ion battery electrodes are constantly evolving to improve their capacity and energy density. The most commonly used materials for positive and negative electrodes are summarized in Table 1.

Table 1: properties of some commonly studied positive and negative electrodes [7]

Compound	Typical specific capacity (mAh/g)	Average voltage vs.Li/Li$^+$ (V)
$LiMn_2O_2$ (LMO)	120	4.1
$LiCoO_2$ (LCO)	145	3.8
$LiFePO_4$ (LFP)	165	3.4
$LiNi_{0.33}Mn_{0.33}Co_{0.33}O_2$ (NMC111)	170	3.85
$LiNi_{0.8}Co_{0.15}Al_{0.05}O_2$ (NCA)	200	3.85
LTO ($Li_4Ti_5O_{12}$)	175	1.55
LiC_6	372	0.07 – 0.19
Si-C composite	1000	**
$Li_{15}Si_4$	3579	0.4

Historically, lithium metal electrode is used for negative electrodes but for safety reasons it was quickly removed and replaced by a graphite electrode deposited on a copper current collector. Other materials are used then such as lithium titanium oxide $Li_4Ti_5O_{12}$ (LTO) or silicon graphite composite (Si/C). The negative electrode contains usually additives like carbon black nanoparticles used to improve the electronic conductivity of the electrode. Typically, sodium carboxymethyl cellulose (CMC-Na) binder, mostly associated with styrene butadiene rubber (SBR), is used to maintain the stack electrode materials/current collector.

Most positive electrodes consist of a transition metal oxide deposited on an aluminum current collector such as $LiCoO_2$ (LCO), $LiFePO_4$ (LFP), or $LiMn_2O_4$ (LMO). Polyvinylidene fluoride (PVDF) binder is typically used for positive electrodes.

NMC compounds are particularly attractive as they offer high capacity and energy density. The current tendency is to adjust the amount of nickel, manganese, and cobalt in NMC material to obtain higher energy density. Other than NMC111, we find NMC442, NMC 532, NMC622, NMC721, and NMC811. For more capacity, manganese is eliminated in favor of nickel in the case of NCA material. Those cathode materials are called "Ni-rich" compounds. Cathode materials can be blended to improve performance (LMO + NMC111, NCO + LCO, LPF + NCA, …).

1.2.2 Electrolyte chemistry

The electrolyte ensures the transport of lithium ions inside the cell. Typically, the liquid LiBs electrolytes contain low molecular weight solvents such as carbonates (Ethylene Carbonate (EC), Dimethyl Carbonate (DMC), Ethyl Methyl Carbonate (EMC), Diethyl Carbonate (DEC),

Propylene Carbonate (PC) …), polar salts such as lithium salts ($LiPF_6$, $LiBF_4$, LiTFSI -lithium bis(trifluoromethane-sulfonyl)imide, LiFSI - Lithium bis(fluoro-sulfonyl)imide), LiBOB - lithium bis(oxalate)borate...) and other additives such as vinylene carbonate (VC - Vinylidene Carbonate, FEC – Fluoroethylene Carbonate …). Additives are typically added to improve the electrolyte properties such as conductivity and chemical/thermal stability.

The following table presents the main characteristic properties of these solvents:

Table 2: Properties of the main solvents in tested electrolytes (from ChemBK database)

	M (g/mol)	**ρ (g/cm3)**	**Tv(mmHg) (At 25°C)**	**Boiling point (°C) (At 760mmHg)**
DMC ($C_3H_6O_3$)	90	1.063	56	91
EC ($C_3H_4O_3$)	88	1.321	0.001	248
PC ($C_4H_6O_3$)	102	1.2	0.04	242
FEC ($C_3H_3FO_3$)	106	1.41	0.023	249.5

The mixture ratios and the chemistry vary depending upon the desired cell properties.
The organic solvents in the electrolyte can be highly flammable (e.g. DMC) and critical to the safety of the batteries. Therefore, researchers continue to work on electrolyte composition to improve the thermal safety behavior of Li-ion batteries. Other types of electrolytes are emerging: ionic liquids (molten salts), polymers …

1.2.3 Separator

To avoid contact between the two electrodes and the internal short circuit, a porous separator made of polymer is added inside the cell. The separator is traditionally a single layer of polyethylene (PE) or polypropylene (PP) or also multilayer membranes of PP/PE/PP.

The separator is not very resistant at high temperatures because of the low melting temperature of polyethylene which starts at about 130°C.
Manufacturers added a coating with ceramics using Al_2O_3 or SiO_2 materials to improve the thermal stability of the separator and increase the collapse temperature of the separator.
The average thickness of separators in commercial cells is 20 µm (from 9 µm to 25 µm, typically) with a pore diameter between 2 nm and 50 nm [8].

1.3 Theory of lithium-ion battery and SEI formation

Initially, when the battery is assembled, the negative electrode (graphite for example) is completely delithiated with a potential close to 1 V ($x \approx 0$) and the positive electrode is lithiated

with a potential close to 2.5 V (x ≈ 1). During charging, lithium is transferred from the positive to the negative electrode. The potential of the positive electrode is limited by the oxidation of the electrolyte and that of the negative electrode must not fall below 0 V to avoid the formation of lithium plating. Figure 4 shows an illustration of the electrode's potential limitation for an LCO/Graphite cell.

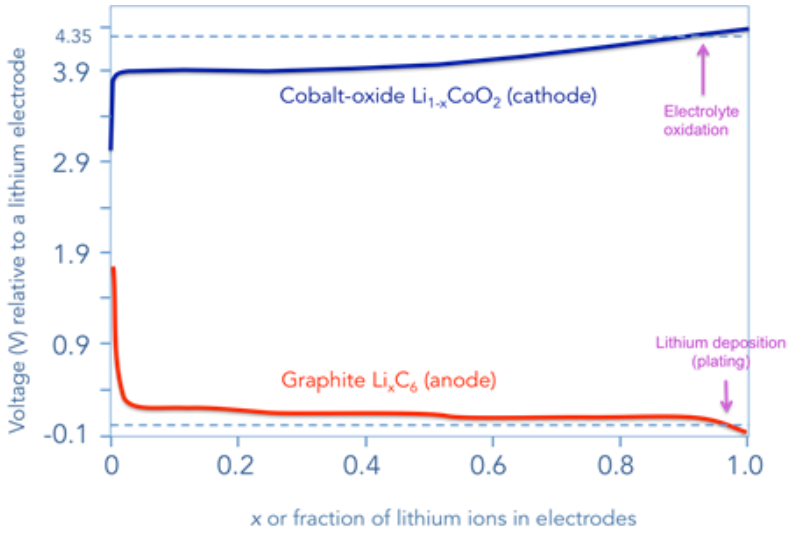

Figure 4: Potential curve of the electrodes of an LCO/C cell, reported from [9]

The electrochemical reduction of the electrolyte solvents is inevitable during the charging process of the cell with a graphite negative electrode. Typically, it starts at about 0.8 V *vs Li/Li*$^+$ and continues until 0.3 V *vs Li/Li*$^+$. Indeed, during the first cell cycling, the lithium ions combine with the electrolyte solvents to form an irreversible passivation layer on the surface of the graphite electrode called SEI (solid electrochemistry interphase). Then, the lithium intercalation inside the negative electrode occurs between 0.25 V *vs Li/Li*$^+$ and 0.01 V *vs Li/Li*$^+$. Typically, about 10 % of the initial capacity of the battery is lost after the SEI formation [10].

Today there is no final agreement on the mechanism of formation of the SEI and its exact composition, the chemical composition of SEI and its structure depend on several factors including graphite morphology, electrolyte composition, formation procedure and operating temperature. Therefore, it is difficult to control the formation of the SEI and its growth.

Mainly, SEI is composed of two layers: an inner layer and an outer layer. The inner layer is adjacent to the graphite and rich in inorganic compounds particularly LiF and Li_2CO_3 compounds. The outer layer at the electrolyte interface is composed mainly of organic products such as ROLi and $ROCO_2Li$ with an R: low molecular weight alkyl group. In particular, the component $(CH_2OCO_2Li)_2$ (or LEDC: lithium ethylene di-carbonate) reduction product of the EC solvent [10], [11]. Similarly, the SEI layer could be formed in the positive electrode/electrolyte interface, but thinner and more chemically stable than graphite [12].

This statement is the common thread between several old and recent studies of SEI characterization in the literature including [8], [10], [13]–[15].

2 Aging of lithium-ion batteries

Li-ion battery's lifetime is generally depending on the operating conditions and it is limited by the aging phenomena. Typically, we identify three types of aging [16], [17]:

- Calendar aging is the degradation of Li-ion batteries during rest periods. Indeed, during battery storage, aging mechanisms occur and lead to irreversible loss of capacity during battery storage [18]. Depending on the storage conditions, especially temperature and SOC, the capacity loss can be different.
- Cycling aging is the aging caused by repeated charge/discharge operations when the battery is used. It is accelerated at high temperature, high charge/discharge rate (C-rate), and the variation in SOC during cycling [19].
- Combined aging, is when the battery is subjected to a sequence of cycles with rest periods. This case is representative of battery aging in electric vehicles.

Different aging mechanisms can occur at different levels inside the cell. A first complete presentation of the degradation mechanisms of lithium-ion batteries was published by Doyle et al. [20] and recently summarized by Hendricks et al. [21] and R. Birkl et al. [22]. An illustration of these mechanisms is presented in Figure 5.

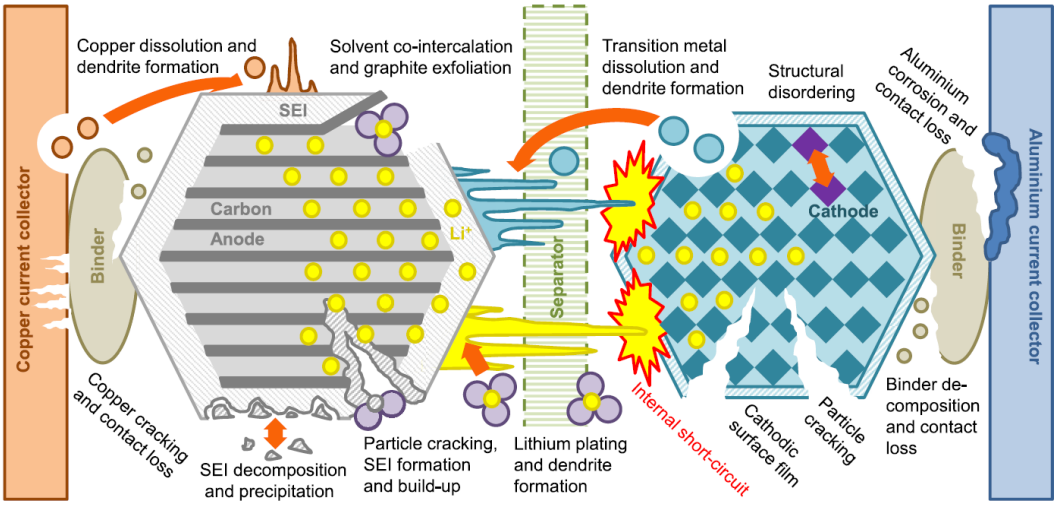

Figure 5: Degradation mechanisms of Li-ion batteries, reported from [16]

These degradation mechanisms can involve the electrode active materials, the electrolyte, and non-active materials, such as current collectors or additives (binders, carbon black …).

The aging of batteries involves a loss of lithium ions caused by SEI layer formation, electrolyte decomposition, or lithium plating formation(deposition of solid lithium on the surface of the negative electrode); and a loss of active material related mainly to mechanical stresses during cycling leading to the cracking or structural changes of the electrode materials [16].

The consequences of these degradation mechanisms have a direct impact on the electrochemical performances and the safety of the battery. The main aging mechanisms affecting the thermal stability of Li-ion batteries are the lithium plating and the SEI layer development and thickening. A detailed description of these phenomena is presented in the following two paragraphs.

2.1 Lithium plating

Under typical operating conditions, lithium cations migrate between negative and positive electrodes through the electrolyte. During the charging cycle, lithium cations intercalate between graphene layers of the graphite electrode. However, when charging at low temperatures and/or with high currents and at high SOCs [16], [22], lithium ions are deposited on the graphite electrode surface instead of intercalating into the graphite structure according to the following reaction [23], [24]:

$$Li^+ + 1e^- \rightarrow Li(s) \qquad (1)$$

Moreover, the presence of lithium plating on the surface of the graphite electrodes is always indicated with a silver-gray color [25]–[27]

Figure 6 shows an illustration of lithium plating formation under different conditions:

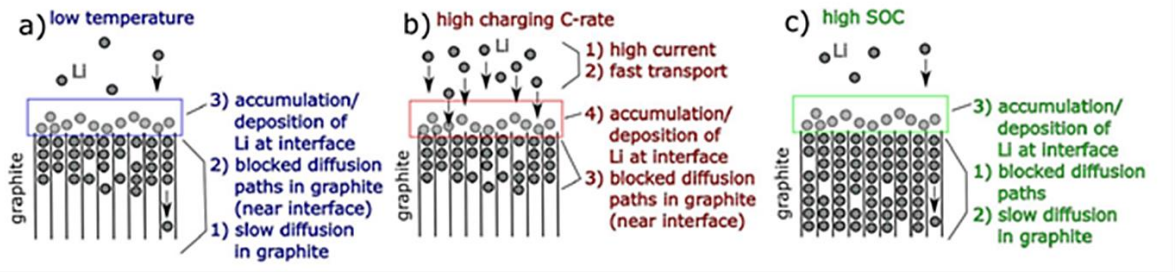

Figure 6: Schematic illustration of the charging behavior of cells at a) low temperature, b) high charge rate and c) high SOC, reported from [23]

The formation of lithium plating occurs always after the accumulation of lithium ions, which makes the electric potential vs Li/Li^+ at the surface of the graphite electrode particles near 0 V or even below. Indeed, the intercalation potential of lithium in graphite is close to 100 mV, it is a little higher than that of its reduction at the surface of the electrode [28]. Thus, when the negative electrode potential tends to 0V vs Li/Li^+, the reduction of lithium-ion may occur according to the reaction (1).

A study performed by T. Waldmann [29] shows the effect of cycling at low and high temperatures on battery performance as reported in Figure 7.

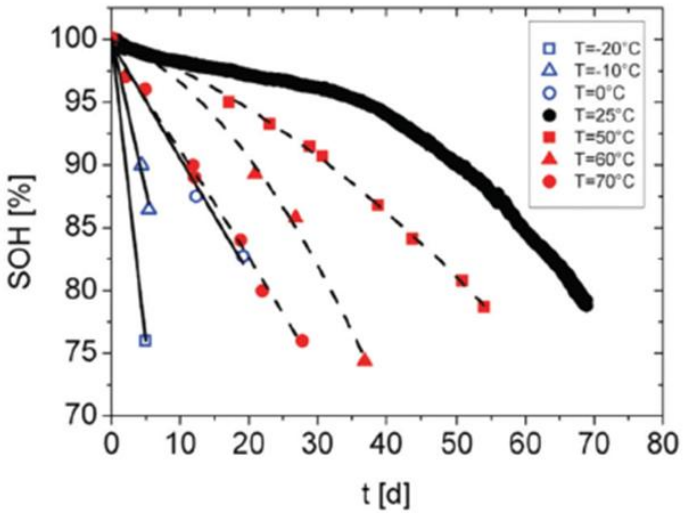

Figure 7: Measured health status as a function of cycle time at 1C and different temperatures, reported from [29]

The health status SOH is defined as the discharge capacity of an aging cell relative to the discharge capacity of the same cell when before aging. Between 25 and 70 °C, their results show that the aging of the cell is decelerated however the state of health decreases significantly between 0 °C and -20 °C. According to the authors, the predominant aging mechanism at low temperatures, leading to rapid capacity loss, is lithium plating.

2.2 SEI development during battery aging

Experimental studies have shown that the morphology and composition of the SEI evolve during aging [16]. The evolution of the SEI depends on many factors, in the case of calendar aging, its evolution depends particularly on the nature of the electrolyte, the state of charge, and the temperature. In the case of cycling aging, the graphite is exposed to a sequence of volume expansion/contraction (±10 %). Thus, the SEI is continuously fractured and new SEI components are formed at the electrode/electrolyte interface. This phenomenon induces the loss of cyclable lithium and the thickening of the SEI which becomes richer in inorganic species (such as LiF and Li_2CO_3) [15].

P. Kuntz et al. [30] performed ante and post-mortem characterization on commercial 18650 cells aged by cycling at different temperatures (0°C, -20°C, 25°C) and by storage at 45 °C and SOC 100 %. They identified that the degradation mechanisms are localized at the negative electrode and are principally manifested by: the thickening of SEI at high temperature during aging by cycling and in calendar mode, as well as the formation of lithium plating by cycling at low temperature (0°C and -20°C)

3 Safety of Li-ion battery and thermal runaway phenomenon

The safety of Li-ion batteries has been carefully studied in the last decade due to the many incidents of failure that have marked the history of lithium-ion technology in recent years. For example, according to the USA federal aviation administration (FAA), 354 aviation-related incidents involving Li-ion batteries have been recorded since 2006. Table 3 presents a selection of some incidents involving Li-ion batteries. These problems have often required costly product recalls.

Table 3: A selection of incidents related to lithium-ion batteries reported in recent years, data are collected from the FAA website and [31]

Date	Reporter	Description of the incident
01/2013	USA	A battery pack caught fire and filled the cabin of a Boeing 787 with smoke.
04/2014	Australia	A Boeing 737 caught fire due to a short circuit in a battery inside a trunk.
01/2016	Norway	A Tesla Model S car caught fire during the charging process.
09/2016	Netherlands	A Tesla Model S crashed into a tree, causing its battery pack to catch fire.
08/2016	Korea	The first explosion of the Samsung Note 7 smartphone was because of its battery.
02/2017	China	A Tesla Model X caught fire after crashing
11/2019	Southwest Airlines	On flight 285, a lithium battery fire occurred during the boarding process.
12/2021	DHL Airlines	A package containing LiBs exploded and caught fire within a cargo facility.

Li-ion cells contain oxygen (mainly in the positive electrode), and combustibles such as lithium and liquid electrolyte. In normal operation, they are safe as long as heat sources are absent. When the cell is heated and in the absence of sufficient cooling, thermal runaway (TR) may occur. By definition, the TR is a loss of temperature control, characterized by the generation of a large amount of heat inside the cell under extreme or accidental conditions of use, which can lead in some cases to the explosion of the battery, often accompanied by a strong gas emission [32]. In most of the reported accidents in Table 3, the battery or battery pack eventually catches fire due to the thermal runaway (TR) phenomenon. It is considered today the major safety issue and represents a permanent danger for Li-ion batteries.

The current standards (IEC-62619, 2017), (IEC-62133-2, 2017) specify the risks and test conditions for characterizing and quantifying the behavior of Li-ion batteries. Typically, the TR is studied by applying strong stress to the cell and following its thermal behavior. The stress can be mechanical (shock, compression, vibration), thermal (high and low temperatures outside the limits set by the fabricant), or electrical (external short-circuit, overcharge, over-discharge) [17].

In all these abusive tests, the root cause of cell destruction is always a thermal solicitation. The electrical and mechanical stresses are only paths to thermal stress, as shown in Figure 8.

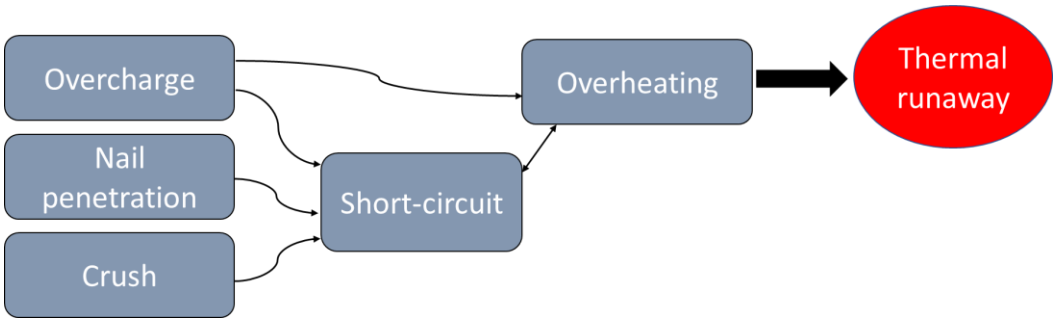

Figure 8: Relationship between the various abuse tests and thermal runaway

The safety and in particular the thermal behavior of Li-ion cells can be evaluated using calorimetry methods. The most commonly used is accelerated rate calorimetry (ARC). For the cell materials, differential scanning calorimeter (DSC) and Calvet calorimeter (C80) are usually used.

Three temperatures could be identified, during calorimetric measurements, based on cell temperature: (1) non-self-heating, (2) self-heating, and (3) thermal runaway [33].
Figure 9 shows the thermal cartography of a 18650 cell (LCO/Graphite) at different SOCs reported by [34] based on ARC measurements results performed by Mendoza-Hernandez et al. [35].

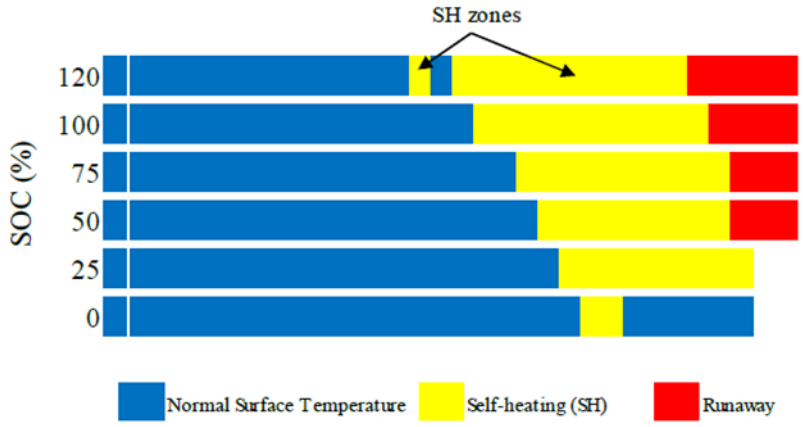

Figure 9: Mapping of LCO 18650 cell at different SOCs and temperatures [35], reported from [34]

The Thermal runaway process is characterized by two temperatures, the self-heating (SH) temperature (T_{onset}) and the thermal runaway temperature.
The self-heating starts with the activation of exothermic degradation reactions of the battery materials (typically at T ≥ 80°C) which release a significant amount of energy [36]. The internal heat of the battery and the temperature progressively increase until reaching the runaway temperature. The situation becomes out of control and the cell temperature increases exponentially. The cell T_{onset} (in Figure 9) shows approximately a linear dependency on the state of charge of the cell. The most unstable case corresponds to the highest SOC.

4 Thermal behavior of Li-ion cell materials

A multitude of scenarios can lead to thermal runaway within the cell. All scenarios include various exothermic degradation reactions that produce heat inside the cell and lead to an unstable thermal situation and then to thermal runaway. These reactions involve mainly the materials of the cell electrodes as well as the electrolyte.

In this part, the main degradation reactions that characterize the thermal runaway of Li-ion batteries will be presented briefly. The bibliography concerning the details of these points (degradation mechanism of these reactions and their contribution during the thermal runaway process) will be discussed in chapter II based on our thesis results.

4.1 Decomposition of the positive electrode

As mentioned previously, the positive electrode is typically made of transition metal oxides such as $LiFePO_4$, $LiCoO_2$, $LiMn_2O_4$, and other LiM_xO_2, with M_x being a mixture of Ni, Mn, and Co or Ni, Co, and Al. These materials are not stable at high temperatures. In TR conditions, the material structure decomposes and liberates oxygen, then an exothermic reaction between this oxygen and the organic electrolyte of the cell may occur and generates heat.

The breakdown temperature of these materials during thermal runaway depends on the nature of the active material and the electrolyte. The thermal stability of these materials is illustrated in Figure 10, based on ARC test results presented by Doughty [37], where the self-heating rate for full Li-ion cells made with different positive electrode are plotted.

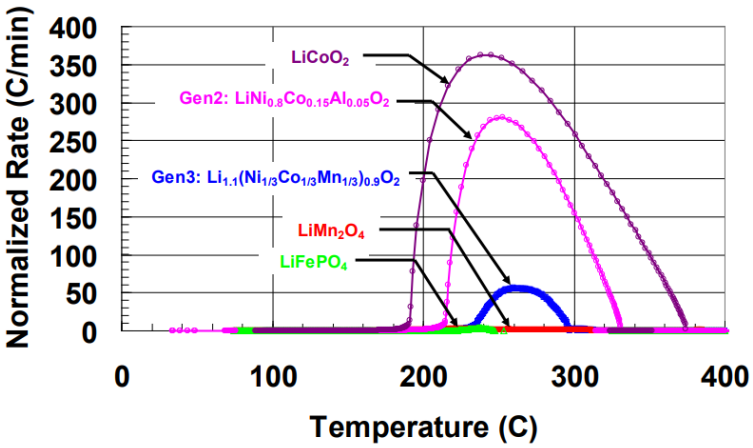

Figure 10: Self-heating rate of 18650 full cells measured by ARC

$LiCoO_2$ cells are the less thermally stable cells, with the lower Tonset and the higher self-heating rate followed by NCA cells. However, the $LiFePO_4$ cells show the lowest self-heating rate during TR; LFP materials do not liberate oxygen even when fully decomposed at high temperatures [37].

Figure 11 shows the differential scanning calorimetry (DSC) profiles of LMO, NCA, and LFP cathode materials analyzed in the same conditions as presented in the figure box.

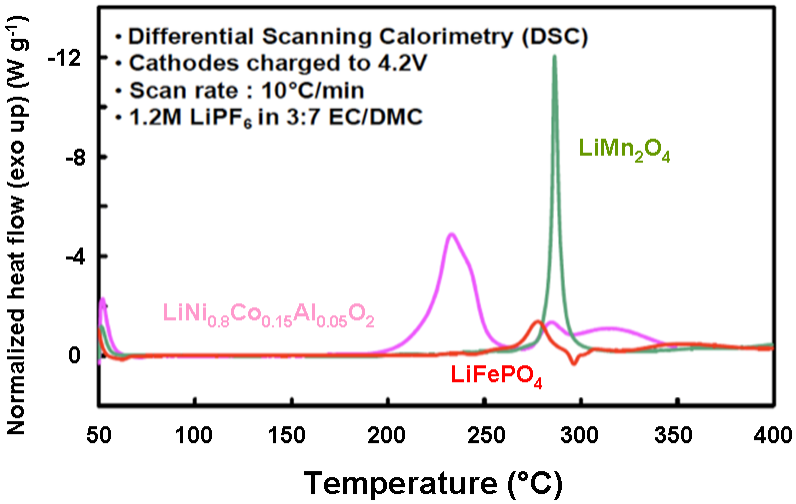

Figure 11: DSC spectra of charged LMO, NCA, and LFP cathodes with traces of electrolyte at 10 °C min^{-1} [38]

The NCA materials are less stable in the presence of the electrolyte compared to the other cathode materials. The NCA breakdown starts at 170 °C with an overall enthalpy of 941 J/g of delithiated NCA.

Wang et al [39] also studied the decomposition of the same material mixed with electrolyte and revealed an onset temperature of 160 °C and an overall enthalpy of 850 J/g of delithiated NCA.

The tested cells in Figure 10 do not necessarily have the same energy (in Wh) or even the same capacity, making it unreliable to compare the thermal behavior of the materials. Hence, the measures proposed in Figure 11. However, only the electrolyte/cathode reaction is studied, which is insufficient.

The release of oxygen after thermal degradation of the positive electrode material is a complex reaction that many scientists are interested to study. It is influenced by many parameters such as the lithiation degree of the material, its chemical composition, and the atomic arrangements in the material structure [40], [41].
The NCA-based electrode decomposes suddenly and mainly in one major step around 200 °C, releasing oxygen rapidly, unlike other positive electrode materials (such as LCO, and NMC) which decompose in several steps [42]–[45].
The released oxygen reacts immediately with the electrolyte, releasing significant heat that accelerates the transformation of the material structure. Recently, this reaction has been presented as a trigger for thermal runaway of Li-ion cells with NMC (811) materials [46]

4.2 Decomposition of the negative electrode

Only, the graphite negative electrode will be discussed in this part. The formed SEI layer on graphite particles is considered to be the first exothermic reaction during thermal runaway, with a breakdown temperature situated between 80 °C and 120 °C [11], [32]. Then, this reaction activates a second exothermic reaction between the intercalated lithium in graphite LiC_6 (case of the charged battery) and the electrolyte [47]–[50]. Most of these studies have analyzed these reactions qualitatively and were published in the early 2000s. However, the materials used in commercial cells have evolved and the understanding and quantification of these reactions remained unclear.

Besides, these two reactions are intimately correlated and very few studies are interested in understanding the degradation mechanism of the graphite-based electrode and quantifying the heat generated in the presence of electrolyte [51].

4.3 Decomposition of the electrolyte

Typically, the liquid electrolyte used in Li-ion batteries contains organic solvents with lithium salts. They are considered the main reactant in the degradation reactions during runaway. They are thermally unstable and highly flammable.

The thermal behavior of $LiPF_6$ in carbonates has been studied by Q.-S. Wang et al. [52]. It was reported that the thermal decomposition of the electrolyte solvents occurs mainly after the lithium salt decomposition as illustrated in Figure 12.

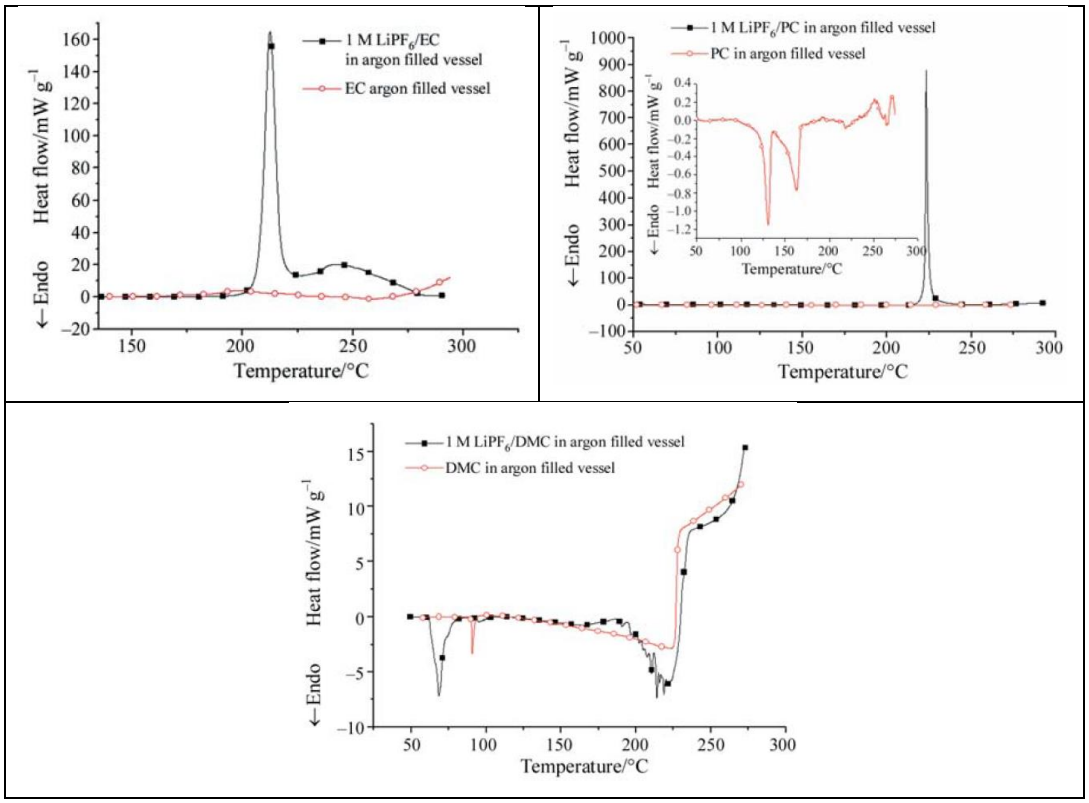

Figure 12: C80 heat flow curves of EC, PC, and DMC tested only and mixed with 1 M of $LiPF_6$ in argon filled vessel, reported from [52]

This result shows that these solvents (very present in the electrolyte of commercial cells) are degraded at roughly the same temperature. In this study, the instability of the mixture solvents/$LiPF_6$ at high temperatures was attributed to some interactions between PF_5, Li^+, and PF_6 products.

In a runaway situation, the electrolyte degrades exothermically but also can react with both electrode active material and oxygen. A decorrelation of these reactions is required to better understand and quantify the contribution of the electrolyte used in commercial cells during thermal runaway situations.

5 Impact of aging on the thermal stability of Li-ion batteries

The aging mechanisms are multiple as mentioned in section 2 and various parameters influence the aging of batteries, such as chemistry, temperature, charge-discharge rate, etc.

The differences in safety behavior between unaged and aged Li-ion cells have been studied mostly at the cell level. Aging under different conditions and its impact on the thermal behavior of Li-ion cells has been evaluated in the literature.

A. Friesen et al. [53] studied the thermal stability of 18650 cells (2.2 Ah NMC532/Graphite) using ARC tests. Some of their study results are reported in Figure 13. They show that the T_{onset} of fresh and fully charged cells starts at 90 °C and increases until reaching 125 °C with discharged cells. They related this shift to the difference in the lithiation state of the graphite electrode. The measured self-heating rate at 100 % of SOC is significantly higher than that at a low state of charge. The author correlated this observation to the higher delithiation state of the NMC material structure at 100 % SOC, which facilitates the release of oxygen that may react with the electrolyte.

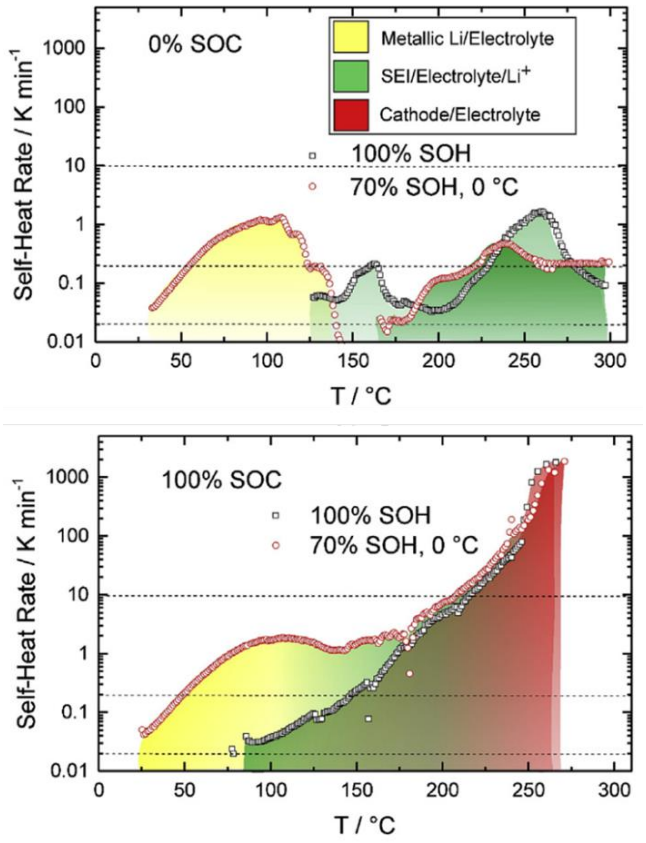

Figure 13: ARC results comparing aged and fresh 18650 NMC/C cells charged to 100 % SOC, reported from [53]

Besides, they show that after aging by cycling at 0°C the T_{onset} of the cell decreases independently of the SOC level with more heat released between 25 °C and 150 °C. They attribute this phenomenon to the presence of lithium plating accumulated during aging and its reaction with the electrolyte.

Feng et al [54] studied the impact of aging by cycling at low and high temperatures on the thermal stability of two different NMC/Graphite cells. They investigate the evolution of T_{onset}

during the ARC test with aging under different temperature conditions, as presented in Figure 14.

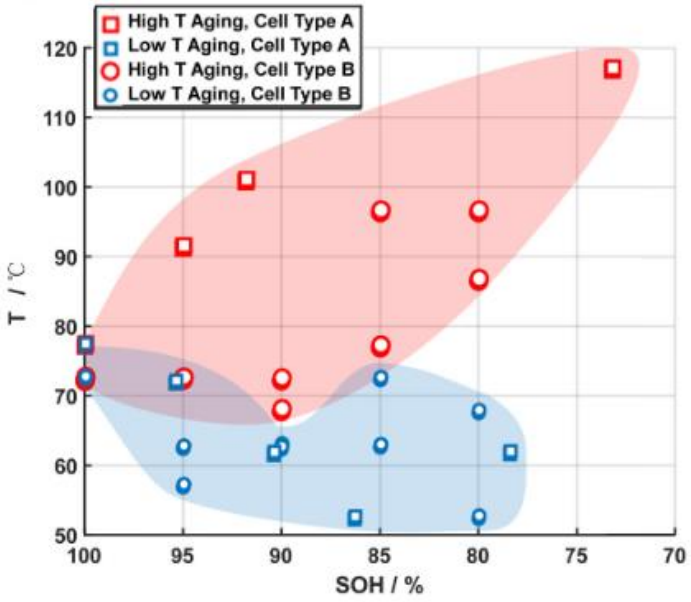

Figure 14: T_{onset} of two types of cells A and B aged at different temperatures, reported from [54]

They show that high-temperature aging resulted in a significant increase in T_{onset}, while low-temperature aging decreased the thermal stability of the cells. The increase in T_{onset} was attributed to the thickening of the SEI layer during high-temperature cycling and its protective effect. However, the decrease in T_{onset} was related to the formation of lithium dendrites during cycling at low temperatures.

M. Fleischhammer et al. [55] demonstrate that high rate cycling aging induces only a small change in the safety behavior of the cell, however, low-temperature cycling aging leads to the formation of lithium deposits and results in a decrease in the self-heating temperature of the cell under adiabatic.

P. Kuntz [56] realized a set of abusive tests (ARC test, over-charging and external short-circuit tests) to evaluate the safety of three different cells aged by cycling and in calendar mode under different temperature conditions. He showed that cycling at -20 °C generates lithium plating formation and increases the reactivity of the cell during abusive tests leading to an earlier and faster TR. On the other hand, he noticed that cells aged at high temperatures are more thermally stable and attributes this observation to the growth of a more stable SEI passivation layer which consequently slows down the cell TR.

The analyses mentioned above are interested in studying the impact of aging on the security at the cell scale and they have a common point: Aging by cycling at low temperature leads to

the formation of lithium plating and could be considered the most unfavorable aging mode in terms of safety and presents a serious hazard for the safety of Li-ion batteries.

To date, very few studies focused on the thermal behavior at the scale of the cell materials in Li-plating aging conditions. Only two relevant studies have been identified in the literature on this subject.

D. Ren et al. [27] have investigated the effects of aging on the thermal behavior of Li-ion pouch cells (24 Ah NMC111/Graphite). The stability of the cells and the electrodes were evaluated by ARC and DSC tests before and after aging under different conditions. They revealed that the cycled cells at low temperatures showed an accelerated degradation due to lithium plating on the negative electrode surface. Besides, they identify a new exothermic peak in DSC, as reported in Figure 15, exclusively when the sample negative electrode(graphite) aged at -5/1C was analyzed and associated this observation with the presence of plated lithium.

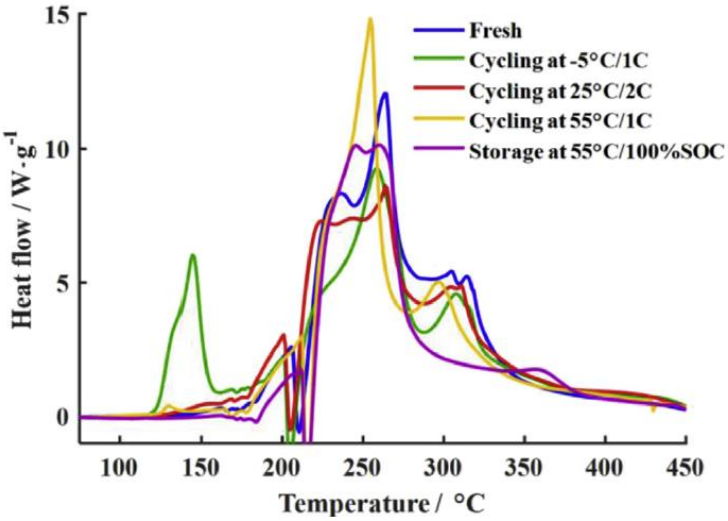

Figure 15: DSC profiles of the anode+electrolyte samples of fresh and aged cells [27]

In addition, they reported that the thermal stability of the aged positive electrodes (NMC111) remained almost the same as that of the fresh cathode.

The second study was conducted by Y. Li, D. Ren, et al. [26]. They worked with a 28.8 Ah Li-ion pouch cell (NMC532/Graphite). In the same way, they evaluated the thermal stability of the negative electrode in the fresh state and after aging by cycling at a high current (at 3C). They observed that aging in this condition accelerates the lithium plating formation on graphite electrodes similarly to aging by cycling at low temperatures. Besides, they confirm the presence of a new exothermic peak between 100 °C and 180 °C in the DSC profile of the sample anode+electrolyte and they attribute this peak to the reaction between plated lithium and the electrolyte which releases 280 J/g for total heat production of 2457 J/g for the mixture.

In summary, these results give qualitative information (at both cell and electrodes scale) that confirms the lithium metal formation during aging by cycling at high current and low temperature. In the presence of the lithium metal on the negative electrode surface, the thermal stability of the electrode degrades and consequently that of the cell.
If we know that the thermal stability of the cell depends mainly on the interaction between the negative electrode and the electrolyte, we still do not know how the presence of lithium plating influences the thermal behavior of Li-ion cells and the plated lithium-electrolyte reaction mechanism. The quantitative relationship between the safety behavior at the electrode scale (especially on graphite electrode) and that at the cell scale remains incomplete and unclear.
More quantitative information in this context is essential for the development of a model to predict the evolution of the thermal stability of the battery during abusive operating conditions.

6 Modeling for the safety of Li-ion batteries

The development of a robust tool to anticipate the safety behavior of a cell, the first scale of failures, is made necessary. This situation has motivated lithium-ion battery developers to understand and predict the safety behavior of LiBs.

The development of mathematical models to predict the thermal stability of Li-ion battery materials has been the subject of numerous research since 1999. Thermal runaway (TR) predictive models have been developed based on degradation kinetic studies of Li-ion battery materials and abusive test results.

Richard and Dahn [57] studied the thermal stability of lithium-containing mesh carbon microbeads (MCMB) materials with organic electrolytes using an accelerating rate calorimeter (ARC) under adiabatic conditions. They proposed a degradation mechanism to explain the heat generation by the exothermic reactions between intercalated lithium and electrolyte at high temperatures. Firstly, the metastable components of the SEI decompose into stable products, and then the reaction between the intercalated Li in the graphite and the electrolyte. They considered that graphite particles are subject to a new formation of SEI components resulting from the Li(C_6)/electrolyte after SEI breakdown. The thickness of SEI increases and slowed down the degradation rate of the material. Based on this degradation mechanism they developed a diffusion kinetic model using Arrhenius laws to predict the self-heating rate profile of this material in the presence of electrolyte [58]. The kinetic parameters of the exothermic reactions were determined from the ARC results.

Based on Richard and Dahn's [58] model, Hatchard et al. [59] developed a 1D model using an LCO/graphite 18650 cell to predict its thermal behavior under an oven abusive test. They

added the thermal decomposition reaction of the LCO material using kinetics parameters derived from MacNeil et al. studies [60], [61] (based on the same material and the cell thermal properties from Al Hallaj's study [62]). The same model was used later by Peng et al. [63] for other cathode materials such as $LiCoO_2$ (LCO), $LiNi_{1/3}Mn_{1/3}Co_{1/3}O_2$ (NMC111), $LiNi_{0.8}Co_{0.15}Al_{0.05}O_2$ (NCA), $LiMn_2O_4$ (LMO), and $LiFePO_4$ (LFP).

Spotnitz and Franklin [11] summarized and analyzed the exothermic degradation reactions of Li-ion batteries studied until 2003, and they improved the Hatchard et al. [59] model by adding the binder degradation reaction and the electrolyte decomposition reaction. They also extended the model to simulate various abusive tests.

Kim et al. [64] extended the 1D model used in Spotnitz and Franklin's [11] study to three dimensions (3D) and studied the non-uniform thermal distribution effects on battery TR behavior by testing different cylindrical cell sizes and local thermal hot spots.

Based on these models, many researchers have investigated the thermal safety behavior of fresh Li-ion batteries with different cell configurations and chemistry under different thermal abusive conditions [63], [65]–[72]. In most of these studies, the kinetic and the specific heat of the degradation reactions are derived from Dahn [58], Hatchard [59], Spotnitz [11], and Kim studies [64] with only differences in the amount and the chemistry of the electrode materials and electrolytes.

For most of these models, kinetic parameters of the dominant exothermic degradation reactions of negative and positive electrode materials are investigated based on Differential Scanning Calorimeter (DSC) test results using Kissinger’s method [73], [74]. Besides, enthalpies and reaction mechanisms are fitted numerically to match the experiment results [51], [75].

A different modeling approach has been proposed by Ping et al. [76] using a C80 microcalorimeter rather than DSC to study the thermal behavior of battery materials and full cells. They proposed a numerical deconvolution method based on an Exponentially Modified Gaussian (EMG) function to separate the overlapped peaks and determined kinetic parameters using deconvolution procedures and Arrhenius law.
Recently Kriston et al. [51] proposed a modeling TR study of an NMC111/graphite cell based on DSC tests combined with gas analysis. The authors proposed a modification of Richard’s degradation model for the graphite electrode and added a degradation in a multistep process for the NMC111 material. Based on this study, the authors developed recently a coupled electrical-thermal model including the chemical decomposition process and the electrical

energy [77]. The obtained TR simulation results are then analyzed by machine learning techniques.

The models used in these previous studies (named ‘State-of-the-Art models” or “SOTA models”), typically called "lumped models", simplify the description of the safety behavior in the battery system and are used to evaluate the thermal behavior of batteries in TR situations. These models do not include any “mass and material balance”. They are suited to capture the onset of TR as mentioned by Richard et al. [57], [58] on specific conditions and stoichiometry. However, because the TR consists of a complex set of reactions including the degradation of all battery components and their interactions [78], the TR is influenced by the initial stoichiometric ratio of materials present in the cells. Then, the evolution of the amount of cell reactants and products in real-time is also influenced by initial stoichiometry. In the same way, the instantaneous heat released by the cell materials during the TR event is also influenced. As a consequence, if the chemical content of the cell change, the TR may not anymore be described by these SOTA models. To summarize, the developed models allow describing TR for a specific studied technology, but their capacity to predict a TR event if the cell design change is uncertain.

Another major output of a TR model is the ability to address TR propagation problems: in a battery pack, if a TR occurs in a cell, there is a major risk of propagation of the TR from cell to cell. In this context, it is important to be able to quantify what is expelled (gases, material) from the damaged cell after the cell venting to evaluate the impacts in terms of post combustions or explosions. So, these models are not able to provide such information.

Therefore, it seems important to introduce a molar balance to the TR model. To date, few studies including the real battery chemistry in the thermal degradation processes exist in the literature. Tanaka et al. [79] were the first to simulate the evolution of the SEI degradation and formation products considering the degradation reaction of lithium ethylene di-carbonate (LEDC) components as the main SEI decomposition reaction. They parameterize and validate the model using DSC simulations of the negative electrode from the literature.
To the best of our knowledge, the first approach to include chemical species balance in the thermal degradation battery model is proposed by F. Baakes et al. [80], published in 2022. They extended the approach of Tanaka et al. [79] by including other degradation reactions and studying the impact of the equilibrium between endothermic and exothermic reactions. The authors used a semi-quantitative analysis of the thermal abuse behavior of batteries and focused only on the early phases of self-heating; considering only the first TR reactions (below 220 °C) such as salt decomposition, solvent boiling, and SEI degradation.

Most of those modeling studies focus on a restricted selection of exothermic reactions and the materials equilibrium of commercial cell materials is not well respected. This can complicate the comparison between realistic scenarios and simulation results.

Moreover, those studies focus on predictive models for specific cells with mainly high states of health. Although, the aging process has a considerable effect on the battery materials and their thermal degradation process, notably for example aging induced by cycling at low temperature with the formation of lithium plating. However, according to our state-of-the-art analysis, there is no research so far conducted on modeling the lithium plating reactivity with electrolyte and its impact on the safety behavior of Li-ion batteries.
In addition, from our point of view, the ultimate purpose of safety models is not only to predict the safety behavior of specific commercial Li-ion batteries under different operating conditions but also to predict the impact of electrode formulation evolution on safety aspects and address the problem of TR propagation at Battery pack scale.
To achieve those ultimate objectives, it seems essential to take into account the main TR chain of reactions, respecting the chemistry and the equilibrium between the electrolyte and active/inactive materials in the commercial cells. Otherwise, the chain of decomposition reactions could be different.

7 Conclusions

In this chapter, the state of the art concerning Li-ion batteries has been presented with a focus on thermal safety at the cell and material scale. Experimental and modeling studies have been mentioned and some results have been extracted to illustrate this literature review. The thermal runaway phenomenon and aging were described. The impact of aging, especially that leading to lithium plating, on battery safety was discussed.

Based on this bibliographic study, two main conclusions regarding thermal runaway mechanisms, the impact of aging on safety behavior, and the safety modeling approaches have been established as guidelines for this thesis:

- The state and type of aging have a major impact on the abusive behavior of the cell materials, in particular the Li-plating aging. More experiments with quantification work are needed to better understand these different mechanisms. This is what we propose to do in Chapters II and III. The study of thermal behavior of a fresh Graphite/Nickel-Rich cell in chapter II and the same study after aging at low temperature in chapter III.
- The modeling work should allow (based on the experimental work) to develop a prediction scheme of the thermal reactions before and after aging, which we propose in chapter IV.

8 References

[1] « The Nobel Prize in Chemistry 2019 », *NobelPrize.org*. https://www.nobelprize.org/prizes/chemistry/2019/press-release/ (consulté le 27 mai 2020).

[2] « The History of the Electric Car », *Energy.gov*. https://www.energy.gov/articles/history-electric-car (available online, May 2020).

[3] « Global EV Outlook 2022 – Analysis », *IEA*. https://www.iea.org/reports/global-ev-outlook-2022 (available online, July 2022).

[4] Q. Wang, B. Mao, S. I. Stoliarov, J. Sun, « A review of lithium ion battery failure mechanisms and fire prevention strategies », *Prog. Energy Combust. Sci.*, vol. 73, p. 95-131, July 2019, doi: 10.1016/j.pecs.2019.03.002.

[5] G. Harper *et al.*, « Recycling lithium-ion batteries from electric vehicles », *Nature*, vol. 575, nº 7781, Art. nº 7781, Nov. 2019, doi: 10.1038/s41586-019-1682-5.

[6] E. Talaie, P. Bonnick, X. Sun, Q. Pang, X. Liang, et L. F. Nazar, « Methods and Protocols for Electrochemical Energy Storage Materials Research », *Chem. Mater.*, vol. 29, nº 1, p. 90-105, Jan. 2017, doi: 10.1021/acs.chemmater.6b02726.

[7] N. Nitta, F. Wu, J. T. Lee, G. Yushin, « Li-ion battery materials: present and future », *Mater. Today*, vol. 18, nº 5, p. 252-264, June 2015, doi: 10.1016/j.mattod.2014.10.040.

[8] S. S. Zhang, « A review on electrolyte additives for lithium-ion batteries », *J. Power Sources*, vol. 162, nº 2, p. 1379-1394, Nov. 2006, doi: 10.1016/j.jpowsour.2006.07.074.

[9] « Are lithium ion batteries becoming unsafe? », *Qnovo*, 17 décembre 2014. https://qnovo.com/are-lithium-ion-batteries-becoming-unsafe/ (available online, May 2020).

[10] S. J. An, J. Li, C. Daniel, D. Mohanty, S. Nagpure, D. L. Wood, « The state of understanding of the lithium-ion-battery graphite solid electrolyte interphase (SEI) and its relationship to formation cycling », *Carbon*, vol. 105, p. 52-76, Aug. 2016, doi: 10.1016/j.carbon.2016.04.008.

[11] R. Spotnitz, J. Franklin, « Abuse behavior of high-power, lithium-ion cells », *J. Power Sources*, vol. 113, p. 81-100, Jan. 2003, doi: 10.1016/S0378-7753(02)00488-3.

[12] N. Dufour, « Modélisation multi-physique de l'électrode de graphite au sein d'une batterie lithium-ion : Etude des hétérogénéités et des mécanismes de vieillissement », Ph-D thesis, Université Grenoble Alpes, 2019. Available online, May 2020. r https://tel.archives-ouvertes.fr/tel-02148211

[13] K. Xu, « Electrolytes and Interphases in Li-Ion Batteries and Beyond », *Chem. Rev.*, vol. 114, nº 23, p. 11503-11618, Dec. 2014, doi: 10.1021/cr500003w.

[14] A. Wang, S. Kadam, H. Li, S. Shi, Y. Qi, « Review on modeling of the anode solid electrolyte interphase (SEI) for lithium-ion batteries », *Npj Comput. Mater.*, vol. 4, n° 1, Dec. 2018, doi: 10.1038/s41524-018-0064-0.

[15] S. K. Heiskanen, J. Kim, B. L. Lucht, « Generation and Evolution of the Solid Electrolyte Interphase of Lithium-Ion Batteries », *Joule*, vol. 3, n° 10, p. 2322-2333, Oct. 2019, doi: 10.1016/j.joule.2019.08.018.

[16] M. Palacín, « Understanding ageing in Li-ion batteries: A chemical issue », *Chem. Soc. Rev.*, vol. 47, May 2018, doi: 10.1039/C7CS00889A.

[17] J. Illig, « Physically based Impedance Modelling of Lithium-Ion Cells », *Phys. Based Impedance Model. Lithium-Ion Cells*, p. 1-202, Jan. 2014, doi: 10.5445/KSP/1000042281.

[18] P. Keil *et al.*, « Calendar Aging of Lithium-Ion Batteries », *J. Electrochem. Soc.*, vol. 163, n° 9, p. A1872, July 2016, doi: 10.1149/2.0411609jes.

[19] D. Galatro, C. D. Silva, D. A. Romero, O. Trescases, C. H. Amon, « Challenges in data-based degradation models for lithium-ion batteries », *Int. J. Energy Res.*, vol. 44, n° 5, p. 3954-3975, 2020, doi: 10.1002/er.5196.

[20] P. Arora, R. E. White, M. Doyle, « Capacity Fade Mechanisms and Side Reactions in Lithium-Ion Batteries », *J. Electrochem. Soc.*, vol. 145, n° 10, p. 3647, Oct. 1998, doi: 10.1149/1.1838857.

[21] C. Hendricks, N. Williard, S. Mathew, M. Pecht, « A failure modes, mechanisms, and effects analysis (FMMEA) of lithium-ion batteries », *J. Power Sources*, vol. 297, p. 113-120, Nov. 2015, doi: 10.1016/j.jpowsour.2015.07.100.

[22] E. Redondo-Iglesias, « Étude du vieillissement des batteries lithium-ion dans les applications “véhicule électrique” : Combinaison des effets de vieillissement calendaire et de cyclage. », 2017, Ph-D thesis, available online, https://tel.archives-ouvertes.fr/tel-01668529, Université Lyon 1.

[23] T. Waldmann *et al.*, « Interplay of Operational Parameters on Lithium Deposition in Lithium-Ion Cells: Systematic Measurements with Reconstructed 3-Electrode Pouch Full Cells », *J. Electrochem. Soc.*, vol. 163, p. A1232-A1238, Jan. 2016, doi: 10.1149/2.0591607jes.

[24] M. Ecker, P. Shafiei Sabet, D. Sauer, « Influence of operational condition on lithium plating for commercial lithium-ion batteries – Electrochemical experiments and post-mortemanalysis », *Appl. Energy*, vol. 206, p. 934-9461, Nov. 2017, doi: 10.1016/j.apenergy.2017.08.034.

[25] M. Petzl et M. A. Danzer, « Nondestructive detection, characterization, and quantification of lithium plating in commercial lithium-ion batteries », *J. Power Sources*, vol. 254, p. 80-87, May 2014, doi: 10.1016/j.jpowsour.2013.12.060.

[26] Y. Li, X. Feng, D. Ren, M. Ouyang, L. Lu, X. Han, « Thermal Runaway Triggered by Plated Lithium on the Anode after Fast Charging », *ACS Appl. Mater. Interfaces*, vol. 11, n° 50, p. 46839-46850, Dec. 2019, doi: 10.1021/acsami.9b16589.

[27] D. Ren *et al.*, « A comparative investigation of aging effects on thermal runaway behavior of lithium-ion batteries », *eTransportation*, vol. 2, p. 100034, Nov. 2019, doi: 10.1016/j.etran.2019.100034.

[28] M. Winter, « The Solid Electrolyte Interphase – The Most Important and the Least Understood Solid Electrolyte in Rechargeable Li Batteries », *Z. Für Phys. Chem.*, vol. 223, n° 10-11, p. 1395-1406, 2009, doi: 10.1524/zpch.2009.6086.

[29] T. Waldmann, M. Wilka, M. Kasper, M. Fleischhammer, M. Wohlfahrt-Mehrens, « Temperature dependent ageing mechanisms in Lithium-ion batteries – A Post-Mortem study », *J. Power Sources*, vol. 262, p. 129-135, Sept. 2014, doi: 10.1016/j.jpowsour.2014.03.112.

[30] P. Kuntz *et al.*, « Identification of Degradation Mechanisms by Post-Mortem Analysis for High Power and High Energy Commercial Li-Ion Cells after Electric Vehicle Aging », *Batteries*, vol. 7, n° 3, Art. n° 3, Sept. 2021, doi: 10.3390/batteries7030048.

[31] D. Ouyang, M. Chen, Q. Huang, J. Weng, Z. Wang, J. Wang, « A Review on the Thermal Hazards of the Lithium-Ion Battery and the Corresponding Countermeasures », *Appl. Sci.*, vol. 9, n° 12, Art. n° 12, Jan. 2019, doi: 10.3390/app9122483.

[32] Q. Wang, P. Ping, X. Zhao, G. Chu, J. Sun, C. Chen, « Thermal runaway caused fire and explosion of lithium-ion battery », *J. Power Sources*, vol. 208, p. 210-224, June 2012, doi: 10.1016/j.jpowsour.2012.02.038.

[33] T. T. D. Nguyen *et al.*, « Understanding the Thermal Runaway of Ni-Rich Lithium-Ion Batteries », *World Electr. Veh. J.*, vol. 10, n° 4, Art. n° 4, Dec. 2019, doi: 10.3390/wevj10040079.

[34] D. Galatro, M. Al-Zareer, C. Da Silva, D. Romero, et C. Amon, « Thermal behavior of lithium-ion batteries: aging, heat generation, thermal management and failure », *Front. Heat Mass Transf. FHMT*, vol. 14, n° 0, Feb. 2020, available online, Aug. 2022. http://thermalfluidscentral.org/journals/index.php/Heat_Mass_Transfer/article/view/1104

[35] O. S. Mendoza-Hernandez, H. Ishikawa, Y. Nishikawa, Y. Maruyama, et M. Umeda, « Cathode material comparison of thermal runaway behavior of Li-ion cells at different state of charges including over charge », *J. Power Sources*, vol. 280, p. 499-504, April. 2015, doi: 10.1016/j.jpowsour.2015.01.143.

[36] X. Feng *et al.*, « Key Characteristics for Thermal Runaway of Li-ion Batteries », *Energy Procedia*, vol. 158, p. 4684-4689, Feb. 2019, doi: 10.1016/j.egypro.2019.01.736.

[37] D. H. Doughty, « Vehicle Battery Safety Roadmap Guidance », NREL/SR-5400-54404, 1055366, Oct. 2012. doi: 10.2172/1055366.

[38] K. Zaghib *et al.*, « Enhanced thermal safety and high power performance of carbon-coated LiFePO4 olivine cathode for Li-ion batteries », *J. Power Sources*, vol. 219, p. 36-44, Dec. 2012, doi: 10.1016/j.jpowsour.2012.05.018.

[39] Y. Wang, J. Jiang, J. Dahn, « The reactivity of delithiated Li(Ni1/3Co1/3Mn1/3)O2, Li(Ni0.8Co0.15Al0.05)O2 or LiCoO2 with non-aqueous electrolyte », *Electrochem. Commun.*, vol. 9, p. 2534-2540, Oct. 2007, doi: 10.1016/j.elecom.2007.07.033.

[40] S. Sharifi-Asl, J. Lu, K. Amine, R. Shahbazian-Yassar, « Oxygen Release Degradation in Li-Ion Battery Cathode Materials: Mechanisms and Mitigating Approaches », *Adv. Energy Mater.*, vol. 9, n° 22, p. 1900551, 2019, doi: 10.1002/aenm.201900551.

[41] M. M. Besli *et al.*, « Thermally-driven mesopore formation and oxygen release in delithiated NCA cathode particles », *J. Mater. Chem. A*, vol. 7, n° 20, p. 12593-12603, May 2019, doi: 10.1039/C9TA01720H.

[42] H. M. Barkholtz *et al.*, « Multi-scale thermal stability study of commercial lithium-ion batteries as a function of cathode chemistry and state-of-charge », *J. Power Sources*, vol. 435, p. 226777, Sept. 2019, doi: 10.1016/j.jpowsour.2019.226777.

[43] I. Belharouak, D. Vissers, K. Amine, « Thermal Stability of the Li (Ni0.8Co0.15Al0.05) O2 Cathode in the Presence of Cell Components », *J. Electrochem. Soc.*, vol. 153, n° 11, p. A2030, Sept. 2006, doi: 10.1149/1.2336994.

[44] A. W. Golubkov *et al.*, « Thermal runaway of commercial 18650 Li-ion batteries with LFP and NCA cathodes – impact of state of charge and overcharge », *RSC Adv.*, vol. 5, n° 70, p. 57171-57186, June 2015, doi: 10.1039/C5RA05897J.

[45] R. C. Shurtz, J. C. Hewson, « Review—Materials Science Predictions of Thermal Runaway in Layered Metal-Oxide Cathodes: A Review of Thermodynamics », *J. Electrochem. Soc.*, vol. 167, n° 9, p. 090543, May 2020, doi: 10.1149/1945-7111/ab8fd9.

[46] Y. Li *et al.*, « Thermal runaway mechanism of lithium-ion battery with LiNi0.8Mn0.1Co0.1O2 cathode materials », *Nano Energy*, vol. 85, p. 105878, July 2021, doi: 10.1016/j.nanoen.2021.105878.

[47] J. Yamaki, H. Takatsuji, T. Kawamura, M. Egashira, « Thermal stability of graphite anode with electrolyte in lithium-ion cells », *Solid State Ion.*, vol. 148, n° 3, p. 241-245, June 2002, doi: 10.1016/S0167-2738(02)00060-7.

[48] T. Kawamura, A. Kimura, M. Egashira, S. Okada, et J.-I. Yamaki, « Thermal stability of alkyl carbonate mixed-solvent electrolytes for lithium ion cells », *J. Power Sources*, vol. 104, nº 2, p. 260-264, Feb. 2002, doi: 10.1016/S0378-7753(01)00960-0.

[49] N.-S. Choi, I. A. Profatilova, S.-S. Kim, E.-H. Song, « Thermal reactions of lithiated graphite anode in LiPF6-based electrolyte », *Thermochim. Acta*, vol. 480, nº 1, p. 10-14, Dec. 2008, doi: 10.1016/j.tca.2008.09.017.

[50] E. P. Roth, D. H. Doughty, et J. Franklin, « DSC investigation of exothermic reactions occurring at elevated temperatures in lithium-ion anodes containing PVDF-based binders », *J. Power Sources*, vol. 134, nº 2, p. 222-234, Aug. 2004, doi: 10.1016/j.jpowsour.2004.03.074.

[51] A. Kriston, I. Adanouj, V. Ruiz, et A. Pfrang, « Quantification and simulation of thermal decomposition reactions of Li-ion battery materials by simultaneous thermal analysis coupled with gas analysis », *J. Power Sources*, vol. 435, p. 226774, Sept. 2019, doi: 10.1016/j.jpowsour.2019.226774.

[52] Q.-S. Wang, J.-H. Sun, G.-Q. Chu, X.-L. Yao, et C.-H. Chen, « Effect of LiPF6 on the thermal behaviors of four organic solvents for lithium ion batteries », *J. Therm. Anal. Calorim.*, vol. 89, nº 1, p. 245-250, July. 2007, doi: 10.1007/s10973-006-7534-1.

[53] A. Friesen *et al.*, « Impact of cycling at low temperatures on the safety behavior of 18650-type lithium ion cells: Combined study of mechanical and thermal abuse testing accompanied by post-mortem analysis », *J. Power Sources*, vol. 334, p. 1-11, Dec. 2016, doi: 10.1016/j.jpowsour.2016.09.120.

[54] X. Feng *et al.*, « Investigating the thermal runaway mechanisms of lithium-ion batteries based on thermal analysis database », *Appl. Energy*, vol. 246, p. 53-64, July. 2019, doi: 10.1016/j.apenergy.2019.04.009.

[55] M. Fleischhammer, T. Waldmann, G. Bisle, B.-I. Hogg, et M. Wohlfahrt-Mehrens, « Interaction of cyclic ageing at high-rate and low temperatures and safety in lithium-ion batteries », *J. Power Sources*, vol. 274, p. 432-439, Jan. 2015, doi: 10.1016/j.jpowsour.2014.08.135.

[56] P. Kuntz, « Evolution du comportement sécuritaire de batterie lithium-ion pendant leur vieillissement », Ph-D thesis, Université Grenoble Alpes, 2020. Available online, April 2021. http://www.theses.fr/2020GRALI069

[57] M. N. Richard, J. R. Dahn, « Accelerating Rate Calorimetry Study on the Thermal Stability of Lithium Intercalated Graphite in Electrolyte. I. Experimental », *J. Electrochem. Soc.*, vol. 146, nº 6, p. 2068, June 1999, doi: 10.1149/1.1391893.

[58] M. N. Richard J. R. Dahn, « Accelerating Rate Calorimetry Study on the Thermal Stability of Lithium Intercalated Graphite in Electrolyte. II. Modeling the Results and Predicting

Differential Scanning Calorimeter Curves », *J. Electrochem. Soc.*, vol. 146, nº 6, p. 2078, June 1999, doi: 10.1149/1.1391894.

[59] T. Hatchard, D. MacNeil, A. Basu, J. Dahn, « Thermal Model of Cylindrical and Prismatic Lithium-Ion Cells », *J. Electrochem. Soc. - J ELECTROCHEM SOC*, vol. 148, July 2001, doi: 10.1149/1.1377592.

[60] D. D. MacNeil, D. Larcher, J. R. Dahn, « Comparison of the Reactivity of Various Carbon Electrode Materials with Electrolyte at Elevated Temperature », *J. Electrochem. Soc.*, vol. 146, nº 10, p. 3596, Oct. 1999, doi: 10.1149/1.1392520.

[61] D. D. MacNeil, L. Christensen, J. Landucci, J. M. Paulsen, J. R. Dahn, « An Autocatalytic Mechanism for the Reaction of LixCoO2 in Electrolyte at Elevated Temperature », *J. Electrochem. Soc.*, vol. 147, nº 3, p. 970, Mar. 2000, doi: 10.1149/1.1393299.

[62] S. Al Hallaj, H. Maleki, J. S. Hong, J. R. Selman, « Thermal modeling and design considerations of lithium-ion batteries », *J. Power Sources*, vol. 83, nº 1, p. 1-8, Oct. 1999, doi: 10.1016/S0378-7753(99)00178-0.

[63] P. Peng, F. Jiang, « Thermal safety of lithium-ion batteries with various cathode materials: A numerical study », *Int. J. Heat Mass Transf.*, vol. 103, p. 1008-1016, Dec. 2016, doi: 10.1016/j.ijheatmasstransfer.2016.07.088.

[64] G.-H. Kim, A. Pesaran, R. Spotnitz, « Three-Dimensional Thermal Abuse Model for Lithium-Ion Cells », *J. Power Sources*, vol. 170, p. 476-489, July 2007, doi: 10.1016/j.jpowsour.2007.04.018.

[65] C. F. Lopez, J. A. Jeevarajan, P. P. Mukherjee, « Characterization of Lithium-Ion Battery Thermal Abuse Behavior Using Experimental and Computational Analysis », *J. Electrochem. Soc.*, vol. 162, nº 10, p. A2163, Aug. 2015, doi: 10.1149/2.0751510jes.

[66] P. Peng, F. Jiang, « Thermal behavior analyses of stacked prismatic LiCoO2 lithium-ion batteries during oven tests », *Int. J. Heat Mass Transf.*, vol. 88, p. 411-423, Sept. 2015, doi: 10.1016/j.ijheatmasstransfer.2015.04.101.

[67] P. T. Coman, S. Rayman, R. E. White, « A lumped model of venting during thermal runaway in a cylindrical Lithium Cobalt Oxide lithium-ion cell », *J. Power Sources*, vol. 307, p. 56-62, Mar. 2016, doi: 10.1016/j.jpowsour.2015.12.088.

[68] X. Feng *et al.*, « Thermal runaway propagation model for designing a safer battery pack with 25 Ah LiNiCoMnO2 large format lithium ion battery », *Appl. Energy*, vol. 154, p. 74-91, Sept. 2015, doi: 10.1016/j.apenergy.2015.04.118.

[69] P. T. Coman, E. C. Darcy, C. T. Veje, R. E. White, « Numerical analysis of heat propagation in a battery pack using a novel technology for triggering thermal runaway », *Appl. Energy*, vol. 203, p. 189-200, Oct. 2017, doi: 10.1016/j.apenergy.2017.06.033.

[70] D. Ren *et al.*, « An electrochemical-thermal coupled overcharge-to-thermal-runaway model for lithium ion battery », *J. Power Sources*, vol. 364, p. 328-340, Oct. 2017, doi: 10.1016/j.jpowsour.2017.08.035.

[71] C. Qi, Y. Zhu, F. Gao, K. Yang, Q. Jiao, « Mathematical model for thermal behavior of lithium ion battery pack under overcharge », *Int. J. Heat Mass Transf.*, vol. 124, p. 552-563, Sept. 2018, doi: 10.1016/j.ijheatmasstransfer.2018.03.100.

[72] Y. Jia, M. Uddin, Y. Li, J. Xu, « Thermal runaway propagation behavior within 18,650 lithium-ion battery packs: A modeling study », *J. Energy Storage*, vol. 31, p. 101668, Oct. 2020, doi: 10.1016/j.est.2020.101668.

[73] H. E. Kissinger, « Reaction Kinetics in Differential Thermal Analysis », *Anal. Chem.*, vol. 29, nº 11, p. 1702-1706, Nov. 1957, doi: 10.1021/ac60131a045.

[74] H. E. Kissinger, « Variation of Peak Temperature With Heating Rate in Differential Thermal Analysis », 1956. doi: 10.6028/jres.057.026.

[75] D. Ren *et al.*, « Model-based thermal runaway prediction of lithium-ion batteries from kinetics analysis of cell components », *Appl. Energy*, vol. 228, p. 633-644, Oct. 2018, doi: 10.1016/j.apenergy.2018.06.126.

[76] P. Ping, Q. Wang, Y. Chung, J. Wen, « Modelling electro-thermal response of lithium-ion batteries from normal to abuse conditions », *Appl. Energy*, vol. 205, p. 1327-1344, Nov. 2017, doi: 10.1016/j.apenergy.2017.08.073.

[77] A. Kriston, A. Podias, I. Adanouj, A. Pfrang, « Analysis of the Effect of Thermal Runaway Initiation Conditions on the Severity of Thermal Runaway—Numerical Simulation and Machine Learning Study », *J. Electrochem. Soc.*, vol. 167, nº 9, p. 090555, Jan. 2020, doi: 10.1149/1945-7111/ab9b0b.

[78] X. Feng, D. Ren, X. He, M. Ouyang, « Mitigating Thermal Runaway of Lithium-Ion Batteries », *Joule*, vol. 4, nº 4, p. 743-770, April 2020, doi: 10.1016/j.joule.2020.02.010.

[79] N. Tanaka, W. G. Bessler, « Numerical investigation of kinetic mechanism for runaway thermo-electrochemistry in lithium-ion cells », *Solid State Ion.*, vol. 262, p. 70-73, Sept. 2014, doi: 10.1016/j.ssi.2013.10.009.

[80] F. Baakes *et al.*, « Unveiling the interaction of reactions and phase transition during thermal abuse of Li-ion batteries », *J. Power Sources*, vol. 522, p. 230881, Feb. 2022, doi: 10.1016/j.jpowsour.2021.230881.

Chapter II: Thermal behavior of a fresh Graphite/Nickel-Rich cell

Contents

List of tables

List of figures

The main desirable features associated with the design of lithium-ion batteries are mainly: safety, long life, high energy, and high-power density. The safety of Li-ion batteries is particularly important due to the thermal runaway (TR) phenomenon. TR is mainly caused by the use of Li-ion batteries in extreme conditions and occurs as a result of thermal stress. When the operating temperature limit is exceeded, multiple exothermic reactions can self-activate involving the different materials of the battery to release heat. The temperature inside the battery increases consequently. The heat release can lead to ignition or even the explosion of the battery. This process (as presented in Figure 1) leads at the end to the TR of the battery.

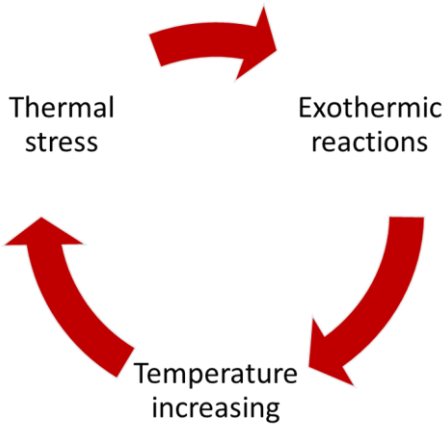

Figure 1: Positive feedback loop leading to the TR phenomenon

The heat generated by the TR exothermic reactions depends on the chemistry and the state of charge (SOC) of the battery. The most unfavorable situation identified experimentally is typically obtained with a charged cell (i.e. lithiated negative electrode and delithiated positive electrode). Our study in this thesis project focuses particularly on this case.

Depending on the battery-cell manufacturer, different active materials, electrolytes, and many additives are used. Thus, commercial Li-ion batteries do not have the same sensitivity to the TR phenomenon.

The previous thermal behavior studies on Li-ion battery materials have focused, in most cases, on performing experiments using synthetized materials and standard mixtures of electrolytes. This approach allows good control of the cell materials composition and experiments without necessarily ensuring representative data of a commercial battery.

In this thesis, our approach is mainly to investigate the thermal stability of a commercial Nickel-rich 18650 cell by studying each of its components and their interactions in abusive conditions. This chapter is dedicated to a detailed study of the thermal stability of the cell materials, each one separately as well as their interactions. The objective is to understand the thermal degradation mechanism of these commercial cell materials and to identify the main exothermic reactions that can generate thermal safety problems leading to TR.

In the first section of this chapter, the established experimental methodology is described. The second and the third sections are dedicated to the discussion of the thermal behavior results of the cell materials. In the last part, an evaluation of the SOC impact on the behavior of the studied materials is presented.

1 The experimental methodology

In this section, some details related to the selected commercial cell are presented. Then, the different analytical techniques employed in this work are briefly described. Finally, the first investigations conducted to identify the key experimental conditions are described and detailed.

1.1 The selected commercial cell

Due to their high energy density, Nickel-rich layered metal oxides, such as NCA, are still considered promising positive electrode candidates. However, some problems related to their structural stability (release of oxygen at high temperature) increase the risk of TR in the presence of liquid electrolytes [1].

In this thesis, we chose a commercial Nickel-rich cell manufactured by SAMSUNG SDI: INR18650-32E. Some specifications of the cell, including the operating limits recommended by the manufacturer, are listed in Table 1.

Table 1: Samsung INR18650-32E specifications [2]

Item	Specification
Nominal capacity	3000 mAh @ 0.2C
Specific energy density	237 Wh/kg
Charging/ Discharge voltage	4.2 V / 2.5 V
Nominal voltage	3.7 V
Cell weight	50 g max

According to previous work carried out at CEA [3], the INR18650-32E is mainly composed of: $LiNi_{0.78}Co_{0.2}Al_{0.02}O_2$ for the positive electrode, graphite for the negative electrode, and a separator based on polyethylene (PE) coated with AlOOH (single layer).

The chemistry of the cell electrolyte is a mixture of ethylene carbonate (EC) 15 %, propylene carbonate (PC) 18 %, dimethyl carbonate (DMC) 29 %, and fluoroethylene carbonate (FEC) 38 % with traces of propionate and succinonitrile. These results are based on SEM (Scanning Electronic Microscopy) coupled with EDX (Energy-dispersive X-ray spectrometer) analysis and GC-MS (Gas Chromatography coupled with Mass Spectroscopy) analysis.

1.2 Cell preconditioning and active material extraction

The received INR18650-32E cells are stored at 50 % of SOC in a controlled temperature room. For the following studies, analyses are performed using materials extracted from discharged and charged cells at respectively 0 % and 100 % of SOC.

CC-CV (Constant Current up to a Constant Voltage) charging/discharging operation was employed using the typical capacity value of the cell. After charging, the voltage and capacity at the end of the operation are close to 4.2 V for a full capacity of 3.2 Ah, as displayed in Figure 2, which is consistent with the manufacturer's data.

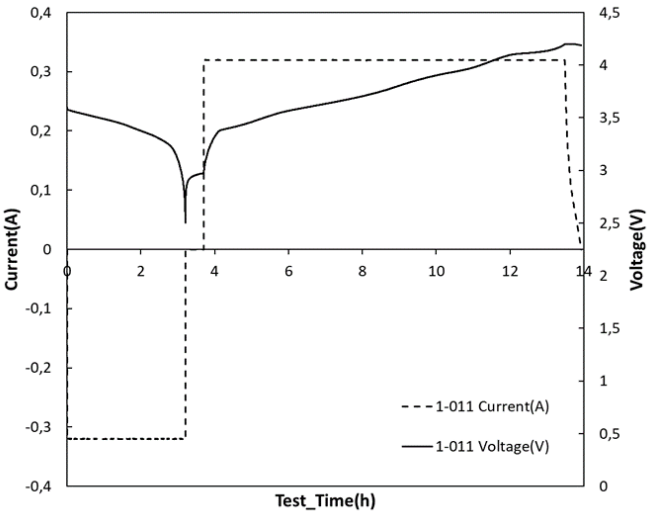

Figure 2: CC-CV charging curve of the INR18650-32E cell

After the SOC calibration, charged and discharged cells were opened in an MBraun MB 200B glove box filled with argon, with adequate atmosphere conditions (H_2O < 0.1 ppm; O_2 < 0.1 ppm) to avoid the degradation of highly air-sensitive materials embedded in the cell. Note that particular attention must be considered during the disassembly of the cell at charged state to avoid the short circuit between electrodes.

Then, the cell components are collected and characterized. The obtained results are reported in Table 2 and Table 3.

Table 2: Dimensions and thickness of the Samsung INR18650-32E electrodes

INR18650-32E	Dimensions (mm)	Electrode thickness (µm)	Current collector thickness (µm)
Negative electrode	660 x 59.5	87 +/- 1 µm	13
Positive electrode	610 x 58	65 +/- 1 µm	15

The thickness measurements were performed, using a TMI digital micrometer, on discharged electrodes i.e., delithiated graphite electrode and lithiated NCA electrode. In the charged state, the electrode thickness might change by ±15µm.

Table 3: Measured weight of delithiated Samsung INR18650-32E components

Samsung INR18650-32E	Materials	weight (g)
Casing	Steel	8.8
Mandrel	Steel	0.4
Separator	PE-AlOOH	1.3
Electrolyte	$LiPF_6$, EC/PC/DMC/FEC	4.2
Negative electrode	Current collector: copper	4.56
	Active material: graphite	12
Positive electrode	Current collector: aluminum	1.44
	Active material: NCA	17
Total cell weight		49.7

The total amount of the cell electrolyte was calculated based on electrode porosity.
A Helium pycnometer measurement was performed and a mean porosity of 20% was obtained. The calculated weight of electrolyte is consistent with the average weight announced by Li-ion battery-cell manufacturers; we noticed that the amount of electrolyte is between 10 – 12 % of the total mass of the battery for 18650 cells format [4].

1.3 Methods of materials characterization

To achieve a comprehensive study of the thermal degradation of the cell materials, multiple characterization analyses were implemented. In the following parts, the analysis techniques employed in this work are described in detail according to the context of use.

1.3.1 Differential scanning calorimetry (DSC)

The Differential Scanning Calorimetry technique (DSC) was selected to investigate the thermal behavior of the commercial cell materials. This differential calorimetric technique evaluates the power generated/absorbed by the analyzed material during a temperature scanning at constant pressure conditions. The scan is performed in a pre-defined temperature range, various temperature-scanning rates can be applied.
The differential calorimeter is composed of a furnace in which the sample is inserted as well as a reference as displayed in Figure 3.

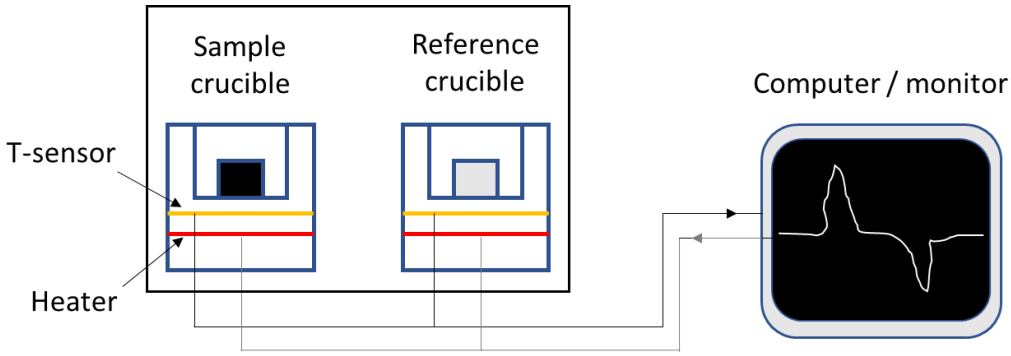

Figure 3: Simplified scheme of DSC analysis principle

The sample and the reference material are subjected to the same heating/cooling program and the temperature varies linearly with time. However, they are heated separately in such a way that their temperatures remain equal. The temperature sensors measure the difference in temperature between the 2 crucibles throughout the heating process. Then, the power that is required to follow this instruction is evaluated and converted into a heat flow by the computer. At the end of the analysis, a curve is obtained showing the heat flow as a function of temperature/time. The obtained DSC profile is directly related to physical or/and chemical transformations that the sample underwent during the analysis.

The DSC tests were performed using DSC 404 F1 Pegasus® high-temperature differential scanning calorimeter (Netzsch, Germany) with a steel oven (Figure 4). High-pressure crucibles made of chrome-nickel steel (Ø 6 mm, 30 µl) with a gold-plated surface were used.

Figure 4: high-temperature DSC 404 F1 Pegasus® (Netzsch, Germany)

The behavior of the sample crucible was compared to a reference empty crucible. Looking at the size of the crucible, the sample needs to be small enough to ensure temperature homogeneity inside the material during heating. Then, the weight of the analyzed samples was maintained in the range of 3 – 5 mg.

DSC samples were prepared inside the glove box. Negative and positive electrode materials were removed from the current collector using a stainless-steel micro spoon spatula. The weight of the sample and the crucible was measured before and after assembling using a Mettler Toledo MS-105 balance (±0.04 mg). Figure 5 summarizes the preparation steps of samples for DSC analysis.

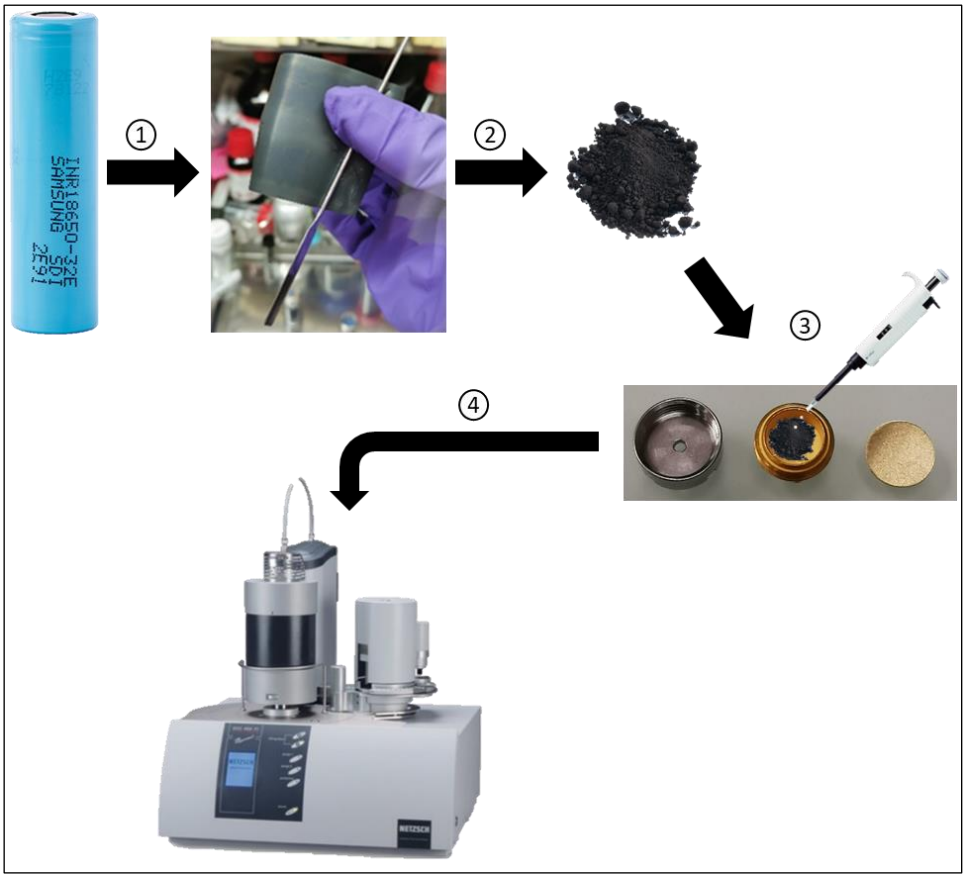

Figure 5: 1) Samsung INR18650-32E cell, 2) reducing electrode to powder, 3) weighing the sample and adding electrolyte, 4) sealing the crucible and launching the DSC analysis

Initially, a calibration step was performed using CsCl, Zn, Bi, In, Sn, biphenyl, and benzoic acid at 2, 5, and 15 $K.min^{-1}$ heating rates. All DSC measurements were performed from 30 °C to 400 °C starting with a 20 min isothermal phase at 30°C under a nitrogen atmosphere. At the end of the dynamic heating phase, 10 min isothermal phase was applied. To ensure reproducibility, measurements were repeated.

1.3.2 X-ray photoelectron spectroscopy (XPS)

X-ray photoelectron spectroscopy (XPS) is a surface analysis technique allowing to probe the first microns of the material. The analysis consists of irradiating the elements at the surface of the material with X-rays. This irradiation generates the ejection of photoelectrons. These photoelectrons are characteristic of the material surface.
The emitted kinetic energy of the photoelectrons is detected and measured with an analyzer and a detector. The measured kinetic energy allows us to identify the binding energy of the chemical elements. This gives information about their atomic or molecular environment. All chemical elements of the periodic classification are detected except hydrogen and helium.

XPS is one of the few methods that allow studying the solid electrolyte interphase (SEI) compounds and their decomposition products [5],[6]. In this work, XPS is employed to characterize the change of the chemistry at the surface of the cell electrode materials. The samples were prepared in the glove box under an inert atmosphere and then transferred to the XPS instrument using a sealed bag.

XPS analysis was performed on a PHI Versaprobe II spectrometer. After being processed in the ATG setup, electrode samples were introduced into the glove box. Then samples are transferred to the XPS chamber using an appropriate air-tight transfer module. The incident X-ray source was extracted from a monochromated Al anode (hv = 1486.7 eV). Charge effects were compensated by using a double neutralization system (electron flood gun at ~14 eV & Ar^+ beam at ~70 eV). All spectra were calibrated by using the F 1s peak in LiF at 685 eV.

High-resolution spectra were recorded with a pass energy of 23 eV corresponding to an energy resolution of ~0.6 eV. Multipak® software was used for spectra resolution. The probing depth here was around 10 nm.

1.3.3 Time Of Flight - Secondary Ion Mass Spectrometry (TOF-SIMS)

Time-of-flight secondary ion mass spectrometry (TOF-SIMS) allows the characterization of the chemical composition at the extreme surface of materials (several nanometers). It is typically used in complementarity with XPS to get more information about the chemical changes at the material surface.
A primary ion source bombards the first nanometres of the sample surface and produces ionized fragments called secondary ions. The emitted ions are concentrated and accelerated in an analyzer called the time-of-flight analyzer. The travel time of the secondary ions inside the analyzer is proportional to their masses. They are selected and separated according to their mass/ charge ratio (m/z). Using a primary ion beam scanning device, a cartography of the different elements present on the material surface is obtained, depending on their m/z ratio.

Typically, two pieces of information are obtained by TOF-SIMS analysis: mass spectrums and mass concentration depth profiles. The mass spectrums give the intensity of elements (proportional to the number of secondary ions) as a function of the mass-to-charge ratio (m/z). The mass concentration depth profiles are obtained by alternating analysis and abrasion sequences on the sample surface.

The analyses were carried out on a TOF.SIMS 5 from Ion Tof. The spectra were conducted at negative polarity, with a 30 kV Bi^+ primary beam, in a non-interlaced mode (pause of 1 s to take account of charge effects) and a cycle time of 100 µs. An area of 300x300 µm was sputtered with a 1 kV Cs^+ beam to achieve the profile concentration of the different molecular fragments in an 80x80 µm window centered in the sputtered crater.
The XPS and TOF-SIMS measurements were driven by E. De Vito (PhD) at CEA-Grenoble.

1.3.4 X-Ray Diffraction (XRD)

X-Ray Diffraction (XRD) analysis provides relevant information on the structure of crystalline materials. It is based on the analysis of the diffraction patterns obtained when the sample is exposed to a monochromatic x-ray beam. Diffracted beams are detected and analyzed based on Bragg's law ($2d.\sin(\theta)=n\lambda$); the angle of the diffracted beam (incident beam wavelength: λ) is directly related to the distance d between the atomic planes in a crystal mesh. The data acquisition consists in recording the intensity of the diffracted beams by simultaneously rotating the sample to an angle θ and the detector to an angle 2θ. The XRD result is composed of a set of peaks allowing the identification of the different crystallographic phases of the analyzed material.

The analysis was conducted on Bruker AXS Advance II (Figure 6) in the Theta-Theta (θ–θ) configuration equipped with a Copper anticathode and a LINXEYE fast detector.

Figure 6: Bruker AXS D8 Advance XRD

The XRD measurements were driven by J.-F. Colin (PhD) at CEA-Grenoble.

1.3.5 MAS-NMR (Magic Angle Spinning - Nuclear Magnetic Resonance spectroscopy)

Nuclear magnetic resonance (NMR) spectroscopy is typically used to characterize the chemistry of materials in a solid state. Materials contain molecules with atoms and their nuclei. These nuclei have a magnetic moment oriented in a random way inside the material. When an external and intense magnetic field (B0) is applied, the magnetic moments orient themselves in the direction (parallel or anti-parallel) of this external magnetic field. To determine the magnetic resonance of the sample, the orientation of the magnetic moments is modified using an energy source like a radio frequency wave. The orientation of the magnetic moments changes and comes back to the equilibrium position. The nuclei create an electromotive force depending on the excited atoms and their chemical environment. This measured electromotive force constitutes the NMR signal. The signal processing generates a spectrum allowing to identify of the chemical structure of the sample molecules.
The chemistry of Li-ion batteries provides a variety of active nuclei that can be detected using NMR analysis, such as ^{1}H, ^{13}C, ^{7}Li, ^{31}P, and ^{19}F [5]. Most Li-ion batteries NMR studies require solid-state magic angle spinning (MAS) measurements because they produce higher resolution spectra [7], [8].

^{7}Li MAS-NMR was performed in this work on Lithium atoms in various local lithium environments: active electrode materials, electrolyte, and plated lithium were analyzed.

^{7}Li NMR spectra were acquired on a Bruker AVANCE III 500 MHz, spectrometer operating at 11.7 T, equipped with a 4 mm Bruker CPMAS probe-head (Larmor precession frequency for ^{7}Li, ω_0 = 194.37 MHz). The Magic Angle Spinning method is used by setting the spinning rate at 8 kHz. The used acquisition sequence was a direct excitation without proton decoupling with a 30° pulse and 2 s recycle delay to reach quantitative conditions. Usually, 800 transients (NS) were accumulated before the application of the Fourier transform. The data were processed using Bruker's TopSpin™ software.
The measurements were performed by M. Bardet (PhD) at CEA-Grenoble.

2 Experimental results investigations

2.1 Preliminary investigations

This part is dedicated to preliminary experimental tests conducted to study the influence of some parameters on the thermal behavior of the cell electrode materials. Firstly, the influence of the electrode washing step during the sample preparation is investigated. Then, the impact

of the electrolyte composition, the state of charge of electrodes, and the active material to electrolyte ratio are presented and discussed.

2.1.1 The electrode washing operation

The washing step is made to remove the amount of residual salt and solvent in the electrodes that may have an impact on the DSC results exploration. In the literature, different approaches are proposed [9]:

- Washing followed by drying before adding the electrolyte.
- Drying (without washing) followed by adding electrolyte.
- Drying only (without washing and without adding electrolyte).

There is no consensus either on the washing time or the drying time.

In this work, our objective is to identify and quantify separately the different degradation reactions of the electrode materials. Since the electrolyte participates in the main part of these reactions, it is necessary to remove electrolyte excess from the electrode material and to control the amount of over-quantity electrolyte added to the material powder. Then, we proceed with a washing step followed by a drying step. DMC solvent was chosen because of its high saturation vapor pressure value at 25 °C: 56 mmHg [10].

A comparison was made on the lithiated negative electrode sample before and after washing for about 3 minutes and without adding supplementary electrolytes. The obtained results, reported in Figure 7, show qualitatively the impact of the washing step on the DSC profiles.

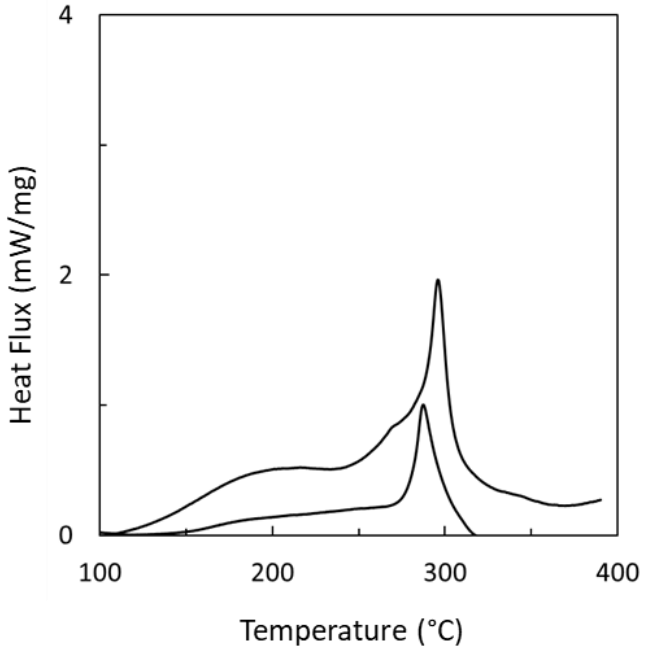

Figure 7: DSC analysis at 5 °C/min of unwashed (upper) and washed (lower) electrode material with DMC

The total energy measured for the unwashed lithiated powder is higher than after washing with DMC. We measured a released heat of 900 J/g for unwashed lithiated graphite versus 600 J/g after DMC washing. The amount of released heat is obtained by integrating the area of the DSC profiles. The excess of energy for unwashed lithiated graphite is related to the residual amount of salt and solvent in the negative electrode sample. This result illustrates that electrode washing is an important step to improve the quantification of DSC results.

Furthermore, it is known that washing modifies considerably the chemical composition at the surface of graphite electrodes, including the SEI layer [11]. For graphite electrodes, the degradation of the SEI is considered the first exothermic reaction that occurs during a TR situation [12]. Then, the duration of the washing step must be controlled to remove the maximum of electrolyte residues without significantly altering the SEI layer.

Therefore, XPS analysis has been performed on unwashed and washed lithiated graphite samples at different times with DMC to find out the optimal washing step duration. DMC is used in this experiment because SEI components are not very soluble in this solvent [13], [14]. Figure 8 presents the XPS spectrum of Li 1s, C 1s, O 1s, P 2p, and F 1s corresponding to unwashed and washed lithiated graphite samples for 30 s, 3x1 min, and 10 min with DMC.

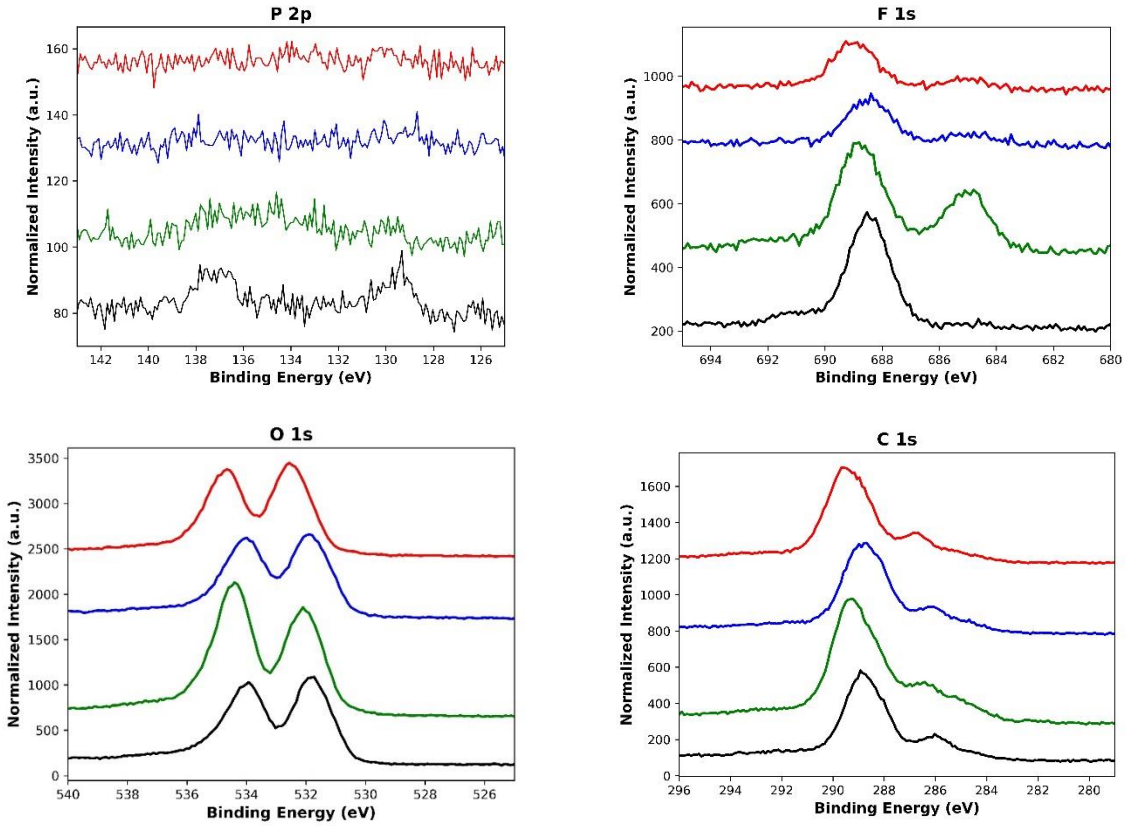

Figure 8: XPS results of lithiated graphite, unwashed (black) and washed at different washing times with DMC (30 s (green), 1 min x 3 (blue), and 10 min (red))

The F 1s signal is dominated by the contribution of the P_yF_z group around 688.5 eV [15]. The high intensity of the P_yF_z peak can be related to a higher $LiPF_6$ content on the electrode surface before washing. Looking at the shape of this peak, the $LiPF_6$ contribution is probably overlapped with another high binding energy peak on the F 1s spectrum. We assume that we have a $LiPF_6/Li_xPF_y$ overlap in the detection limit on the F 1s.

Moreover, F 1s spectra underline that LiF (peak at ~685 eV [15]) is not detected on the unwashed sample and appears only after the first wash. It should be reminded that precipitates from the drying electrolyte such as $LiPF_6$ could conceal the SEI and confuse the trends in the XPS data above. This is why LiF is more intense after the 30 s of washing. However, it is not obvious why LiF is less intense after 3x1 min and 10 min washing.

From the P 2p spectra, the high binding energy contribution (peak at roughly 137 eV) is related to phosphorous–fluorine compounds [16] as the PF_6 group. This signal disappears partially after a 30 s wash and totally after a 3x1 min wash.

By performing a relative quantification between F 1s and P 2p, and assuming an overlap of two elementary peaks for the peak at 688.5 eV, a coherence between P and F can be found as reported in Table 4.

Table 4: carbon, oxygen, fluorine, lithium, and phosphorus relative atomic concentration obtained from the survey spectra quantification of each analyzed sample

% Atom	Unwashed	30 s	3x1 min	10 min
C	16	21.1	17.1	19
O	15.7	18.2	15.4	16.5
F	2.4	3.4	1.3	1.3
P	0.4	0.3	0	0

There is a trend for $LiPF_6$ salt molecules to disappear with the washing times. In addition, the low atomic concentrations of F and P, 2-3 % of F and 5-10 times less of P, may explain that no P is seen after washing while a small amount of F is still detected.

We suggested that P involved in the "PF_6 chemical group" falls below the detection limit after 3 x 1min of washing. Also, for the 3 x 1min and 10min cases, the detected F is ~1 %, which corresponds to a lower P concentration (6F for 1P in $LiPF_6$). The relative sensitivity factor (RSF) used for P 2p is 4 times smaller than that of F 1s, which explains why P is no more detected after 3x1 min of washing.

For the C 1s signal in Figure 8, the peak at roughly 288-289 eV is largely assigned to C-O compounds such $(ROCO_2Li)_2$ which originate from SEI compounds [15]. These components

are also visible in the O 1s spectra as C-O and R-O-Li features at respectively 534-535 eV and 532 eV [15]. Looking at the O 1s and C 1s spectra, we observe that the contributions of O and C change slightly with washing, suggesting that washing has little effect on the SEI. Except that the O 1s signal confirms the previous suggestion for the sample after the 30 s of washing, the only one for which the high BE peak is more intense.

According to XPS results, we can conclude that the changes in the SEI composition are not very pronounced after washing for 30 seconds when compared to the fresh sample. At the same time, F contribution that may correspond to $LiPF_6$ is still detected.
Thereby, it cannot be stated that the surface of the electrodes is completely free of residual salt after 30 seconds of DMC washing. However, it is reasonable to say that a moderate washing level, between the 30s and 3 times 1min protocols, is the best compromise to get access to the SEI layer without modifying it.
Lastly, it is worth mentioning that XPS measurements are very localized. Probing a larger sample at different locations on the electrode to get a more accurate insight should be required to consolidate this conclusion.

Since we are interested to study the degradation of lithiated electrodes, it is important to verify the impact of the washing operation on the lithiation state of the electrode. Consequently, XRD analysis was performed on charged negative electrodes before and after washing with DMC. The obtained result is reported in Figure 9.

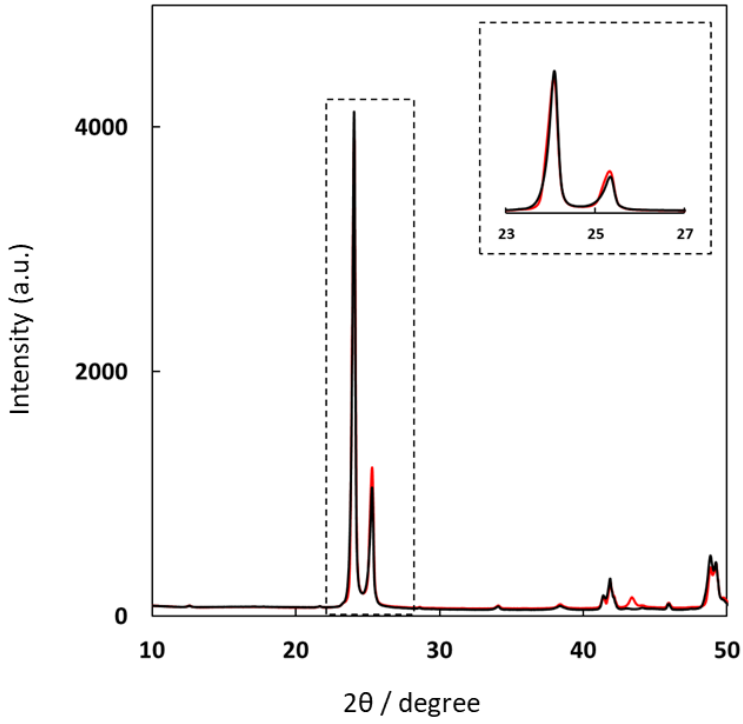

Figure 9: XRD curve of negative powder from a fresh cell before (red line) and after (black line) the washing step

The result shows clearly a similar XRD pattern for both cases with mainly the two characteristic peaks of lithiated graphite; the first peak detected around 24.1° corresponds to LiC_6 material and the less pronounced peak at ~25.3° is attributed to the LiC_{12} crystal structure. These values are consistent with those found in the literature [17].
It can be seen that the XRD spectra of the two samples overlap very well. In proportion, the contribution of LiC_6 in the unwashed sample is 81 % against 78 % after washing.

In conclusion, the washing step does not affect that much the lithiation state of the graphite but mainly removes the residual lithium salt ($LiPF_6$) as verified by XPS analysis.

Combing these observations, the following protocol was selected for the preparation of DSC samples:

- Step 1: washing step with DMC for 30 seconds.
- Step 2: drying step for 10 minutes in the antechamber of the glove box.

2.1.2 What type of electrolyte for the thermal behavior study?

In this thesis, we aim to investigate the thermal degradation of the INR18650-32E cell materials. This implies reproducing the chemistry of the commercial cell electrolyte concerning the active material to electrolyte mass ratio. In the literature, these precautions are not respected.

In the following part, we studied two types of electrolytes with different chemistry and how they can modify the thermal behavior of the negative electrode. The Samsung INR18650-32E cell electrolyte composed of 1M $LiPF_6$ in EC:PC:DMC:FEC (1:1:2:2 volume ratio) and a standard LP30 electrolyte (1M $LiPF_6$ in EC/DMC (1:1 volume ratio)) were used. The following table (Table 5) presents the main characteristic properties of these electrolytes' solvents.

Table 5: Properties of the main electrolyte solvents (collected from ChemBK database)

	M (g/mol)	ρ (g/cm^3)	Tv(mmHg) (at 25°C)	Boiling T (°C) (at 760 mmHg)
DMC	90	1.063	56	91
EC	88	1.321	0.001	248
PC	102	1.2	0.04	242
FEC	106	1.41	0.023	249.5

The DSC profiles of the cell electrolyte (solid line) and the LP30 electrolyte (dotted line) at a 5 °C.min^{-1} heating rate are presented in Figure 10.

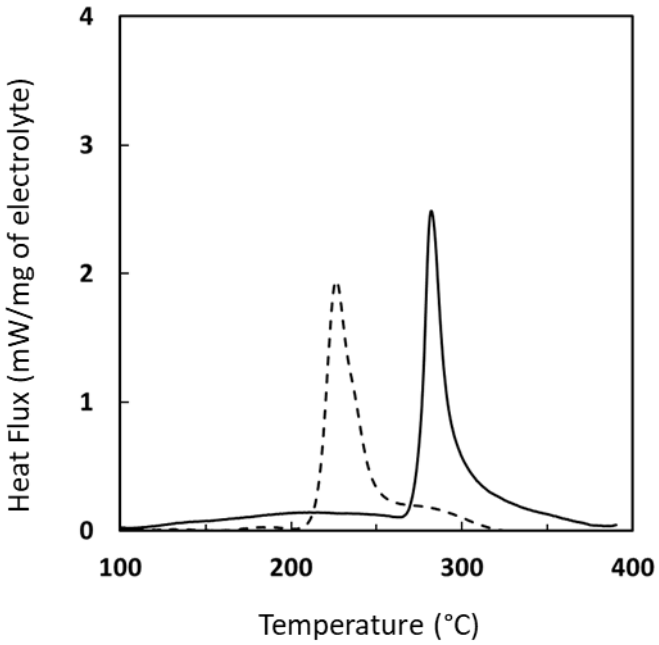

Figure 10: DSC heat flow of INR18650-32E cell electrolyte (dashed line) and LP30 electrolyte (solid line) with a 5 °C min-1 heating rate.

According to the DSC results, we found that the degradation process of the cell electrolyte starts near 200 °C and shows mainly an exothermic peak centered around 226 °C with about 375 J/g of heat followed by a broad peak covering the range of 250-320 °C with 171 J/g of generated heat. The LP30 electrolyte degradation process starts at around 110 °C with a shape peak with 190 J/g of heat followed by a significant exothermic peak centered at 291 °C that generates 500 J/g of heat.

We observed that the onset temperature (T_{onset}) of the electrolyte degradation is different depending on its solvent chemical composition. The LP30 electrolyte has a higher degradation T_{onset} than the electrolyte containing PC and FEC with a difference of 60 °C as illustrated in Figure 10. Then, the thermal stability of the electrolyte decreases when PC and FEC solvents are added.

To verify whether the electrolyte composition has an impact on the thermal behavior of the electrode active materials, we performed a DSC analysis on lithiated negative electrode samples mixed with the INR18650-32E cell electrolyte (with a solid line in Figure 11) and LP30 electrolyte (with a dashed line in Figure 11) at 5 °C.min^{-1}. The same active material to electrolyte ratio was applied in both cases (5 mg+1 µL).

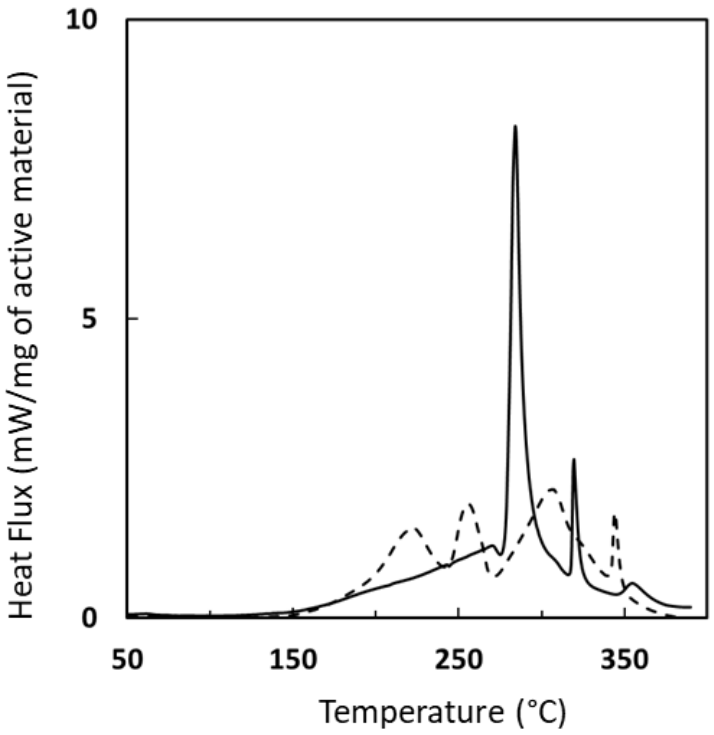

Figure 11: DSC heat flow of lithiated graphite with LP30 electrolyte (solid line) and cell electrolyte (dashed line)

Interestingly, the type of electrolyte has a remarkable influence on the thermal behavior of the negative electrode on DSC. When mixed with the cell electrolyte, the negative electrode degradation profile shows four exothermic peaks with a maximum heat flux at around 2.5 mW/mg of lithiated graphite. However, with LP30 electrolyte mainly two exothermic peaks are observed with a maximum heat flux of 8 mW/mg of lithiated graphite.

Using the same heating rate (5°C/min), the total measured heat for both samples is found to be in the range of 2000 and 2500 J/g of lithiated graphite as presented in Figure 12.

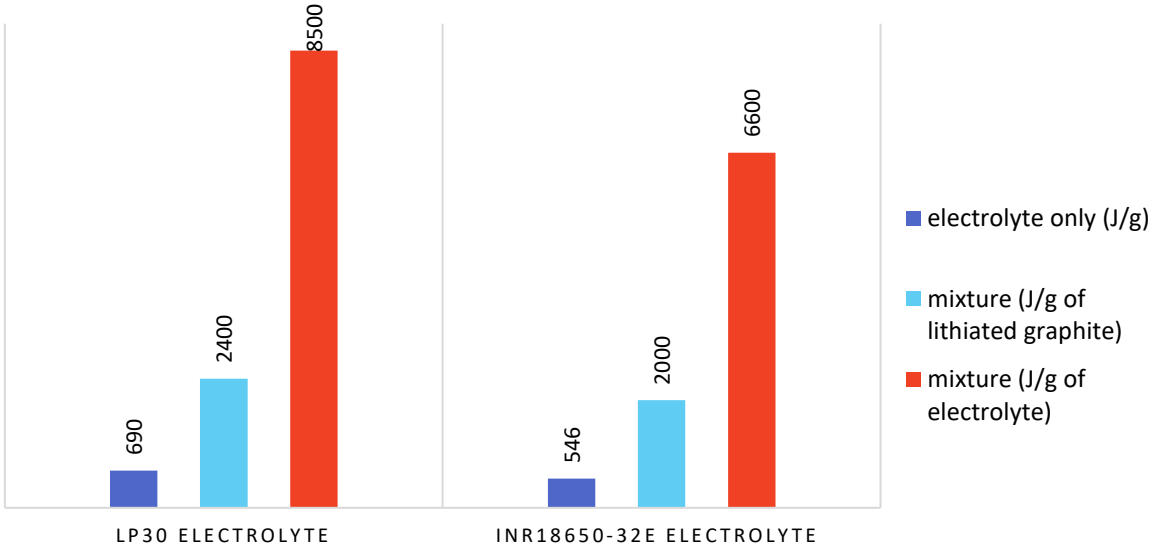

Figure 12: Total heat generated heat by lithiated graphite mixed with LP30 and Samsung INR18650-32E electrolyte

In the range of 150 °C-270 °C (Figure 11), the released heat flux of the lithiated graphite mixed with the cell electrolyte is higher. The difference is probably caused by the presence of PC and FEC additives. Indeed, it was reported that using FEC additive increases the reactivity between lithiated graphite and electrolyte above 130 °C [18].

Note: DSC analysis in Figure 11 was conducted to investigate qualitatively the effect of the electrolyte chemistry on the negative electrode material thermal degradation. The thermal degradation mechanisms of the cell materials will be presented in more detail in sections 2 and 4.

For better prediction of the thermal behavior of the commercial cell materials, the cell electrolyte will be used in the following DSC analysis of electrode materials.

2.1.3 Mass ratio effect on the thermal behavior of the electrode material

Commonly, Li-ion batteries contain a small amount of liquid electrolyte compared to the total amount of the electrode. Thereby, the amount of electrolyte added to the electrode samples for DSC analysis must be controlled to get representative results on the commercial cell scale.

In this part, the impact of the active material to electrolyte mass ratio is investigated by conducting DSC analysis in three different cases: using only the active material without additional electrolyte (ratio of 100:0 %wt), then using equal proportions (ratio of 50:50 %wt) and finally with a ratio of 77:23 %wt. The last ratio is representative of the material proportions of a full cell. It was calculated using the weight and the porosity of the commercial cell electrodes. The obtained DSC results are presented in Figure 13.

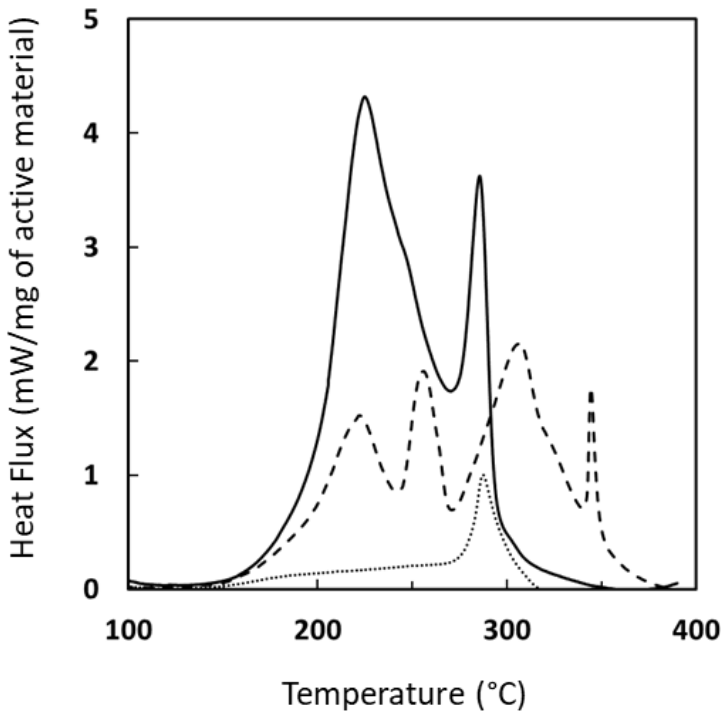

Figure 13: DSC heat flow of graphite with cell electrolyte, 50:50 %wt (solid line), 77:23 %wt (dashed line), and without electrolyte (dotted line)

Without adding supplementary electrolytes, mainly one exothermic peak is detected at high temperatures. When the electrolyte is added, other peaks appear. Four peaks are observed by analyzing the mixture of lithiated graphite/electrolyte with a mass ratio of 77:23 %wt; however, only two peaks are detected with 50:50 %wt.

These DSC profiles show a linear tendency between the generated heat of the mixture and the mass fraction of the lithiated graphite in the ratio. A comparison between the total heat generated in these different cases is presented in Figure 14. We measured heat of 212 J/g, 2000J/g, and 3600 J/g of lithiated graphite for respectively 100:0 %wt, 77:23%wt, and 50:50 %wt ratios.

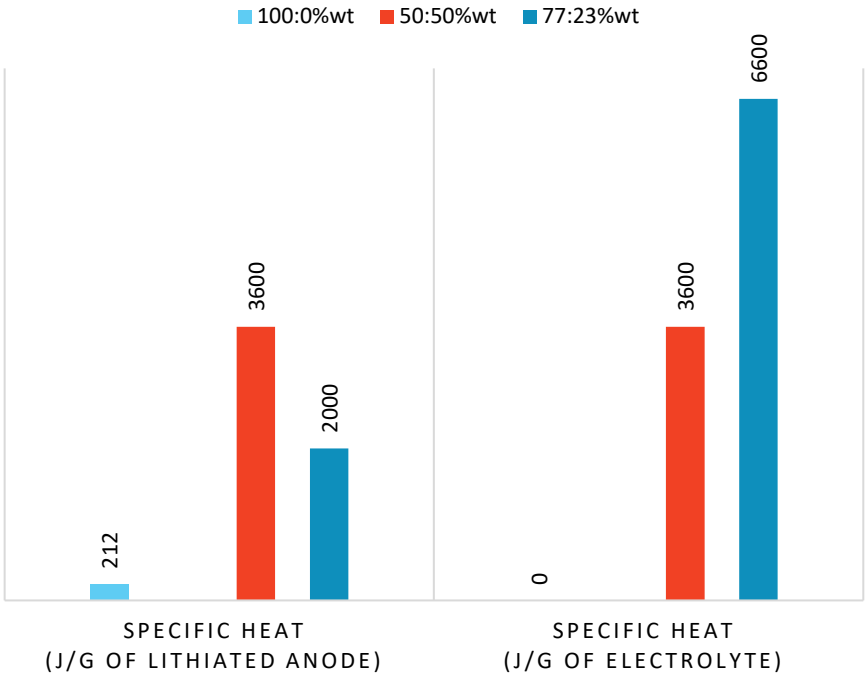

Figure 14: Total heat generated heat by lithiated graphite without (100:0 %wt) and after adding electrolyte (50:50 %wt and 77:23 %wt)

Technically, reproducing the same mass ratio during sample preparation for DSC analysis is a challenging task. Particularly, because of the size of crucibles (Ø 6 mm, 30 µL) which limits the maximum weight of tested samples between 3 mg and 5 mg. Moreover, the high viscosity of the electrolyte (~1.45 g/cm^3 at ambient temperature) makes it hard to add less than 1 µL to the mixture. However, we tried in most of conducted DSC analyses to avoid exceeding 25 %wt electrolytes in the mixture.

These results show clearly that the active material to electrolyte mass ratio has a significant impact on the thermal behavior of the lithiated negative electrode samples.

In the following sections, a detailed study of the negative and positive electrode materials will be presented and discussed.

3 Thermal degradation of the negative electrode

In this section, we propose a detailed investigation of the thermal degradation mechanism of the fresh INR18650-32E negative electrode. The aim is to identify and quantify the different exothermic reactions that occur inside the negative electrode material during thermal runaway situations. To understand the successive degradation reactions, our approach is based essentially on DSC analysis and completed with structural characterization analysis. Several samples were analyzed to understand the mechanism of the thermal degradation reactions and to quantify separately the energy released by each exothermic reaction. Numerical

deconvolution was performed using OriginPro software to estimate the enthalpy of reactions difficult to obtain from the DSC results.

Figure 15 shows the thermal degradation profile of the fresh lithiated negative electrode mixed with INR18650-32E cell electrolyte, 77:23 %wt ratio, at 5 °C/min.

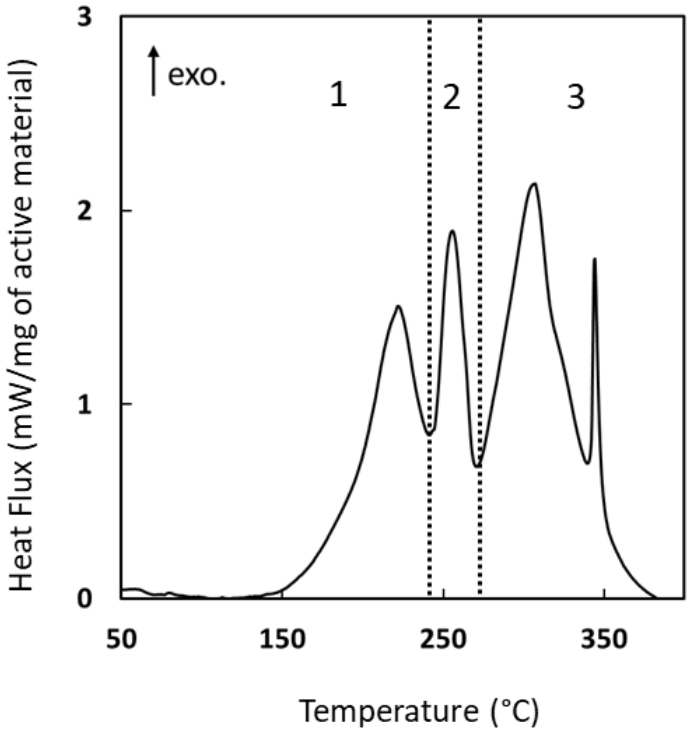

Figure 15: DSC result of fresh lithiated graphite + cell electrolyte with 77:23 %wt ratio at 5 °C.min^{-1}

We identify three different regions with exothermic peaks depending on the temperature range as mentioned in 1, 2, and 3 in Figure 15.

By diversifying the DSC experiments, we investigated the identification of the different reaction and their related observed exothermic peaks. Notably, The SEI thermal breakdown and the reaction between intercalated lithium and the electrolyte in area 1; the electrolyte thermal degradation in area 2, and the last area reactions between intercalated lithium, binder, and other products. The obtained results are presented and discussed separately in the following parts.

3.1 Area 1 [100 °C – 220 °C]

3.1.1 SEI thermal breakdown

The first area includes typically two exothermic reactions: the breakdown of the SEI followed by the reaction of intercalated lithium with electrolyte. As already mentioned, the passivation layer SEI is formed during the first cycling of the battery and covers the graphite particles. Usually, it contains thermally stable components (such as LiF and Li_2CO_3) and organic

components such as $(CH_2OCO_2Li)_2$ (LEDC) and CH_3OCO_2Li (LMC), called metastable components. The SEI breakdown T_{onset} and released heat depends on the chemistry of the electrolyte, the morphology of graphite particles, and the first cell cycling conditions.

The SEI degradation reaction was studied separately considering a delithiated fresh negative electrode sample, without washing to preserve as much as possible the structure of the layer and without adding electrolyte. Figure 16 shows the obtained result. Repeatability is indicated with a dashed line.

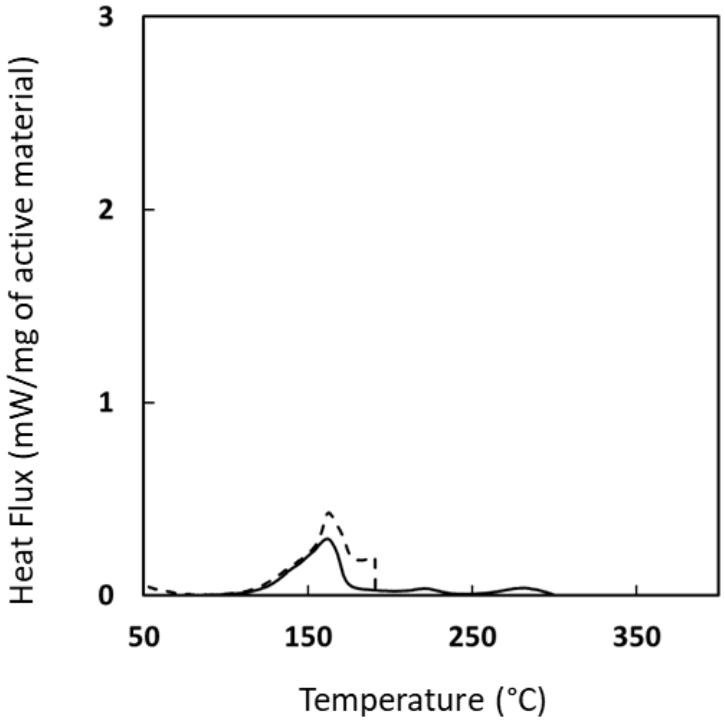

Figure 16: DSC results of fresh delithiated graphite samples at 5 °C.min^{-1}

Based on the DSC result, the SEI breakdown starts at 90 °C with a relatively small peak at 164 °C with a measured released heat of ~100 J g^{-1} of delithiated graphite. The generated heat is generally associated with the exothermic decomposition of SEI metastable components such as LEDC and LMC as follows [1], [12]:

$$(CH_2OCO_2Li)2\ (LEDC) \rightarrow Li_2CO_3 + C_2H_4 + CO_2 + \tfrac{1}{2}\,O_2 \quad (1)$$

$$CH_3OCO_2Li\ (LMC) \rightarrow CO_2 + CH_3OLi \quad (2)$$

In our case, the electrolyte of the studied commercial cell contains FEC and PC. These additives give compactness to the structure of the SEI during the formation cycles with a high amount of thermally stable components such as LiF and Li_2CO_3 [19], [20] because of their high reduction potential (E_{FEC}>E_{EC}>E_{PC}>E_{DMC}). For this reason, the amount of released energy by the SEI degradation is not significant.

Another analysis was conducted by adding 1 µL of the cell electrolyte to the sample. The DSC result in Figure 17 shows mainly two exothermic peaks. The first exothermic peak is located between 100 °C and 170 °C and is associated with the SEI degradation with ~75 J g^{-1} of heat. The second exothermic peak around 220 °C is attributed to electrolyte degradation.

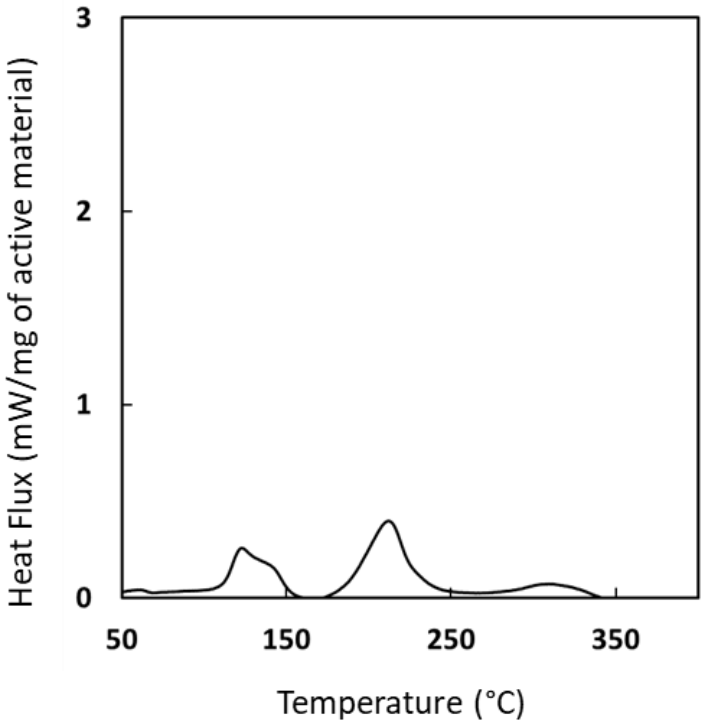

Figure 17: DSC result of fresh delithiated graphite + electrolyte at 5 °C.min^{-1}

Compared to the result without adding electrolyte presented in Figure 16, the heat generated by the SEI degradation peak is lower after adding electrolyte and the reaction peak temperature is shifted. Differences in the thermal behavior before and after adding electrolytes could be related to the interaction between $LiPF_6$ salt and SEI compounds. Indeed, the P-F bond in $LiPF_6$ molecules is unstable and easily hydrolyzed in the presence of traces of humidity, even at ambient temperature. While dry $LiPF_6$ decomposes into PF_5 and HF at around 200 °C, it was reported that the decomposition of $LiPF_6$ starts between 90 °C and 100 °C in presence of trace amounts of water impurities [21] and produces corrosive products as HF gas according to the following reactions ((3)-(6)).

$LiPF_6 + H_2O \leftrightarrows LiF + POF_3 + 2HF$	(3)
$LiPF_6 + H_2O \rightarrow LiOH + PF_5 + HF$	(4)
$PF_5 + H_2O \rightarrow POF_3 + 2HF$	(5)
$POF_3 + H_2O \leftrightarrows HPO_2F_2 + HF$	(6)

$LiPF_6$ salt decomposition products, PF_5 and HF, may participate in the degradation of the SEI according to the following reactions ((7)-(12)).

$HF + CH_3OCO_2Li \rightarrow RCH_3OH + CO2 + LiF$	(7)
$2HF + Li_2CO_3 \rightarrow CO_2 + H_2O + 2LiF$	(8)
$PF_5 + Li_2CO_3 \rightarrow 2LiF + POF_3 + CO_2$	(9)
$2PF_5 + (CH_2OCO_2Li)2 \rightarrow 2LiF + C_2H_4F_2 + 2POF_3 + 2CO_2$	(10)
$PF_5 + CH_3OCO_2Li \rightarrow LiF + CH_3F + POF_3 + CO_2$	(11)
$PF_5 + CH_3OCO_2Li \rightarrow LiF + POF_3 + CH_3COF$	(12)

Based on the standard enthalpies of the formation of products and reactants, the change in enthalpy of these reactions was calculated (the obtained values are reported in chapter IV). The standard enthalpies of formation have been collected from the NIST Chemistry Webbook. According to the calculation result, most of these reactions are endothermic. Thereby, the lower heat measured by the SEI decomposition after adding the electrolyte may be related to these endothermic reactions.

The heat generated by the electrolyte degradation peak in Figure 17 is about 450 J/g of electrolyte. This value is consistent with that measured when the cell electrolyte is tested only (see 2.1.2). Then, we could conclude that the degradation of SEI is an independent reaction and no interaction with solvents between 100 °C and 200 °C is detected.

In order to better understand the decomposition processes involved at the surface of the negative electrode, the evolution at the surface of delithiated negative electrodes was investigated using XPS and TOF-SIMS analysis before and after heating at different temperatures. The DSC of the delithiated negative electrode sample is stopped at three different end temperatures 110 °C, 160 °C, and 190 °C. These temperatures are associated respectively with the beginning, the maximum, and the end of the SEI degradation reaction peak as shown in Figure 18.

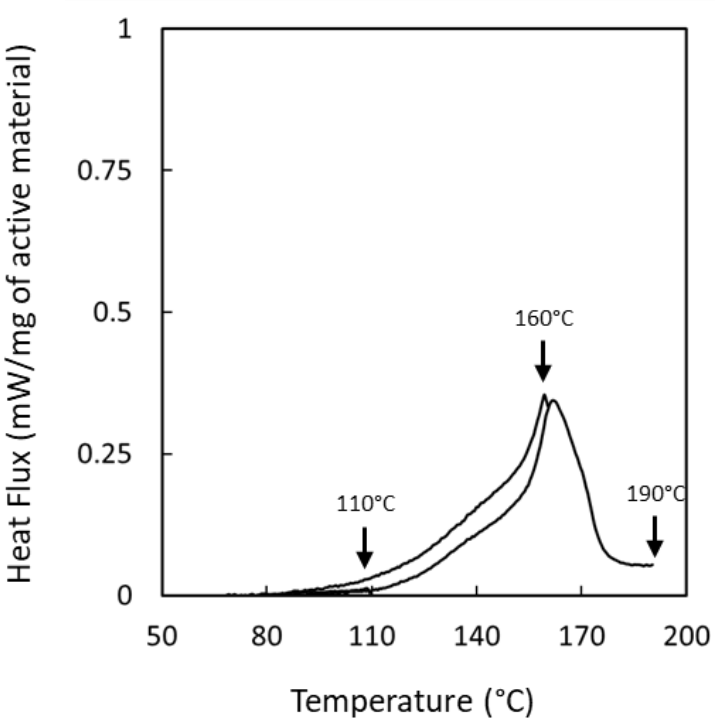

Figure 18: DSC profiles stopped at 110 °C, 160 °C, and 190 °C of a delithiated negative electrode at 5 °C.min^{-1}

The evolution of the composition on the surface of the graphite electrode can be followed by tracking the chemical elements such as carbon and oxygen, which gives an idea of the SEI structure:

- Fluorine and phosphor for the residual amount of $LiPF_6$ salt and other LiPOF bounds.
- Sodium to identify the type of the negative electrode binder such as CMC-Na, commonly used in graphite electrodes [22].

Investigated C 1s, O 1s, Li 1s, F 1s, P 2p, and Na 1s orbitals for delithiated negative electrode samples before and after heating by 110 °C, 160 °C, and 190 °C are presented in Figure 19.

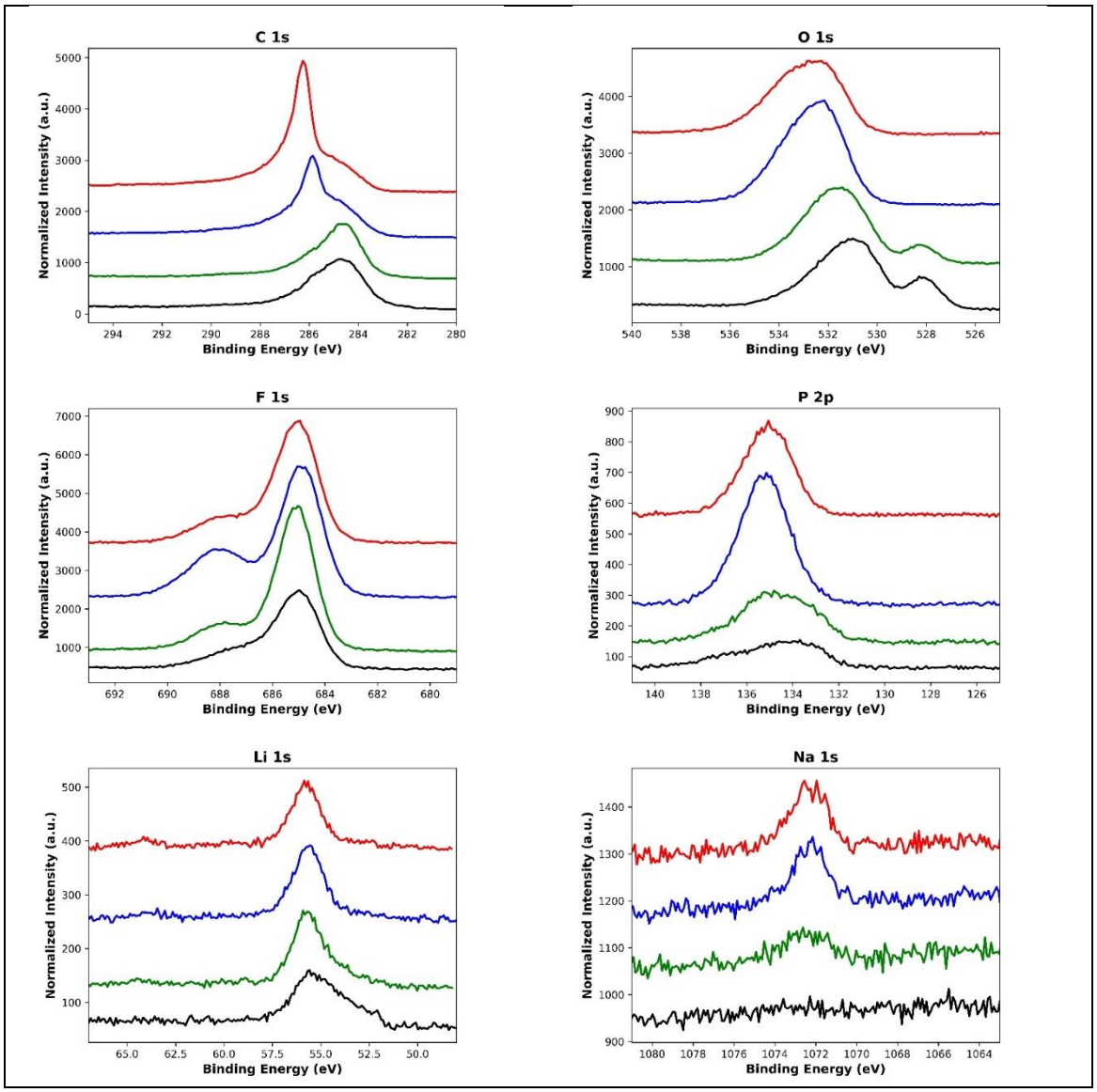

Figure 19: XPS results of a delithiated graphite, unheated (black) and heated at different temperatures 110 °C (green), 160 °C (blue), and 190 °C (red)

There is a trend of evolution from lower to higher energy environments after heating in most of the analyzed spectra. The O 1s spectra show peaks occurring at ~528.5 eV which are related to the presence of lithium oxides (Li-O bond) in the SEI and gradually disappear with the temperature increase and vanish at 160 °C and 190 °C after SEI degradation.

A second peak is detected between 530 eV and 532 eV which is related to a mixture of C-O and C=O environments. This peak might be associated with organic by-products such as R-OCO_2-Li or R-OH-Li commonly found in the SEI [23].

C 1s spectra contain a large peak covering the energy range between 283.5 eV and 286.5 eV before heating. On this interval, the contribution of C-C containing species detected usually at ~284.5 eV is overlapped with C-O and C=O containing species detected at ~286 eV [24]. After heating at 160 °C and 190 °C, the contribution of C-C bounds decreases progressively while

that of C-O bounds increases. Such fading of the peak related to C-C bonds is similar to what was observed for the Li-O bond in O 1s spectra. Interestingly, there is no contribution around ~290 eV, which corresponds to the presence of carbonates (Li_2CO_3). Thereby, the contribution of CO_3 bonds is very low.

F1s spectra show mainly a strong peak at ~685 eV confirming the presence of LiF species in the SEI for all investigated temperatures, even though there is a relative increase of the higher binding energy peak relative to $Li_xPO_yF_z$ species with increasing temperature.
The intensity of this peak remains high even at the highest temperature, which is consistent with the properties of LiF as one of the most stable components in the SEI. Moreover, at high energies, an increase in the contribution of $Li_xP_yF_z$ is detected after heating (except for 190 °C) with a decrease of $Li_xPO_yF_z$ species. This statement is related to the peak position in P 2p spectra for which a shift of the peak, attributed to $Li_xPO_yF_z$ species at ~134 eV, towards higher energies is observed and characteristic of a more oxidizing chemical environment for fluorine ($Li_xPO_yF_z \rightarrow Li_xPF_y$).

Li 1s spectra appear as a broad peak which is probably a superposition of peaks associated with LiF at roughly 56 eV; lithium alkoxide or hydroxide as Li-O bound at 55.5 eV and Li_2O species at 54 eV [25], [26]

Comparing the Li 1s spectra before and after heating, Li_2O species disappear progressively with temperature and disappear almost at 190 °C. The same trend is observed in the O 1s spectrum concerning the contribution of lithium oxide species at ~528.5 eV.

Na signal is also detected in the Na 1s spectrum at ~1072.5 eV with increasing temperature, which could be related to the CMC-Na in the electrode. In addition, this observation might be a clear indication that the SEI at the surface of the electrode is getting thinner with increasing temperature allowing the detection of the electrode binder.

These observations were confirmed by a quantitative result of the analyzed elements presented in Figure 20.

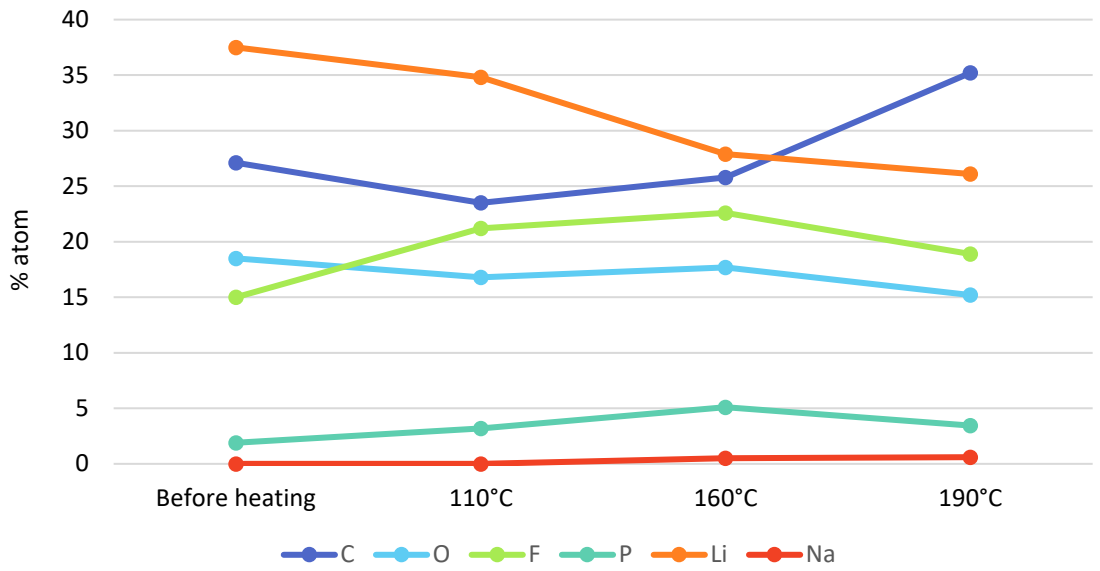

Figure 20: Table showing negative electrode surface composition estimated from the survey spectra quantification of each XPS analysis before and after heating at 110 °C, 160 °C, and 190 °C

Finally, the trend is mainly an increase in the amount of C and a decrease in the amount of Li. Since the sample was delithiated graphite, Li is only present in the SEI layer. The SEI degrades with temperature, thus gets thinner and the amount of Li detected in XPS decreases consequently. At the same time, we start to see more elements under the SEI layer, i.e., carbon (graphite) and Na.

The XPS observations are completed with a TOF-SIMS analysis conducted using the same samples. Figure 21 presents TOF-SIMS concentration profiles of the delithiated negative electrode samples at 110 °C and 160 °C. The result shows the variation of C_6^-, LiF_2^-, LiO^- and CO_3^- secondary ion fragments intensity with sputtering time. These fragments represent the negative electrode particle variation from the extreme surface (at 0s in the sputter time axis) to the maximum depth reached.

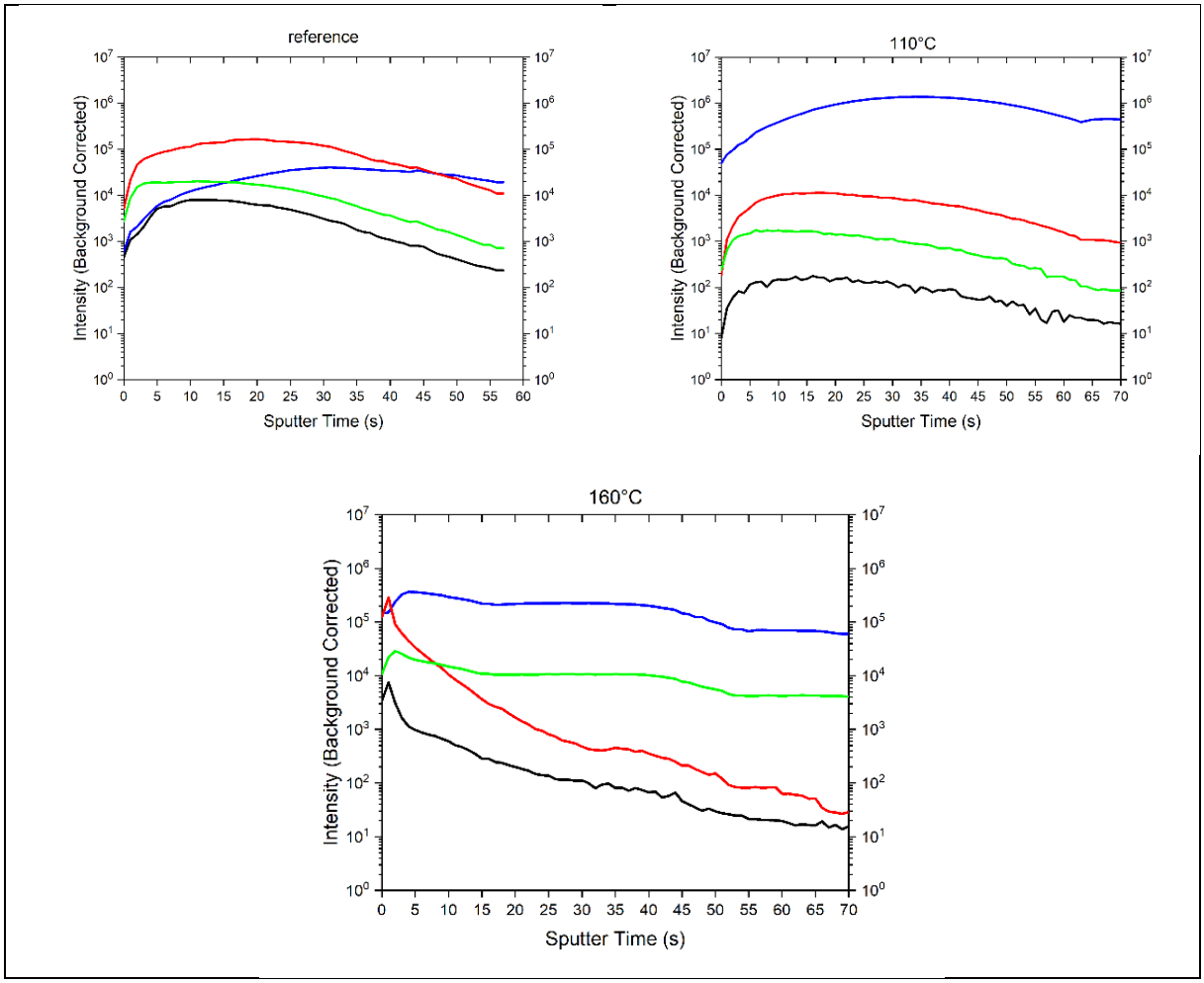

Figure 21: TOF-SIMS analysis results showing C_6^- (blue), LiF_2^- (red), CO_3^- (black) and LiO^- (green) fragments variation of the delithiated negative electrode sample before and after heating at 110 °C and 160 °C

The observed intensity variation is related to species in the electrode sample from which the ions are emitted. C_6^- and CO_3^- are associated to respectively, Li_xC_6 and organic compounds. LiF_2^- is indicative of LiF and $Li_xP_yF_z$ species and LiO^- for lithium oxides.

The global tendency is a variation of the intensity which increases slightly and then declines. The intensity is associated with the relative position of the species that generates the detected fragments during TOF-SIMS analysis. It is not obvious to evaluate the obtained variations but we propose in the following paragraph some explanations.

The variations in Figure 21 are related to the thickness of the layer containing the fragments. Coherence can be observed by comparing the curves before and after heating. Indeed, the higher the heating temperature is, the weaker the curvature is. Moreover, the intensity decreases rapidly indicating the degradation of the material and the reduction of the thickness. As the C_6^- (blue line) is slow to rise especially between 0 and 30s, this zone corresponds probably to the SEI interface. However, for the CO_3^- and LiO^- fragments (green and black line),

the maximum of the curve is reached more quickly (±10 s). This means that organic species are located mostly at the extreme surface of the material.

By comparing the curves in Figure 21, much less CO_3^- is present before than after heating at 110 °C (the max passed from 10^4 to 10^2). This means that a part of the SEI layer is degraded. The intensity of the same fragment is higher after heating at 160 °C. This is probably related to the presence of SEI compounds between the graphite particles which can be detected after abrasion of the extreme surface. The signal decreases rapidly as those species are present in very small quantities. Besides, a plateau is almost reached on the C_6^- curve after heating to 160 °C. According to our analysis, most of the SEI layer may have been removed and more graphite than SEI compounds are finally detected.

With careful precautions, the thickness of the SEI layer can be estimated to be 6 – 7 nm based on the average path of an electron through the SEI layer composed mainly of Li_2CO_3 with a kinetic energy of Ec=1200 eV.

3.1.2 Lithiated graphite / electrolyte reaction

The heat released by SEI breakdown (Figure 16) could not explain the powerful peak detected in area 1 - Figure 15. This peak can then be considered to be related to the SEI decomposition but also a second reaction, namely the reaction between the SEI-free lithiated graphite and the electrolyte.

These reactions are highly correlated and occur simultaneously between 100 °C-200 °C. Then, to study separately the second reaction, the contribution of the SEI breakdown peak has to be removed. Thus, we proposed different experimental approaches to erase the SEI layer from the negative electrode of the INR18650-32E cell.

The first proposed approach consists of storing the negative electrode at a temperature higher than the limit one indicated by the fabricant (60° C) and close enough to the SEI degradation temperature, which is typically in the range of 80 °C-100 °C. Coin cells were made using negative electrode samples from the commercial cell, metallic lithium electrode, and the INR18650-32E cell electrolyte. Those samples were stored at different temperatures between 65 °C and 100 °C for 48h. Before and after heating, the cells were cycled using cyclic voltammetry (CV) with a slow scan rate (25 µV/s) starting from 10 mV vs Li/Li^+. CV is an electrochemical technique typically used (at a low scan rate) to study the kinetics of lithiation/delithiation processes of graphite.
A comparison was made then between the obtained CV curves before and after storing the cell at 90 °C. The SEI formation was detected during the reduction scans (I<0) between 0.6 V

and 1 V, which is consistent with the literature [27], indicating the re-formation of the passivation layer after storing at 90 °C.
This result confirms that SEI is partially removed by storing the negative electrode at this temperature. Then the associated sample can be used in DSC analysis to study the reaction between intercalated lithium and electrolyte without the SEI breakdown interference.

Unfortunately, some operating conditions and reproducibility difficulties were identified in this approach. The experiments were not easy to control and requires a considerable operation time. Then an alternative methodology was identified.

Our choice was oriented to synthesize chemically some lithiated graphite. The KS6 Timrex (IMERYS Graphite & Carbons) graphite was selected for the experiment.

Figure 22 shows a comparison between the KS6 graphite particles and commercial INR18650 32E graphite using scanning electron microscopy (SEM) observations.

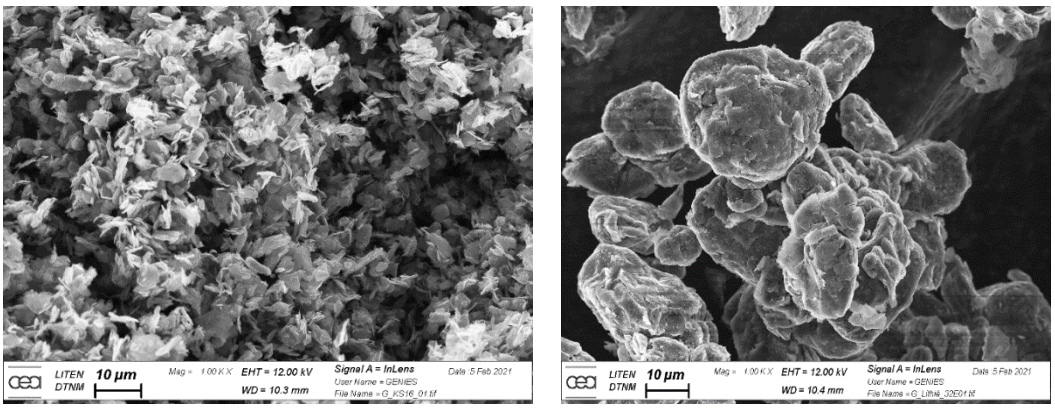

Figure 22: SEM images of (left) KS6 TIMREX, (right) Samsung INR18650 32E negative electrode

Combining the SEM images with the D50 diameter and BET surface area values listed in Table 6, the graphite particles of the commercial cell appear more comparable to the SMG-N-20 natural graphite than KS6 graphite.

Table 6: Physical properties of KS6 graphite and the INR18650 32E graphite

	KS6 TIMREX [28]	**SMG-N-20 [29]**
Diameter, D_{50}/ µm	3.4	19.5
BET surface area/ $m^2\ g^{-1}$	26	5.1

However, it is important to know that the smaller the particle size of graphite, the easier the intercalation of lithium into graphite particles. Thereby, it was decided to work with the KS6 graphite to achieve successfully the synthesis of the chemical LiC_6.

Firstly, the graphite powder was dried under vacuum at 100 °C for 24 hours to remove any trace of moisture. Then, the experiment was performed under an inert atmosphere in the glove box using dried graphite, metallic lithium foil, a Nickel crucible, and an electric heating plate to reach the lithium melting temperature of 180 °C. The proportion of the metallic lithium is fixed to be about 10% of the initial graphite weight to obtain the Li_1C_6 material, according to the stoichiometry of carbon and lithium in reaction (13):

$$Li^0 + C_6 \rightarrow Li_1C_6 \quad (13)$$

At the end of the experiment, a golden powder was obtained, characteristic color of LiC_6 material, as shown in Figure 23.

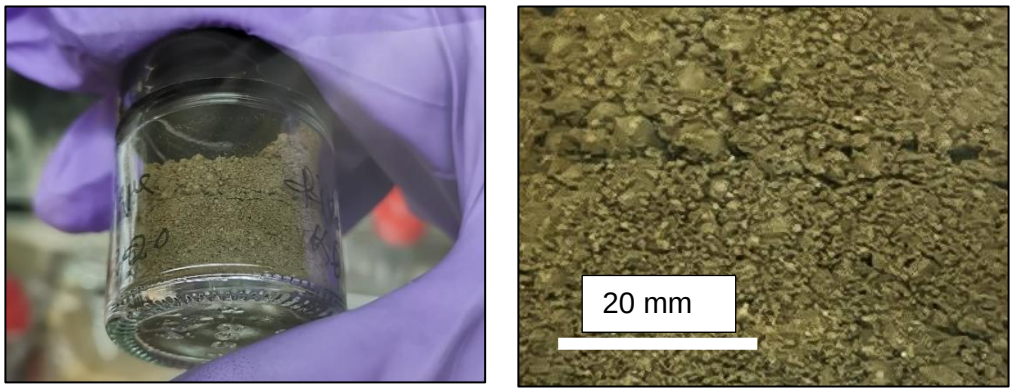

Figure 23: photos of the synthetized chemical lithiated graphite

To verify the lithiated stages of graphite intercalation compound (GIC), XRD analysis was conducted on the sample and the result is reported in Figure 24.

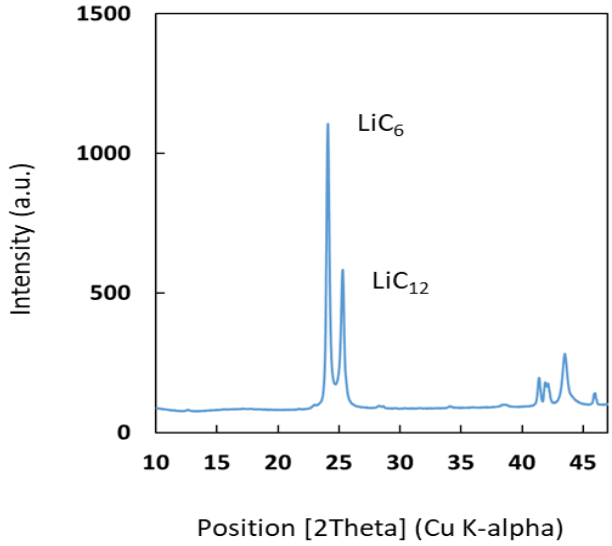

Figure 24: XDR pattern of the synthetized chemical lithiated graphite

The obtained result is consistent with the XRD pattern of the lithiated negative electrode (reported in Figure 9) with a peak at 24.1° characteristic of LiC_6 and a peak around 25.3° which corresponds to LiC_{12}. The only noted difference between the XRD results in Figure 9 and Figure 24 is the LiC_{12}/LiC_6 ratio; it represents about 30% in the commercial cell negative electrode and around 50 % in the synthetized graphite.

Finally, the experiment is executed with success and the synthetized chemical lithiated graphite can be used to study independently the reaction between the LiC_6 and electrolyte.

Therefore, the chemical LiC_6 sample was tested in DSC mixed with the cell electrolyte. The result is reported in Figure 25.

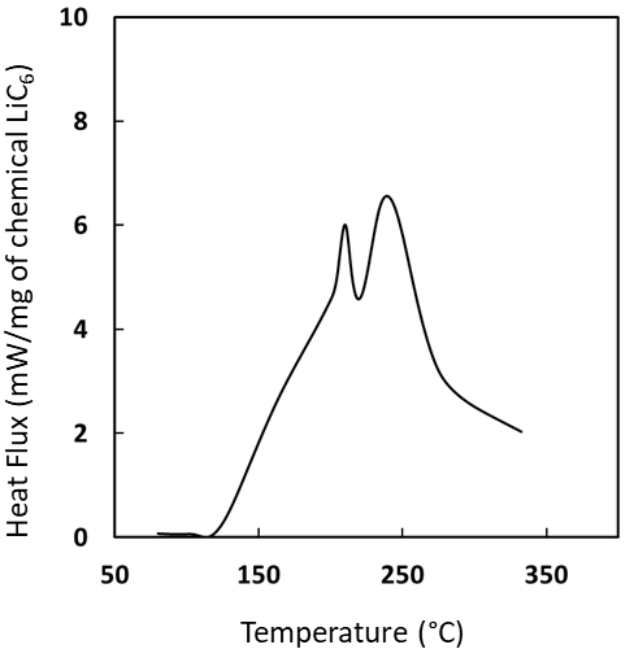

Figure 25: DSC result of chemical LiC_6 mixed with cell electrolyte at 10 °C.min^{-1}

Because of some technical problems related to DSC, this analysis was performed at 10 °C/min. The DSC measurement shows mainly two exothermic peaks. The first peak starts at about 120 °C with a maximum of ~220 °C and is followed by a second exothermic peak at ~240 °C.

In Figure 15, area 1 is dominated by an exothermic peak that starts at 100 °C and is centered at ~220 °C. We suggest that this peak is probably the same detected in Figure 25 and comes from the interaction between lithium and the electrolyte according to the following exothermic reactions [1], [12] :

$2Li(C_6) + C_3H_4O_3\ (EC) \rightarrow Li_2CO_3 + C_2H_4$	(14)
$2Li(C_6) + 2\ C_3H_4O_3\ (EC) \rightarrow (CH_2OCO_2Li)2 + C_2H_4$	(15)
$2Li(C_6) + C_3H_6O_3\ (DMC) \rightarrow Li_2CO_3 + C_2H_6$	(16)
$2Li(C_6) + C_4H_6O_3\ (PC) \rightarrow Li_2CO_3 + C_3H_6$	(17)
$3Li(C_6) + C_3H_3FO_3\ (FEC) \rightarrow Li_2O + LiF + CO + CH_3CHO$	(18)

However, due to the difference in graphite particles in the two samples, the profile of this reaction peak in Figure 25 seems to be different from that detected in area 1 - Figure 15. Indeed, depending on the type of graphite, the thermal behavior of LiC_6 in the presence of electrolyte can be different at high temperatures [29].

3.2 Area 2 [220 °C – 270 °C]

3.2.1 $LiPF_6$ salt melting

In area 2 - Figure 15, a peak appears at about 255 °C. Tested alone, the electrolyte has an exothermic reaction between 200 and 250 °C as displayed in Figure 10. We suggested that the exothermic peak in the second area is due mainly to the heat release by the electrolyte degradation.

The cell electrolyte contains $LiPF_6$ salt which decomposes reversibly according to the following endothermic reaction [30]

$LiPF_6 \leftrightarrows LiF(s) + PF_5(g)$	(19)

We found that pure $LiPF_6$, as shown in Figure 26, has a melting peak at 195 °C followed by a large decomposition peak occurring in the temperature range of 250-380 °C.
The obtained DSC profile of $LiPF_6$ salt powder is consistent with the literature.

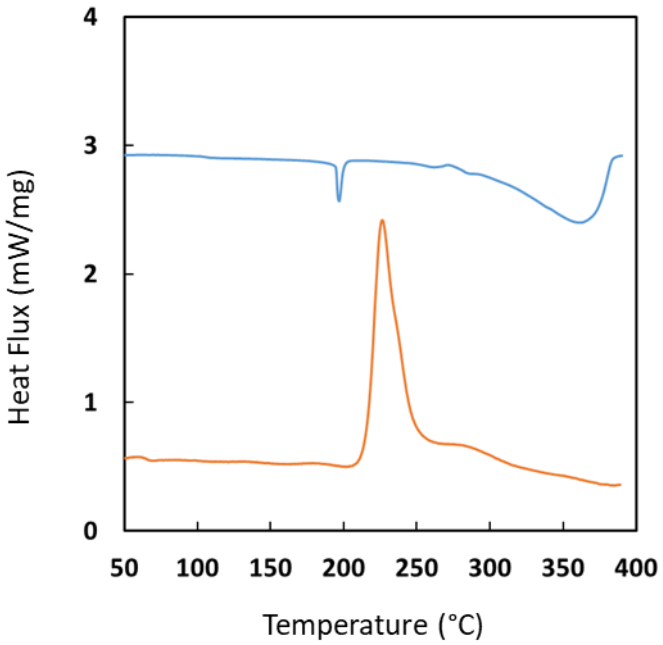

Figure 26: DSC heat flow of INR18650-32E cell electrolyte (orange line) and $LiPF_6$ melting (blue line) with a 5 °C min^{-1} heating rate.

Based on this DSC result, we could mention a correlation between the salt melting and the T_{onset} of the electrolyte degradation. It is clear that the exothermic degradation of the electrolyte occurs after the melting of $LiPF_6$.

3.2.2 Electrolyte solvents decomposition

The decomposition of the electrolyte occurs probably when the electrolyte solvents react exothermically with the PF_5 gas formed by the reaction (19). Indeed, it is known that PF_5 reacts preferentially with the electrolyte EC solvent and generates Fluorinated Polyethylene Oxide (PEO) and CO_2 [31] according to the following exothermic reaction:

$$C_3H_4O_3\ (EC) + PF_5 \rightarrow CO_2(\mathrm{g}) + (\mathrm{PEO})\ (\mathrm{s}) \qquad (20)$$

Besides, we note that the peak temperature of the electrolyte degradation is different when tested alone (see Figure 10) or mixed with the negative electrode powder (see area 2 - Figure 15). This shift is probably due to the contribution of the solvent in area 1, which could slow down the kinetic of the electrolyte degradation reaction. Indeed, the decomposition products in the first area can have a dragged effect and slow down the kinetics of the electrolyte degradation in the mixture.

Such a statement is consistent with the results of the mass ratio study in section 2.1.3. In fact, with the increase of the negative electrode material amount, the concentration of electrolyte per total volume of the mixture decreases, and thus the degradation mechanism is slowed down.

The impact of the active material on electrolyte mass ratio was previously investigated (Figure 13). The same result is reported differently in Figure 27. It shows the DSC profile of the graphite powder mixed with electrolyte; the solid line represents the ratio of 50:50 %wt and the dashed line for the 75:25 %wt ratio.

The heat flux is displayed on two different scales, mW/mg of electrolyte (right curve) and mW/mg of active material (left curve).

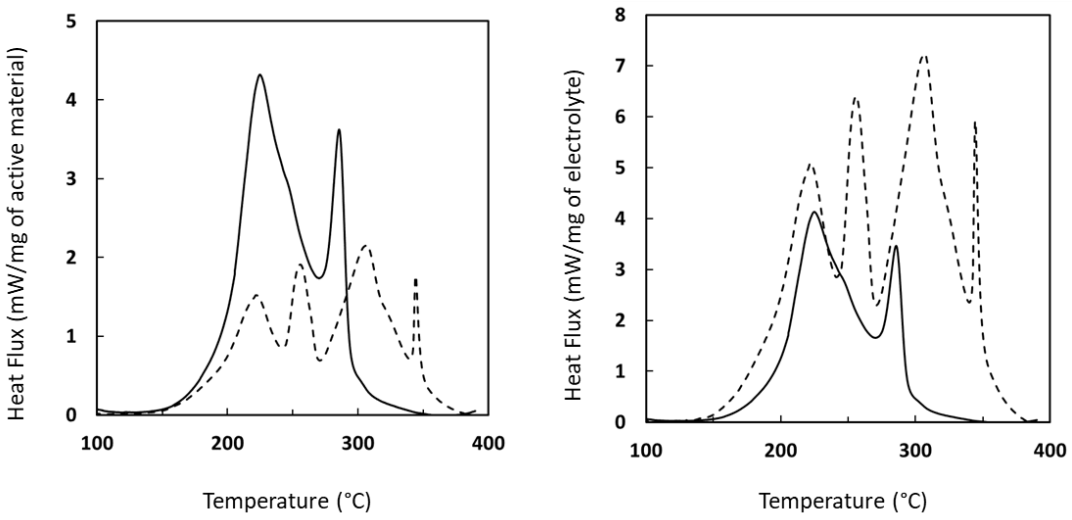

Figure 27: DSC heat flow of graphite with cell electrolyte, 50:50%wt (solid line), 77:23 %wt (dashed line) at 5 °C.min^{-1}, the heat flux is expressed in mW/mg of active material (left) and in mW/mg of electrolyte (right)

By increasing the amount of the electrolyte in the mixture, the first peak at 220 °C dominates the DSC profile of the graphite in the range of 150 °C - 280 °C. The result shows that the electrolyte includes the limited reactant that drives the first reaction.

Combining the results discussed above, the impact of the electrolyte is especially noted between ~100 °C and ~270 °C. Thus, we can say that the electrolyte affects especially the first part of the degradation process of the graphite.

We suggest that “area 2 - Figure 15” is dominated by the electrolyte degradation reaction but we mentioned that other possible reactions may occur after salt melting between intercalated lithium, and SEI components [32]. These reactions will be discussed in chapter IV.

3.3 Area 3 [270 °C – 370 °C]

By observing the broad shape of the exothermic peak in “area 3 - Figure 15”, we suggest that this zone hides more than one exothermic reaction. In this part, we will try to identify the reaction(s) that occur(s) at this temperature range.

In the literature, the peak in this temperature range is usually attributed to the reaction between binder and lithiated graphite [33], [34].

For the INR18650-32E cell, the nature of the electrode binder is not specified by the fabricant. However, according to the XPS analysis of the negative electrode discussed in section 3.1.1, we detected the presence of the Na element, which can be associated to CMC-Na polymers present in the negative electrode material. This suggestion will be confirmed by the DSC analysis presented and discussed in the following parts.

3.3.1 Lithium – Binder interaction

To investigate the interaction between the intercalated lithium and the binder, three different DSC results are reported in the following Figure 28. The curve “a” for lithiated negative electrode without electrolyte, the curve “b” for CMC-Na binder mixed with cell electrolyte, and finally the curve “c” represents the electrolyte tested individually. A shift between the curves was added for better visibility of the results.

The curve “b” shows an exothermic peak detected at ~230 °C followed by an endothermic peak at ~310 °C. The first exothermic peak is consistent with the electrolyte degradation peak as observed in curve “c”. The thermal decomposition of the organic binder begins above 250 °C with a weight loss of 45 wt.% at 300 °C according to [35]. These values are consistent with the endothermic peak identified in curve “b”. Then, the endothermic peak occurs when the CMS-Na binder melts; however, no exothermic interaction is detected with the cell electrolyte.

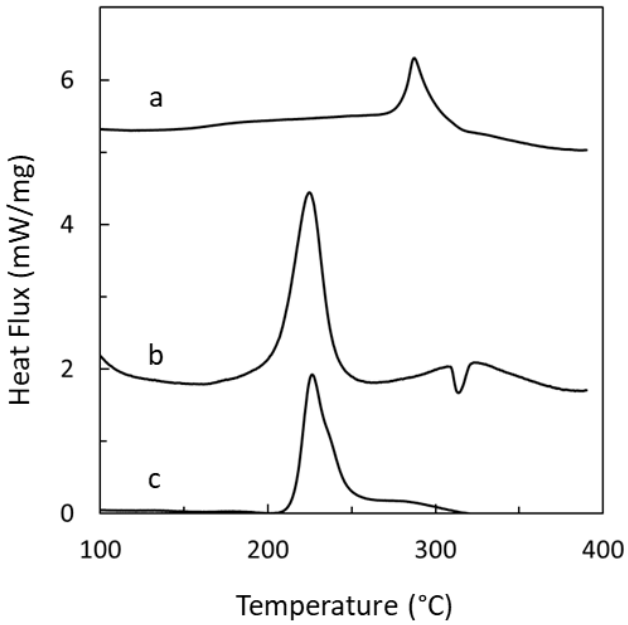

Figure 28: DSC profiles at 5 °C.min^{-1} of (a) lithiated negative electrode (mw/mg of active material) (b) CMC-Na binder + cell electrolyte (25:75 wt%) and (c) cell electrolyte only (mw/mg of electrolyte)

In the case of the lithiated negative electrode without adding supplementary electrolyte (curve “a”), an exothermic peak starts at around 270 °C and reaches a maximum of 290 °C. While

this peak is detectable only in the lithiated state, it is not existing in this range of temperature with the same electrode in the delithiated state.

Thus, we can suppose based on this observation that the detected exothermic peak in the curve “a” might be associated with the interaction between the intercalated lithium and CMC-Na binder.

The reactivity of CMC-Na binder is probably due to the hydroxyl functional groups in CMC (see reaction (21)) After decomposition, it might react with the residual amount of intercalated lithium in the negative electrode following the reaction (22) [9]

$$\mathrm{CMC-Na} \rightarrow \mathrm{levoglucosan(s)} + \mathrm{CO_2} + \mathrm{H_2O(g)} \quad (21)$$

$$\mathrm{CMC-OH} + \mathrm{Li} \rightarrow \mathrm{CMC-Oli(s)} + \tfrac{1}{2}\,\mathrm{H_2(g)} \quad (22)$$

Besides, the exothermic peak in the curve “a” generates only 160 J g^{-1} of lithiated graphite. This interaction is not energetic because it is limited by the amount of CMC-Na that does not exceed usually 2-4 wt% of the total negative electrode weight. Then, we assume that the CMC-Na/lithium reaction cannot explain the considerable heat generated in “area 3 - Figure 15”, with an average of 1300 J g^{-1} of lithiated graphite obtained by peaks deconvolution.

Therefore, we suggested that area 3 in Figure 15 involves other(s) exothermic reaction(s) than the CMC-Na/lithium reaction.

3.3.2 Lithium – PEO interaction

We particularly focused on the interaction between the intercalated lithium and the degradation products of the electrolyte (PEO), which can occur in this temperature range.

Therefore, to study this reaction independently, a sample of lithium metal foil was tested in DSC in presence of the cell electrolyte. The obtained result is reported in Figure 29.

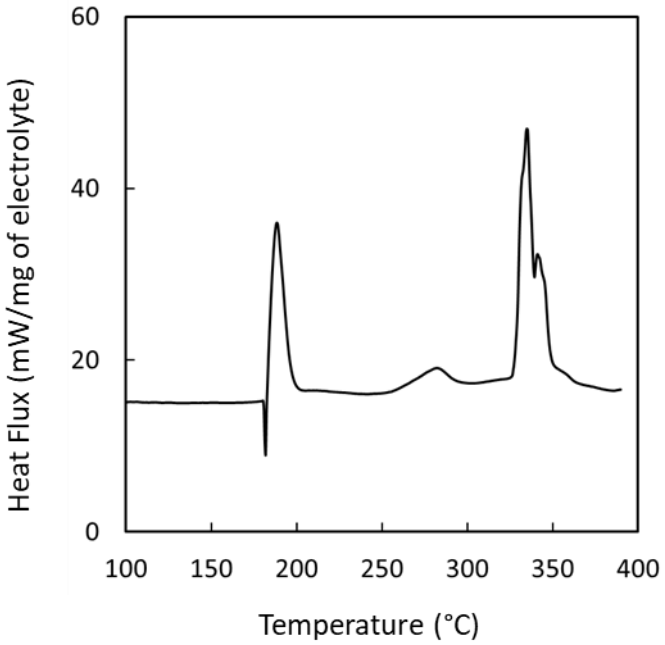

Figure 29: DSC profiles of lithium metal mixed with cell electrolyte at 5 °C.min^{-1}

The observed first endothermic peak occurs after the melting of lithium at 180 °C and is followed by an exothermic peak at nearly the same temperature. The board exothermic peak detected between 250 °C and 270 °C is attributed to electrolyte degradation.

The last exothermic peak starts near 320 °C with a maximum of 330 °C and released a significant amount of energy measured as 7500 J/g of lithium metal (2150 J g^{-1} of electrolyte). This powerful exothermic reaction is probably the second reaction that occurs at the same time as the CMC-Na/lithium reaction in “area 3 in Figure 15” between the residual intercalated lithium and the electrolyte degradation products. Such interaction is observed when PEO polymers, used in all-solid-state batteries, are tested in DSC with lithium [36].

According to the previous discussions, we could say that at least two exothermic reactions occur in “area 3 in Figure 15” including CMC-Na/lithium but mainly PEO/lithium.

4 Thermal degradation of the positive electrode

In this section, we present the thermal decomposition reactions for fresh NCA-based electrode and their contribution during the thermal runaway process of a loaded commercial INR18650-32E cell. From a thermodynamic point of view, layered metal oxides Li_xMO_2 such as NCA and NMC electrode material are thermally unstable in a delithiated state and release oxygen at high temperature; oxygen species may contribute as oxidizers and increase the risk of thermal runaway [37], [38]. The thermal decomposition of layered metal oxides is characterized by a transformation from the initial structure into a spinel structure followed by a production of rock salt and oxygen [37]–[39].

Usually, for $Li_xNi_aCo_bAl_cO_2$ material with low lithium content (x<0.5) and high nickel content (a≥80%), the initial phase change occurs theoretically near 200 °C according to the following reaction [38]:

$$xLiMO_2 + (1-x)MO_2 \rightarrow xLiM_2O_4 + (1-2x)MO_2 \quad (23)$$

With M: $Ni_aCo_bAl_c$

Reaction (23) is exothermic with about 210 J/g of $Li_{0.5}MO_2$ and produces no oxygen [38].

Then the excess of MO_2 in reaction (23) is converted to MO according to reaction (24):

$$2xLiMO_2 + 2(1-x)MO_2 \rightarrow 2xLiM_2O_4 + 2(1-2x)MO + (1-2x)O_2 \quad (24)$$

And finally,

$$2\,LiM_2O_4 \rightarrow 2LiMO_2 + 2\,MO + O_2 \quad (25)$$

According to [38], MO formation reactions ((24) - (25)) are endothermic and generate oxygen species.

The same experimental approach applied to study the negative electrode material thermal behavior was adopted to investigate the positive electrode material. The same type of electrolyte was also used and the obtained DSC results are presented and discussed in the following parts.

4.1 Delithiated NCA thermal behavior

The result in Figure 30 presents the obtained thermal decomposition profile of delithiated NCA before (dotted line) and after adding electrolyte (solid line). The delithiated Li_xNCA sample is obtained from the loaded fresh INR18650-32E cell with a lithium amount (x) situated in the interval [0.3 - 0.5].

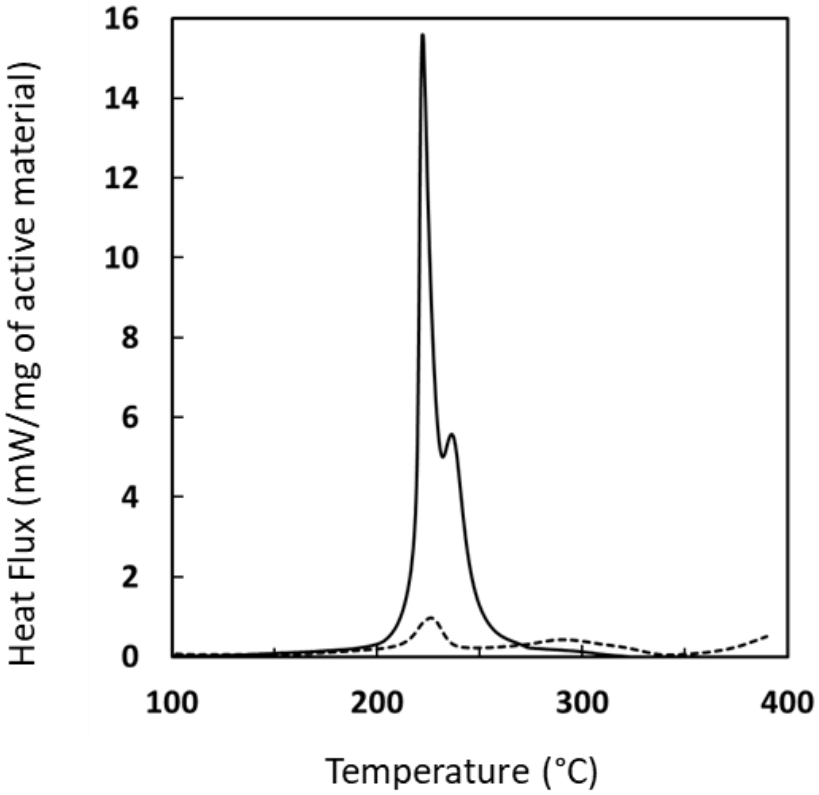

Figure 30: DSC profile at 5 °C.min^{-1} of delithiated NCA only (dotted line) and mixed with cell electrolyte (solid line) with 66:34 mass ratio

Without adding electrolyte (dashed curve), the delithiated NCA material shows mainly one small exothermic peak at 227 °C and generates 160 J/g of delithiated NCA, followed by a board peak centered around 300 °C. The total associated heat is about 350 J/g of delithiated NCA. According to the thermodynamic data, we suggest that the T_{onset} and the amount of energy generated by the first exothermic peak are linked to the first structural change of delithiated NCA according to reaction (23).

Mixed with the cell electrolyte (solid line), the detected DSC profile shows a considerable difference. Two energetic exothermic peaks were observed, the first exothermic peak starts at about 200 °C and reaches a maximum at 222 °C, followed by a second peak at 236 °C.
The total heat measured in this case is about 2400 J/g of delithiated NCA. This value is consistent with the thermodynamic calculation presented in [38].

After the first structural change under 200 °C, the second transformation of delithiated NCA material occurs according to the endothermic reactions (24) and (25) and liberates some dioxygen. Simultaneously, dioxygen reacts exothermically with the organic solvent of the cell electrolyte towards complete and incomplete oxidation reactions [38], as shown below:

$$2\,EC + 5\,O_2 \rightarrow 6\,CO_2 + 4\,H_2O \quad (26)$$

$$2\,PC + 8\,O_2 \rightarrow 8\,CO_2 + 6\,H_2O \quad (27)$$

$$2\,DMC + 6\,O_2 \rightarrow 6\,CO_2 + 6\,H_2O \quad (28)$$

$$2\,EC + O_2 \rightarrow 2\,CO_2 + 4\,CO + 4\,H_2 \quad (29)$$

$$2\,PC + 2\,O_2 \rightarrow 2\,CO_2 + 6\,CO + 6\,H_2 \quad (30)$$

$$2\,DMC + O_2 \rightarrow 2\,CO_2 + 4\,CO + 6\,H_2 \quad (31)$$

The powerful peak, detected in Figure 30, at 222 °C is probably related to one or more of these exothermic reactions.

Based on these reactions, the full-oxidation reactions require between 2.5 and 4 dioxygen atoms (see reactions (26)-(28)). However, the partial-oxidation reactions require only 0.5 to 1 dioxygen molecule (reactions (29)-(31)).
Then, to better understand the relationship between these reactions and the heat detected in Figure 30, we must focus on the NCA material/electrolyte mass ratio used in this analysis.

The global decomposition of delithiated NCA is given in [28], as follows:

$$1\,Li_x(NiCoAl)O_2 \rightarrow Li_x(NiCoAl)O_{1+x} + \frac{1}{2}(1-x)O_2 \quad (32)$$

As mentioned above, x is located between 0.3 and 0.5 for delithiated NCA. Therefore, it may produce between 0.35 and 0.25 of dioxygen based on the relation (32).

In the DSC result of the delithiated NCA+electrolyte sample (solid line curve in Figure 30), about 3 mg of active material were added with 1 mg of electrolyte.
Thus, according to reaction (32), the amount of liberated dioxygen is estimated to be around 0.5 and 0.7 mg. Since the electrolyte oxidation reactions are controlled by the amount of released oxygen in the mixture, the estimated amount of oxygen (0.5 - 0.7 mg) is not sufficient to achieve complete oxidation of the electrolyte solvents.
Thereby, the second exothermic peak detected at 235 °C is probably related to the degradation of the residual solvents after $LiPF_6$ melting and/or other interactions with NCA oxides. After peaks deconvolution, the heat released by the solvent oxidation in the first peak is estimated to be in the range of 1100 – 1300 J/g of delithiated NCA and between 1200 – 1300 J/g of delithiated NCA for the second peak detected at 235 °C. Since the energy generated by the electrolyte degradation is lower than 600 J/g of electrolyte, we conclude that other interactions between NCA oxides and electrolyte (salt + residual solvent) may occur and generate the second exothermic peak in Figure 30 (solid line curve).

To better understand the dependency between the amount of released oxygen and the solvent oxidation, two different mass ratios of delithiated NCA/electrolyte are tested in DSC; 80:20 and 66:34 ratio. The results are presented in Figure 31 in logarithmic and linear scale; a dotted line indicates repeatability.

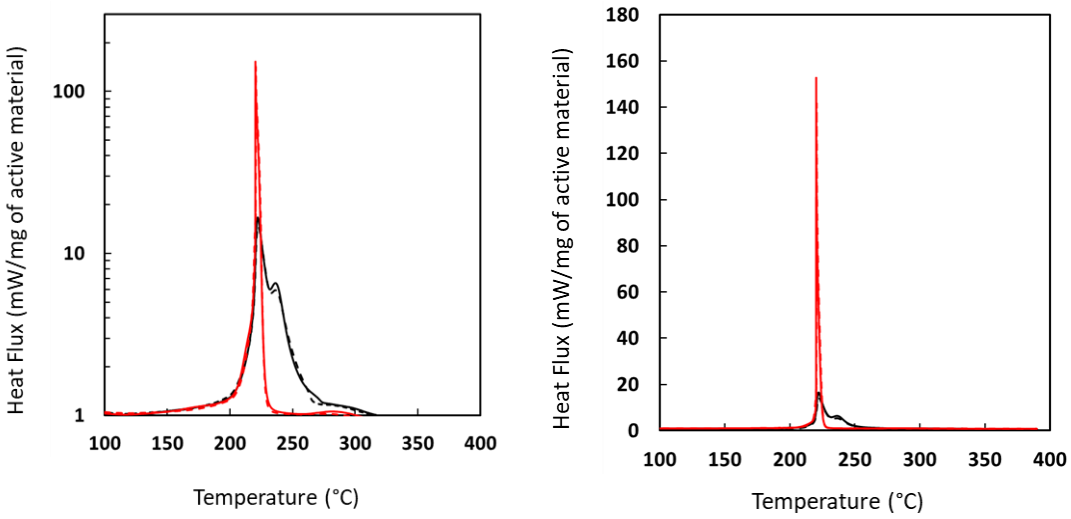

Figure 31: DSC profile at 5 °C.min^{-1} of delithiated NCA mixed with cell electrolyte with 80:20 ratio (red line) and 66:34 ratio (black line), presented in logarithmic (left figure) and linear scale (right figure)

By comparing the DSC profiles obtained with two different mass ratios, a coherence is mentioned between the amount of the electrolyte in the mixture and the generated heat flux by the oxidation peak detected in both cases at 222 °C.

However, the maximum heat power of this peak with a 66:34 ratio is very different from that with an 80:20 ratio; a significant change is observed when the amount of electrolyte in the mixture decreases by ~20 % which illustrates the high-energy oxidation reaction of the electrolyte solvents.

Indeed, the released heat by full-oxidation reactions is much higher than in partial-oxidation reactions. Considering the EC solvent, for example, the enthalpy of its full-oxidation is 1180.6 kJ/mol of solvent. However, only 43 kJ/mol of solvent is released when the oxidation is partial. According to reaction (26), full-oxidation occurs when the number of moles of oxygen is at least more than twice the number of moles of EC. With the 80:20 mass ratio, the number of moles of oxygen is twice the number of moles of solvent, making the full-oxidation as obtained in the DSC results possible.

Moreover, according to reaction (32), the amount of O_2 is directly proportional to the amount of delithiated NCA. If we consider the same sample weight in both cases, we have 20 % more oxygen with the 80:20 ratio sample. Then, as oxygen is the limiting element, we should have more complete than partial oxidation in the case of an 80:20 ratio and therefore a more powerful reaction in this case, which is consistent with the obtained results. The oxygen

amount released from the delithiated NCA with the 80:20 ratio is higher than that released with the 66:34 ratio, leading to a full-oxidation reaction of the electrolyte as shown in Figure 31 (red line curves).

Interestingly, a deformation was observed on the top part of the crucible used in the DSC experiment of the delithiated NCA + electrolyte mixture with an 80:20 mass ratio as shown in Figure 32.

Figure 32: crucible photo after the DSC experiment (results in Figure 31)

Such observation confirms the high power that could be generated by the full-oxidation reaction. The total measured heat in the temperature range [100 °C; 350 °C] is relatively the same, for both ratios, with an average of 2400 J/g of delithiated NCA.

4.2 Oxygen-free NCA thermal behavior

The thermal degradation of delithiated NCA material was studied without and after adding the cell electrolyte. The degradation of delithiated NCA powder mixed with cell electrolyte was marked by the oxidation reaction between the released oxygen from NCA and the electrolyte solvent leading to an exothermic peak at 220 °C with significant heat.
More investigation on the structural transformation of the NCA material with temperature was conducted and the obtained results are discussed in this part.

XRD analysis was performed on the delithiated NCA powder before and after heating at 300 °C. It was reported that most O_2 is liberated from the material at this temperature [40].
Firstly, the NCA sample was heated up to 300 °C, using a BUCHI glass oven, for 30 min. Then, the powder of the oxygen-free NCA sample was prepared for XRD analysis in the glove box.

Figure 33 shows the XRD results of fresh delithiated NCA powder after heating to 300 °C.

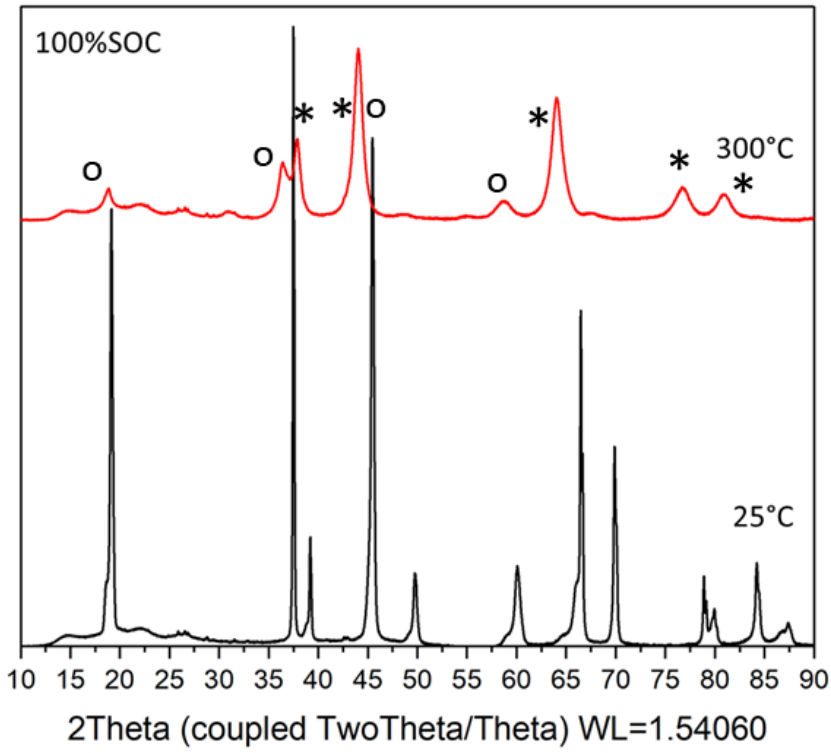

*Figure 33: XRD pattern of a conventional lamellar phase at 25 °C (in black: 2 lamellar phases ($LixMO_2$)). XRD pattern of a lamellar phase after 300 °C thermal treatment (in red: spinel phase M_3O_4 ($Li_{0.5}Co_{2.5}O_4$) o, rock salt phase MO ($Li_{0.39}Ni_{0.61}O$) *)*

The obtained XRD patterns are in good agreement with the data reported in the literature. Significant changes in the structure of the delithiated NCA were detected after heating; the material is initially transformed from the layered phase R-$\bar{3}$m to the disordered spinel Fd-$\bar{3}$m then to the rock salt phase Fm-$\bar{3}$m.

These transformations are indicated by the changes in the intensity of XRD signals and the conjoining of peaks. The change of delithiated NCA from the initial layered phase to the spinel phase is especially indicated by the decrease in the intensity of the first peak around 20° and the expansion of peaks between 35° and 47°. This illustrates the migration of Ni, Co, and Al cations from the bulk material to the Li layer. Then, the NiO-type rock salt phase is indicated by the conjoining of peaks situated between 60° and 90°.

DSC analysis is performed to study the reactivity of the oxygen-free NCA powder mixed with the cell electrolyte. The aim is to validate the solvent oxidation reaction discussed in the previous part. The obtained DSC result is presented in Figure 34 (red line curve) and compared with the DSC profile of the same sample before heating (black line curve).

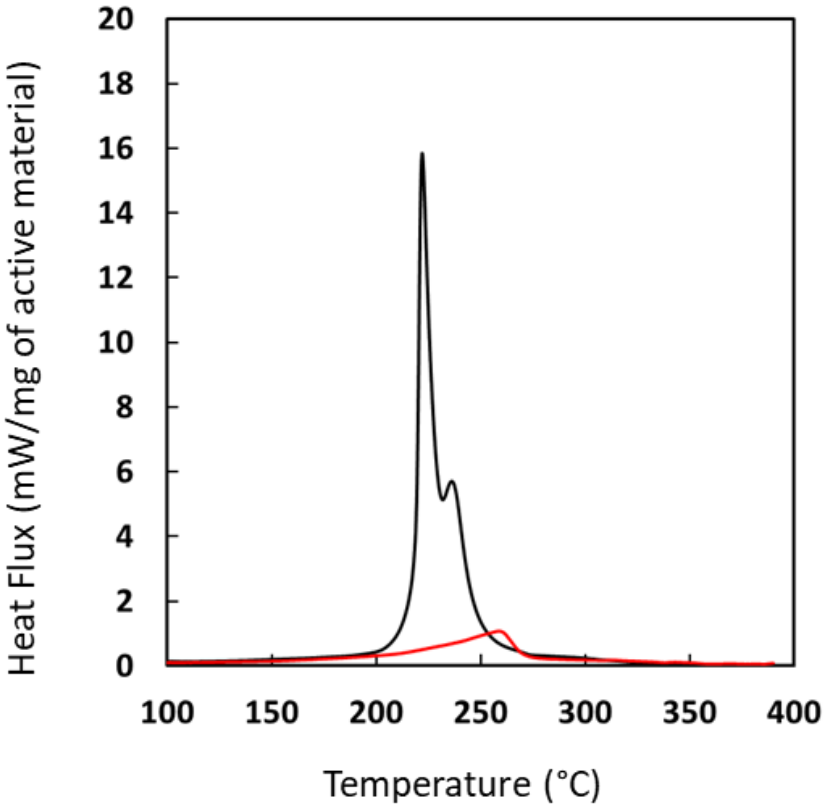

Figure 34: DSC profile at 5 °C.min^{-1} of oxygen-free NCA (red line with 78:22 ratio) and fresh NCA (black line with 66:34 ratio) mixed with the cell electrolyte

Interestingly, the electrolyte mixed with heated delithiated NCA does not show an exothermic peak around 220 °C. This result revealed that the outgassing operation inhibits the energetic reactivity between the active material and the electrolyte. The only board peak observed around 250 °C is probably due to the electrolyte degradation reaction.

Combined with the above discussion, an illustration of the degradation process of delithiated NCA in presence of electrolyte is proposed by the following model:

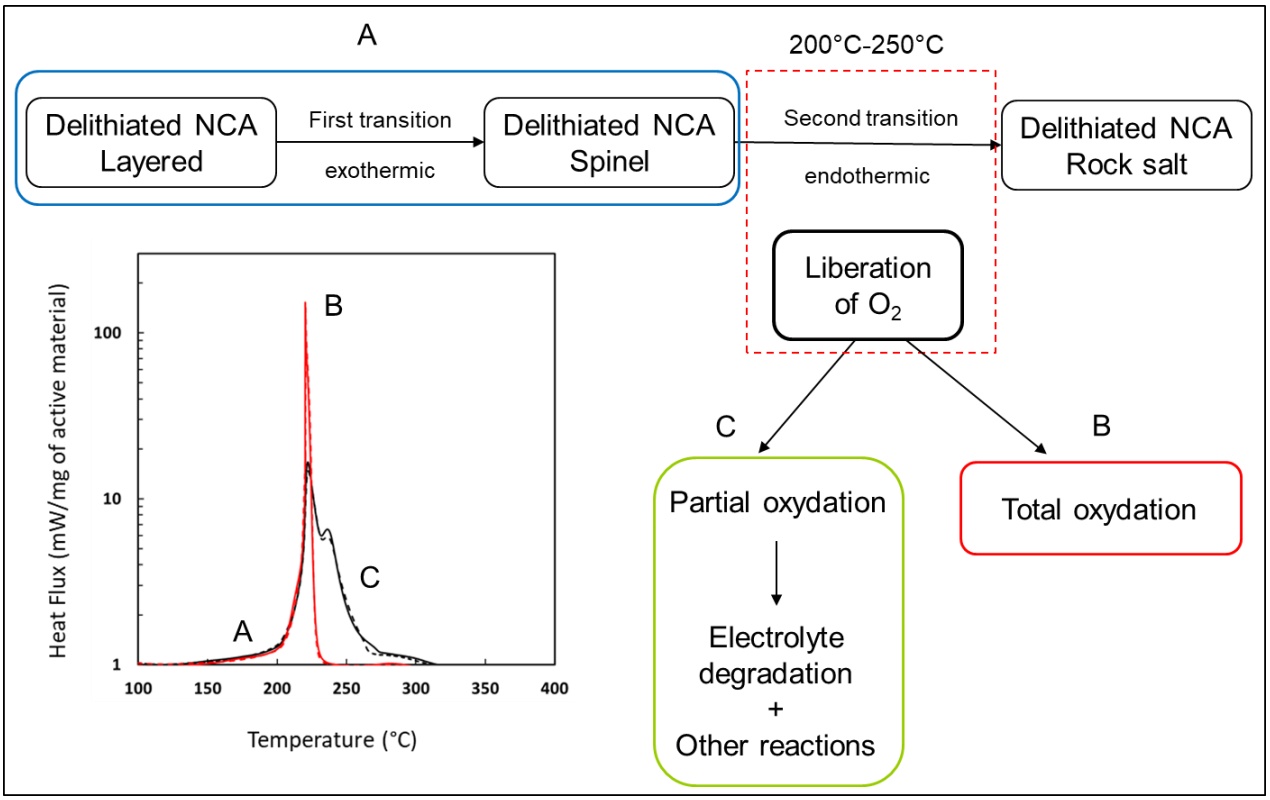

Figure 35: Degradation process of delithiated NCA in presence of the cell electrolyte, DSC profile at 5 °C/min of delithiated NCA mixed with cell electrolyte with 80:20 ratio (red line) and 66:34 ratio (black line), presented in logarithmic scale

5 Impact of SOC on the thermal degradation reactions

Before concluding this chapter, we present in this section a brief comparison between the thermal degradation profile of the cell materials in the lithiated and delithiated states. Indeed, our study was based on the commercial cell material at 100 % of SOC, which represents the worst-case scenario in terms of safety for Li-ion batteries. However, to show the influence of the state of charge on the thermal behavior of the cell materials, we propose here a comparison of the thermal degradation profiles of fresh lithiated and delithiated electrodes.

The DSC test experiments were carried out under the same conditions and using materials collected from the same cell at 0 % and 100 % of SOC. The active materials were mixed with the cell electrolyte with the same ratio. The obtained results are plotted, by mW/mg of active material, in Figure 36.

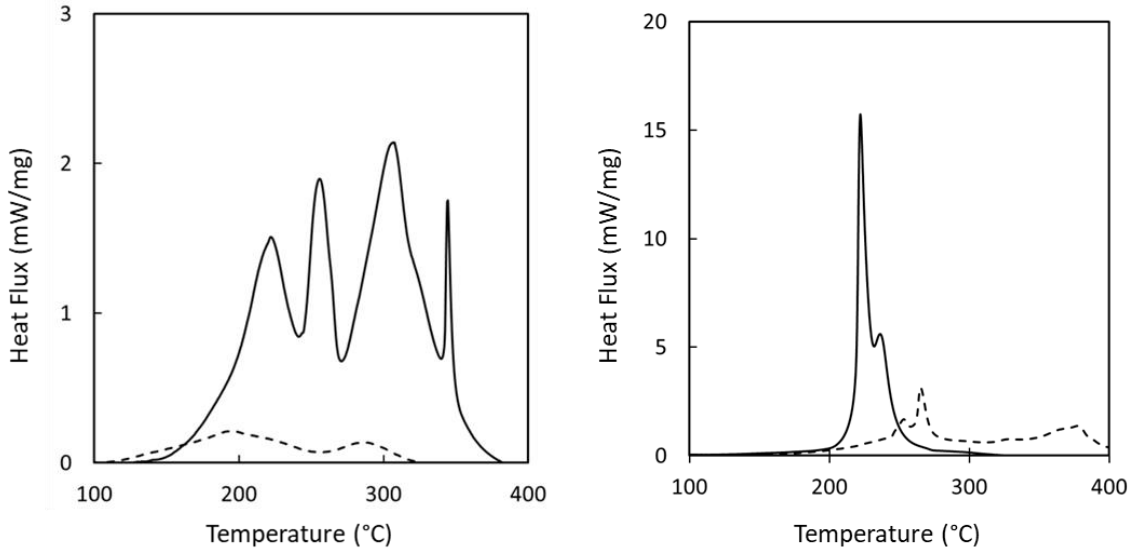

Figure 36: DSC heat flow at 5 °C/min of the graphite (left) and NCA (right) mixed with cell electrolyte, at SOC of 100 % (solid line) and 0 % (dashed line)

Visibly, and in agreement with the literature, the state of lithiation of the electrodes has a direct effect on Thermal Runaway. In the case of the negative electrode (left curves), the DSC profiles show that the more lithium left in the graphite structure the more heat is released. The heat generated by the thermal degradation of the lithiated negative electrode mixed with electrolyte is 5 times higher than the delithiated negative electrode, as reported in Figure 37. Thus, lithium can be considered a key element in the thermal degradation mechanism of the negative electrode material.

Besides, we note that the degradation T_{onset} of the lithiated and delithiated negative electrode is approximately the same (~100 °C), which is related to the SEI breakdown reaction identified as independent of the lithiation state of the negative electrode as discussed in section 3.1.1.

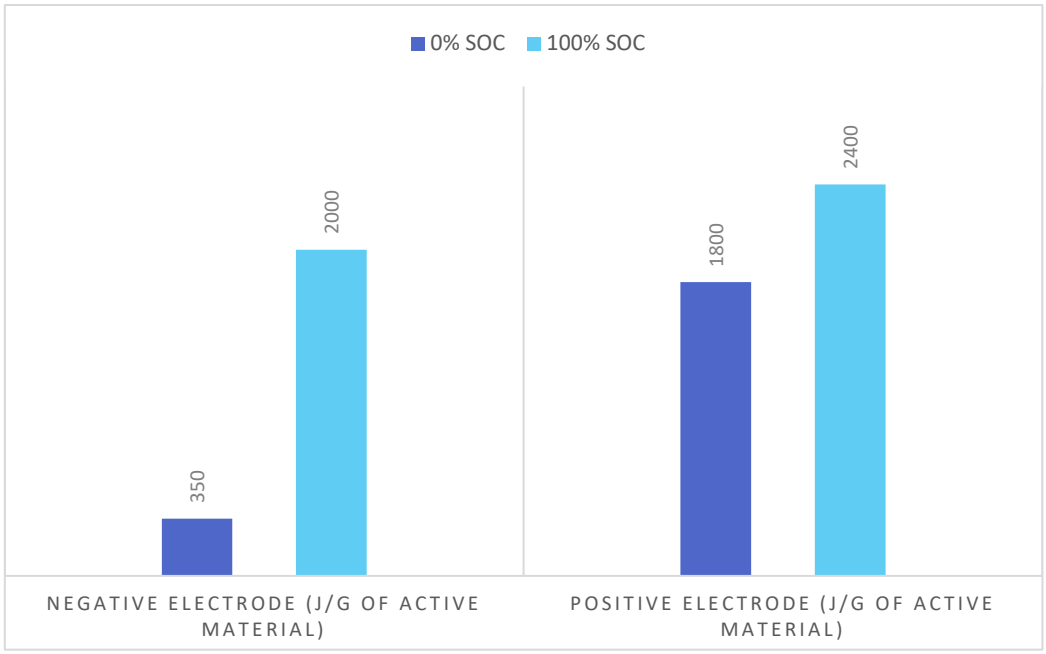

Figure 37: Total generated heat in J/g of active material by lithiated / delithiated negative and positive electrodes, based on DSC profiles reported in Figure 36

The change of the NCA thermal stability before and after lithiation is validated according to the DSC profiles in Figure 36 (right curves). The delithiated positive electrode material exhibits a lower thermal degradation T_{onset} than the lithiated NCA. Moreover, the pronounced exothermic peak obtained with the delithiated NCA/electrolyte mixture is not detected with the lithiated sample. The NCA structure is more stable in the lithiated state, then a very small amount of oxygen is released at high temperatures and the oxidation reaction of the electrolyte is inhibited.

This comparison demonstrates that our decision to work only with charged electrode material is not arbitrary and confirms the statement that Li-on cells are thermally unstable at 100 % SOC.

6 Conclusions

In this chapter, we have presented and discussed the experimental behaviors based on the study of fresh INR18650-32E cell materials by combining DSC analysis with different characterization techniques (XRD, XPS, and TOF-SIMS).
Our approach has mainly been oriented to achieve a better understanding of the thermal behavior of the cell materials before aging by analyzing the thermal stability of each component and their interactions.

To get representative results, the DSC experiments were performed under almost the same conditions, with materials from the same cell and by adding the cell electrolyte with similar proportions to a full cell. We have tried, in most of the DSC analyses performed, to avoid exceeding 25 % by weight of electrolytes in the mixture.

A preliminary study was carried out to determine the best conditions for experimental work.
It was decided that the preparation of the DSC samples starts with a washing step with DMC solvent for 30 s to remove the amount of residual electrolyte in the electrodes and to ensure better quantification of the results. And we checked that this washing step has no significant effect neither on the composition of SEI nor on the lithiation state of the electrode.

The thermal degradation reactions of the commercial cell components were analyzed and the main heat sources during a thermal runaway scenario were identified.
For each electrode different exothermic reactions have been observed, they are highly correlated and occur at various ranges of temperature. Most of these reactions were studied separately by testing multiple samples and configurations (different materials present or missing). The characteristics of the main detected exothermic reaction of the negative and positive active electrodes are summarized in Table 7. They are listed according to their appearance with the temperature. Two different colors are used to distinguish the reactions of the negative and positive electrodes.

Table 7: Reaction properties for the negative / positive electrode thermal degradation with the electrolyte of the charged cell

Exothermic reaction	Onset T (°C)	Peak T (°C)	Specific reaction heat (J g^{-1} of active material)	
			Post-treated numerical deconvolution	DSC elementary results
SEI decomposition	80 – 90	165	100 (fixed)	100 – 245
LiC_6 / solvent reaction	120 – 150	220	511 – 900	-
NCA first transition	180 – 200	-	160 (fixed)	160
Solvent oxidation	~200	220	1100 – 1300	-
Electrolyte degradation	200 – 220	250	240 – 360 [J/g of electrolyte]	375 [J/g of electrolyte]
NCA oxides/salt reaction + other reactions	~220	240	1200 – 1300	-
LiC_6/CMC-OH reaction	270 – 280	300	900 – 1740	160
LiC_6/PEO reaction	300 – 310	330		-
Other reaction	330 – 340	360	0 – 90	-

The reported heat of reactions in Table 7 was calculated after deconvolution of different DSC profiles performed at different heating rates (2,5 and 15°C/min). The energy was measured based on DSC results conducted between 50 °C and 400 °C using charged electrodes. Based on the TR reactions of the fresh INR18650-32E cell presented in Table 7, the SEI breakdown on the negative electrode (graphite-based) is the first reaction in the TR process of this cell and releases enough energy to trigger the chain of the other exothermic reactions in adiabatic condition.

In addition, the cell electrolyte is very reactive to oxygen released from the positive electrode material (NCA-based). The solvent oxidation seems to be a powerful reaction compared to other TR reactions. it could be considered as the key reaction in the thermal degradation mechanism of the fresh cell materials until 200 °C.

The impact of aging by cycling at -20 °C on the thermal stability of the INR18650-32E cell materials will be studied and presented in detail in the next chapter and compared to results obtained on fresh cells. The results discussed in the first chapter are fundamental for the next part of the work.

7 References

[1] A. W. Golubkov *et al.*, « Thermal runaway of commercial 18650 Li-ion batteries with LFP and NCA cathodes – impact of state of charge and overcharge », *RSC Adv.*, vol. 5, nº 70, p. 57171-57186, June 2015, doi: 10.1039/C5RA05897J.

[2] « SPECIFICATION OF PRODUCT », nº 2, p. 19.

[3] P. Kuntz, « Evolution du comportement sécuritaire de batterie lithium-ion pendant leur vieillissement », thesis, Université Grenoble Alpes, 2020. available online: April 2021, http://www.theses.fr/2020GRALI069

[4] T. Waldmann, R.-G. Scurtu, K. Richter, et M. Wohlfahrt-Mehrens, « 18650 vs. 21700 Li-ion cells – A direct comparison of electrochemical, thermal, and geometrical properties », *J. Power Sources*, vol. 472, p. 228614, Oct. 2020, doi: 10.1016/j.jpowsour.2020.228614.

[5] T. Waldmann *et al.*, « Review—Post-Mortem Analysis of Aged Lithium-Ion Batteries: Disassembly Methodology and Physico-Chemical Analysis Techniques », *J. Electrochem. Soc.*, vol. 163, nº 10, p. A2149-A2164, 2016, doi: 10.1149/2.1211609jes.

[6] K. N. Wood et G. Teeter, « XPS on Li-Battery-Related Compounds: Analysis of Inorganic SEI Phases and a Methodology for Charge Correction », *ACS Appl. Energy Mater.*, vol. 1, nº 9, p. 4493-4504, Sept. 2018, doi: 10.1021/acsaem.8b00406.

[7] F. C. Strobridge *et al.*, « Characterising local environments in high energy density Li-ion battery cathodes: a combined NMR and first principles study of LiFexCo1−xPO4 », *J. Mater. Chem. A*, vol. 2, nº 30, p. 11948-11957, July 2014, doi: 10.1039/C4TA00934G.

[8] C. P. Grey et Y. J. Lee, « Lithium MAS NMR studies of cathode materials for lithium-ion batteries », *Solid State Sci.*, vol. 5, nº 6, p. 883-894, June 2003, doi: 10.1016/S1293-2558(03)00113-4.

[9] A. Kriston, I. Adanouj, V. Ruiz, et A. Pfrang, « Quantification and simulation of thermal decomposition reactions of Li-ion battery materials by simultaneous thermal analysis coupled with gas analysis », *J. Power Sources*, vol. 435, p. 226774, Sept. 2019, doi: 10.1016/j.jpowsour.2019.226774.

[10] « Chemical Database Online ». https://www.chembk.com/en available online Feb. 2022).

[11] S. J. An, J. Li, C. Daniel, D. Mohanty, S. Nagpure, et D. L. Wood, « The state of understanding of the lithium-ion-battery graphite solid electrolyte interphase (SEI) and its relationship to formation cycling », *Carbon*, vol. 105, p. 52-76, Aug. 2016, doi: 10.1016/j.carbon.2016.04.008.

[12] R. Spotnitz et J. Franklin, « Abuse behavior of high-power, lithium-ion cells », *J. Power Sources*, vol. 113, p. 81-100, Jan. 2003, doi: 10.1016/S0378-7753(02)00488-3.

[13] J. Jones, M. Anouti, M. Caillon-Caravanier, P. Willmann, et D. Lemordant, « Thermodynamic of LiF dissolution in alkylcarbonates and some of their mixtures with water », *Fluid Phase Equilibria*, vol. 285, nº 1, p. 62-68, Nov. 2009, doi: 10.1016/j.fluid.2009.07.020.

[14] J. Jones, M. Anouti, M. Caillon-Caravanier, P. Willmann, P.-Y. Sizaret, et D. Lemordant, « Solubilization of SEI lithium salts in alkylcarbonate solvents », *Fluid Phase Equilibria*, vol. 305, nº 2, p. 121-126, June 2011, doi: 10.1016/j.fluid.2011.03.007.

[15] « Photoelectron Spectroscopy for Lithium Battery Interface Studies - IOPscience ». https://iopscience.iop.org/article/10.1149/2.0051602jes (available online Jan. 2022).

[16] S. Malmgren *et al.*, « Comparing anode and cathode electrode/electrolyte interface composition and morphology using soft and hard X-ray photoelectron spectroscopy », *Electrochimica Acta*, vol. 97, p. 23-32, May 2013, doi: 10.1016/j.electacta.2013.03.010.

[17] R. L. Sacci, L. W. Gill, E. W. Hagaman, et N. J. Dudney, « Operando NMR and XRD study of chemically synthesized LiCx oxidation in a dry room environment », *J. Power Sources*, vol. 287, p. 253-260, Aug. 2015, doi: 10.1016/j.jpowsour.2015.04.035.

[18] L. Ma, J. Xia, X. Xia, et J. R. Dahn, « The Impact of Vinylene Carbonate, Fluoroethylene Carbonate and Vinyl Ethylene Carbonate Electrolyte Additives on Electrode/Electrolyte Reactivity Studied Using Accelerating Rate Calorimetry », *J. Electrochem. Soc.*, vol. 161, nº 10, p. A1495, July 2014, doi: 10.1149/2.0091410jes.

[19] A. Wang, S. Kadam, H. Li, S. Shi, et Y. Qi, « Review on modeling of the anode solid electrolyte interphase (SEI) for lithium-ion batteries », *Npj Comput. Mater.*, vol. 4, nº 1, Dec. 2018, doi: 10.1038/s41524-018-0064-0.

[20] T. Hou *et al.*, « The influence of FEC on the solvation structure and reduction reaction of LiPF6/EC electrolytes and its implication for solid electrolyte interphase formation », *Nano Energy*, vol. 64, p. 103881, Oct. 2019, doi: 10.1016/j.nanoen.2019.103881.

[21] S. Solchenbach, M. Metzger, M. Egawa, H. Beyer, et H. A. Gasteiger, « Quantification of PF5 and POF3 from Side Reactions of LiPF6 in Li-Ion Batteries », *J. Electrochem. Soc.*, vol. 165, nº 13, p. A3022, Sept. 2018, doi: 10.1149/2.0481813jes.

[22] N. Lingappan, L. Kong, et M. Pecht, « The significance of aqueous binders in lithium-ion batteries », *Renew. Sustain. Energy Rev.*, vol. 147, p. 111227, Sept. 2021, doi: 10.1016/j.rser.2021.111227.

[23] A. L. Michan *et al.*, « Fluoroethylene Carbonate and Vinylene Carbonate Reduction: Understanding Lithium-Ion Battery Electrolyte Additives and Solid Electrolyte Interphase Formation », *Chem. Mater.*, vol. 28, nº 22, p. 8149-8159, Nov. 2016, doi: 10.1021/acs.chemmater.6b02282.

[24] S. Huang, L.-Z. Cheong, D. Wang, et C. Shen, « Thermal stability of solid electrolyte interphase of lithium-ion batteries », *Appl. Surf. Sci.*, vol. 454, p. 61-67, Oct. 2018, doi: 10.1016/j.apsusc.2018.05.136.

[25] V. Etacheri *et al.*, « Effect of Fluoroethylene Carbonate (FEC) on the Performance and Surface Chemistry of Si-Nanowire Li-Ion Battery Anodes », *Langmuir*, vol. 28, nº 1, p. 965-976, Jan. 2012, doi: 10.1021/la203712s.

[26] S. Dalavi, P. Guduru, et B. L. Lucht, « Performance Enhancing Electrolyte Additives for Lithium Ion Batteries with Silicon Anodes », *J. Electrochem. Soc.*, vol. 159, nº 5, p. A642, Mar. 2012, doi: 10.1149/2.076205jes.

[27] M. Nie, D. P. Abraham, D. M. Seo, Y. Chen, A. Bose, et B. L. Lucht, « Role of Solution Structure in Solid Electrolyte Interphase Formation on Graphite with LiPF6 in Propylene Carbonate », *J. Phys. Chem. C*, vol. 117, nº 48, p. 25381-25389, Dec. 2013, doi: 10.1021/jp409765w.

[28] « TIMCAL TIMREX® KS6 Primary Synthetic Graphite datasheet ». http://www.lookpolymers.com/polymer_TIMCAL-TIMREX-KS6-Primary-Synthetic-Graphite.php (available online Jan. 2022).

[29] Z. Chen *et al.*, « Multi-scale study of thermal stability of lithiated graphite », *Energy Environ. Sci.*, vol. 4, nº 10, p. 4023-4030, Sept. 2011, doi: 10.1039/C1EE01786A.

[30] I. Belharouak, D. Vissers, et K. Amine, « Thermal Stability of the Li (Ni0.8Co0.15Al0.05) O2 Cathode in the Presence of Cell Components », *J. Electrochem. Soc.*, vol. 153, nº 11, p. A2030, Sept. 2006, doi: 10.1149/1.2336994.

[31] Q. Wang, J. Sun, X. Yao, et C. Chen, « Thermal stability of LiPF6/EC+DEC electrolyte with charged electrodes for lithium ion batteries », *Thermochim. Acta*, vol. 437, nº 1, p. 12-16, Oct. 2005, doi: 10.1016/j.tca.2005.06.010.

[32] « Nonaqueous Liquid Electrolytes for Lithium-Based Rechargeable Batteries | Chemical Reviews ». https://pubs.acs.org/doi/10.1021/cr030203g (Available online Aug. 2021).

[33] Q. Wang, B. Mao, S. I. Stoliarov, et J. Sun, « A review of lithium ion battery failure mechanisms and fire prevention strategies », *Prog. Energy Combust. Sci.*, vol. 73, p. 95-131, July 2019, doi: 10.1016/j.pecs.2019.03.002.

[34] A. W. Golubkov *et al.*, « Thermal-runaway experiments on consumer Li-ion batteries with metal-oxide and olivin-type cathodes », *RSC Adv*, vol. 4, nº 7, p. 3633-3642, 2014, doi: 10.1039/C3RA45748F.

[35] P. Jakóbczyk, M. Bartmański, et E. Rudnicka, « Locust bean gum as green and water-soluble binder for LiFePO4 and Li4Ti5O12 electrodes », *J. Appl. Electrochem.*, vol. 51, nº 3, p. 359-371, Mar. 2021, doi: 10.1007/s10800-020-01496-z.

[36] C. Capiglia, J. Yang, N. Imanishi, A. Hirano, Y. Takeda, et O. Yamamoto, « DSC study on the thermal stability of solid polymer electrolyte cells », *J. Power Sources*, vol. 119-121, p. 826-832, June 2003, doi: 10.1016/S0378-7753(03)00280-5.

[37] Y. Huang *et al.*, « Thermal Stability and Reactivity of Cathode Materials for Li-Ion Batteries », *ACS Appl. Mater. Interfaces*, vol. 8, nº 11, p. 7013-7021, Mar. 2016, doi: 10.1021/acsami.5b12081.

[38] R. C. Shurtz et J. C. Hewson, « Review—Materials Science Predictions of Thermal Runaway in Layered Metal-Oxide Cathodes: A Review of Thermodynamics », *J. Electrochem. Soc.*, vol. 167, nº 9, p. 090543, May2020, doi: 10.1149/1945-7111/ab8fd9.

[39] M. D. Radin *et al.*, « Narrowing the Gap between Theoretical and Practical Capacities in Li-Ion Layered Oxide Cathode Materials », *Adv. Energy Mater.*, vol. 7, nº 20, p. 1602888, 2017, doi: 10.1002/aenm.201602888.

[40] M. M. Besli *et al.*, « Thermally-driven mesopore formation and oxygen release in delithiated NCA cathode particles », *J. Mater. Chem. A*, vol. 7, nº 20, p. 12593-12603, May 2019, doi: 10.1039/C9TA01720H.

Chapter III: Thermal behavior of Graphite/Nickel-Rich cell aged at low temperature

Contents

List of tables

List of figures

Under extreme conditions, in particular when charging at low temperature and/or with high currents (fast charging) or at high SOC, the formation of lithium plating on the surface of the graphite-based electrode is accelerated [1]–[3].

In previous work carried out at CEA Grenoble [4], abusive tests were performed on Ni-rich cells before and after aging under different conditions. These safety tests have revealed the impact of aging on the safety behavior of these cells; especially after aging by cycling at low temperature. Figure 1 shows the thermal behavior of the INR18650-32E cell during an ARC test before and after aging by cycling at -20 °C.

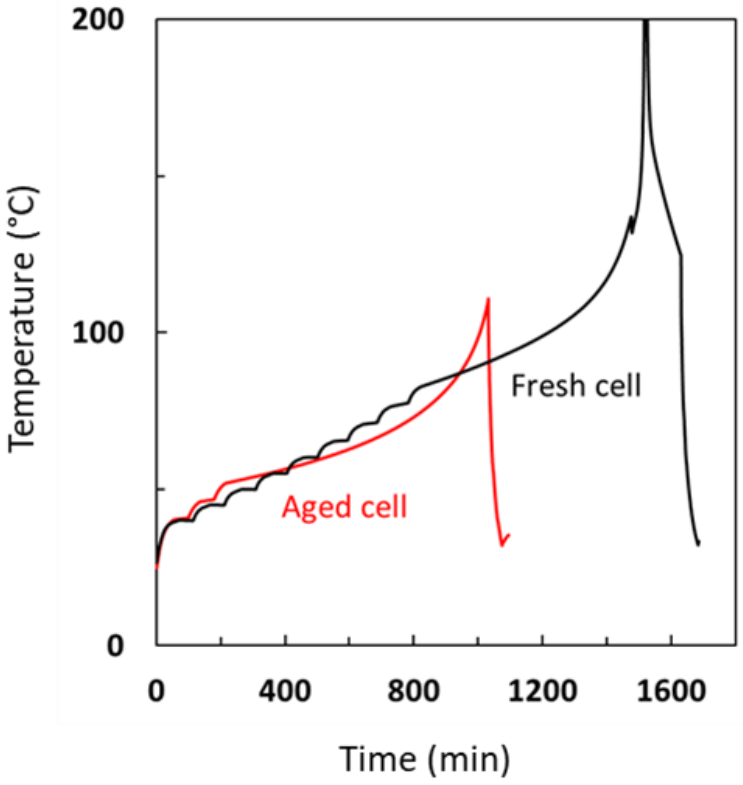

Figure 1: ARC test of charged INR18650-32E cell before and after aging (Charge/Discharge at -20 °C cycles)

The ARC test result shows a significant difference in the self-heating temperature (T_{onset}), under adiabatic conditions, of the cell before (black curve) and after aging by cycling at -20 °C (red curve). For the fresh cell, the recorded T_{onset} was 77 °C, however, after aging the cell goes into TR earlier with a detected T_{onset} at about 53 °C.

A relationship between aging by cycling at low temperature and the increase of the self-heating of the cell under adiabatic conditions was highlighted in this study [4], [5]. The same correlation was mentioned in some other studies [6]–[8]. Nevertheless, more investigations are needed at the material scale to better characterize the early thermal runaway after aging at low temperatures and segregate the problems from each other to better understand the sequence of events.

In this context and considering the strong link established between aging at low temperature and lithium plating formation on graphite electrodes, the thermal behavior of the INR18650-32E cell materials after aging by cycling at -20 °C is investigated with a particular focus on the negative electrode material. To our knowledge, there is no similar study published to date on this subject. In this chapter, the obtained results of this study are presented and discussed in detail.

The first section is dedicated to a description of the adopted aging protocol followed by an observation of the impact of low temperature aging on the negative electrode material illustrated with ^{7}Li NMR MAS analysis. Then, a quantification study of the lithium plating formed on aged graphite electrodes is detailed in the second section. The third and the fourth sections are dedicated to the discussion of the thermal behavior results of the aged INR18650-32E cell materials based on DSC analysis. Finally, an energy balance of the cell is presented based on the obtained results.

1 Low-temperature aging of the INR18650-32E cell

1.1 The selected aging method

Lithium-ion batteries are tested before commercialization to investigate their performances, reliability, and safety under different operating conditions. Therefore, a series of test procedures were published to normalize the use of lithium-ion batteries. Specifically, the ISO 12405 and the IEC 62660 are used to determine the applicability of lithium-ion batteries in hybrid and battery electric vehicles [9].

In order to perform representative aging of the battery in electric vehicles, we followed the IEC 62660-1 standard (Secondary lithium-ion cells for the propulsion of electric road vehicles - Part 1: Performance testing [10]) to simulate the use of the battery in an electric vehicle during a driving test. The aging cycle as introduced in the IEC 62660-1 standard is composed of a charge cycle and a succession of discharge profiles containing charge and discharge pulses. The total duration of the aging protocol following the IEC 62660-1 standard is 28 days. In this period, the number of cycles achieved varies depending on the cell between 1500 and 2000 cycles. For our investigation, INR18650-32E cells were introduced in a battery test chamber with a temperature fixed at -20 °C. These cycling conditions were chosen to accelerate the lithium plating formation and give a reasonable time frame for the study.
After completing the aging period, cells were stored at 50 % of SOC at ambient temperature.
To better understand the impact of aging at low temperatures on the cell materials, the aged cells were divided into two batches according to their duration of aging. Half of the cells were

removed after 14 days of cycling, and the remaining cells were removed at the end of the aging event.

1.2 The impact of low-temperature aging on the cell materials

The aged cells were disassembled in the glove box and the electrode materials were prepared for the following characterization analyses. We noted that positive and negative electrodes of aged cells are fragile and easily fractured. We focused in this part on the negative electrode, which revealed much more interesting information.

Figure 2 shows optical photos of the charged negative electrode (anode) taken before and after aging at low temperature:

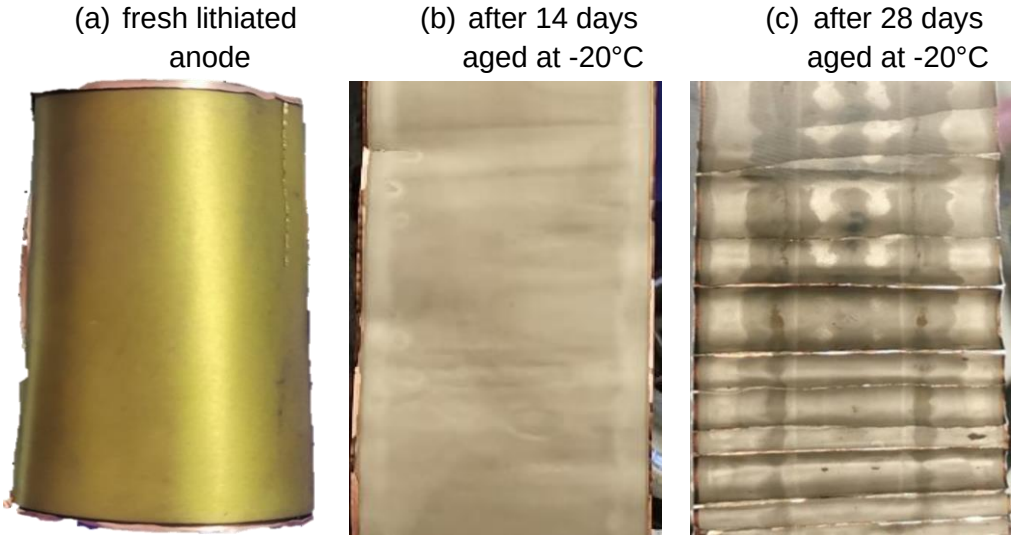

Figure 2: photos of the negative electrode surface including (a) fresh lithiated anode (b) aged lithiated anode after 14 days at -20 °C (c) aged lithiated anode after 28 days at -20 °C

Before aging, the observed gold color on the surface of the fresh negative electrode, (photo (a) in Figure 2)is the typical coloration of the lithiated graphite LiC_6 crystal [11], [12], This confirms the full lithiation of the electrode.

After 14 days of aging at -20 °C (photo (b) in Figure 2), the surface of the negative electrode was covered with a relatively homogeneous gray coating on the separator side. After 28 days of aging, a very located gray coating with more contrast was observed on the same electrode side (photo (c) in Figure 2). The observed gray coloration indicates typically the presence of lithium metal.

In this part, we give some explanation of the Li plating occurrence confirmed by these observations. Under typical operating conditions, lithium cations migrate between electrodes through the electrolyte. During the charging cycle, lithium cations intercalate between

graphene layers of the graphite electrode. During discharging cycle, lithium cations are inserted into the structure of the positive electrode material(s).

The transport of lithium ions between the electrodes is mainly controlled by diffusion, which depends on the temperature. At -20 °C, the mobility of lithium ions decreases, and diffusion slows down [13]. Moreover, the lithiation kinetics inside the negative electrode material decrease, and lithium intercalation becomes difficult at low temperatures. The accumulation of lithium ions makes the electric potential in the liquid phase (electrolyte) vs Li/Li^+ at the surface of the graphite particles near 0 V or even below. The reduction of lithium becomes favored at this potential range, according to the following reaction [14]

$$\mathbf{Li^+ + 1e^- \rightarrow Li(s)} \quad (1)$$

As observed in Figure 2, the lithium plating looks uniform on the electrode surface after 14 days of aging. However, heterogeneity of lithium plating was observed after 28 days at -20 °C. The fast development of plated lithium on the electrode surface, even after only 14 days, is related to the very low-temperature cycling which accelerates the aging mechanisms.

Moreover, a difference in the distribution of the lithium plating was also noticed by comparing the center side and the outside of the 28 days aged electrode. Figure 3 shows the difference between both sides of the same electrode.

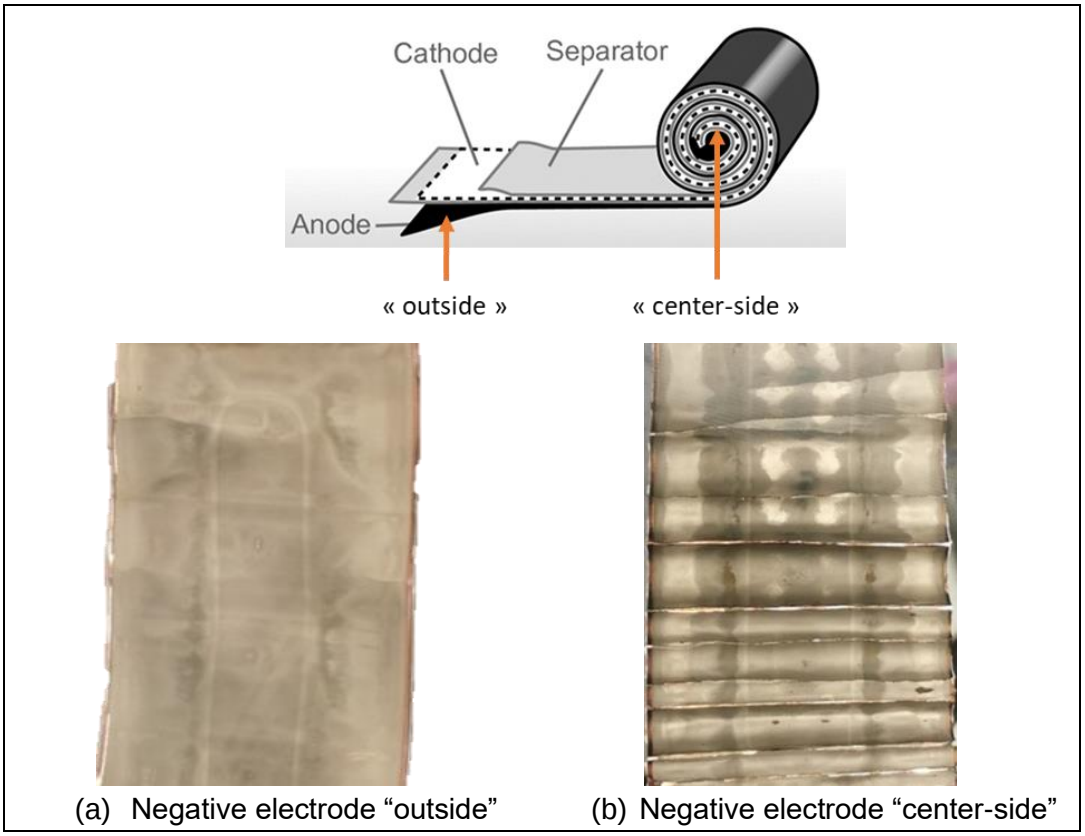

Figure 3: photos illustrating lithium plating at (a) the outside surface and (b) the inside surface of the 28 days aged anode at -20 °C

The non-homogeneity of the Li plating formation between the two sides is probably related to different mechanical constraints applied on the electrode that may have an impact on the material as well as the Li-plating formation. Indeed, the cylindrical cell is rolled up and maintained in a limited volume inside a metallic hard casing. When the Li-ion battery is formed and during every charge, the negative electrode expands (at least 10 %, as the mesh parameter of graphite increases from 3.35 A° to 3.71 A° for LiC_6). At the same time, the mesh parameter of the positive electrode does not decrease significantly [15]. This volume expansion induces internal mechanical constraints on electrodes and materials at every charge/discharge cycle. Due to the limited compression capacity of the separator, some global mechanical constraints remain and the induced strains generate deformation where some free space exists i.e., in the center of the cylindrical cell [16].

At the same time, the global resistance of the electrodes may increase more in the center of the cell due to those mechanical strains. But certainly, the local resistance (electrical + ionic + ...) at the mesh scale does not grow equally across the electrode area. When lithium metal is formed on the surface, its re-dissolution (chemical and electrochemical) may be very slow and the lithium metal formation may be accelerated locally.
In a conclusion, the constraints and induced strains during cycling may justify the non-homogeneity of the Li plating observed in Figure 3.

On the other hand, the negative electrode becomes extremely fragile after 28 days of cycling at low temperature compared to the fresh and 14 days aged electrodes. We note that the electrode coating is easily detached from the current collector.
The detached material has been collected and observed. Interestingly, at least three colors were detected: dark blue, dark red, and gold colors when the electrode coating is observed on the current collector side (Figure 4).

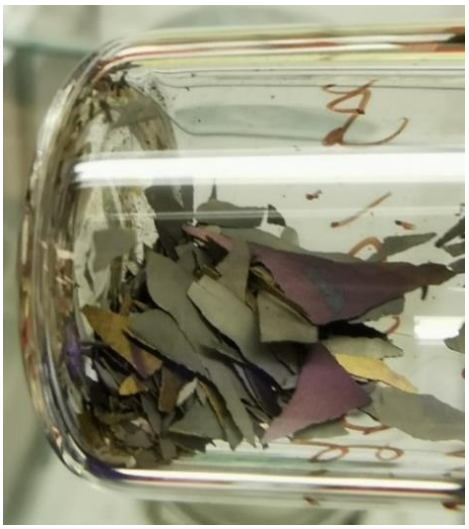

Figure 4: samples extracted from 28 days aged negative electrode at -20 °C

These colors indicate typically the evolution of the graphite structure depending on lithium intercalation level as represented in Figure 5.

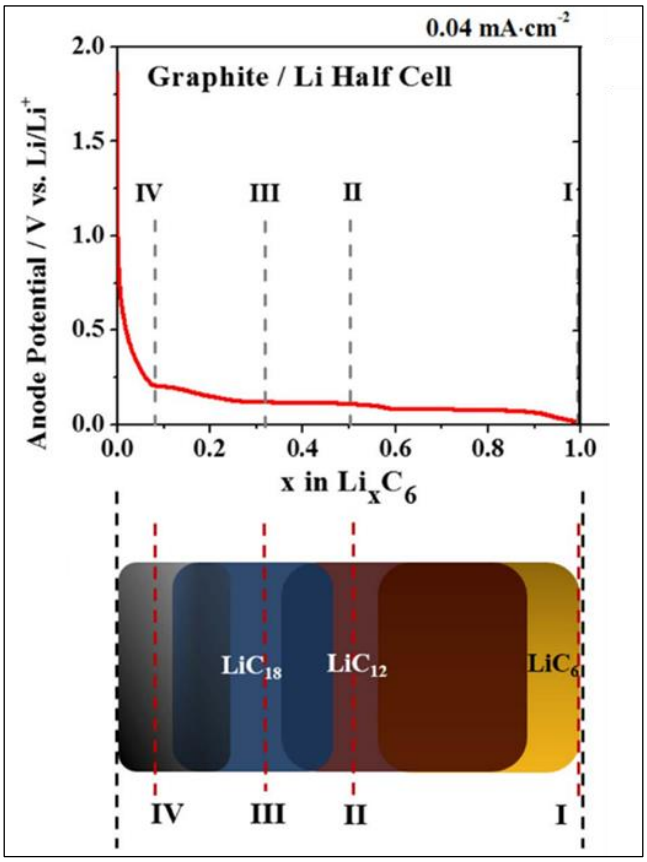

Figure 5: Stage formation in graphite (upper) cell charge potential vs. Li/Li+ as a function of lithiation state in a Li-graphite half-cell, with stages marked for corresponding voltage plateaus, (lower) color changes observed during staging [12]

Depending on the intercalation stage, the graphite color changes, going from black to blue, to red, to gold [14], [17]. Therefore, three lithiation states might be identified at least based on the electrode fragments' colors as seen in Figure 4; notably LiC_{18}, LiC_{12}, and LiC_6 composition.

The lithium metal formation reaction (***1***) is partly irreversible and some lithium is finally lost during the successive charges of the graphite electrode at low temperature. Then, after aging, some lithium ions are no longer available to be cycled between the electrodes. As a result, the LiC_6 phase of the graphite material can no longer be reached at full loading and other graphite stages such as LiC_{12} and LiC_{18} appear.

Besides, low diffusivity at low temperature may have an impact on the heterogeneity of loading at the end of the charging process, but the major effect may be the low ionic conductivity in the electrolyte at low temperature. At low temperatures, the ionic conductivity of organic solvents is low (typically 0.3 S/m; divided by 2 at -20 °C compared to the value at 20 °C [18]).
The electronic conductivity in the solid phase (graphite particles) is very high (higher than 200 S/m [19]) and then the voltage drop in the solid phase can be neglected. Then, an electrical

potential drop exists in the liquid phase between the current collector and the separator. This voltage drop has a direct impact on the instantaneous OCV voltages of graphite particles and then on their relative charging. At the end of the charge, the graphite particles near the separator are then expected to be more lithiated than the particles near the current collector.

These observations show that the phenomenon is not only in the x-y direction but also in the depth of the electrode. Not only the lithiation is different if the graphite is in direct contact with the current collector or not but also it depends on the position of the electrode in the cell; near the center-side or towards the outside.

For further investigation, analyses have been performed at CEA-Saclay-NIMBE/LEEL on the samples presented in Figure 4. The aim was to follow the evolution of the lithium concentration in the depth of the electrode using the ion beam analysis technique with a nuclear microprobe. Unfortunately, the exercise was very challenging. The obtained results were inconclusive and will not be presented in this chapter.

The problem is relatively complex to solve and electrochemical models in porous electrodes like the discrete fracture network (DFN) model [20] that uses coupled diffusion and electrical equations should be required to quantitatively justify these explanations.

1.3 Lithium plating detection by ^{7}Li NMR MAS

^{7}Li NMR MAS analyses have been performed on fresh and aged negative electrode samples to characterize the lithium plating. The samples were extracted from the center-side zone of the 14 days and 28 days aged electrodes. This analysis allows us to detect the contribution of lithium plating as Li(s) distinctly from the lithium related to other chemical environments such as lithiated graphite Li_xC_6, $LiPF_6$ salt, or SEI components. The obtained ^{7}Li NMR results are presented in Figure 6.

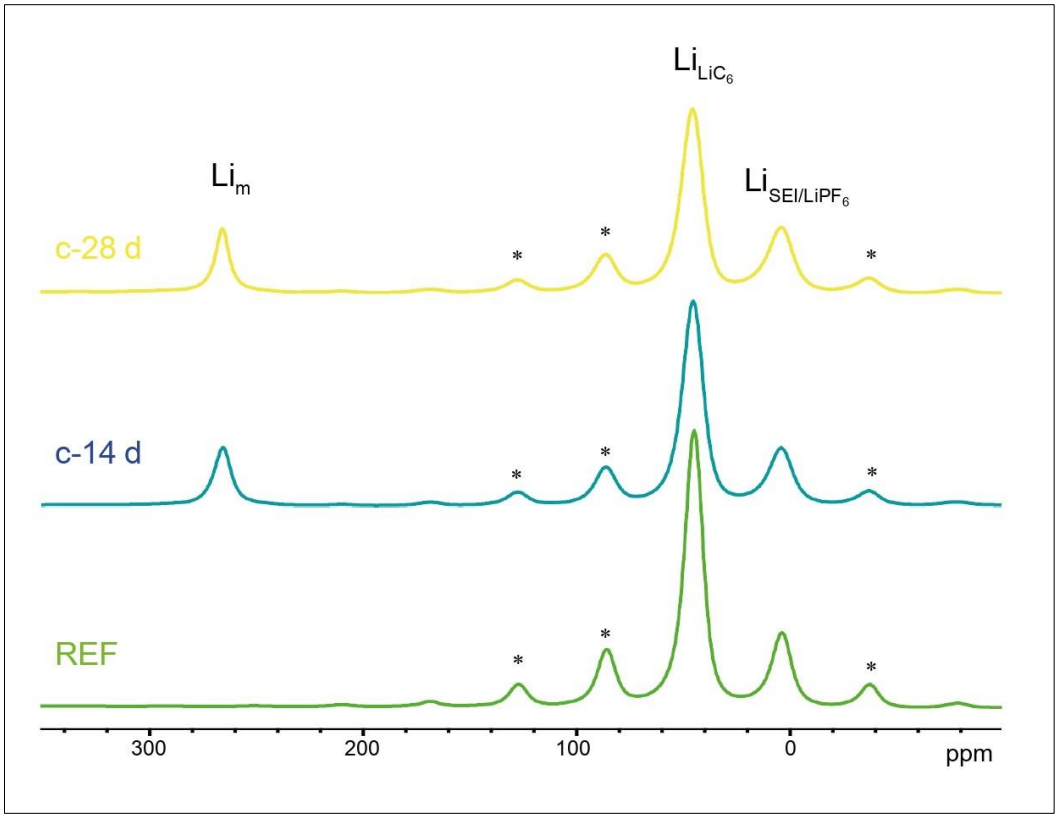

*Figure 6: 7Li NMR spectra of the loaded negative electrode samples presented in Figure 2, including the fresh lithiated anode (green), 14 days cycle-aged anode at -20 °C (blue), and 28 days cycle -aged anode at -20 °C (yellow), spinning side band are indicated with **

The ^{7}Li NMR spectrum of the fresh sample (green curve in Figure 6) shows two main peaks: the Li_xC_6 signal at roughly 45 ppm and the peak at 3 ppm related to the lithium salt and the SEI layer. The aged sample spectra reveal a new peak at ~270 ppm (yellow and blue curves in Figure 6), which has already been associated with the lithium metal element in the literature [8], [21].

A comparison was also made between the fresh, 14 days, and 28 days aged samples extracted from the outside and the center side of the electrode. The obtained ^{7}Li NMR spectrum is reported in Figure 7. The ^{7}Li NMR results were normalized by the weight of the samples and the data acquisition performed under the same analysis operating conditions.

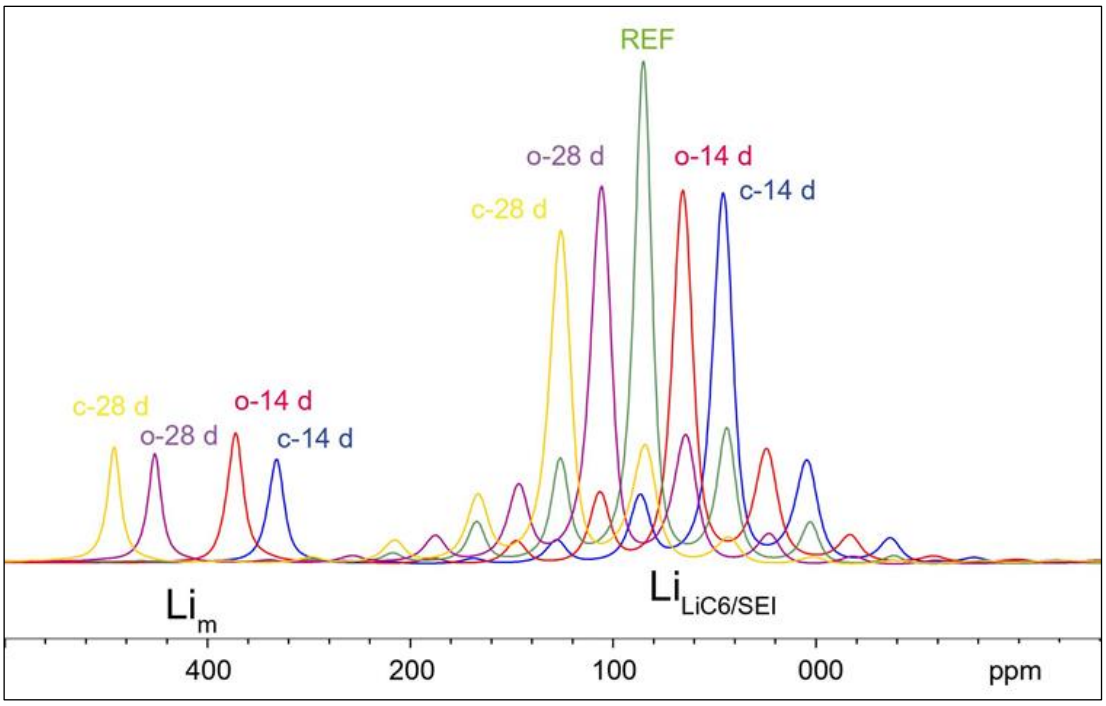

Figure 7: ^{7}Li NMR spectra at 8.0 kHz of the anode sample exposed in Figure 2, including the fresh lithiated anode (green), aged anode after 14 days at -20 °C (red and blue), and aged anode after 28 days at -20 °C (yellow and purple). « c- » for the center side sample and « o- » for the outside sample. The spectra were 20 ppm shifted related to « the center side 14 days aged sample » result noted « c-14 d»

A slight difference was detected between the center side noted « c- » and the outside noted « o- » samples for both aging periods: 14 days and 28 days. For better visualization of the results, the ^{7}Li NMR spectra were 20 ppm shifted related to « the center side 14 days aged sample » result noted « c-14 d».

According to the Li_m peaks intensity, the effect of the aging period was not very significant between the 14 days and the 28 days aged samples. However, the highest Li_m peak intensity was detected with the center side 28 days aged negative electrode sample confirming the observation in Figure 2 and Figure 3.

Moreover, the LiC_6 signals intensity of aged samples was lower than that of the fresh sample indicating the difference in the distribution of lithium in the electrode before and after aging. Indeed, the amount of lithium in the lithiated negative electrode is divided between $Li(C_x)$, Li_m, and $Li(SEI/LiPF_6)$ for the same sample. This observation explains the different lithiation stages of the aged electrode observed in Figure 4, associated as mentioned above with partial lithiation of the negative electrode during low-temperature cycling.

Moreover, the peak intensity of the Li related to the SEI was approximately the same before and after aging proving that the SEI structure and thickness do not change that much after aging and confirming that the main mechanism of aging during cycling at low temperature is Li plating.

By integrating the area under the ^{7}Li NMR spectra, the percentage of plated lithium (Li_m) by the total lithium (Li_{total}) in the electrode was estimated and reported in Table 1.

Table 1: the percentage of Li_m by total Li estimated from the ^{7}Li NMR spectra of the fresh and aged samples

	Analyzed sample mass (mg)	**% Li_m / Li_{total}**
Center-14days	18	15
Outside-14days	20	16
Fresh sample	18	**0**
Center-28days	19	11
Outside-28days	18	12

Remarkably, the Li_m/Li_{total} of the 14 days aged samples was slightly higher than for the 28 days aged samples. However, the ^{7}Li NMR result may not be exactly representative of the entire electrode since only ±20 mg of the electrode material was used for the analysis.

2 Quantification of plated lithium

The detection of plated lithium is possible using the ^{7}Li NMR technique as described previously. However, its quantification remains a challenging task. The plated lithium deposited on the graphite electrode is usually not stable. During cycling, it can be re-inserted (inside the graphite) or stripped which makes an accurate quantification of the plated lithium difficult to make especially after cycling during a long period at a low temperature.

Two different approaches are proposed in this work to estimate the amount of the plated lithium developed during the low-temperature cycling of the INR18650-32E cell. The first approach consists of estimation by dosing the lithium in the aged negative electrode. The second approach is an approximation of the plated lithium amount using the ^{7}Li NMR results. These approaches are presented in detail and the obtained results are discussed in the following parts.

2.1 Quantification by lithium dosage

This quantification approach is based on an experimental method entitled « method for determining the quantity of alkali metal or alkaline-earth metal present in a material » patented by CHAVILLON Benoît, MAYOUSSE Eric, and BLANC Lionel in CEA Grenoble. The patent was published at the European Patent Office in 2020 under the index EP 3614140 B1.

The process as described in the patent (EP 3614140 B1) involves a reaction of lithium metal with water with the production of dihydrogen (H_2) and lithium hydroxide (LiOH). The measured quantity of the resulting gas is then correlated to the quantity of lithium metal.

This method was previously used at CEA-LITEN to quantify the amount of active and inactive lithium in lithium metal cells, by determining the amount of lithium in the passivation layer formed on the surface of the lithium metal electrode.

In the context of this thesis, we tested for the first time this method to quantify the total amount of lithium present in the lithiated negative electrode. Samples are extracted from the INR18650-32E cell aged by cycling at -20 °C for 28 days, then they contain Li(s), Li(C_6), and Li(SEI/LiPF_6). The experimental installation, used for this method, contains two glass bottles, a funnel, and a vessel filled with water represented by a blue cylinder in Figure 8.

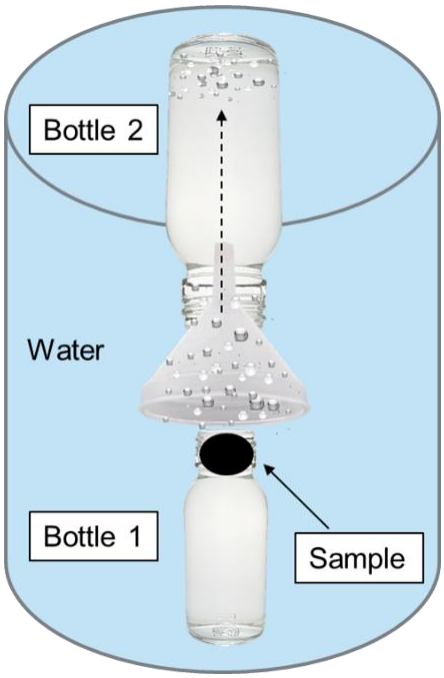

Figure 8: Simplified scheme of the lithium dosage experiment

Initially, the electrode sample is introduced inside the bottle (1) in the glove box under an inert atmosphere and its total mass (m1) is measured. The bottle (2) is filled with water and its total mass (m2) is measured. Then the bottles are immersed vertically in the water-filled vessel as shown in Figure 8. The funnel is placed between the bottles with the wider part turned towards the bottle containing the electrode sample.

The total lithium in the sample reacts instantly with water and the bubbles of produced gas are collected by the bottle (2), as indicated with the dashed black arrow in Figure 8. This gas is mainly composed of H_2 and occupies a specified volume (V_{gas}) in the bottle. It is produced according to the following reactions (2) and (3).

$$\mathbf{Li_s + H_2O \rightarrow LiOH + \frac{1}{2} H_2} \quad (2)$$

$$LiC_6 + H_2O \rightarrow LiOH + C_6 + \frac{1}{2} H_2 \quad (3)$$

At this stage, we suggest that reactions between lithium and water include only Li(s) and Li(C_6). The contribution of lithium related to the SEI layer is supposed to be negligible. Also, the residual $LiPF_6$ salt was removed before processing by rinsing the sample with DMC.

The quantification of the total lithium in the sample is carried out based on equation (*4*):

$$\boldsymbol{n_{Li} = \frac{\frac{m_{H_2}}{T_{H_2}} \times \left(P_{atm} - P_{H_2O}\right) - \frac{m_{H_2O}}{T_{H_2O}} \times P_{atm}}{a \times R - \frac{V_{mol,Li} - P_{atm}}{T_{H_2O}}}} \quad (4)$$

Where:

- n_{Li} is the total amount of lithium in the material, expressed in moles;
- P_{atm} corresponds to the atmospheric pressure, expressed in mm of Hg;
- P_{H_2O} corresponds to the water pressure, expressed in mm of Hg;
- T_{H_2O} and T_{H_2} are respectively the temperature of water and dihydrogen, expressed in K;
- m_{H_2} is the amount of the produced dihydrogen, calculated according to the weight of the bottle (2) before and after the operation;
- m_{H_2O} is the amount of water displaced into the bottle (1), calculated according to the weight of the bottle (1) before and after the operation;
- $V_{mol,Li}$ is the molar volume of lithium ($V_{mol,Li}$ = 13 cm^3/mole);
- R is the constant of perfect gases (R = 62359 mm Hg.cm^3. °K^{-1}.mol^{-1});
- a is the stoichiometric coefficient assigned to dihydrogen in reactions (2) and (3).

The water pressure P_{H_2O} is evaluated, as reported in the patent, by equation (5)

$$P_{H_2O} = T_{H_2O}{}^2 \times 0.0272638 + 6.664428 \quad (5)$$

After calculation, the total mass of lithium is estimated to be ~5.5 % of the active material in the negative electrode.

Finally, by combining this result with the ^{7}Li NMR results, we determined the mass of plated lithium present in the aged cell according to the following equation:

$$\mathbf{Li_m total\ weight} = \frac{\mathbf{Li_m}}{\mathbf{total\ lithium}}(\%) \times \frac{\mathbf{total\ lithium}}{\mathbf{aged\ electrode\ weight}}(\%) \times \mathbf{aged\ electrode\ weight} \quad (6)$$

This relation is proposed for the first time in this thesis and no similar approach is published to date in the literature.

The first percentage in equation (*6*) is obtained from the ^{7}Li NMR results and the second one from the lithium dosage results. The weight of the aged negative electrode is directly measured after disassembling the cell.

Finally, the calculated total mass of the plated lithium in the aged cells, using equation (6), is between 80 and 90 mg.

2.2 Quantification by direct calculation

In this part, we propose another method to estimate the amount of plated lithium based on our ^{7}Li NMR results, presented in section 1.2.

Firstly, we assume that at least 90 % to 95 % of lithium was loaded in the lithiated graphite electrode at the end of charging, which corresponds to 0.1±0.01 moles of lithium according to the initial capacity of the cell. Then, the total amount of lithium in the negative electrode is about 0.7 g to 0.8 g.

Therefore, according to the values of Li_m/Li reported in Table 1, the amount of the plated lithium in the negative electrode might be in the range of [77 mg – 96 mg] and [105mg – 128 mg] for 28 days and 14 days aged cells respectively.

There is no reference in the literature to evaluate the obtained quantification results of plated lithium in this cell; however, we notice a remarkable coherence between the results obtained with the two lithium quantification methods.

Conclusion

Based on these approaches, the amount of plated lithium formed in the INR18650-32E cell after aging at -20 °C should be between 77 mg and 128 mg.

Typically, we need about 0.3 g of lithium to produce 1 Ah of energy and 18650 Li-ion cells contain usually about 1 g of lithium [22][23]. Therefore, according to our quantification results, approximately 8 – 13 % of the total lithium might be plated on the negative electrode surface after aging at -20 °C by cycling according to the IEC 62660-1 standard.

3 Study of the thermal behavior of the negative electrode after aging

In this section, the thermal behavior of the negative electrode after aging at -20 °C is investigated. The same DSC analysis conditions used in the previous chapter were applied to perform this study. The aim is to identify the impact of the detected lithium plating on the

thermal behavior of the negative electrode material and to quantify the new reactions that occur inside the negative electrode material after aging.

Figure 9 shows the DSC profiles of the aged and the fresh lithiated negative electrode mixed with the INR18650-32E electrolyte at 5 °C/min with the mass ratios of 67:33 %wt and 77:23 %wt, respectively. Note that the DSC profile of the fresh sample is presented and discussed in detail in the previous chapter (see chapter II - section 3).

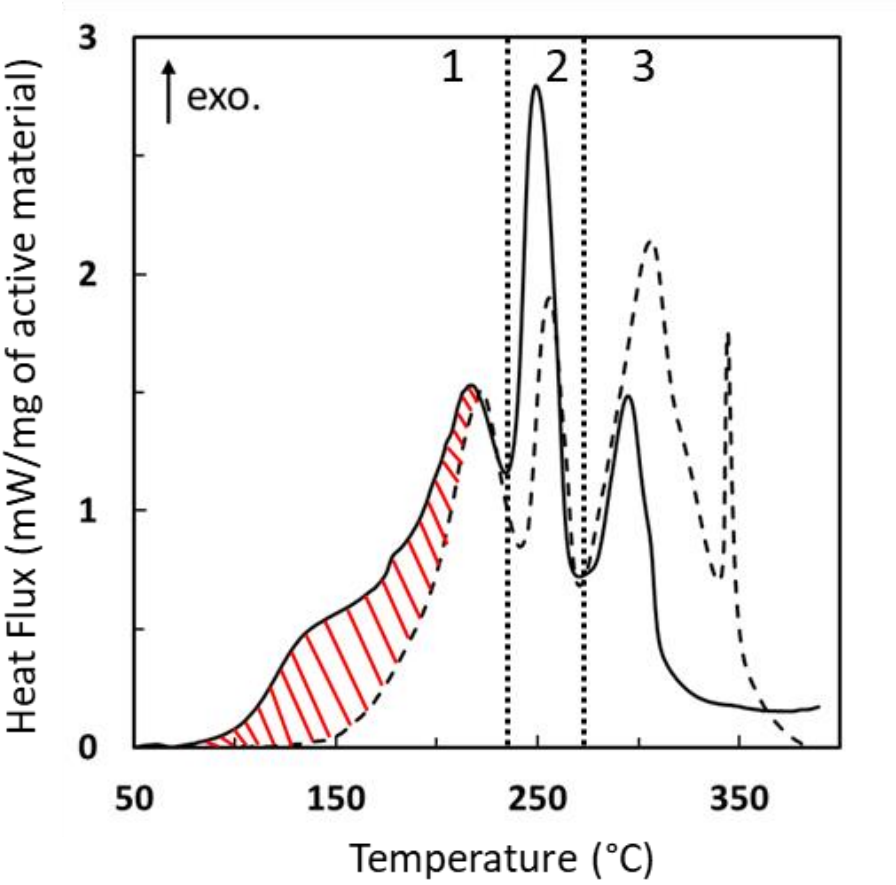

Figure 9: DSC result of the lithiated negative electrode before (dashed line) and after aging (solid line) mixed with electrolyte at 5 °C.min^{-1} with 77:23%wt and 67:33 %wt mass ratio respectively

The obtained DSC profiles of the mixtures before and after aging are consistent “in shape”: We identify mainly the same exothermic regions for both samples; however, differences in the generated heat in some areas are identified.

By comparing the DSC profiles before and after aging, the impact of aging on the different areas will be discussed in the following parts.

3.1 Area 1

This area is characterized by the first exothermic peak centered at 220 °C. In the previous chapter, two exothermic reactions were identified in this area and attributed to this peak; the

SEI breakdown (T_{onset} ~ 90 °C) and the reaction between lithiated graphite and electrolyte (T_{onset} ~ 120 °C).

An excess of the released energy was detected on the DSC profile of the aged sample as indicated by red lines in Figure 9 between 50 °C and 220 °C. Since the tested electrode materials have approximatively the same state of lithiation, the generated heat by the lithiated graphite/electrolyte reaction should be the same for both samples. In addition, the heat generated by the SEI breakdown, quantified in the previous chapter for the same sample, was the lowest in the thermal degradation process and cannot justify the additional heat observed in the DSC curve of the aged sample between 50 °C and 220 °C.

Considering the impact of the low-temperature aging observed on the negative electrode surface and discussed in sections 1 and 2, we suggest that a new exothermic reaction between plated Lithium and electrolyte occurs below 170 °C.
This new peak is centered at ~140 °C and overlapped with the other peaks. The quantification of the energy released by this new exothermic reaction was complicated considering that two other exothermic reactions occur in the same area. Therefore, in order to separate the exothermic reactions, a DSC analysis was performed using the aged negative electrode sample at 0 % of SOC mixed with the INR18650-32E electrolyte.
The obtained result is reported in Figure 10 with the DSC profile obtained for the same mixture before aging.

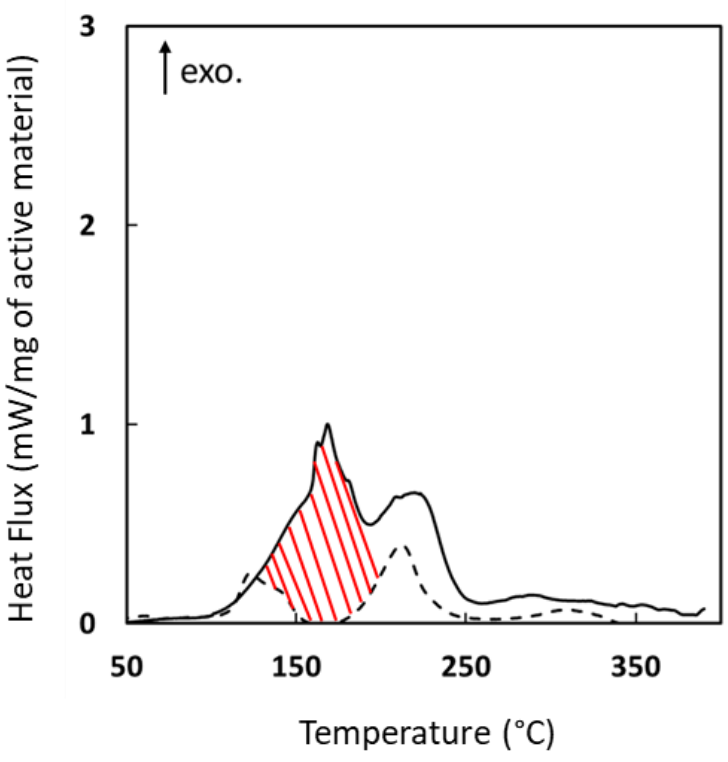

Figure 10: DSC result of the delithiated negative electrode before (dashed line) and after aging (solid line) mixed with electrolyte at 5 °C.min^{-1}

The DSC profile of the aged sample (solid line in Figure 10) shows two exothermic peaks. The first exothermic peak is centered at 160 °C and followed by a second peak at around 230 °C. The first peak includes the SEI breakdown and the reaction between plated lithium and the electrolyte, which occurs in the same temperature range. Then, the second peak is attributed to the electrolyte degradation reaction.

The determination of the heat generated by the plated lithium/electrolyte reaction is possible based on data presented in Figure 10: ~350 J/g of the aged active material is obtained by integrating the area indicated with red lines and taking into account the amount of heat generated by the SEI breakdown.

Moreover, by multiplying the analyses we found that doing the same DSC analysis, presented in Figure 9, with a standard electrolyte allows a better representation of the exothermic reactions at low temperature. Then, the same comparison between the fresh and the aged negative electrode samples was carried out using the LP30 electrolyte.
The obtained DSC profiles are reported in Figure 11.

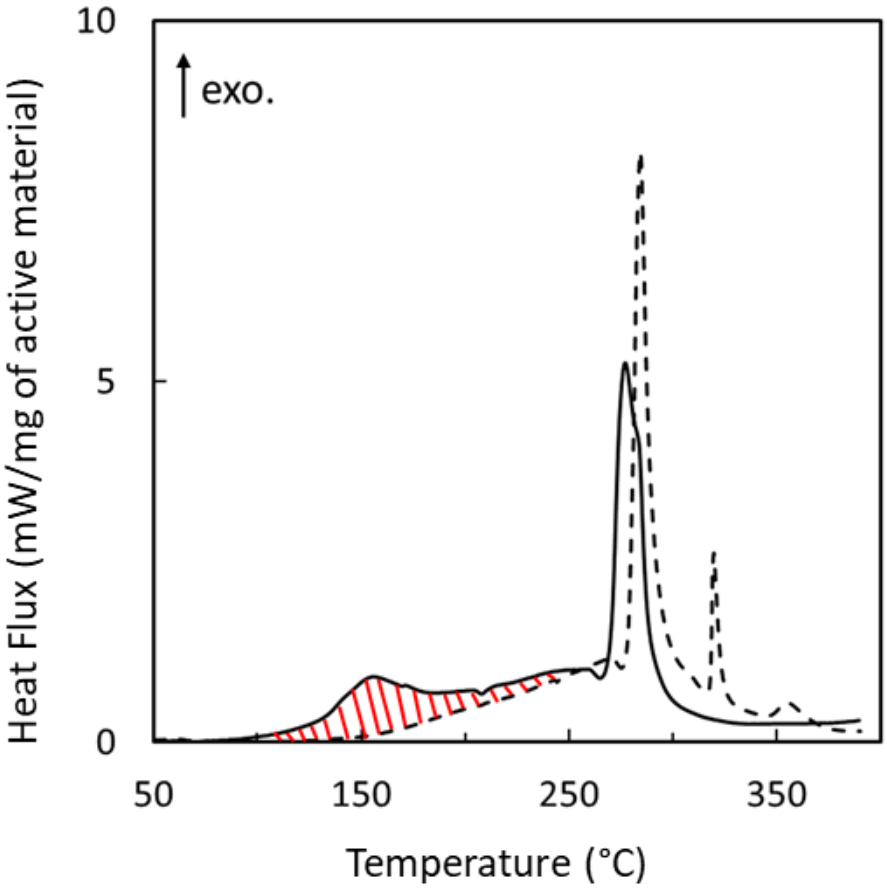

Figure 11: DSC profile at 5 °C.min^{-1} of a lithiated aged anode (red line) and fresh anode (black line) mixed with LP30 electrolyte

By comparing the two DSC profiles, the aged sample is characterized by a new exothermic peak detected separately at low temperature and centered at ~155 °C. This peak is consistent

with that detected in Figure 9 and Figure 10 and should be related to the reaction between plated lithium and the electrolyte. The measured heat released by this peak was ~300 J/g of aged active material, the value was obtained by integrating the area marked with red lines in Figure 11.

At this stage, we suggest that the reactions between plated lithium and the electrolyte solvents responsible for the additional heat at low temperatures occur according to reactions (7)-(11) :

$\mathbf{2Li + C_3H_4O_3\ (EC) \rightarrow Li_2CO_3 + C_2H_4}$	(7)
$2Li + 2\ C_3H_4O_3\ (EC) \rightarrow (CH_2OCO_2Li)2 + C_2H_4$	(8)
$2Li + C_3H_6O_3\ (DMC) \rightarrow Li_2CO_3 + C_2H_6$	(9)
$2Li + C_4H_6O_3\ (PC) \rightarrow Li_2CO_3 + C_3H_6$	(10)
$3Li + C_3H_3FO_3\ (FEC) \rightarrow Li_2O + LiF + CO + CH_3CO$	(11)

We consider that lithium reacts typically with the organic solvents according to reactions (7)-(11) regardless of its origin; inserted or plated lithium. Nevertheless, it does not mean that the mechanism and the kinetics of these reactions are the same in both cases as can be observed in DSC curves (Figure 9 and Figure 11); In addition, the plated lithium/electrolyte reaction occurs at low temperature with a maximum heat released between 140 °C and 160 °C, which is remarkably lower than the melting temperature of lithium metal (180 °C).
Indeed, the deposited lithium on the graphite electrode is more accessible than the intercalated lithium inside graphite particles. The diffusion of lithium ions and electrons through the graphite particles and the SEI layer represents a barrier that slows down the interaction between intercalated lithium and electrolyte. Moreover, even if plated lithium particles have their own SEI, the lithium metal particles can be considered more accessible and be able to react faster with electrolytes. Therefore, it is possible to get lower activation energy for the plated lithium reaction with electrolyte than for the intercalated lithium reaction with electrolyte.

In order to consolidate this statement and validate the interaction between plated lithium and the electrolyte solvents below 150 °C, an experimental approach has been tested. The plated lithium was reproduced on the negative electrode surface by using a physical vapor deposition (PVD) method called resistive thermal evaporation (Figure 12).

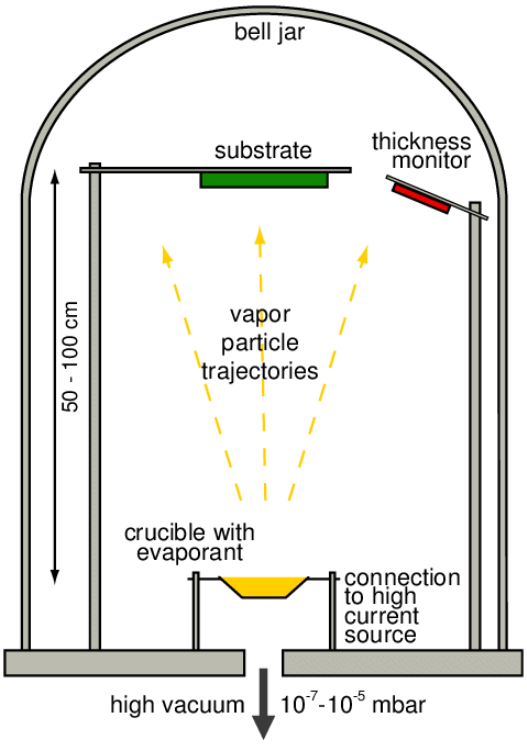

Figure 12: Schematic diagram of a resistive thermal evaporation system, reported from [24]

During the operation, the lithium metal was heated and vaporized by the Joule effect. A high vacuum is required to facilitate the evaporation and transfer the lithium to the substrate (sample) on the top. The INR18650-32E delithiated negative electrode was used in the analysis. Using this technique, the thickness of the lithium film is well controlled. A 5 µm thick lithium metal was deposited on the delithiated negative electrode sample. The obtained result is presented in Figure 13:

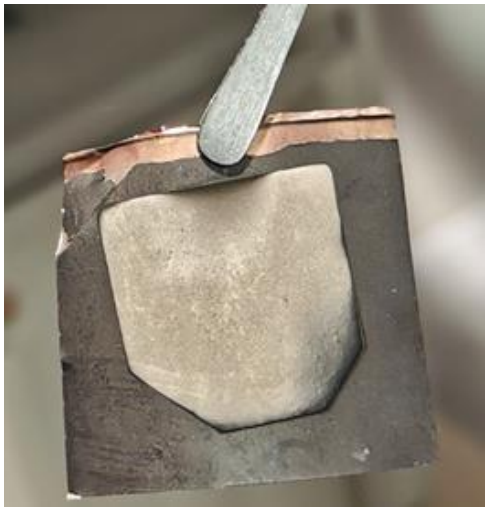

Figure 13: Photo of the obtained lithium deposit using the thermal evaporation technique

The deposited lithium with PVD is then scratched from the electrode sample (presented in Figure 13) and tested in DSC mixed with the cell electrolyte. The obtained DSC profile is reported with a red line in Figure 14 and compared to the lithiated aged sample (black curve)

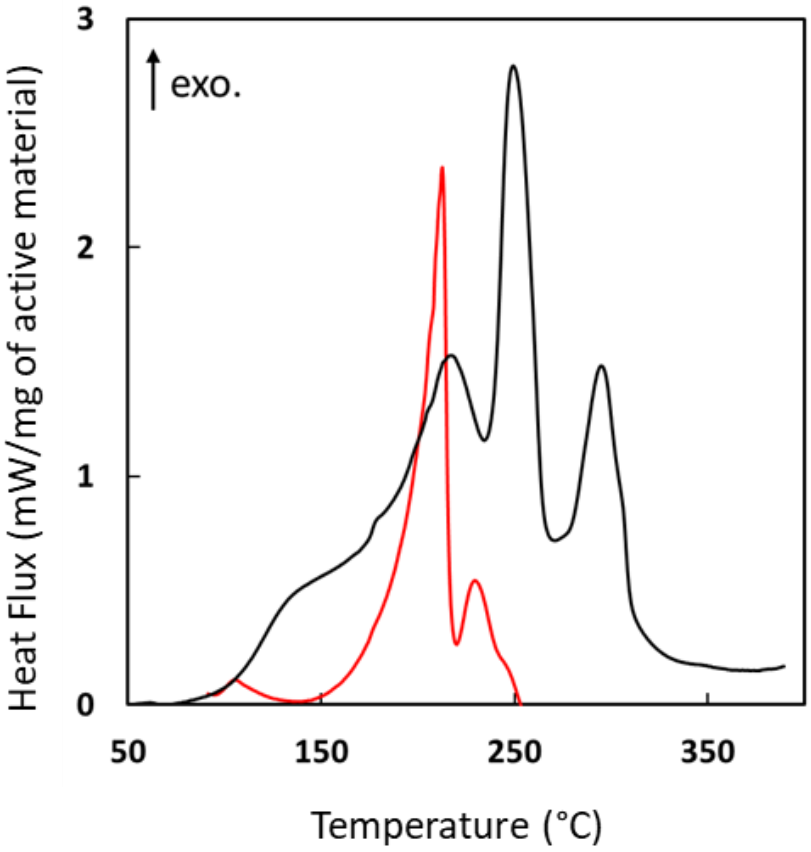

Figure 14: DSC result of the lithiated aged negative electrode (black line) and delithiated graphite with PVD lithium deposition (red line) mixed with electrolyte at 5 °C.min^{-1} with 67:33 %wt and 66:34%wt mass ratio respectively

The DSC red profile shows mainly three exothermic peaks. Looking at the small heat released by the first peak is supposed to be related to the SEI breakdown. The second peak is correlated to the LiC_6/electrolyte reaction followed by the last peak attributed to the electrolyte degradation reaction after $LiPF_6$ melting. The first two exothermic reactions are well separated as we can see in Figure 14, however, there is no interaction between the deposited lithium and the electrolyte at around 150 °C. As a consequence, it was, unfortunately, difficult to get more information on DSC using this sample. Instead, we tried another type of substrate by performing the same type of lithium deposit on a copper foil. The obtained deposit has been analyzed in the presence of the electrolyte; however, similarly, no interaction around 150 °C was detected in DSC.

This observation could be related to different factors. Firstly, we noted that the lithium film obtained with PVD is not stable at the negative electrode surface; after a few days in the glove box, we observed that the lithium was inserted in the graphite forming LiC_6 crystal as we can see in Figure 15 with gold coloration. The Effects of rest time on Li plating stability were studied by T. Waldmann and Margret. W-M [25] and a similar observation was mentioned.

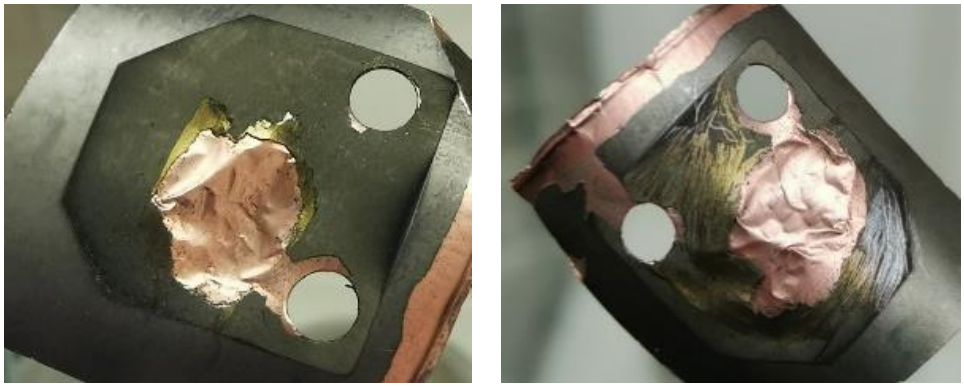

Figure 15: Photos of the same sample in Figure 13 after 10 days

As a perspective, we suggest performing the same experience using a charged negative electrode as a substrate to improve the stability of the lithium deposit on the graphite surface and avoid its insertion.

Besides, we have seen that even with the deposited lithium on a copper film, we were not able to detect the Li(s)/electrolyte reaction in DSC. Then, we suppose that the reactivity of plated lithium with the electrolyte is more related to the morphology of the deposited lithium particles. Indeed, the morphology of the plated lithium resulting from the aging at low temperature is possibly very different from the lithium deposit obtained with the PVD technique or even bulk lithium.

Recently, it was reported that the lithium plating formed at -20 °C results in small nuclei size (Ø < 3 µm) with high nucleation density (~5.10^6/cm^2), and dispersed growth of Li metal, as presented in Figure 16, according to [26]:

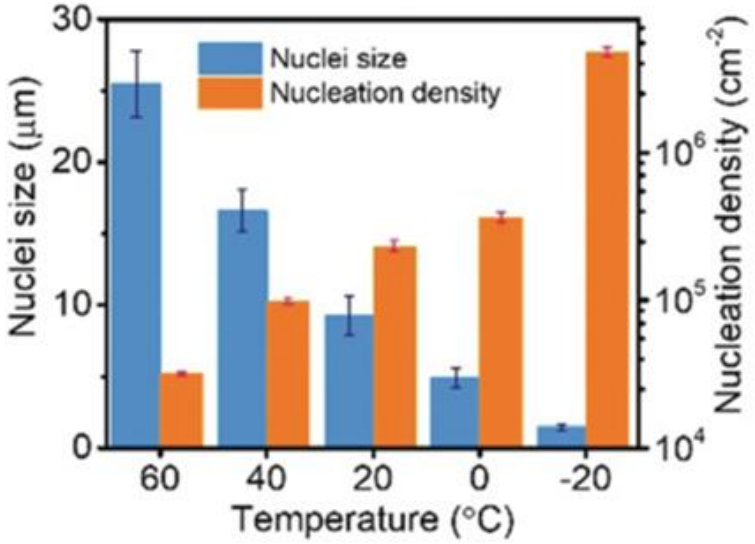

Figure 16: Statistic histograms of Li nuclei size and nucleation density for Li plating at 0.05 mA.cm^{-2}, copied from [26]

With the resistive thermal evaporation method (presented in Figure 12), the film of lithium is obtained at ambient temperature and the size of the lithium particles cannot be controlled

during the operation. Then, the deposited lithium nuclei size is probably much higher than plated lithium particles at -20 °C with higher nucleation density, probably close to bulk lithium morphology.
The lithium plating formation process used in the referenced study [26] is different from that used in this thesis; however, we are making the hypothesis that the plated lithium obtained by cycling at -20 °C, as observed in Figure 2, could have similar lithium nuclei size and nucleation density as reported in Figure 16 for -20 °C temperature.

Now admitting that this hypothesis is true and the plated lithium is characterized by a high nucleation density and a small nuclei size lithium; this leads to a very high contact area between lithium and the electrolyte solvents. This aspect could accelerate the interaction and decrease significantly the activation energy. In addition, it is known that nanomaterials have lower melting points than bulk material. The size of the lithium nanomaterials can be evaluated according to their melting temperature using the Gibbs-Thomson equation described as follows:

$$\mathbf{T_M(d) = T_{MB}\left(1 - \frac{4\,\sigma_{sl}}{H_f\,\rho_s\,d}\right)} \quad (12)$$

Where:
T_{MB}, the bulk metal melting temperature; H_f, the bulk heat of fusion; ρ_s, the density of the solid material; σ_{sl}, the material solid-liquid interface energy and d, the lithium-particle diameter.

Therefore, using equation (12) we can estimate the size of lithium particles deposited on the surface of graphite particles after aging by cycling at -20 °C.
Based on DSC profiles of the aged negative electrode mixed with electrolyte reported in Figure 9, Figure 10, and Figure 11, the plated lithium/electrolyte interaction can be probably initiated between 100 °C and 120 °C with a maximum peak at ~160 °C. Assuming that the melting temperature of the lithium nanomaterials is situated in this temperature range, then, the diameter of plated lithium particles was calculated to be about 5 to 16 nanometers.

3.2 Area 2

The second area in Figure 9, between 220 °C and 270 °C, is now commented. As discussed in the previous chapter for the fresh negative electrode sample, the exothermic peak in this area was attributed to the electrolyte degradation reaction after the $LiPF_6$ melting. The same exothermic peak appears at the same temperature with the aged sample with higher intensity.

Indeed, the amount of the electrolyte mixed with the aged sample is 1mg higher than in the fresh electrode sample mixture. Thus, this might explain the excess of released energy in this area for the aged sample.

3.3 Area 3

As discussed in the previous chapter, two main exothermic reactions are identified in this area on the DSC profile of the fresh negative electrode sample: the reaction between the CMC-Na binder/lithium and the interaction between PEO products resulting from the electrolyte degradation and the lithium. Both reactions start approximately at around 270 °C and have their maximum at respectively 300 °C and 330 °C. We have mentioned also that the heat generated by these exothermic reactions is proportional to the amount of the binder, PEO products, and residual lithium. Since the CMC-Na binder amount is the same for aged and fresh samples, the reaction between lithium and CMC-Na depends only on the residual amount of lithium in the mixture above 250 °C. However, the reaction including lithium with the PEO products is limited by both residual amounts of lithium and electrolyte after their reactions below 250 °C.

As shown in Figure 9, this exothermic peak is detected at around 290 °C with the aged sample. However, it is ~50 % less energetic compared to the same peak obtained with the fresh sample. In the case of the aged sample, we suggest that the plated lithium is no longer available at this temperature since it has already reacted around 150 °C and the amount of intercalated lithium is mostly consumed before 250 °C. Therefore, less lithium reacts with binder and PEO products, and less heat is released in area 3 - Figure 9 with the aged sample. Another DSC result obtained with 14 days aged sample mixed with electrolyte confirms this statement. The obtained profile is presented with a green line in Figure 17 to make a comparison with the other curves presented in Figure 9.

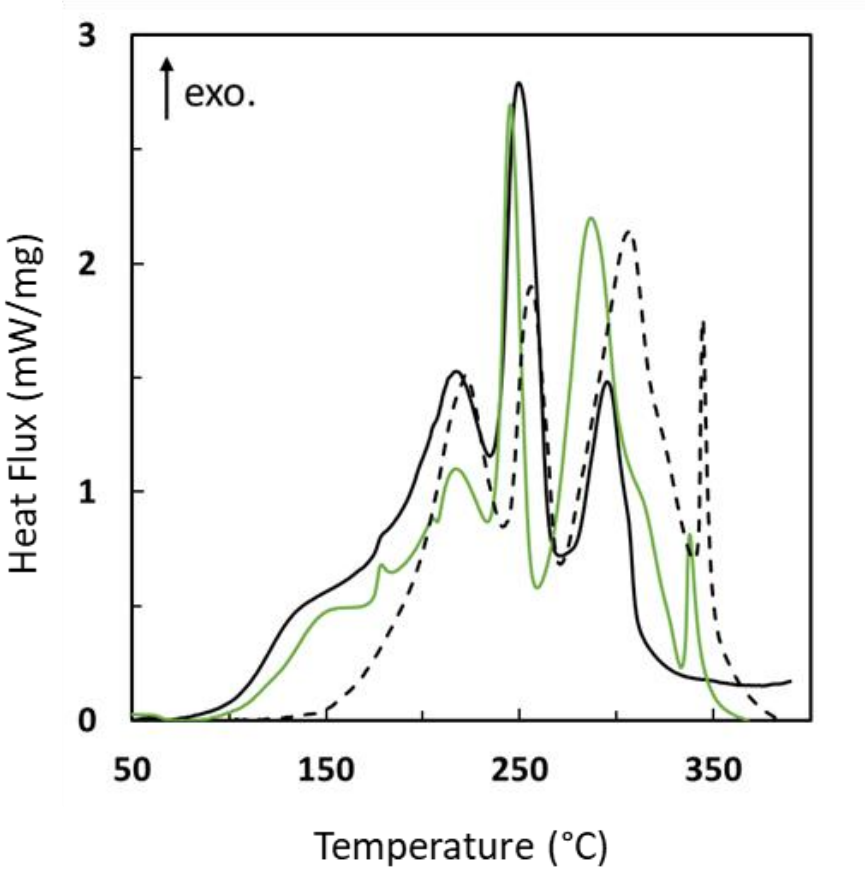

Figure 17: DSC result of the lithiated fresh anode (dashed line), 28 days aged anode (solid black line), and 14 days aged anode (green line) mixed with electrolyte at 5 °C.min^{-1} with 77:23 %wt, 67:33 %wt, and 74:26 %wt mass ratio respectively

The peak detected after 250 °C with the 14 days aged sample is more energetic than the one obtained with the 28 days aged sample in area 3 - Figure 9.

In the case of fresh and 14 days aged samples, all the CMC is consumed and the lithium remains available at the end to react with PEO products. Moreover, based on the peak's intensity, less lithium was probably consumed in the case of the 14 days aged sample below 250 °C compared to the other samples. This means that there is more lithium left to react at the end. After 28 days of aging, we assume that there is not enough lithium left in the electrode to consume all the CMC and in this case, the reaction with the PEO does not occur because of the lack of lithium.

Interestingly, the small peak around 350 °C is only visible with fresh and 14 days aged samples and inexistent after 28 days. This last peak could be associated with the reaction involving the PEO products in the presence of lithium.

In summary, the above results show that the decomposition of the aged negative electrode starts at a lower temperature and release significantly higher heat at a low temperature compared to the fresh negative electrode. These results reveal that aging at low temperatures accelerates the degradation of the negative electrode material due to the presence of lithium

plating. The plated lithium reacts with the electrolyte exothermically and generates about 300 – 400 J/g of the aged negative electrode between 50 °C and 200 °C. This reaction may increase the risk of TR and might be responsible for the early TR detected with the aged cell at low temperature as reported in the ARC test in Figure 1.

The thermal stability of the positive electrode materials was not impacted by the aging process. Hence, we have only focused on the negative electrode. Nevertheless, to simulate the safety behavior of the INR18650-32E cell before and after aging and to obtain more representative results, this study will be completed by an investigation using a miniature full cell sample presented with more details in the following section.

4 Thermal behavior of full cell sample

The main exothermic reactions which occur during the thermal degradation of the charged INR18650-32E cell materials were identified and characterized based on DSC results. We analyzed separately several reactions involving the active materials of the negative and positive electrodes mixed with the electrolyte of the cell by respecting their proportions in the INR18650-32E cell.

The cell components are presented with their measured weight in Table 2.

Table 2: Samsung INR18650-32E cell components and their weight

Cell compounds	Materials		Weight (g)
Negative electrode	Active material	Graphite	12
	Current collector	Copper	4.6
	Binder/additives[1]	CMC-Na/-	-
Positive electrode	Active material	NCA	16
	Current collector	Aluminum	1.4
	Binder/additives[2]	PVDF/-	-
Electrolyte	Salt	LiPF6	4.4
	Solvents	EC/PC/DMC/FEC	
Separator	-	PE – AlOOH	1.3
Casing + mandrel	-	Steel	10

Typically, there are at least five types of materials in the cell: a negative and positive electrode, lithium salt electrolyte and solvents, and the separator. At high temperatures, the separator melts creating contact between the two electrodes. The resulting short circuit in the cell might trigger new exothermic reactions and creates new degradation mechanisms between the

materials of the charged negative and positive electrodes. Therefore, it is important to identify these reactions for a better comprehension of the TR mechanism inside a real complete Li-ion cell.

In this context, the security behavior of the INR18650-32E cell materials in a full configuration was investigated before and after cycling aging at -20 °C. For this, a mini full cell was designed and tested using DSC. The proposed system is composed of negative and positive mini-electrodes separated with the cell separator and mixed with the cell electrolyte, which is the real scenario in the full commercial cell.

The preparation steps of this sample are summarized in Figure 18.

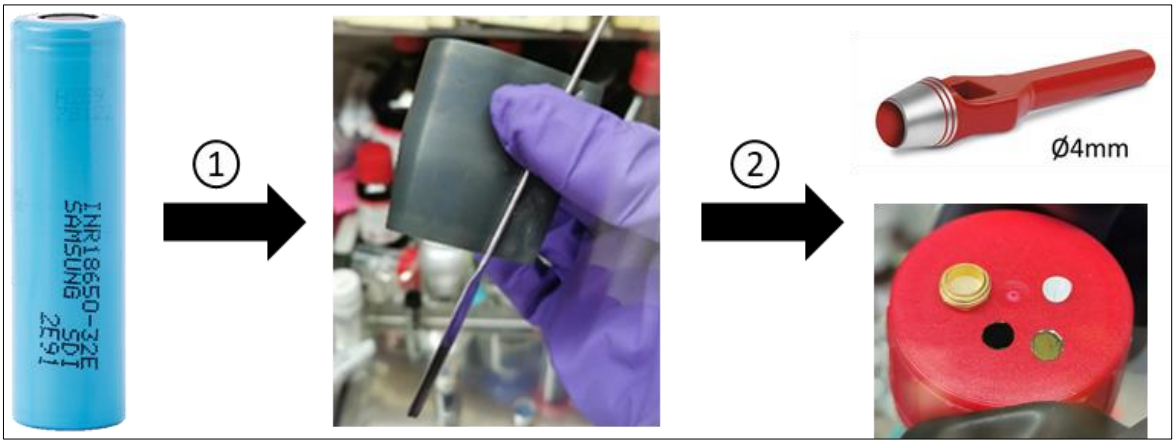

Figure 18: 1) Samsung INR18650-32E cell disassembling, 2) mini electrodes sample preparation using an electrode-cutting tool

The mini-electrodes were prepared using a 4 mm electrode-cutting tool as represented in Figure 18. The same DSC crucibles (Ø5mm) were used in this part. The separator was included in the mini full cell with sufficient size to ensure the isolation between the electrodes. A simplified scheme of the full mini cell configuration is proposed in Figure 19.

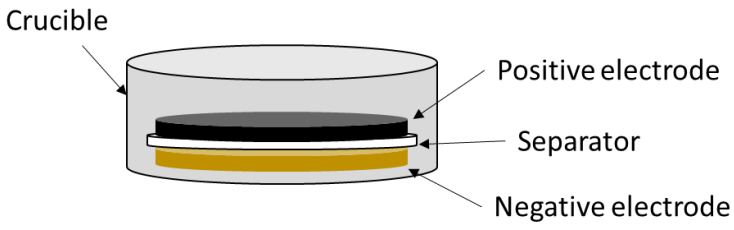

Figure 19: the used mini full cell configuration

The proportion of the different materials (electrode, separator, and electrolyte) are chosen according to the commercial INR18650-32E cell components weight reported in Table 2.

4.1 Fresh full mini-cell behavior

Figure 20 shows the DSC result of a charged mini cell composed of a lithiated negative electrode and a delithiated positive electrode extracted from a charged fresh INR18650-32E cell. The mass proportion between negative/positive electrodes and the added electrolyte was calculated as 21:53:27 %wt (-/+/el). It should be noted that the same mass ratio for the INR18650-32E cell was calculated based on Table 2 as 36:50:14 %wt. However, the material was easily removed from the current collector during the sample preparation and complicated the reproduction of the mass proportion as in the INR18650-32E cell. Thus, the amount of the electrolyte was higher at the detriment of the negative active material quantity in the designed cell compared to the commercial cell.

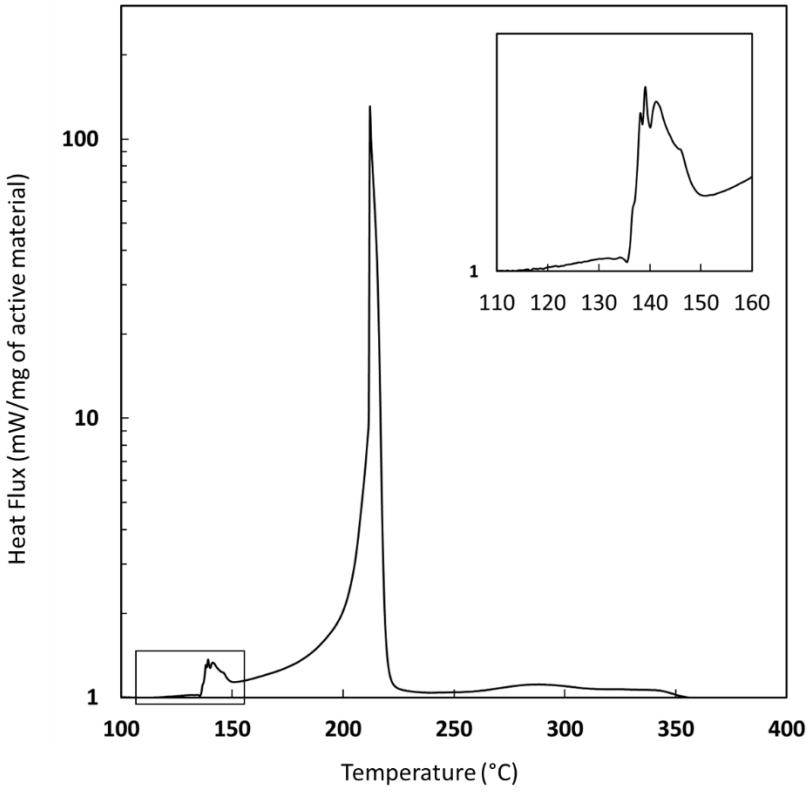

Figure 20: DSC profile at 5 °C.min^{-1} of the fresh charged mini full cell (-/+/electrolyte, 21:53:27 %wt), for better visibility of the result, the DSC profile is represented on a logarithmic scale.

The DSC profile in Figure 20 shows mainly a small exothermic peak at around 135 °C followed by a powerful exothermic peak at 220 °C.

The first peak is probably related indirectly to the separator melting. Indeed, the INR18650-32E cell separator melting is an endothermic reaction starting at around 135 °C as presented in Figure 21, and consumes ~100 J/g of the separator. Consequently, an internal short circuit (ISC) occurs between the loaded electrodes at around 135 °C as seen in the zoomed square in Figure 20. The resulting heat from the ISC is relatively low (about 20 J/g), however, we suppose that the first exothermic peak is triggered by the separator melting.

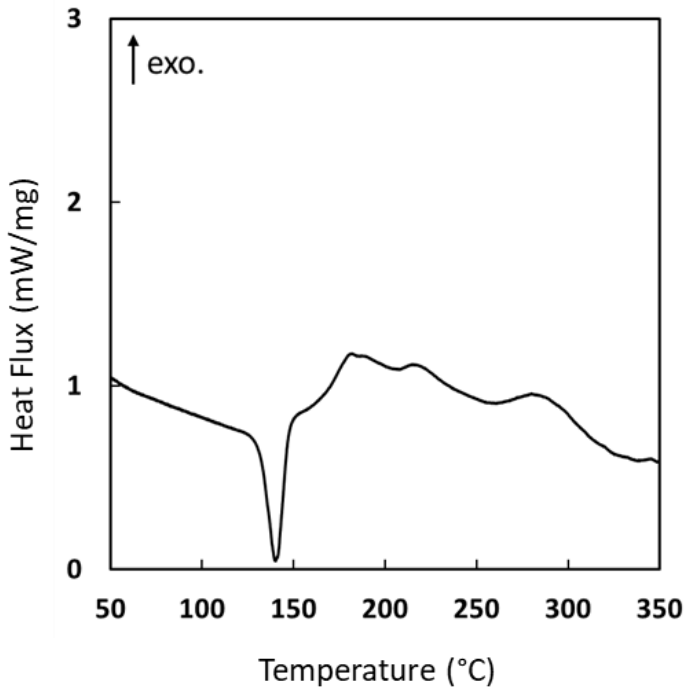

Figure 21: the Samsung INR18650-32E cell separator melting

In a compact 18650 cell, we believe that the ISC produces higher energy. However, in the mini cell sample, no pressure is applied to the electrodes inside the crucible then the contact resistance is significantly higher and the resulting ISC is not vigorous. After the ISC, the power increases exponentially and progressively until reaching a maximum of 220 °C.

According to the TR chain of reactions of the electrodes discussed in chapter II and reported in Figure 22, the heat flow generated under 200 °C is mainly related to the thermal degradation of the negative electrode material; mainly the SEI breakdown followed by the reaction between lithiated graphite and electrolyte solvent. Above this temperature, the thermal degradation of the delithiated NCA material occurs, leading to the oxidation of the electrolyte solvents as observed by the powerful peak in Figure 20 at 220°C.

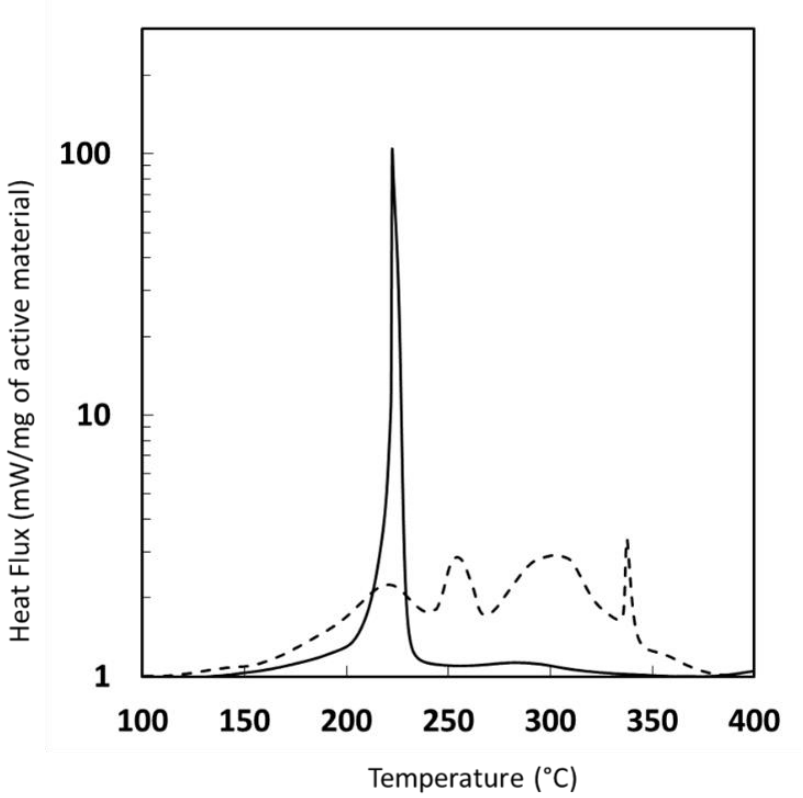

Figure 22: DSC profile at 5 °C.min^{-1} of fresh lithiated negative electrode+electrolyte (dashed line) and delithiated positive electrode+electrolyte (solid line); for better visibility of the result, the DSC profile is represented on a logarithmic scale.

As demonstrated in the previous chapter, the violent reaction between the liberated oxygen and the electrolyte solvent is more than twenty times more energetic when full combustion occurs compared to partial combustion. Complete combustion is suggested in this case. In addition, the same peak with approximately the same heat power has been detected when the fresh positive electrode/electrolyte sample was tested with an 80:20 mass ratio, as discussed in chapter II (see Figure 22)

Interestingly, after 250 °C, no significant exothermic peak has been detected indicating that most of the involved active material and/or electrolyte solvents were consumed before this temperature.

4.2 Full mini-cell behavior after aging

The thermal behavior of the same configuration has been tested in DSC using aged electrodes extracted from the charged INR18650-32E cell aged at -20 °C. The mass proportion between the negative/positive electrode and the added electrolyte was calculated for the aged mini full cell as 30:50:20 %wt. The obtained profile of the sample before and after aging is reported in Figure 23.

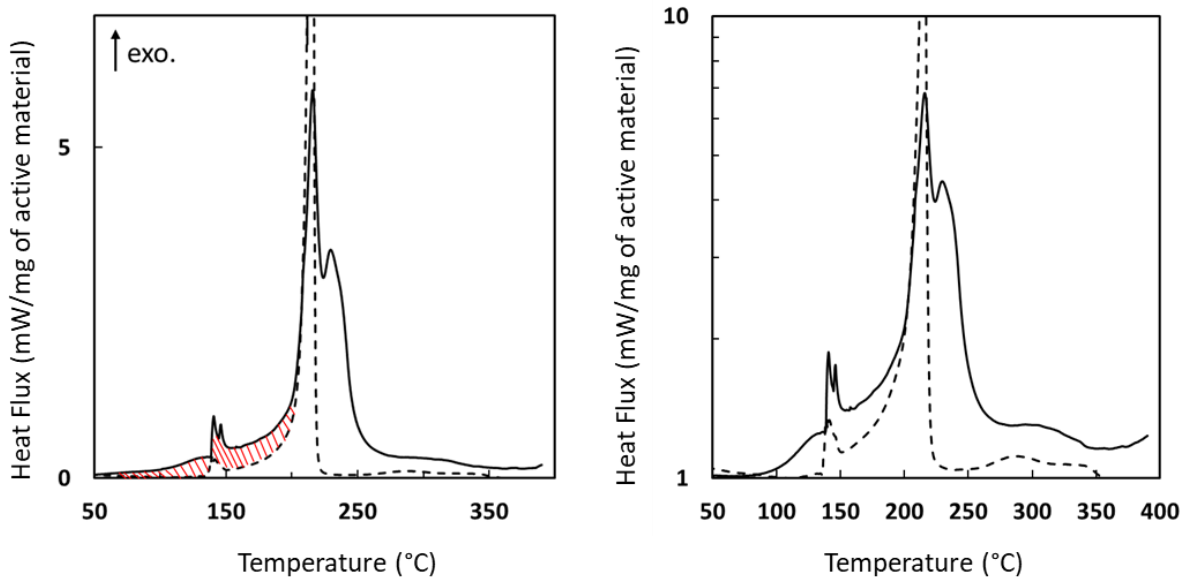

Figure 23: DSC profile at 5 °C.min^{-1} of the charged mini full cell before (dashed line) and after (solid line) aging with anode/cathode/electrolyte mass ratio of 21:53:27 %wt and 30:50:20 %wt respectively; for better visibility of the DSC profile is represented on a logarithmic scale (right curve)

More energy was detected as indicated by the red dashed lines in Figure 23 between 50 °C and 200 °C. This observation is perfectly in coherence with the thermal behavior of the aged negative electrode material behavior discussed in section 3.1.

The second part of the profile with a solid line in Figure 23, i.e., after 200 °C, looks more like incomplete combustion of the electrolyte followed by the degradation of the remaining electrolyte, the same behavior was observed when the fresh positive electrode was tested with electrolyte with 67:33 mass ratio (see chapter II – section 3)

Moreover, for fresh and aged samples, the first reactions are between Li (intercalated or plated) and the solvents. The only difference is that for the aged cell, the reaction occurs earlier. In addition, the amount of solvent still available at 200°C should be very low in both cases and must be completely oxidized.
If we now compare the 2 situations (fresh/aged), there is much less solvent available for the aged cell because of the reaction with Li plating. Therefore, it seems obvious that the oxidation peak at 220 °C is less powerful in the case of the aged cell.

Since we don't see the second peak in the case of fresh mini-cell, it means that it involves an element in excess on the aged sample. This can be the oxygen species, as we had less solvent to oxidize, then some oxygen must remain available after 220°C.

The total heat realized by the fresh and aged mini-cell was respectively 3500 J/g of active materials and 2200 J/g of active materials. The difference between the measured energy might be related to differences in the mass proportions of the tested cells.

4.3 Interaction between the negative and positive electrode

In this part, we investigate the consequences of a scenario that can happen in some particular conditions inside the cell where the charged electrodes are in contact with a very limited quantity of liquid electrolyte inside the cell. For example, we can mention the cells after calendar aging or aging by cycling at room temperature. In this case, the initial amount of electrolyte decreases significantly inside the cell. It is mainly consumed during aging in the development of the SEI layer that grows during these aging conditions.

Then, a sample was prepared with only the lithiated negative electrode and delithiated positive electrode with a mass proportion of 44:56 %wt. The obtained DSC result is reported in Figure 24 and compared in the same figure with the DSC profile of the lithiated graphite electrode and the delithiated NCA-based electrode tested separately without adding electrolyte.

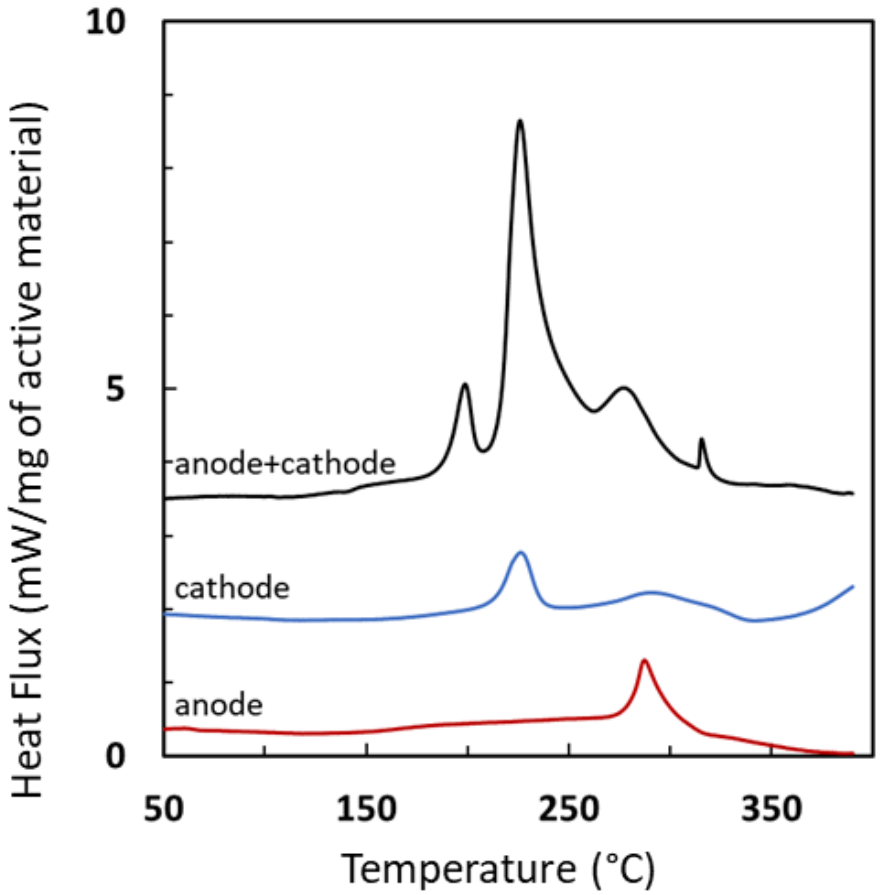

Figure 24: DSC profile at 5 °C.min^{-1} of charged anode/cathode with a mass ratio of 44:56 %wt. (black line), lithiated anode (red line), and delithiated cathode (blue line) without adding electrolyte

Based on Figure 24, no ISC between the charged electrodes was identified at 135 °C. This was expected because no electrolyte is present in the mixture. However, three exothermic peaks were observed. A first peak was detected at 195 °C followed by a second exothermic

peak centered at 227 °C, then one board peak centered at 280 °C. The last small peak is not considered in this part.

By comparison with the DSC curves of the electrode tested separately (blue and red curves), the first and the third peak might be related with some shift to the first exothermic structural change of the delithiated NCA at roughly 190 °C-200 °C and the interaction between lithiated graphite and the decomposed CMC-Na binder after 250°C, respectively.

Moreover, the main exothermic peak that generates the most heat in the mixture is probably associated with the interaction between the liberated oxygen from the positive electrode and the lithiated graphite according to the following reaction [27]:

$$\mathbf{O_2 + 4\,LiC_6 \leftrightarrows 2\,Li_2O + 4\,C_6} \quad (13)$$

Based on Figure 24 the total heat generated by this reaction was approximately 2500 J/g of active material. This indicates that the chemical interaction between the charged electrodes even without the presence of the electrolyte is far from negligible. Such interaction was reported recently as a possible pathway of oxygen in the presence of lithiated graphite [27].

If the oxygen is already consumed by the solvent, which must be the case in a real cell, there will not be many remaining oxygen species to interact with the graphite.

Furthermore, the same configuration was tested using aged negative/positive electrodes. The obtained DSC profile is reported in Figure 25 and compared to the fresh sample.

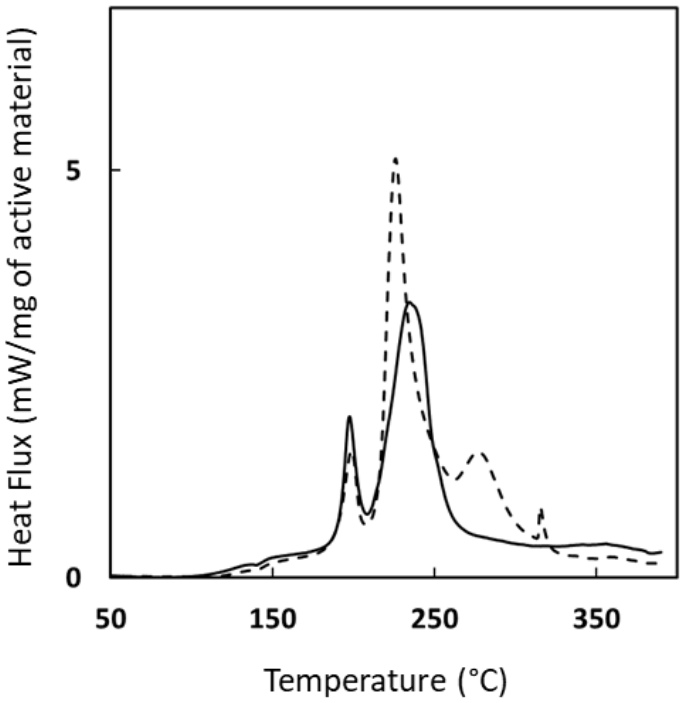

Figure 25: DSC profile at 5 °C.min^{-1} of charged anode/cathode before (dashed line) and after aging (solid line) with a mass ratio of 44:56 wt% and 28:72 wt% respectively

The reactivity of the aged electrodes without adding the cell electrolyte was very similar to that of the fresh electrodes' mixture. As the mass ratio was slightly different, the peak amplitude was not the same.

The first exothermic peak, around 195 °C attributed to the delithiated NCA decomposition, was detected similarly at the same temperature range in both curves. But with higher intensity for the aged negative/positive material mixture since it contains a higher positive electrode material weight. Besides, the difference in the amplitude of the second peak around 230 °C could be correlated to the difference in mass of the negative electrode material.

The reactivity between LiC_6 and oxygen is confirmed by the DSC profile of the aged sample. However, less energy was released between 200 °C and 250 °C with the aged sample since less LiC_6 was available in the mixture compared to the fresh sample.

The last peak on the DSC profile of the fresh sample was attributed to the interaction between the residual amount of LiC_6 and the CMC-Na binder. However, this peak is absent on the DSC profile of the aged sample due to the low amount of LiC_6 initially present in the sample and mostly consumed before 250 °C according to reaction (13).

In conclusion, we suggest that the charged negative/positive electrode interaction is dominated by the LiC_6/O_2 reaction.

The total energy generated by these samples was measured as 2500 J/g and 1700 J/g of active material for respectively fresh and aged negative/positive material mixture. To sum up, the total energy measured for all charged negative/positive material configurations tested in this section is reported in Figure 26.

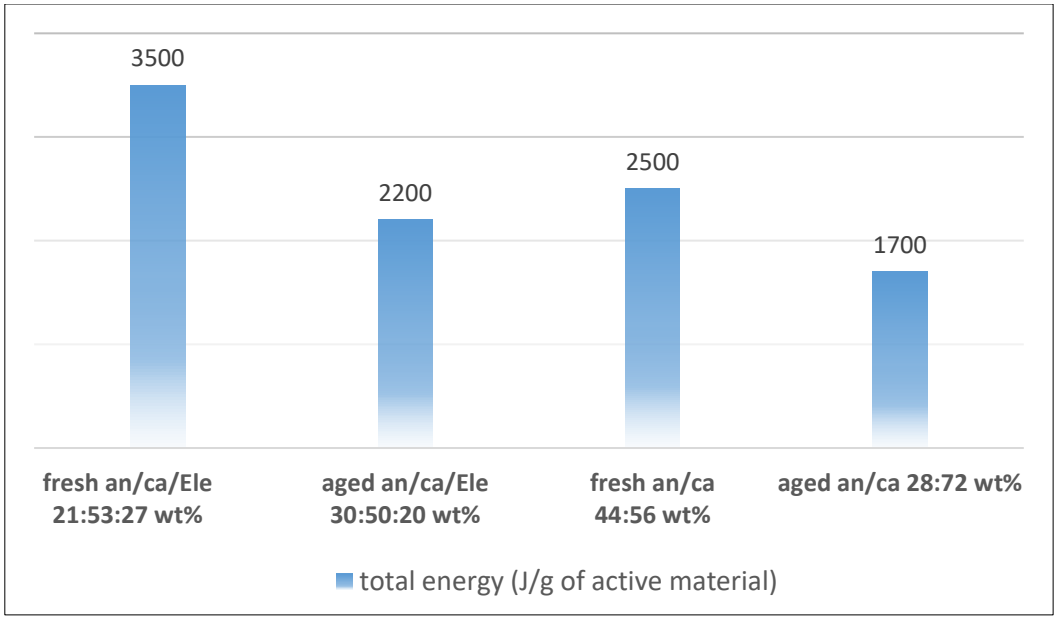

Figure 26: Total heat generated heat by charged an/ca and an/ca/Ele samples before and after aging

5 Total energy balance of the Samsung INR18650-32E cell

On the bases of all DSC analyses conducted on the Samsung INR18650-32E cell presented and discussed in detail in chapters II and III, an energy balance is proposed in this part according to the total energy quantified and measured for the charged NCA/Gr system before and after aging by cycling at -20 °C. The obtained data are reported in Table 3.

Table 3: the specific and total energy of the INR18650-32E cell electrodes

Samsung INR18650-32E cell	**Average specific energy (min-max)**	**Total energy (min-max)**
Negative electrode + electrolyte	2 – 3 kJ/g lithiated graphite	24 – 36 kJ
Positive electrode + electrolyte	2.5 – 3 kJ/g delithiated NCA	42.5 – 51 kJ
Full mini cell	2 – 3 kJ/g mixture	66 – 99 kJ

The considered assumptions are:

- ✓ The exothermic reactions are those of the negative and positive electrode material extracted from the charged Samsung INR18650-32E cell, i.e., 100% SOC, in the presence of the cell electrolyte.
- ✓ The specific energy of those reactions is determined based on DSC results performed between 50 °C – 400 °C using high-pressure closed crucibles.
- ✓ The total energy of the cell is calculated based on the total active material weight quantified and reported in Table 2.

Recently, a study was reported on the TR behavior of 18650 Li-ion cells [28]. Measurements were made to evaluate the total energy that can be released by the runaway of these cells. The average total energy reported in this study is situated between 60 kJ and 75 kJ for cells with a capacity of 2.9 Ah to 3.5 Ah. These values are consistent with those measured in this thesis with the NCA/Gr mini cell in Table 3 and confirm the relevance of our experimental approach.

6 Conclusions

In this chapter, the impact of aging by cycling at low temperature on the safety behavior of the INR18650-32E cell was investigated. The study was performed with a particular focus on the negative electrode material after lithium plating formation. The plated lithium was detected using NMR analysis and quantified by different methods. The average amount of the plated lithium was estimated to be ~100 mg formed in the negative electrode (12 g) of the full cell (47 g) after aging at -20 °C.

The thermal behavior of the negative electrode material was tested after aging using DSC. By comparison with the fresh electrode, more heat was detected with the aged sample below 150 °C. This was associated with the reactivity between plated lithium and the electrolyte solvents.

Combining DSC analysis on the electrodes tested individually and in a full “mini-cell” system was a good option to demonstrate and quantify the main reactions involved in the thermal runaway of the INR18650-32E cell before and after aging at low temperature:
Firstly, the SEI breakdown and the interaction between LiC_6 and the electrolyte are the two reactions that initiate the thermal degradation of the charged NCA/Gr system. The degradation of the negative electrode and the onset of the thermal degradation in the complete system in adiabatic conditions (ARC experiment) is extremely correlated. When the heat flux of the negative electrode material increases due to the lithium plating, the system T_{onset} decreases. Indeed, the presence of lithium plating accelerates the chain of the exothermic reactions in the cell due to the high reactivity of the plated lithium with electrolyte. This effect increases significantly the amount of generated heat between 50 °C and 200 °C.
Moreover, oxygen appeared as the key element that controls the thermal runaway of the charged NCA/Gr system before and after aging. This is due to its high reactivity with both electrolyte and LiC_6, which generated the major part of the heat in the samples between 200 °C and 250 °C. In the real scenario system, the exothermic reaction of oxygen/electrolyte and oxygen/LiC_6 may occur simultaneously and generates the main heat source in the charged NCA/Gr system. However, we believe that the oxygen consumption is mainly related to the oxygen/electrolyte exothermic reaction since the oxygen pathway reaction with electrolyte is shorter (direct contact) compared to the one with intercalated lithium on the graphite side.

The main point is that the trio "electrolyte + negative electrode + positive electrode" leads to a more important reaction than dissociated reactants. This is key in the thermal runaway reaction mechanism. Then, if we find a way to avoid the interaction between electrodes and use more thermally stable electrolytes, we strongly limit the thermal runaway.

7 References

[1] M. Ecker, P. Shafiei Sabet, et D. U. Sauer, « Influence of operational condition on lithium plating for commercial lithium-ion batteries – Electrochemical experiments and post-mortem-analysis », *Appl. Energy*, vol. 206, p. 934-946, Nov. 2017, doi: 10.1016/j.apenergy.2017.08.034.

[2] M. Petzl et M. A. Danzer, « Nondestructive detection, characterization, and quantification of lithium plating in commercial lithium-ion batteries », *J. Power Sources*, vol. 254, p. 80-87, May 2014, doi: 10.1016/j.jpowsour.2013.12.060.

[3] A. Senyshyn, M. J. Mühlbauer, O. Dolotko, et H. Ehrenberg, « Low-temperature performance of Li-ion batteries: The behavior of lithiated graphite », *J. Power Sources*, vol. 282, p. 235-240, May 2015, doi: 10.1016/j.jpowsour.2015.02.008.

[4] P. Kuntz, « Evolution du comportement sécuritaire de batterie lithium-ion pendant leur vieillissement », thesis, Université Grenoble Alpes, 2020. Available online April 2021, http://www.theses.fr/2020GRALI069

[5] P. Kuntz *et al.*, « Identification of Degradation Mechanisms by Post-Mortem Analysis for High Power and High Energy Commercial Li-Ion Cells after Electric Vehicle Aging », *Batteries*, vol. 7, nº 3, Art. nº 3, Sept. 2021, doi: 10.3390/batteries7030048.

[6] A. Friesen *et al.*, « Impact of cycling at low temperatures on the safety behavior of 18650-type lithium ion cells: Combined study of mechanical and thermal abuse testing accompanied by post-mortem analysis », *J. Power Sources*, vol. 334, p. 1-11, Dec. 2016, doi: 10.1016/j.jpowsour.2016.09.120.

[7] M. Fleischhammer, T. Waldmann, G. Bisle, B.-I. Hogg, et M. Wohlfahrt-Mehrens, « Interaction of cyclic ageing at high-rate and low temperatures and safety in lithium-ion batteries », *J. Power Sources*, vol. 274, p. 432-439, Jan. 2015, doi: 10.1016/j.jpowsour.2014.08.135.

[8] Y. Li, X. Feng, D. Ren, M. Ouyang, L. Lu, et X. Han, « Thermal Runaway Triggered by Plated Lithium on the Anode after Fast Charging », *ACS Appl. Mater. Interfaces*, vol. 11, nº 50, p. 46839-46850, Dec. 2019, doi: 10.1021/acsami.9b16589.

[9] N. Omar *et al.*, « Standardization Work for BEV and HEV Applications: Critical Appraisal of Recent Traction Battery Documents », *Energies*, vol. 5, nº 1, Art. nº 1, Jan. 2012, doi: 10.3390/en5010138.

[10] « IEC 62660-1:2010 | IEC Webstore | battery, energy efficiency, energy storage, smart city, transportation, mobility ». https://webstore.iec.ch/publication/7331&preview=1 (available online Feb. 2022).

[11] C. Birkl, M. Roberts, E. McTurk, P. Bruce, et D. Howey, « Degradation diagnostics for lithium ion cells », *J. Power Sources*, vol. 341, p. 373-386, Feb. 2017, doi: 10.1016/j.jpowsour.2016.12.011.

[12] A. Shellikeri *et al.*, « Investigation of Pre-lithiation in Graphite and Hard-Carbon Anodes Using Different Lithium Source Structures », *J. Electrochem. Soc.*, vol. 164, nº 14, p. A3914, Dec. 2017, doi: 10.1149/2.1511714jes.

[13] T. Waldmann, B.-I. Hogg, et M. Wohlfahrt-Mehrens, « Li plating as unwanted side reaction in commercial Li-ion cells – A review », *J. Power Sources*, vol. 384, p. 107-124, April 2018, doi: 10.1016/j.jpowsour.2018.02.063.

[14] C. Uhlmann, J. Illig, M. Ender, R. Schuster, et E. Ivers-Tiffée, « In situ detection of lithium metal plating on graphite in experimental cells », *J. Power Sources*, vol. 279, p. 428-438, April 2015, doi: 10.1016/j.jpowsour.2015.01.046.

[15] K. Ishidzu, Y. Oka, et T. Nakamura, « Lattice volume change during charge/discharge reaction and cycle performance of Li[NixCoyMnz]O2 », *Solid State Ion.*, vol. 288, p. 176-179, May 2016, doi: 10.1016/j.ssi.2016.01.009.

[16] « A Mechanical Aging Mechanism in Lithium-Ion Batteries - IOPscience ». https://iopscience.iop.org/article/10.1149/2.1001410jes (available online Aug. 2022).

[17] P. Maire, A. Evans, H. Kaiser, W. Scheifele, et P. Novák, « Colorimetric Determination of Lithium Content in Electrodes of Lithium-Ion Batteries », *J. Electrochem. Soc.*, vol. 155, nº 11, p. A862, Sept. 2008, doi: 10.1149/1.2979696.

[18] E. J. Plichta et W. K. Behl, « A low-temperature electrolyte for lithium and lithium-ion batteries », *J. Power Sources*, vol. 88, nº 2, p. 192-196, June 2000, doi: 10.1016/S0378-7753(00)00367-0.

[19] C.-H. Chen, F. B. Planella, K. O'Regan, D. Gastol, W. D. Widanage, et E. Kendrick, « Development of Experimental Techniques for Parameterization of Multi-scale Lithium-ion Battery Models », *J. Electrochem. Soc.*, vol. 167, nº 8, p. 080534, Jan. 2020, doi: 10.1149/1945-7111/ab9050.

[20] J. Newman et W. Tiedemann, « Porous-electrode theory with battery applications », *AIChE J.*, vol. 21, nº 1, p. 25-41, 1975, doi: 10.1002/aic.690210103.

[21] H. Ge *et al.*, « Investigating Lithium Plating in Lithium-Ion Batteries at Low Temperatures Using Electrochemical Model with NMR Assisted Parameterization », *J. Electrochem. Soc.*, vol. 164, nº 6, p. A1050, Mar. 2017, doi: 10.1149/2.0461706jes.

[22] « Is Lithium-ion the Ideal Battery? », *Battery University*, 15th July 2010. https://batteryuniversity.com/article/is-lithium-ion-the-ideal-battery (available online Mar. 2022).

[23] « LithiumBattery_JobAid.pdf ». Available online Mar. 2022, https://www.fedex.com/content/dam/fedex/us-united-states/services/LithiumBattery_JobAid.pdf

[24] B. Stuhrmann, « Self-Organized Active Biopolymer Networks in Migrating Living Cells », 2009, Ph-D Thesis, Universität Leipzig, available online https://www.researchgate.net/profile/Bjoern-Stuhrmann/publication/228334971_Self-Organized_Active_Biopolymer_Networks_in_Migrating_Living_Cells/links/0912f4ffacdf4d093b000000/Self-Organized-Active-Biopolymer-Networks-in-Migrating-Living-Cells.pdf , Aug. 2022.

[25] T. Waldmann et M. Wohlfahrt-Mehrens, « Effects of rest time after Li plating on safety behavior—ARC tests with commercial high-energy 18650 Li-ion cells », *Electrochimica Acta*, vol. 230, p. 454-460, Mar. 2017, doi: 10.1016/j.electacta.2017.02.036.

[26] K. Yan *et al.*, « Temperature-Dependent Nucleation and Growth of Dendrite-Free Lithium Metal Anodes », *Angew. Chem. Int. Ed.*, vol. 58, n° 33, p. 11364-11368, 2019, doi: 10.1002/anie.201905251.

[27] J. Hou *et al.*, « Unlocking the self-supported thermal runaway of high-energy lithium-ion batteries », *Energy Storage Mater.*, vol. 39, p. 395-402, Aug. 2021, doi: 10.1016/j.ensm.2021.04.035.

[28] W. Q. Walker *et al.*, « Decoupling of heat generated from ejected and non-ejected contents of 18650-format lithium-ion cells using statistical methods », *J. Power Sources*, vol. 415, p. 207-218, Mar. 2019, doi: 10.1016/j.jpowsour.2018.10.099.

Chapter IV: Modeling and Simulation for thermal behavior prediction

Contents

List of tables

List of figures

The objective of the modeling part of this thesis is not to build a fit of thermal runaway reactions, but to develop a predictive physical model for the safety at the cell scale for Li-ion battery technologies. For this purpose, the development of a thermal runaway model involving all the exothermic thermal degradation reactions of the fully charged INR18650-32E cell before and after cyclic-aging at -20 °C is presented in detail in this chapter.

1 The global modeling methodology

The developments are based on the experimental data collected mainly from DSC analysis of the cell materials. In this first development, the proposed model does not consider ISC (Internal Short Circuit due to separator melting) and reactions induced by “out of the cell” reactants (after cell venting, the external oxygen may contribute to significant additional heat generation).

The kinetic parameters and the degradation mechanism of the reactions are firstly studied and determined based on Chapter II and III results. Then, a thermal degradation scheme of the cell electrodes is proposed based on the chemistry of the cell and some of the reactions from the literature. The specific enthalpies of the reactions are calculated from experimental measurements. Besides, a reaction path and a species balance are proposed.
The initial quantities of the materials as well as their proportions are respected compared to the studied INR18650-32E cell. In addition, the interaction between lithium and the electrolyte is included for the first time in the proposed predictive model.

By coupling the chemical kinetic models of eight exothermic reactions, a battery TR model is then developed. For validation purposes, the proposed model is used at first to predict the ARC test of the fully charged INR18650-32E cell before and after aging at -20 °C in adiabatic conditions and then to simulate oven tests at different heating temperatures.

This model offers a detailed description and quantification of the TR reactions, their interactions, and their influence on the self-heating phase of a fresh cell and a Li-plated cell, and this for a temperature range from 50 °C to 400 °C.

2 Modeling of the thermal degradation of the battery materials

In the following section, we present our modeling methodology and the experimental data used for the model parameterization and validation. The assumed hypotheses and the mathematical formulation of the model are then detailed.

2.1 Kinetics analysis of exothermic reactions

Typically, chemical degradation reactions are characterized mainly by three parameters: kinetic, enthalpy, and the mechanism of the reaction. The first step in our modeling approach is to determine, based on DSC results, kinetic parameters and related enthalpies using a simplified model independently of the cell chemistry and exact degradation reactions mechanism. A detailed description of the thermal degradation pathway and species balance will be presented later in parts 2.3, 2.4, and 2.5.

Kinetic parameter definition

The total heat generation by the electrode materials degradation is equal to the sum of the heat generated by the degradation reactions identified with DSC. Besides, the specific power q_x related to each reaction peak is calculated via equation (1):

$$\boldsymbol{q_x = k_x H_x} \quad (1)$$

Where, k_x is the kinetic of the reaction (1/s), H_x is the heat related to peak $\boldsymbol{x}$ (J/g); here the term “reaction” does not necessarily mean one specific reaction but can be related to two or more reactions that occur simultaneously in the same peak.

The kinetic chemical reaction is described as follows [1]:

$$\boldsymbol{k_x = -\frac{dC_x}{dt} = A_x\, exp\left(-\frac{E_{a,x}}{RT}\right) f_x(C_x)} \quad (2)$$

k_x is the reaction kinetic. C_x(∈ [0,1]) is the concentration of the limiting reactant normalized to its initial concentration. $A_x, E_{a,x}$ are the kinetics parameters (pre-exponential factor and activation energy).

$f_x(C_x)$ is a mathematical function describing the kinetic model (or mechanism) of each reaction. The decomposition processes are often unknown and require an understanding of the physics that governs the degradation at the particle scale which complicates the determination of this function. A generic analytical (but physically insignificant) form was proposed by Šesták & Berggren [2] and reviewed by Koga [3]. It is written as follows:

$$\boldsymbol{f(x) = x^m\,(1-x)^n(-ln\,(1-x))^p} \quad (3)$$

Where $\boldsymbol{n}$, m, and p are three empirically determined parameters, to best describe the experimental curves and at least one of which is zero. Usually, to simplify the problem the mechanism function is expressed by equation (4) [4]:

$$\boldsymbol{f_x(C_x) = C_x^n} \quad (4)$$

With n is the order of the reaction.

Enthalpy parameter identification

The main exothermic reactions for the negative and the positive electrodes, presented and discussed in Chapters II and III are reported in

Table 1.

Table 1: Thermal degradation phenomena assumed for the negative and positive electrodes, related specific power notations, and onset temperature

Exothermic reaction	Notation	Onset T (°C)
SEI decomposition	q_{SEI}	80 – 90
Plated lithium and electrolyte solvent's reaction	q_{Li-ELe}	80
Intercalated lithium and electrolyte solvent's reaction	$q_{Li(C_6)-ELe}$	120 – 150
Electrolyte degradation (after lithium salt melting)	q_{ELe}	200 – 220
Intercalated lithium and negative electrode binder reaction	$q_{Li(C_6)-CMC}$	270 – 280
Intercalated lithium and degradation products of the electrolyte (PEO) reaction	$q_{Li(C_6)-PEO}$	300 – 310
First phase transition of delithiated NCA	q_{NCA}	180 – 200
The reaction between the oxygen released from the delithiated NCA and the electrolyte solvents	q_{O_2-ELe}	~190 – 200
Interactions between NCA oxides and electrolytes after the lithium salt melting	$q_{NCA-ELe}$	~220

The heat generated by all those reactions was determined based on DSC profiles obtained at three different heating rates of charged negative and discharged positive electrodes mixed

with cell electrolyte (see Figure 1); thus, a range of enthalpy values is calculated and listed in Table 2.

Table 2: specific heat released in each peak quantified based on DSC results

Enthalpy	Released heat (J g^{-1} of active material) min – max	Released heat (J g^{-1} of electrolyte) min – max
H_{SEI}	75 – 100 (1)	-
H_{Li-ELe}	300 – 400	1000 – 1320
$H_{Li(C_6)-ELe}$	510 – 900	1700 – 3000
H_{ELe}	250 – 375	800 – 1240
$H_{Li(C_6)-CMC}$	160 (1)	-
$H_{Li(C_6)-PEO}$	750 – 1600	2500 – 5300
H_{NCA}	160 (2)	-
H_{O_2-ELe}	1100 – 1300	2200 – 2600
$H_{NCA-ELe}$	1200 – 1300	2400 – 2600

(1) Specific heat of the reaction tested individually in DSC, (2) value from literature

$E_{a,x}$ and A_x parameters identification

The pre-exponential factor A_x and activation energy $E_{a,x}$ are determined with DSC curves using Kissinger's approach [5]. For overlapped peaks, some adjustments are performed. The main advantage of Kissinger's approach is based on the opportunity to get kinetic parameters without fixing the reaction mechanisms. According to this approach, at minimum three DSC profiles of the same sample at different heating rates are needed to determine kinetic parameters. Figure 1 shows respectively the DSC profiles of the lithiated negative electrode/electrolyte sample and the delithiated positive electrode/electrolyte sample at 2, 5, and 15 °C.min^{-1}.

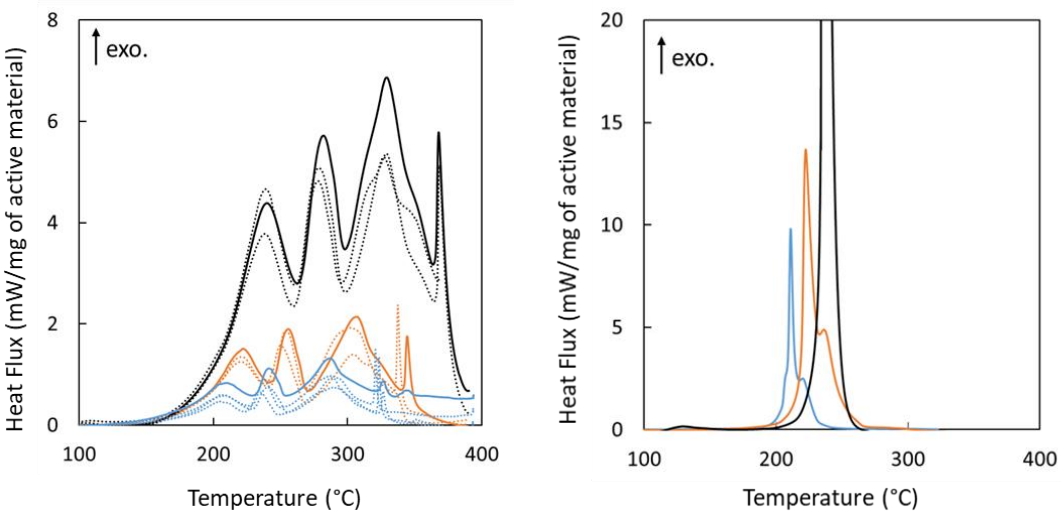

Figure 1: DSC curves of lithiated anode + electrolyte sample (left) and delithiated positive electrode + electrolyte sample (right) from the fresh INR18650-32E cell at heating rates of 2 °C min^{-1} (blue lines), 5 °C min^{-1} (orange lines), and 15°C min^{-1} (black lines); reproducibility is represented with dashed lines.

DSC tests with the negative electrode/electrolyte sample were repeated three times respecting the mass ratio of the full cell, dashed lines denote replicated tests. Despite some deviation, due to differences in the exact amount of active material or electrolyte, a good reproducibility can be mentioned as observed in Figure 1.

Some difficulties were observed when analyzing the materials of the positive electrode with electrolyte and good reproducibility was difficult to obtain. We suggest that this is due to the very sensitive and energetic oxidation reaction of the electrolyte and the difficulty to prepare samples (the electrolyte may partially evaporate during the DSC sampling preparation). The peak temperature of the second peak on the 15 °C/min DSC profile in Figure 1 (right curves) was fitted respecting the linearity with the temperature of the same peak in the two other DSC profiles.

The peak temperatures shifted to higher values as the heating rate increased in DSC tests as observed in Figure 1. This observation is consistent with the Kissinger methods of exploitation that are based on the hypothesis of a kinetic reaction driven by an Arrhenius law (equation *(2)*).

According to Kissinger's approach, the variation of the peak temperature with the heating rate follows equation (5).

$$ln\left(\frac{\beta}{T_p^2}\right) = ln\left(\frac{A_x R}{E_{a,x}}\right) - \frac{E_{a,x}}{R\,T_p} \qquad (5)$$

Where β is the heating rate, T_p is the peak temperature.

The variation of $ln\left(\frac{\beta}{T_p^2}\right)$ versus $\frac{1}{T_p}$ for each detected peak in DSC is plotted in Figure 2 and Figure 3. The green lines represent the best fits of DSC curves data.

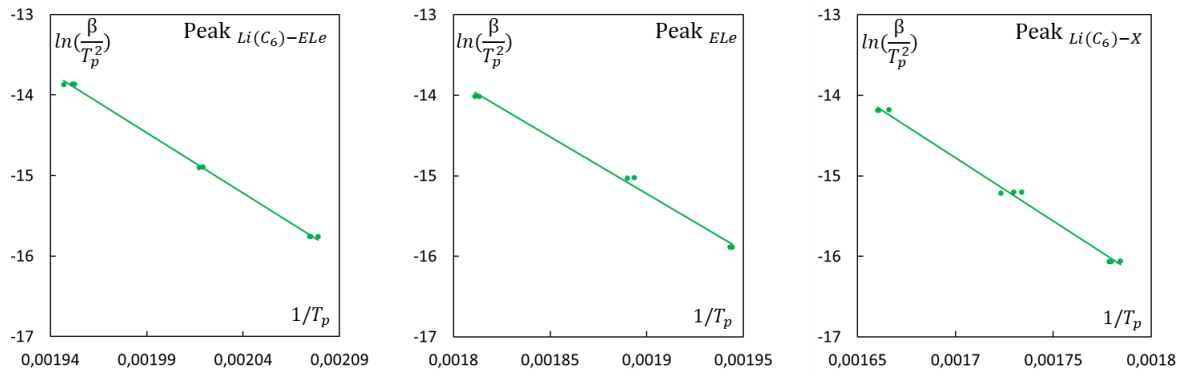

Figure 2: Kissinger plot of $Peak_{Li(C_6)-ELe}$, $Peak_{ELe}$ and $Peak_{Li(C_6)-X}$ (*), using data plots from Figure 1

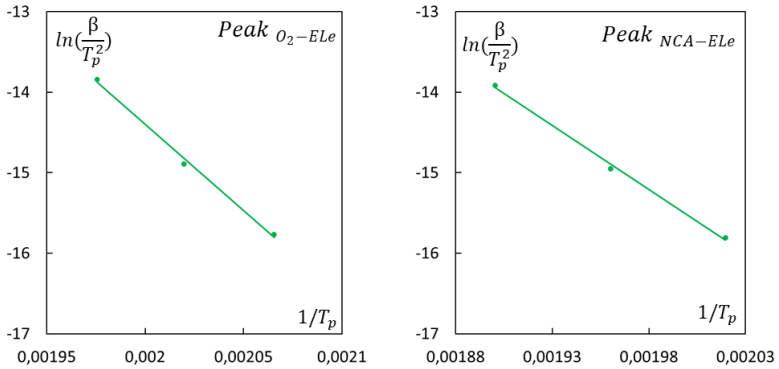

Figure 3: Kissinger plot of $Peak_{O_2-ELe}$ and $Peak_{NCA-ELe}$, using data plots from Figure 1

(*) The $Peak_{Li(C_6)-X}$ corresponding data concerns both of $Li(C_6)-CMC$ and $Li(C_6)-PEO$ reactions parameters. For most of the plots in Figure 2 and Figure 3, a good linear correlation between $ln\left(\frac{\beta}{T_p^2}\right)$ and $\frac{1}{T_p}$ can be observed.

The peak temperature of the SEI decomposition reaction is difficult to obtain from these DSC profiles with accuracy. Therefore, the kinetic parameters of the SEI decomposition reaction were identified separately using DSC profiles of delithiated anode reported in Figure 4.

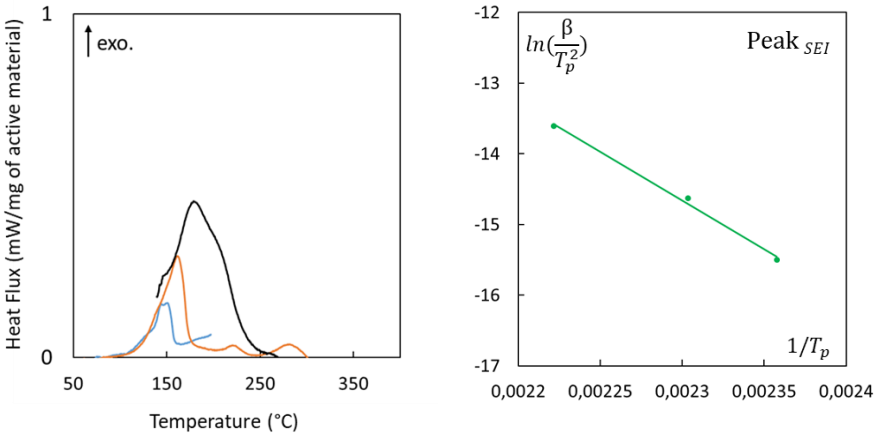

Figure 4: (left) DSC curves of delithiated anode samples from the fresh INR18650-32E cell at heating rates of 2 °C min^{-1} (blue lines), 5 °C min^{-1} (orange lines), and 15 °C min^{-1} (black lines); (right) Kissinger plot of the $Peak_{SEI}$

Then, the activation energy $E_{a,x}$ is derived from the slope of the fitting straight green line for each peak (Figure 2, Figure 3, and Figure 4). The pre-exponential factor A_x is obtained from the intercept on the ordinate of the straight lines. The estimated parameters for each peak are finally listed in Table 3.

Table 3: kinetic parameters of each peak of DSC profiles of the electrodes

Peak	$E_{a,x}$ (J.mol^{-1})	A_x (s^{-1})
$Peak_{SEI}$	1.22 10^5 (±0.02)	4.13 10^{11}
$Peak_{Li-ELe}$	1.15 10^5	1.53 10^{12}
$Peak_{Li(C_6)-ELe}$	1.25 10^5 (±0.02)	7.30 10^{10}
$Peak_{ELe}$	2.46 10^5 * (±0.03)	1.60 10^{22} *
$Peak_{Li(C_6)-CMC}$ $Peak_{Li(C_6)-PEO}$	1.655 10^5 * (±0.02)	2.51 10^{12} *
$Peak_{NCA}$	1.18 10^5 **	1.00 10^{11} **
$Peak_{O_2-ELe}$	3.86 10^5 **	5.00 10^{38} **
$Peak_{NCA-ELe}$	3.14 10^5 *	1.91 10^{30} *

(*) values obtained by Kissinger's approach and then adjusted against experimental DSC results for better prediction. (**) values fitted using experimental DSC results.

2.2 Enthalpy and Kinetic Parameter validation:

DSC test simulations were performed to validate the kinetic parameters. A comparison is made between the DSC experimental results and the model predicted DSC curves. The validation is performed on fresh and aged negative and positive electrode samples and at different heating rates.

The kinetic of each chemical reaction of the model used in this part is described as follows:

- The SEI decomposition reaction:

$$k_{SEI} = -\frac{dC_{SEI}}{dt} = A_{SEI}\, exp\left(-\frac{E_{a,SEI}}{RT}\right) C_{SEI} \quad (6)$$

- The reaction between the plated lithium and the electrolyte solvents:

$$k_{Li\_ELe} = -\frac{dC_{Li\_ELe}}{dt} = A_{Li\_ELe}\, exp\left(-\frac{E_{a,Li\_ELe}}{RT}\right) C_{Li\_ELe}^{5} \quad (7)$$

- The reaction between the intercalated lithium and the electrolyte solvents:

$$k_{Li\_ELe} = -\frac{dC_{Li(C6)\_ELe}}{dt} = A_{LiC6\_ELe}\, exp\left(-\frac{E_{a,Li(C6)\_ELe}}{RT}\right) C_{Li(C6)\_ELe} \quad (8)$$

- The degradation of the electrolyte after melting of the lithium salt:

$$k_{ELe} = -\frac{dC_{ELe}}{dt} = A_{ELe}\, exp\left(-\frac{E_{a,ELe}}{RT}\right) C_{ELe} \quad (9)$$

- The reaction between the intercalated lithium and the negative electrode binder:

$$k_{LiC6\_CMC} = -\frac{dC_{LiC6\_CMC}}{dt} = A_{LiC6\_CMC}\, exp\left(-\frac{E_{a,LiC6\_CMC}}{RT}\right) C_{LiC6\_CMC} \quad (10)$$

- The reaction between the intercalated lithium and the degradation products of the electrolyte (PEO):

$$k_{LiC6\_PEO} = -\frac{dC_{LiC6\_PEO}}{dt} = A_{LiC6\_PEO}\, exp\left(-\frac{E_{a,LiC6\_PEO}}{RT}\right) C_{LiC6\_PEO} \quad (11)$$

- The first phase transition of the delithiated NCA material:

$$k_{NCA} = -\frac{dC_{NCA}}{dt} = A_{NCA}\, exp\left(-\frac{E_{a,NCA}}{RT}\right) C_{NCA}^{4} \quad (12)$$

- The oxidation reaction between the oxygen released from the delithiated NCA and the electrolyte solvents:

$$k_{O_2\_ELe} = -\frac{dC_{O_2\_ELe}}{dt} = A_{O_2\_ELe}\, exp\left(-\frac{E_{a,O_2\_ELe}}{RT}\right) C_{O_2\_ELe}^{1/4} \quad (13)$$

- The interactions between NCA oxides and the electrolyte after melting of the lithium salt:

$$k_{NCA\_ELe} = -\frac{dC_{NCA\_ELe}}{dt} = A_{NCA\_ELe}\, exp\left(-\frac{E_{a,NCA\_ELe}}{RT}\right) C_{NCA\_ELe} \quad (14)$$

The order of reaction in equations (7), (12), and (13) were determined by numerical optimization against the experimental result.

The temperature T of the samples is correlated to the constant heating rate and calculated by:

$$\frac{dT}{dt} = \beta \quad (15)$$

Where β is the heating rate (K/s).

The DSC tests were simulated using three heating rates 2 °C/min, 5 °C/min, and 15 °C/min between the initial temperature (30 °C) and the ending temperature (400 °C). The temperature ramps at different heating rates are plotted in Figure 5.

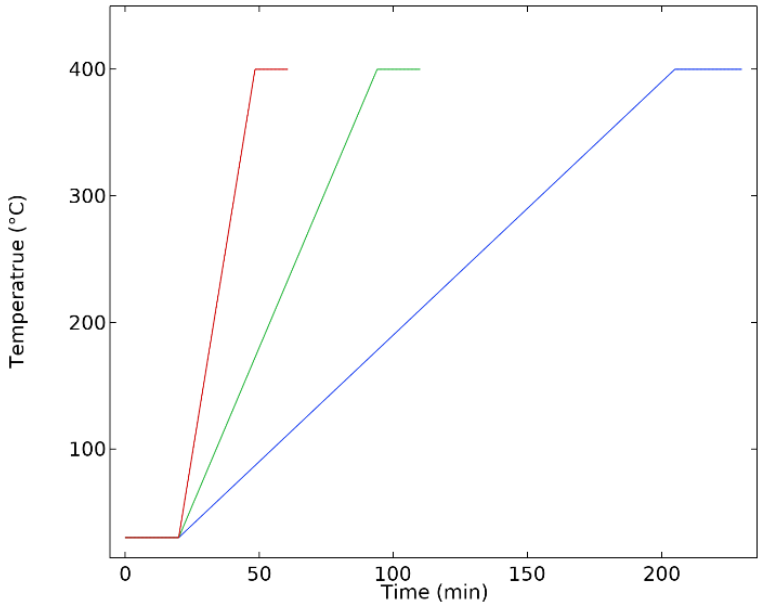

Figure 5: DSC heating profiles at 15 °C.min^{-1} (red), 5 °C.min^{-1} (green), and 2 °C.min^{-1} (blue)

The total heat flow of the negative electrode/electrolyte sample is calculated by the following summation of the separated exothermic reaction listed in

Table 1:

$$Q_{neg/ELe} = q_{SEI} + q_{Li-ELe} + q_{Li(C_6)-ELe} + q_{ELe} + q_{Li(C_6)-CMC} + q_{Li(C_6)-PEO} \quad (16)$$

The heat generated by the reaction including plated lithium (q_{Li-ELe}) is considered only for the aged negative electrode. The obtained heat simulation result of the fresh negative electrode material is presented in Figure 6.

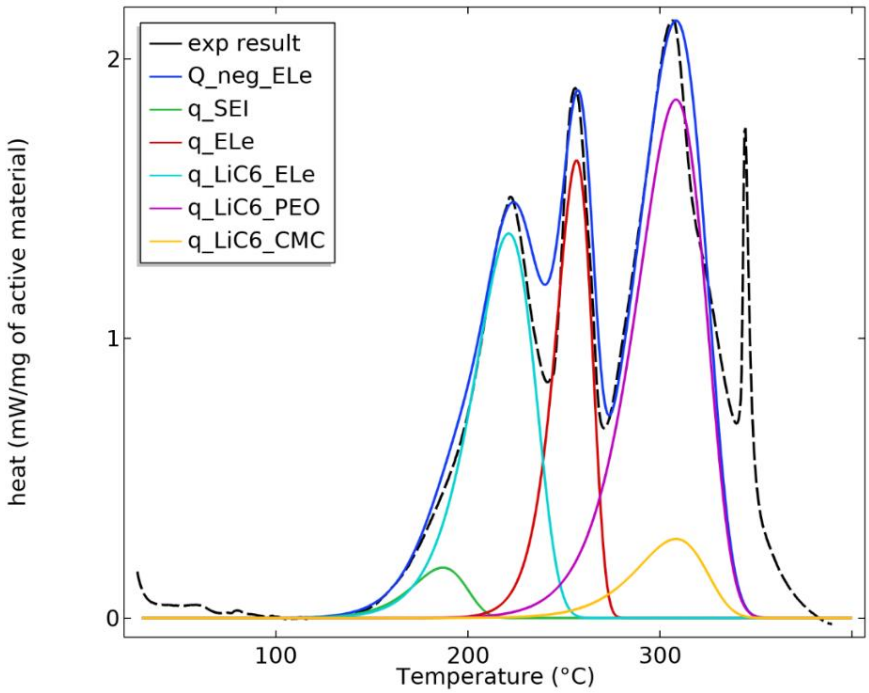

Figure 6: Simulation results of the thermal degradation peaks of fresh lithiated negative electrode material mixed with cell electrolyte (77:23 %wt.), dotted black line designates the experimental DSC result. Temperature heating rate: 5 °C.min^{-1}

We can see that the model reproduces well the experimental DSC curve. Since the contribution of the last peak is very low in terms of energy compared to the other peaks (area under the DSC curve) and appears at high temperatures, this peak is not considered in this model.
Simulations at different heating rates are conducted and the results are presented in Figure 7.

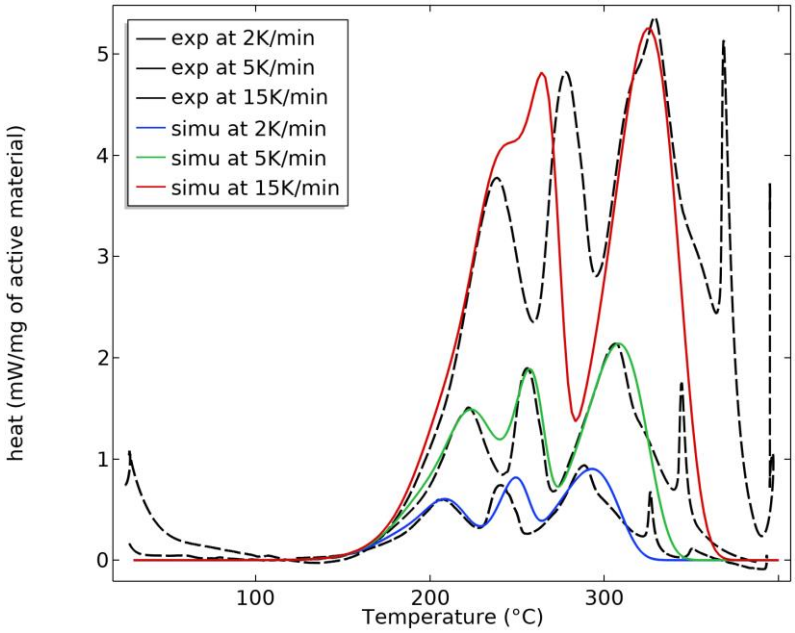

Figure 7: lithiated negative electrode material+electrolyte DSC profiles simulations at 2, 5, and 15 °C.min^{-1}

Simulations at 2 °C. min^{-1} and 5 °C. min^{-1} is well reproduced, but the one at 15 °C.min^{-1} matches less with the experimental DSC curve. The observed shift of the second peak at 15 °C.min^{-1} may be explained by an error in the kinetic parameter evaluation.

After aging, the exothermic reaction between the lithium plating and the electrolyte induces an excess of energy at low temperatures (Figure 8). We assumed that this interaction is independent of other reactions and can be calibrated separately. Then, the kinetic parameters of this reaction are adjusted against the experimental data of aged anode samples using the model (equation (7). The simulation result of the plated lithium and electrolyte reaction peak is presented in Figure 8 with a red line.

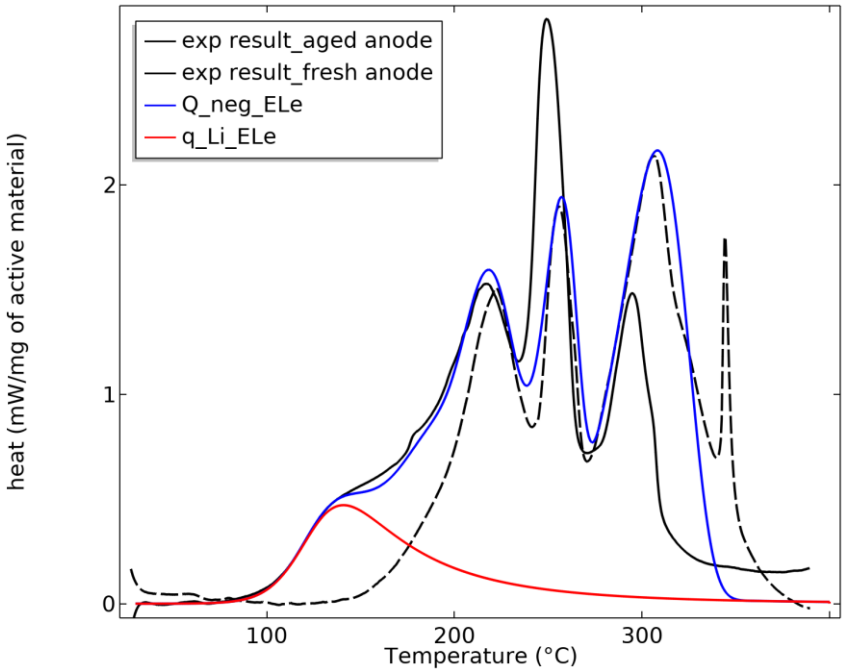

Figure 8: Simulation result of the Li-ELe reaction peak (red line) and aged lithiated negative electrode material mixed with cell electrolyte (blue line), dotted and solid black line designates the experimental DSC result of fresh (77:23 %wt.) and aged (67:33 %wt.) sample respectively. Temperature heating rate: 5 °C.min^{-1}

The differences in the amplitude of the peaks observed between the DSC profiles of the fresh sample (dashed black line) and aged sample (solid black line) may be related to the difference in the proportions of the materials in the two mixtures and solvent stoichiometry changes due to the prior reaction between Li-metal and the electrolyte on the aged sample (Chapter 3). In this step, we are only interested in calibrating the placement of the peaks by determining A_x and $E_{a,x}$ for each peak. However, a species balance will be proposed and discussed later to follow the variation of the peak amplitude according to the amount of the reacting materials.

On the other hand, the total heat generation of the positive electrode/electrolyte sample is similarly assumed to be the summation of three exothermic reactions (listed in

Table 1) and can be calculated as follows:

$$\boldsymbol{Q_{pos/ELe} = q_{NCA} + q_{O_2-ELe} + q_{NCA-ELe}} \quad (17)$$

The simulation result of the positive electrode material mixed with cell electrolyte is presented in Figure 9.

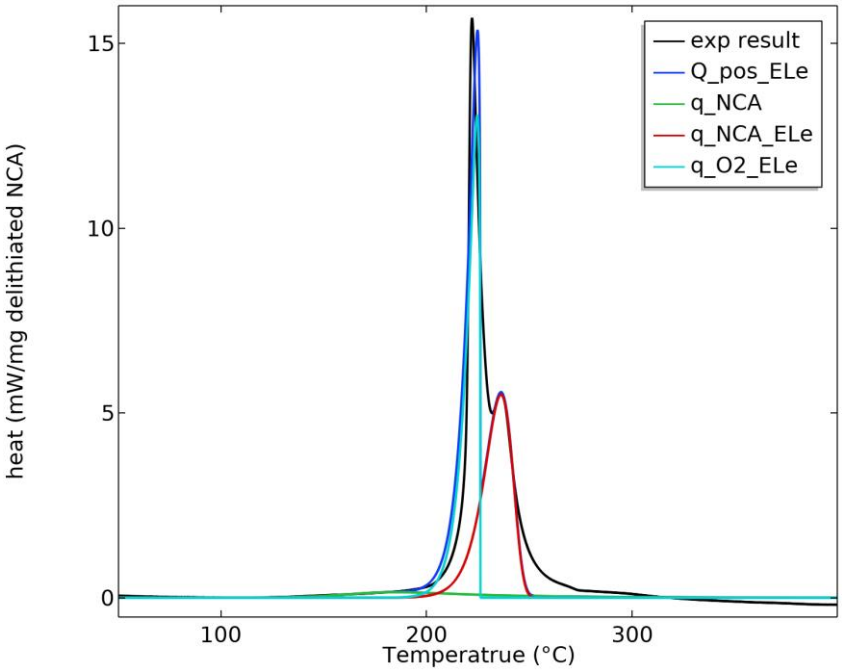

Figure 9: Simulation results of the thermal degradation peaks of delithiated positive electrode material mixed with cell electrolyte (66:34 %wt.), the experimental DSC profile is indicated with the black line

The predicted peaks are in good agreement with the experimental results and indicate that the calculated kinetic parameters adequately describe the reaction mechanisms.

This first part allowed us to validate the kinetic parameters of the different exothermic peaks, which characterize the TR of the fully charged INR18650-32E cell. The kinetic parameters for each peak were determined for both negative and positive electrode material mixed with electrolyte using Kissinger's approach and the experimental DSC results. The specific enthalpy for each peak normalized to the mass of the active material in the mixture used in the model was quantified based on experimental results.

2.3 Thermal runaway process pathway

In the previous section, we focused on the parameterization of the peaks that characterize the thermal degradation of both negative and positive electrode material. The kinetics and the mechanism of each peak were determined and validated using DSC results.
To understand and follow the evolution of the cell species and their interaction, it is essential to identify a TR process scheme according to the cell chemistry and to model the evolution of the specified amount during the TR process.

Therefore, a thermal runaway reactions pathway is proposed according to our DSC results presented in the previous chapters and also based on the literature data. The reactions are presented according to their order of appearance depending on the temperature. One or more reactions are proposed accordingly and the enthalpy of the reactions is calculated using the

standard enthalpies of the formation of products and reactants. Data have been collected mainly from the NIST Chemistry Webbook [6].

Used data are reported in Table 4. The calculation of some enthalpy of reactions was not possible because of missing data. The (-) sign preceding the enthalpy value is added for exothermic reactions, it is replaced by a (+) sign for endothermic reactions.

Table 4: Enthalpy data for the INR18650-32E cell TR reactions

	Component	Molecular weight (g/mol)	Heat of formation		
			$\Delta_f H°$ (kJ/mol)	$\Delta_f H°$ (kJ/g)	References
Anode	Copper	63.546	0.00	0.00	-
	Lithiated Graphite LiC_6	79.007	-11.65 (-13)	-0.15	[7]
	CMC $[C_6H_7O_2(OH)_{2.3}(OCH_2COONa)_{0.7}]n$	218.160	-1093.38	-5.01	[8]
	Lithium Ethylene Dicarbonate (LEDC) $(CH_2OCO_2Li)_2$ (s)	161.946	-1513.2	-9.34	[7]
	Lithium methyl carbonate (LMC) CH_3OCO_2Li (s)	81.9844	-769.41	-9.38	calculated
	Lithium Fluoride LiF (s)	25.938	-616.93	-23.78	[6]
	Lithium carbonate Li_2CO_3 (s)	73.888	-1216.04	-16.46	[6]
Cathode	Aluminum	26.982	0.00	0.00	-
	$LiNi_{0.8}Co_{0.18}Al_{0.05}O_2$ (NCA)	-	-221.6	-	[7]
	$LiNi_{0.8}Co_{0.18}Al_{0.05}O$	-	-33.6	-	[7]
	Polyvinylidene Fluoride (PVDF) $(C_2H_2F_2)n$	64.035	-390.93	-6.10	[8]
Separator	Polyethylene (PE) $(C_2H_4)n$	28.054	43.46	-1.55	[8]
	Aluminum hydroxide oxide ($AlHO_2$)	59.9883	-460.24	7.68	[6]
Electrolyte	Ethylene Carbonate (EC) $C_3H_4O_3$	88.062	-531	-6.03	[6]
	Dimethyl Carbonate (DMC) $C_3H_6O_3$	90.078	-608.76	-6.76	[6]
	Propylene Carbonate (PC) $C_4H_6O_3$	102.089	-614.1	-6.02	[6]
	Fluoroethylene carbonate (FEC) $C_3H_3FO_3$	106.05	-	-	-
	Lithium Hexafluorophosphate $LiPF_6$	151.905	-2296	-15.11	[9]
Decomposition products	Phosphorus pentafluoride (PF_5)	125.9657	-1594.41	-12,657	[6]
	Ethane, 1,1-difluoro- (C_2H4F_2)	66.05	-497.0	-7,525	[6]
	Phosphoryl fluoride (POF_3)	103.968	-1254.25	-12,064	[6]
	Lithium methoxide (CH_3LiO)	37.975	-433.1	-11,405	[6]
	acetyl fluoride (C_2H_3FO)	62.0430	-445	-7.17	[6]
	hydrogen fluoride (HF)	20.006	-272.55	-13,623	[6]
	Methyl fluoride (CH_3F)	34.0329	-247	-7.257	[6]
	Carbon dioxide (CO_2)	44.009	-393.52	-8.94	[6]
	Ethylene (C_2H_4)	28.053	52.4	1.87	[6]
	Ethane (C_2H_6)	30.0690	-84	-2.79	[6]
	Propane (C_3H_6)	42.0797	20.41	0,485	[6]
	Polypropylene (PP) (C_3H_6) n	42.080	-62.93	-1.50	[8]
	H_2O	18.0153	-241.83	-13,42	[6]
	lithium hydroxide (HLiO)	23.948	-484.93	-20.25	[6]
	Methyl Alcohol CH_4O	32.0419	-205	-6,398	[6]
	Carbone monoxide CO	28.01	-110.53	-3,94	[6]
	dilithium oxide Li_2O	29.881	-598.73	-20,03	[6]

2.3.1 The reaction of plated lithium with electrolyte (70 – 90 °C): R1

Based on DSC results, the reaction between plated lithium and electrolyte is identified as the first one that occurs during the thermal runaway in the case of aged cells with lithium plating formation. The plated lithium could react with the electrolyte solvents according to the following reactions (18)-(24):

Reactants		Products	Reaction Enthalpy	
$2Li(s) + C_3H_4O_3$ (EC)	→	$Li_2CO_3 + C_2H_4$	-633 kJ/mol	(18)
$2Li(s) + 2\ C_3H_4O_3$ (EC)	→	$(CH_2OCO_2Li)2 + C_2H_4$	-399 kJ/mol	(19)
$2Li(s) + 2\ C_3H_4O_3$ (EC)	→	$LiO(CH_2)_4OLi + 2CO_2$	-	(20)
$2Li(s) + C_3H_6O_3$ (DMC)	→	$Li_2CO_3 + C_2H_6$	-691 kJ/mol	(21)
$2Li(s) + 2\ C_3H_6O_3$ (DMC)	→	$2\ CH_3OCO_2Li + C_2H_6$	-405 kJ/mol	(22)
$2Li(s) + C_4H_6O_3$ (PC)	→	$Li_2CO_3 + C_3H_6$	-582 kJ/mol	(23)
$3Li(s) + C_3H_3FO_3$ (FEC)	→	$Li_2O + LiF + CO + CH_3CHO$	-	(24)

According to the quantification of plated lithium after aging at -20 °C using ^{7}Li NMR analysis, presented in chapter 2, the amount of plated lithium is estimated to be in the range of 77 mg and 128 mg i.e., 11 mmol – 19 mmol of plated lithium in the cell (8 – 13 % of the total lithium). Besides, looking at the total amount of electrolyte solvents in the cell (see Table 5), metallic lithium is the default reactant in reactions (18)-(24). We assume that plated lithium reacts preferentially with PC solvent in this temperature range.

2.3.2 SEI layer decomposition (~ 90 °C): R2

The generated heat by the SEI breakdown is associated mainly with the exothermic decomposition of SEI metastable components as follows [10], [11]:

Reactants		Products	Reaction Enthalpy	
$(CH_2OCO_2Li)2$ (LEDC)	→	$Li_2CO_3 + C_2H_4 + CO_2 + ½\ O_2$	-44 kJ/mol	(25)
CH_3OCO_2Li (LMC)	→	$CO_2 + CH_3OLi$	-57 kJ/mol	(26)

Other possible reactions between intercalated lithium and SEI components are attributed to the SEI breakdown in the literature [12]:

Reactants		Products	Reaction Enthalpy	
$2Li(C_6) + (CH_2OCO_2Li)2$	→	$Li_2CO_3 + C_2H_4$	-368 kJ/mol	(27)
$2Li(C_6) + (CH_2OCO_2Li)2$	→	$(COOLi)_2 + (CH_2OLi)_2$	-	(28)
$2Li(C_6) + CH_3OCO_2Li$	→	$(COOLi)_2 + 2CH_3OLi$	-	(29)
$2Li(C_6) + Li_2CO_3$	→	$2Li_2O + CO$	-79 kJ/mol	(30)

The SEI could contain metastable components (such as LEDC and LMC) and stable components (such as LiF and Li_2CO_3). However, according to the XPS results discussed in chapter 2, the Li_2CO_3 quantity is low at the graphite electrode surface. Moreover, the SEI breakdown was tested only in DSC and we showed that it is independent of the amount of intercalated lithium in the graphite electrode. Therefore, only reactions (25)-(26) are selected for the SEI breakdown.

The measured heat of this reaction in DSC was situated in the range of 75 – 100 J/g of active material. When considering the heat generated by mole of metastable SEI components according to reactions (25) and (26). The released heat of SEI breakdown is estimated to be 480 – 610 J/g of SEI. Therefore, the weight fraction of the SEI layer in the negative electrode active material is deduced to 1.6 – 2 wt.%.

Calculation example if SEI is composed of 50 % of LEDC + 50 % of LMC, then:
H_{SEI} = 0.5 x ((-44 kJ/mol LEDC) / (162 g/mol LEDC) + (-57 kJ/mol LMC) / (82 g/mol LMC))
= ~483 J/g of SEI

2.3.3 The reaction of intercalated carbon with electrolyte (~120 °C): R3

After the SEI breakdown, the electrolyte solvents reach the surface of the graphite electrode and react with the intercalated lithium. The reactions start at around 120° according to reactions (31)-(37):

Reactants		**Products**	**Reaction Enthalpy**	
$2Li(C_6) + C_3H_4O_3\ (EC)$	→	$Li_2CO_3 + C_2H_4$	-607 kJ/mol	(31)
$2Li(C_6) + 2\ C_3H_4O_3\ (EC)$	→	$(CH_2OCO_2Li)2 + C_2H_4$	-373 kJ/mol	(32)
$2Li(C_6) + 2\ C_3H_4O_3\ (EC)$	→	$LiO(CH_2)_4OLi + 2CO_2$	-	(33)
$2Li(C_6) + C_3H_6O_3\ (DMC)$	→	$Li_2CO_3 + C_2H_6$	-665 kJ/mol	(34)
$2Li(C_6) + 2\ C_3H_6O_3\ (DMC)$	→	$2\ CH_3OCO_2Li + C_2H_6$	-379 kJ/mol	(35)
$2Li(C_6) + C_4H_6O_3\ (PC)$	→	$Li_2CO_3 + C_3H_6$	-556 kJ/mol	(36)
$3Li(C_6) + C_3H_3FO_3\ (FEC)$	→	$Li_2O + LiF + CO + CH_3CHO$	-	(37)

These reactions are highly exothermic compared to the SEI breakdown. Based on data reported in Table 2, the released heat by this reaction is ~500 J/g of lithiated graphite or ~1700 J/g of electrolyte when the ratio of 75:25 wt.% is representative of a full cell is respected.
According to reactions (**31**)-(37), the reaction enthalpy values are roughly the same with the different solvent respecting their stoichiometry coefficient; they release a meanly 700 kJ/mol of solvent. Besides, the molar weight of the electrolyte solvents is mostly the same (~100

g/mol), then 7000 J/g of solvent can be calculated. This value is consistent with the reaction heat measured in DSC based on the 25 wt.% of the electrolyte in the tested samples.

Then, some calculations are made to identify the default reactant for these reactions.
The fully lithiated graphite contains:
(370 mAh / g of C_6) x (0.92 g of C6 / g of electrode) x (3.6 A s/ mAh) x (1/96.500 mol Li / A s) = 0.013 mol of Li / g of electrode = 0.15 mol of Li
The 32E cell negative electrode weighs approximately 12 – 13 g, thereby it holds 0.16 – 0.17 mol of Li.
Then, the solvent and the salt amount were calculated based on the total quantified weight of the cell electrolyte. Results are reported in the following table:

Table 5: solvent and salt amount calculation of the cell electrolyte

	Density (g/cm^3)	**Weight (g)**	**Molar amount (mol)**
Cell electrolyte	$\rho_{el} \simeq 1.45$	m_{el} = 4.5	-
DMC $\boldsymbol{X_{DMC}}$ = 0.29%	ρ_{DMC} =1.063	m_{DMC} = 0.92	n_{DMC} = 0.01
EC $\boldsymbol{X_{EC}}$ = 0.15%	ρ_{EC} =1.321	m_{EC} = 0.61	n_{EC} = 0.007
PC $\boldsymbol{X_{PC}}$ = 0.18%	ρ_{PC} =1.21	m_{PC} =0.67	n_{PC} = 0.007
FEC $\boldsymbol{X_{FEC}}$ = 0.38%	ρ_{FEC} =1.41	m_{FEC} =1.66	n_{FEC} = 0.016
Total solvents	-	$m_{solvents}$ = 3.86	$n_{solvents}$ = 0.04
$LiPF_6$	-	m_{LiPF_6} = 0.64	n_{LiPF_6} = 0.004

The density of the INR18650-32E cell electrolyte was determined experimentally.

The weight of the electrolyte solvents was calculated by:

$$\boldsymbol{m_s = \frac{\rho_s \times X_s \times m_{el}}{\rho_{el}}} \quad (38)$$

The amount of intercalated lithium is notably higher than the electrolyte solvents. Accordingly, the heat generated by reactions (31)-(37) is limited by the electrolyte solvents amount when the negative electrode is fully charged.
Based on the properties of the different solvents, the evaporation temperature of DMC is much lower (90 °C) than other solvents, then we hypothesized that DMC reacts preferentially with intercalated lithium here following reaction (34).

2.3.4 Positive active material decomposition (170 – 200 °C): R4

As discussed in the previous chapters, the delithiated NCA material $Li_x(Ni_{0.7}Co_{0.13}Al_{0.02})O_2$, with $x \in [0.35, 0.5]$, is unstable when subjected to temperatures above ~170 °C.

The NCA structure changes from layered to rock salt structure with the liberation of O_2 gas following two steps (39)-(40):

First structural change:

Reactants		Products	Reaction Enthalpy	
$\mathrm{Li_x(Ni_{0.7}Co_{0.13}Al_{0.02})O_2}$ (layered)	→	$\mathrm{Li_x(Ni_{0.7}Co_{0.13}Al_{0.02})O_2}$ (layered + spinel)	-40 kJ/mol	(39)

Second structural change:

Reactants		Products	Reaction Enthalpy	
$\mathrm{Li_x(Ni_{0.7}Co_{0.13}Al_{0.02})O_2}$ $(spinel)$	→	NCA $(rock\ salt) + \mathrm{O_2}$	+133 kJ/mol	(40)

The initial structure transformation is exothermic and generates theoretically -40 kJ/mol of produced spinel NCA or -210 J/g of $\mathrm{Li_{0.5}(Ni_{0.80}Co_{0.15}Al_{0.05})O_2}$ [13]. This value is consistent with the heat generated in DSC when the delithiated NCA of the fresh INR18650-32E cell is tested only without adding electrolyte and -160 J/g of delithiated NCA was measured. Noted that the amount of released heat is proportional to the chemistry of the NCA material and the amount of lithium remaining in the delithiated structure, which could explain the difference between the thermodynamic enthalpy and that measured experimentally.

The second structural change is endothermic and produces oxygen; it consumes theoretically about +133 kJ/mol of produced O_2 [13]. The oxygen species react simultaneously with the electrolyte solvents.

2.3.5 Electrolyte oxidation (~200 °C): R5

The oxidation of the electrolyte solvents occurs then after the NCA degradation. It is highly powerful and could be partial or total according to the following reactions (41)-(46)

Reactants		Products	Reaction Enthalpy	
$\mathrm{2\ C_3H_4O_3\ (EC)\ + 5\ O_2}$	→	$\mathrm{6\ CO_2\ +\ 4\ H_2O}$	-1181 kJ/mol	(41)
$\mathrm{2\ C_4H_6O_3\ (PC)\ + 8\ O_2}$	→	$\mathrm{8\ CO_2\ +\ 6\ H_2O}$	-1817 kJ/mol	(42)
$\mathrm{2\ C_3H_6O_3\ (DMC)\ + 6\ O_2}$	→	$\mathrm{6\ CO_2\ +\ 6\ H_2O}$	-1430 kJ/mol	(43)
$\mathrm{2\ C_3H_4O_3\ (EC)\ +\ O_2}$	→	$\mathrm{2\ CO_2\ +\ 4\ CO\ +\ 4\ H_2}$	-43 kJ/mol	(44)
$\mathrm{2\ C_4H_6O_3\ (PC)\ + 2\ O_2}$	→	$\mathrm{2\ CO_2\ +\ 6\ CO\ +\ 6\ H_2}$	-111 kJ/mol	(45)
$\mathrm{2\ C_3H_6O_3\ (DMC)\ +\ O_2}$	→	$\mathrm{2\ CO_2\ +\ 4\ CO\ +\ 6\ H_2}$	-6 kJ/mol	(46)

The nature of the oxidation reaction depends mainly on the amount of the solvent and the liberated oxygen from delithiated NCA. If we consider the reactions presented here, for complete oxidation the molar amount of oxygen must be respectively 2.5 / 3 / 4 times higher than the amount of EC / DMC / PC solvents.

We need then to calculate the amount of oxygen that can be released in the cell in the worst case i.e., a completely delithiated positive electrode, and to compare it with the total amount of solvents available in the cell at this temperature.
The amount of released oxygen depends on the lithiation state of the delithiated NCA cathode. A simplified scheme of the full degradation reaction is given by the following reaction [11]:

$$\mathbf{Li_x(NiCoAl)O_2} \rightarrow \mathbf{Li_x(NiCoAl)O_{1+x}} + \frac{\mathbf{1}}{\mathbf{2}}\mathbf{(1-x)O_2} \qquad (47)$$

Then, the amount of liberated O_2 is estimated by:

$$\boldsymbol{n_{O_2}} = \frac{\mathbf{1}}{\mathbf{2}}\mathbf{(1-}\boldsymbol{x}\mathbf{)}\ \boldsymbol{n}_{\mathbf{NCA}} = \frac{\mathbf{(1-}\boldsymbol{x}\mathbf{)}\ \boldsymbol{m}_{\mathbf{NCA}}}{\mathbf{2}\ \boldsymbol{M}_{\mathbf{NCA}}} \qquad (48)$$

If we assumed that x is between 0.35 and 0.5 when the cell is fully charged, the calculation of released oxygen is:

$$\boldsymbol{n_{O_2}} = [\mathbf{3-4}\,]\mathbf{10^{-3}}(\boldsymbol{mol/g}) \times \boldsymbol{m}_{\mathbf{Li_x(Ni_{0.7}Co_{0.13}Al_{0.02})O_2}}(\mathbf{g}) \qquad (49)$$

The total weight of the positive electrode is 16 – 17 g in the INR18650-32E cell, and then the total released oxygen could be estimated to be 50 mmol at the minimum and 70 mmol at the maximum. These values are consistent with those of Golubkov and al. [11]

Now if we consider that the first two reactions involving lithium plated lithium and intercalated lithium consume preferentially the PC and DMC solvent respectively, then the equilibrium between the amount of released O_2 and the solvent includes only the amount of EC solvent (see Table 5) since the FEC solvent is not implicated in the selected oxidation reactions (41)-(46).

Therefore, considering the chain of thermal runaway reactions presented until this temperature range, the molar amount of oxygen released by the delithiated positive electrode at this temperature is 7 - 10 times higher than the EC solvent molar amount.
In the case of the fresh negative electrode, there is no metallic lithium to react with the PC solvent, then the equilibrium between the O_2 and the solvent must include the amount of EC and PC solvents. Thus, the ratio O_2/solvent decrease to 3.5 – 5 in this case.

Consequently, in both cases, total oxidation is rather favorable. Interestingly, this calculation is coherent with the DSC results performed on the positive electrode using different active material to electrolyte ratio, where the energy and the power of the oxidation peak were correlated to the electrolyte amount in the mixture.

Before proceeding to the next reaction, it is important to note that a reaction between oxygen and lithiated graphite occurs at this temperature range in the absence of electrolyte as follows:

Reactants		Products	Reaction Enthalpy	
$O_2 + 4\,LiC_6$	⇆	$2\,Li_2O + 4\,C_6$	-1144 kJ/mol	(50)

When the charged negative/positive material mixture was tested in DSC (see chapter III), the exothermic peak associated to this reaction released 2500 J/g of active material. We believe that such interaction may occur in a full cell after the electrolyte oxidation with the residual amount of oxygen.

2.3.6 Electrolyte decomposition (~220 °C): R6

The cell electrolyte contains solvents and $LiPF_6$ salt. As outlined in the previous chapter, $LiPF_6$ salt melts at around 200 °C and produces PF_5 and LiF.

Reactants		Products	Reaction Enthalpy	
$LiPF_6$	⇆	$LiF + PF_5$	+85 kJ/mol	(51)

Generally, it is not possible to completely avoid the H_2O contamination in the electrolyte present in commercial LIBs, which can be more than 20 ppm [14]. Therefore, some interactions between $LiPF_6$, PF_5, and water traces are inevitable and produce corrosive products such as HF gas and other products such as phosphine oxides according to the following reactions [14], [15]:

Reactants		Products	Reaction Enthalpy	
$LiPF_6 + H_2O$	→	$LiF + POF_3 + 2HF$	+126 kJ/mol	(52)
$LiPF_6 + H_2O$	→	$LiOH + PF_5 + HF$	+186 kJ/mol	(53)
$\mathbf{PF_5 + H_2O}$	→	$POF_3 + 2HF$	+37 kJ/mol	(54)
$\mathbf{PF_5 + H_2O}$	→	$PF_4OH + HF$	-	(55)
$\mathbf{PF_4OH}$	→	$POF_3 + HF$	-	(56)
$\mathbf{POF_3 + H_2O}$	→	$POF_2OH + HF$	-	(57)

The produced PF_5 from reactions (51) and (53) could initiate also some polymer formation with preferentially EC solvent to form polyethylene oxide (PEO) or polyethylene glycol (PEG)

through reaction (58). The exact role of PF_5 in the polymerization mechanism of EC is not yet well known [16].

$\mathbf{C_3H_4O_3}$ **(EC)**	→	$\mathbf{CO_2} + (-\mathbf{C_2H_4O}-)_\mathbf{n}$ **(PEO, PEG)**	-	(58)

The produced POF_3 from reaction (54) or reaction (56) could participate in the decomposition reaction of DMC solvent [17]

$\mathbf{POF_3} + \mathbf{C_3H_6O_3}$ **(DMC)**	→	$\mathbf{CH_3F} + \mathbf{PF_2O_2CH_3} + \mathbf{CO_2}$	-	(59)

These two transformations of EC and DMC are exothermic and describe the degradation of the electrolyte. Usually, it was reported that EC transformation occurs preferentially than DMC degradation. It is complicated to validate this suggestion experimentally and the enthalpy of the reactions (58)-(59) cannot be calculated due to the lack of information on some products in the literature.

Moreover, when the electrolyte was tested only, about 400 J/g of electrolyte is released. However, the quantified heat released by the same degradation peak when the electrolyte is mixed with lithiated anode was 800 – 1200 J/g of electrolyte as reported in Table 2. Therefore, we suggested other exothermic reactions including anode active material and the electrolyte or its degradation products in this temperature range.

It was reported that PF_5 and HF, may participate in the degradation of the new SEI components produced by R1, R2, and R3 in this temperature range according to the following reactions [12]

Reactants		**Products**	**Reaction Enthalpy**	
$PF_5 + CH_3OCO_2Li$	→	$LiF + CH_3F + POF_3 + CO_2$	+639 kJ/mol	(60)
$PF_5 + CH_3CO_2Li$	→	$LiF + POF_3 + CH_3COF$	+48 kJ/mol	(61)
$PF_5 + Li_2CO_3$	→	$2LiF + POF_3 + CO_2$	-71 kJ/mol	(62)
$2\,PF_5 + (CH_2OCO_2Li)2$	→	$2LiF + C_2H_4F_2 + 2POF_3 + 2CO_2$	-325 kJ/mol	(63)
$HF + CH_3OCO_2Li$	→	$CH_3OH + CO_2 + LiF$	-174 kJ/mol	(64)
$2HF + Li_2CO_3$	→	$CO_2 + H_2O + 2LiF$	-108 kJ/mol	(65)

As we can see, most of these reactions are exothermic and can be potentially present in this temperature range.

We supposed that the new SEI layer is composed mainly of Li_2CO_3 components produced by reactions (18), (25), (31). Then, Li_2CO_3 reacts exothermically with HF and PF_5 according to reactions (62) and (65). Only these reactions are considered in this temperature range and occur simultaneously with the EC degradation.

2.3.7 The reaction of lithiated graphite with CMC binder and PEO polymers (~300 °C): R7

After decomposition, the CMC-Na binder reacts with the residual amount of intercalated lithium in the negative electrode (as demonstrated in chapter 2) following the reaction [12], [18]:

$$\mathbf{CMC-OH} + \mathbf{LiC_6} \rightarrow \mathbf{CMC-OLi} + \tfrac{1}{2}\,\mathbf{H_2} \quad (66)$$

Typically, the negative electrode contains about 2-4 wt.% binder. The most used binder in graphite electrodes is based on CMC-Na + SBR (Styrene Butadiene Rubber) but is not studied here because it is chemically more stable than CMC-Na.

Additives such as carbon black or others could be present in the negative electrode material but are not considered in this part.
If the negative electrode material is 98 wt.% LiC_6 and 2wt.% CMC-Na and considering that the total weight of lithiated anode is 12 – 13 g, then it contains probably 0.24 - 0.26 g of CMC. This reaction is limited by CMC when the negative electrode is fully lithiated.

In the same range of temperature, the electrolyte degradation products PEO or PEG reacts with intercalated lithium. To date, there is no exact chemical reaction to this interaction. Therefore, the heat of the peak associated with this reaction and quantified in DSC (reported in Table 2) will be used.

2.4 Assumed thermal runaway reactions

In this part, we summarize the chain of thermal runaway reactions selected for the TR predictive model of the INR18650-32E cell. We assume that the heat leading to thermal runaway comes from the exothermic decomposition reactions of the active materials and the electrolyte occurring in the cell between 30 and 400 °C. These reactions and their enthalpies are reported in Table 6.

Table 6: Assumed thermal runaway reactions of the INR18650-32E cell

Index	Assumed reactions	$\Delta H_{r,x}$ at 298 K, (kJ / mol)	
R1	$2\mathrm{Li(s)} + \mathrm{C_4H_6O_3(PC)} \rightarrow \mathrm{Li_2CO_3} + \mathrm{C_3H_6}$	-582	$Li - PC$
R2	$(\mathrm{CH_2OCO_2Li})2 \rightarrow \mathrm{Li_2CO_3} + \mathrm{C_2H_4} + \mathrm{CO_2} + ½\,\mathrm{O_2}$	-44	SEI_I
	$\mathrm{CH_3OCO_2Li} \rightarrow \mathrm{CO_2} + \mathrm{CH_3OLi}$	-57	
R3	$2\mathrm{Li(C_6)} + \mathrm{C_3H_6O_3(DMC)} \rightarrow \mathrm{Li_2CO_3} + \mathrm{C_2H_6}$	-665	$Li(C_6) - DMC$
R4	$\mathrm{NCA\ (layered)} \rightarrow \mathrm{NCA\ (layered + spinel)}$	-40	NCA
R5	$2\,\mathrm{C_3H_4O_3(EC)} + 5\,\mathrm{O_2} \rightarrow 6\,\mathrm{CO_2} + 4\,\mathrm{H_2O}$	-1181	$EC - O_2$
	$2\,\mathrm{C_3H_4O_3(EC)} + \mathrm{O_2} \rightarrow 2\,\mathrm{CO_2} + 4\,\mathrm{CO} + 4\,\mathrm{H_2}$	-43	
R6	$\mathrm{C_3H_4O_3(EC)} \rightarrow \mathrm{CO_2} + (-\mathrm{C_2H_4O}-)_n$ (catalyzed by PF_5)	-270	EC
	$\mathrm{PF_5} + \mathrm{Li_2CO_3} \rightarrow 2\mathrm{LiF} + \mathrm{POF_3} + \mathrm{CO_2}$	-71	SEI_II
	$2\mathrm{HF} + \mathrm{Li_2CO_3} \rightarrow \mathrm{CO_2} + \mathrm{H_2O} + 2\mathrm{LiF}$	-108	
R7	$\mathrm{Li} + \mathrm{CMC-OH} \rightarrow \mathrm{CMC-OLi} + ½\,\mathrm{H_2}$	-8000(1)	$Li(C_6) - CMC$
	$\mathrm{Li} + \mathrm{PEO} \rightarrow ?$	-5500(2)	$Li(C_6) - PEO$

Note that:

- R1: reaction between plated lithium and PC solvent; the average amount of plated lithium is supposed to be 10 wt.% of total lithium (based on results reported in section 2.3.1), for the calculation the amount of total lithium in the 18650 cells is estimated to be 0.8 grams. The plated lithium is the default reactant.
- R2: SEI first breakdown; two exothermic reactions were selected for the metastable SEI degradation. Based on the analysis presented in section (2.3.2) and the DSC analysis of the SEI we assume that the metastable layer is composed of LEDC: LMC with 25:75 %wt.
- R3: reaction between intercalated lithium and DMC solvent; the amount of intercalated lithium is higher than DMC in both fresh and aged negative electrode samples. Then, the DMC solvent is the limiting reactant.
- R4: first exothermic reaction of NCA decomposition; the reaction enthalpy of this transformation is taken from [13]
- R5: interaction between released O_2 and EC solvent; the complete and partial oxidation of EC solvent is selected for this reaction; the enthalpy of the reaction is calculated according to the amount of O_2 and EC in the sample.
- R6: EC solvent degradation and second SEI breakdown; the EC solvent degradation is selected to represent the electrolyte degradation, its enthalpy is unknown and difficult to

calculate, then it is estimated based on the specific peak enthalpy of the electrolyte degradation reported in Table 2. Simultaneously, the second SEI breakdown occurs in presence of HF and PF_5 (see 2.3.6). The kinetic parameters of the second SEI breakdown reaction were considered to be the same as those of the EC degradation reaction.

- R7: reaction of intercalated lithium with CMC and PEO products; the enthalpy of lithium/CMC reaction is calculated based on the specific peak enthalpy of this reaction (reported in Table 2), however, the enthalpy of lithium/PEO reaction is adjusted against experimental DSC profile for lack of data.

2.5 Species balance

The kinetic equations ((6)-(14)) calibrated and validated through the DSC analysis of the battery materials remain valid. However, a molar balance of the reactants is required for full battery simulations since some reactants can be involved in more than one degradation reaction. Therefore, the heat generation of each reaction in Table 6 can be calculated by:

$$\boldsymbol{q_x = k_x\ \Delta H_{r,x}\ n_x} \quad (67)$$

Where, k_x is the kinetic of the reaction (1/s), $\Delta H_{r,x}$ is the reaction enthalpy (J/mol) and n_x the molar amount of the default reactant. The amount of each species will be tracked during the TR process using the following calculation for a given reaction:

$$\boldsymbol{y_A\ A + y_B\ B \rightarrow\ y_P\ P} \quad (68)$$

Considering that A is the limiting reactant and y_A its stoichiometric coefficient, then the relative conversion rate α of A is defined theoretically (for a closed system) as:

$$\boldsymbol{\alpha_A = \frac{n_{A,0} - n_A}{n_{A,0}} = (1 - C_A)} \quad (69)$$

With n_A is the molar amount of A, $\boldsymbol{n_{A,0}}$ is the initial molar amount of A and $(\boldsymbol{1 - C_A})$ represents the rate of consumption of A with C_A its normalized concentration, defined in equation *(2)*.

Thus,

$$\boldsymbol{n_A = n_{A,0} - (n_{A,0} \times (1 - C_A))} \quad (70)$$

And,

$$\boldsymbol{n_B = n_{B,0} - \frac{y_B}{y_A}(n_{A,0} - n_A)} \quad (71)$$

$$n_P = \frac{y_P}{y_A}(n_{A,0} - n_A) \quad (72)$$

Besides, if the excess reactant B is consumed in multiple reactions $(R1, R2, \dots, Rn)$, then:

$$n_B = n_{B,0} - \sum_{j \in z} \frac{y_{B_j}}{y_{A_j}} \left(n_{A,0} - n_{A_j} \right), \quad z \in [R1, R2, \dots, Rn] \tag{73}$$

Similarly, when the same product P is produced in multiple reactions $(R1, R2, \dots, Rn)$,

$$n_P = \sum_{j \in z} \frac{y_{P_j}}{y_{A_j}} \left(n_{A,0} - n_{A_j} \right), \quad z \in [R1, R2, \dots, Rn] \tag{74}$$

The heat generation was calculated for each peak according to the limiting reactant.

The obtained results using this model will be presented and discussed in the following section.

3 Simulation results and discussions

3.1 DSC test

3.1.1 Negative electrode

Fresh sample: for the fresh negative electrode + electrolyte sample, the total heat generation is calculated based on reactions R2, R3, R6, and R7 listed in Table 6.

The DSC profiles, in this case, are simulated according to the following equation:

$$Q_{neg/ELe} = q_{SEI\_I} + q_{Li(C_6)-DMC} + q_{EC} + q_{SEI\_II} + q_{Li(C_6)-CMC} + q_{Li(C_6)-PEO} + q_{endo} \tag{75}$$

The obtained result is presented in Figure 10:

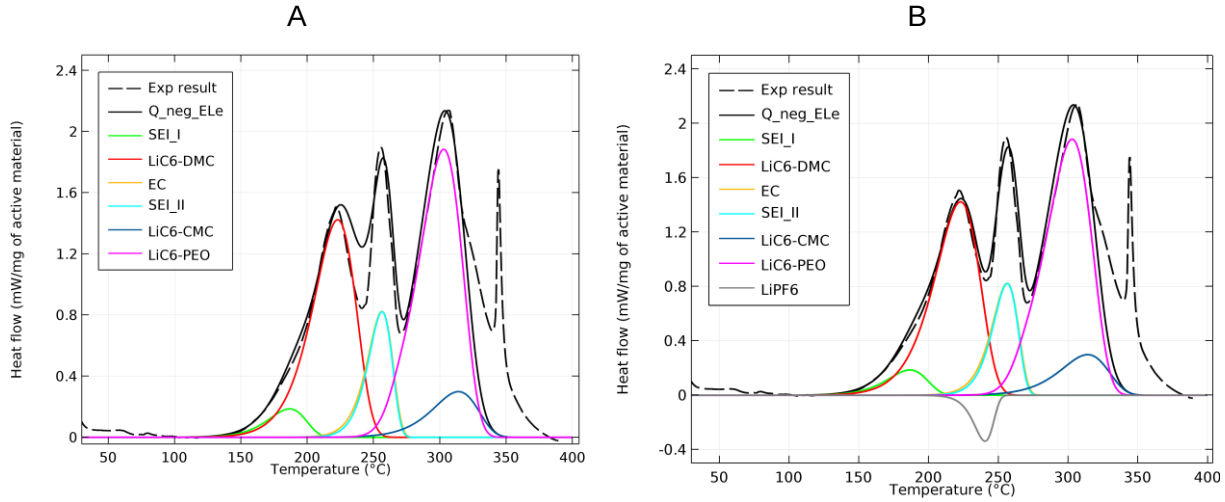

Figure 10: Simulation DSC results of the fresh lithiated anode mixed with electrolyte with 77:23 %wt at 5 °C.min^{-1}, before (A) and after adding endothermic reactions peak (B)

Figure 10 shows the simulation DSC profiles of the total heat generated by the sample (Q_neg_ELe) and the six exothermic peaks individually presented with different colors.

Compared to the experimental result (Exp result in Figure 10), the total heat is correctly simulated using equation (*75*). However, we observed that the simulated profile in Figure 10–A could be optimized between 220 °C and 250 °C by adding an endothermic reaction. Indeed, we assume that endothermic reactions like lithium salt fusion and its interaction with humidity which start around 220 °C could be added to the model to improve the prediction of the total DSC profile.

After adding the endothermic reactions ($\boldsymbol{q}_{endo}$), the simulation result is presented in Figure 10–B. The used enthalpy for the endothermic peak was calculated based on reactions (51) and (52). The kinetic parameters for this peak were adjusted against the experimental result and the used A_{endo} and Ea_{endo} parameters are respectively 1.6 10^{30} s^{-1} and 3.16 10^{5} $J.mol^{-1}$.

Aged sample: after aging at -20 °C the reaction including plated lithium is added to the degradation reactions system of the lithiated negative electrode (see reaction R1 in Table 6). Then, the degradation profile of the aged sample is simulated by the following equation:

$$\boldsymbol{Q_{neg/ELe} = q_{SEI\_I} + q_{Li-PC} + q_{Li(C_6)-DMC} + q_{EC} + q_{SEI\_II} + q_{Li(C_6)-CMC} + q_{Li(C_6)-PEO} + q_{endo}} \quad (76)$$

The obtained result is presented in Figure 11:

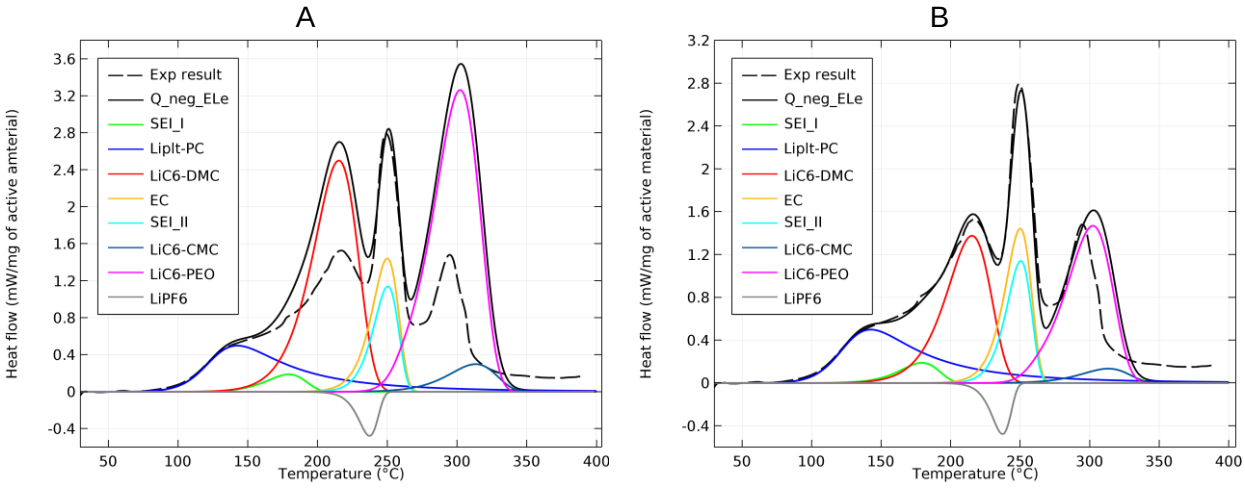

Figure 11: Simulation DSC results of the aged lithiated anode mixed with electrolyte with 66:34 %wt at 5 °C.min^{-1}, without corrective factor (left) and with corrective factor (right).

Figure 11–A shows the simulation DSC profiles of the total heat generated by the sample (Q_neg_ELe) after aging (black solid line) and the separated exothermic peaks presented with different colors.

We found that the model reproduces correctly the experimental curve except for the reactions involving the intercalated lithium (LiC_6-DMC, LiC_6-CMC, and LiC_6-PEO). Indeed, the lithium distribution in the negative electrode after aging at -20 °C is not homogenous and the model does not take into account the incomplete lithiation identified in chapter III of the negative

electrode. Thus, a higher peak intensity was obtained compared to the experimental result with the LiC_6-PC, LiC_6-CMC, and LiC_6-PEO peaks. A corrective factor is then introduced to better fit these peaks after aging (Figure 11–B)

3.1.2 Positive electrode

The heat generation of the positive electrode material mixed with cell electrolyte is calculated based on three exothermic reactions:

- The first exothermic structural change of delithiated NCA (R4 in Table 6),
- The electrolyte oxidation: the EC/O_2 mass ratio is calculated initially according to the weight of active material and electrolyte in the sample. Then partial or total oxidation reaction is attributed to the peak (R5 in Table 6),
- As discussed in chapter II, more than one reaction can occur after the electrolyte oxidation. In Table 1, the last positive electrode degradation reaction was attributed to the interactions between NCA oxides and electrolytes after the lithium salt melting ($q_{NCA-ELe}$). In view of the complexity of identifying the theoretical reactions that can represent the heat generated in this peak we have used the measured enthalpy ($H_{NCA-ELe}$), reported in Table 2. To make the distinction between the two models, this peak will be notes as q_{NCA_II}

Therefore, the DSC profiles of this sample can be simulated by:

$$\boldsymbol{Q_{pos/ELe} = q_{NCA\_I} + q_{EC-O_2} + q_{NCA\_II}} \quad (77)$$

The obtained result is presented in Figure 12:

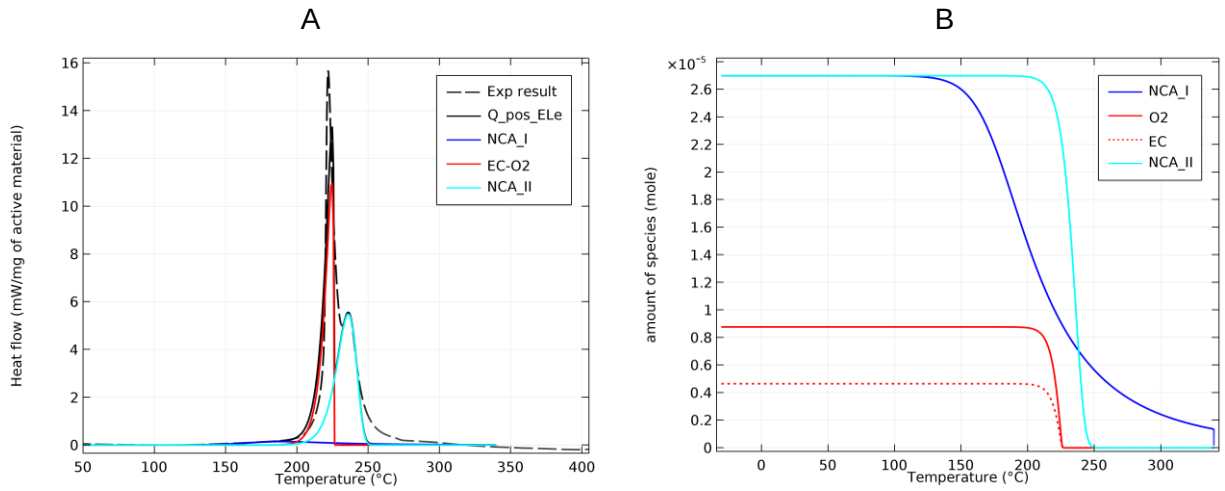

Figure 12: Simulation DSC results of the delithiated cathode mixed with electrolyte with 67:33 %wt at 5 °C.min^{-1} (A), and the evolution of the amount of reactant (B)

Figure 12–A shows the simulation DSC profiles of the total heat generated by the sample (Q_pos_ELe) and the separated exothermic peaks presented with different colors. We see that the total simulated profiles are very close to the experimental one.

The evolution of the quantity of reactants in the sample is also presented (Figure 12–B) and shows their distribution in the sample during the degradation process. This result shows that the amount of oxygen and EC are consumed almost totally before 240 °C. Considering the amount of EC initially present in the mixture, its degradation is not expected in this case and it is suggested that other reactions between the NCA oxides and the other electrolyte solvents or lithium salt might be at the origin of the last peak.

3.1.3 Full mini-cell configuration

In the same way, the model of degradation of the separate electrodes is validated in the case of a complete system including negative/positive electrodes and electrolytes.
The experimental results of the mini cell presented in chapter III were simulated. The obtained results of fresh and aged cells are presented in Figure 13 A and B.

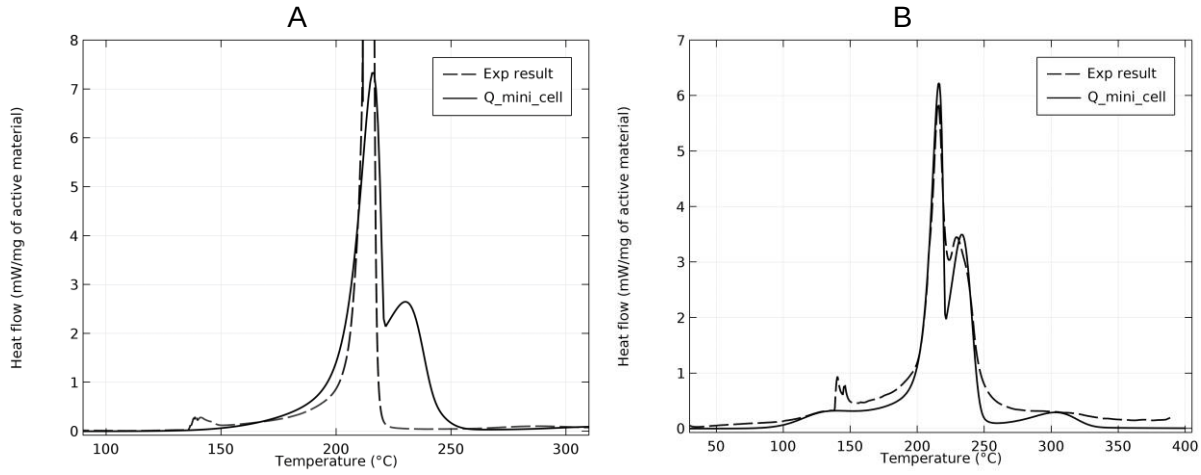

Figure 13: Simulation DSC results of the mini cell before (A) and after aging (B) at 5 °C.min^{-1}

The simulation results are obtained by integrating the reaction system of both the negative and positive electrodes and by considering the same proportions of material in the experiments.

The experimental result is successfully simulated before and after aging. This simulation result validates the selected TR reactions for the cell and the model at the electrode scale. We validated also that the plated Li/electrolyte reaction is responsible for the additional amount of heat between 100 °C and 150 °C in the aged cell as we can see in Figure 13-B.
However, since the melting of the separator at around 135 °C is not considered in the model. The heat generated by the ISC of the electrodes is not simulated, which requires the implementation of an electrochemical model.

Figure 14-A shows the distribution of the peaks that make up the total profile of the aged cell.

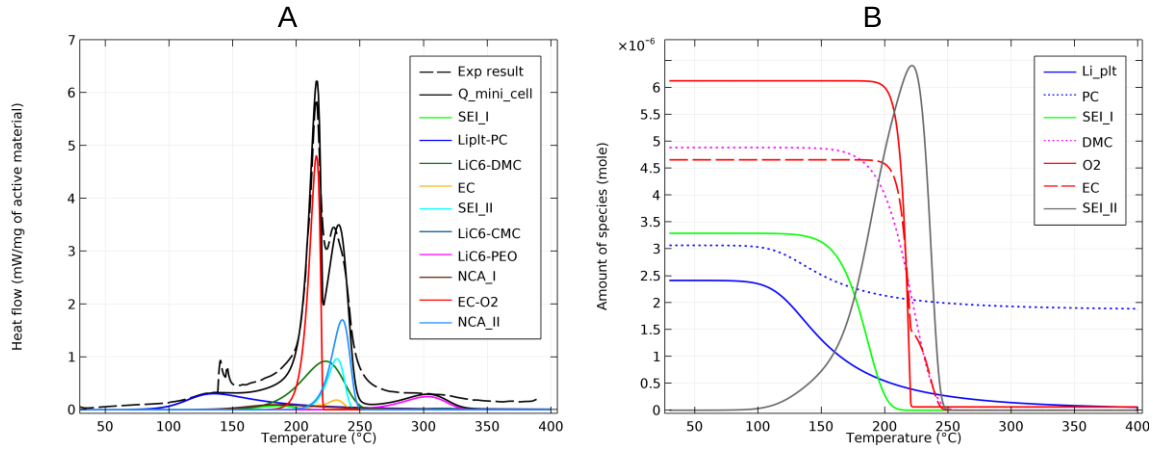

Figure 14: Simulation DSC results of the aged full cell at 5 °C.min^{-1} (A), Evolution of the amount of species during the thermal degradation of the aged full cell at 5 °C.min^{-1} (B)

The variation in the amount of material presented in Figure 14-B is representative of the equilibrium between the different reactants in the full cell. The initial amount of oxygen is calculated based on equation (48) using the weight of the positive electrode in the sample.

Figure 14-B shows that the PC solvent is in excess compared to the plated lithium (quantified in chapter III) in the aged cell, and some PC solvent remains after 200 °C. Besides, EC is mainly consumed in the oxidation reaction considering the equilibrium between EC and O_2 species.

CO_2 gas prediction

The TR reactions assumed in Table 6 generate mainly CO_2 gas. Using the model, we simulated the total amount of gas produced during the degradation process of the cell following reactions R2, R5, and R6 in Table 6. The obtained result is presented in Figure 15.

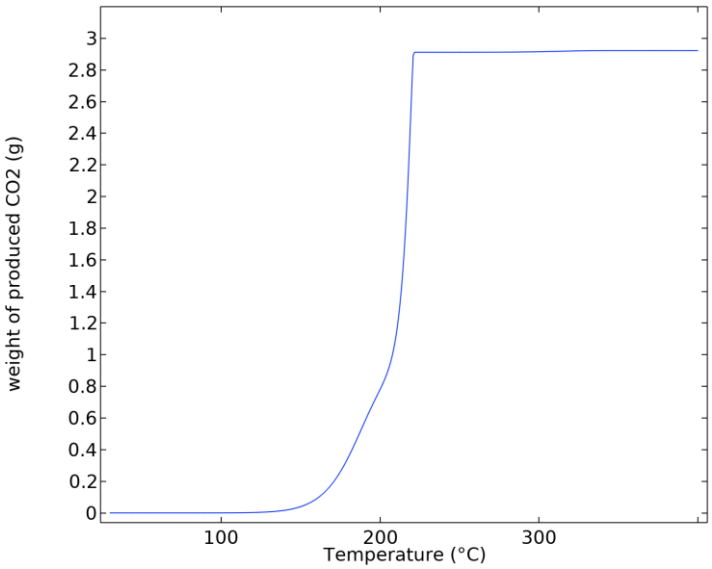

Figure 15: CO_2 gas generation during the TR of the INR18650-32E cell

The amount of produced CO_2 following only reactions R2, R5, and R6 is about 3 g for the INR18650-32E cell. If we consider that 1 mole of CO_2 occupied a volume of 22.4 L in STP (standard temperature and pressure) conditions, then the total volume of produced CO_2 could be estimated to be 150 10^{-5} m^3. As the total casing volume of 18650 cells is 1.654 10^{-5} m^3, it is obvious that such gas production can cause the venting or even the explosion of the cell.

3.2 ARC test

In this section, the thermal modeling of the INR18650-32E full cell during an ARC test is presented. For this purpose, a simplified thermal model is used to predict the behavior of the cell during the abusive test. It provides the temperature distribution at each time in the system according to the following heat equation:

$$\frac{dT}{dt} = \frac{Q_{gen} + Q_{diss}}{\rho\, C_p} \tag{78}$$

where T is the cell temperature, ρ is the cell density, C_p is the average specific heat capacity of the cell. Q_{gen} and Q_{diss} are respectively the total heat generation rate and that dissipated from the cell (J m^{-3} s^{-1}). The dissipated heat rate is assumed negligible during the ARC test.
The heat generated by the cell is considered as the sum of the heat generation rates of the exothermic reactions that characterize the thermal degradation of positive and negative electrode materials studied in sections 3.1.1 and 3.1.2 ($Q_{gen} = \sum q_i$). The amount of heat generated by the reaction (q_i) is calculated, for each reactant i, in relation to the total volume of the electrode active material in the cell, as follows:

$$q_i = k_i H_i W_i \tag{79}$$

Where k_i is the reaction kinetic (s^{-1}) presented in section 2.2, H_i is the specific heat released by the reaction (J g^{-1}), Wi is the specific amount of the active material that contains the reactant in the cell (g m^{-3}). Wi is calculated for all active material in the cell (the positive/negative electrode, the electrolyte, and the plated lithium) values are reported in Table 7.

Table 7: list of parameters used in the thermal model

Parameter	Description	Value
$\boldsymbol{M}$	Average total weight of the INR18650-32E cell (g)	48
$\boldsymbol{A}$	The total area of the INR18650-32E cell (m^2)	$4.2\ 10^{-3}$
$\boldsymbol{V}$	The total volume of the INR18650-32E cell (m^3)	$1.654\ 10^{-5}$
$\boldsymbol{\rho}$	The calculated density of the INR18650-32E cell (kg m^{-3})	2902
$\boldsymbol{C_p}$	Estimated specific heat capacity of the cell (J kg^{-1} K^{-1})	1.46
$\boldsymbol{W_{neg}}$	The specific amount of the negative electrode active material in the cell (kg m^{-3})	1371
$\boldsymbol{W_{pos}}$	The specific amount of the positive electrode active material in the cell (kg m^{-3})	1943
$\boldsymbol{W_{el}}$	The specific amount of the electrolyte in the cell (kg m^{-3}	503
$\boldsymbol{W_{Li\_plt}}$	The specific amount of the plated lithium in the cell (kg m^{-3})	18

W_{neg} was used in q_{SEI_I}, $q_{Li(C_6)-DMC}$, $q_{Li(C_6)-CMC}$ and $q_{Li(C_6)-PEO}$; W_{pos} in q_{NCA_I}, q_{EC-O_2} and q_{NCA_II}; W_{el} in q_{EC} and q_{SEI_II}; W_{Li_plt} in q_{Li-PC}

The simulation results were compared with the experimental results of the ARC performed on the INR18650-32E cell before and after aging presented in chapter III. Figure 16 shows the average surface temperature of the fresh INR18650-32E cell (black curve) and the temperature simulated using the model (blue curve).

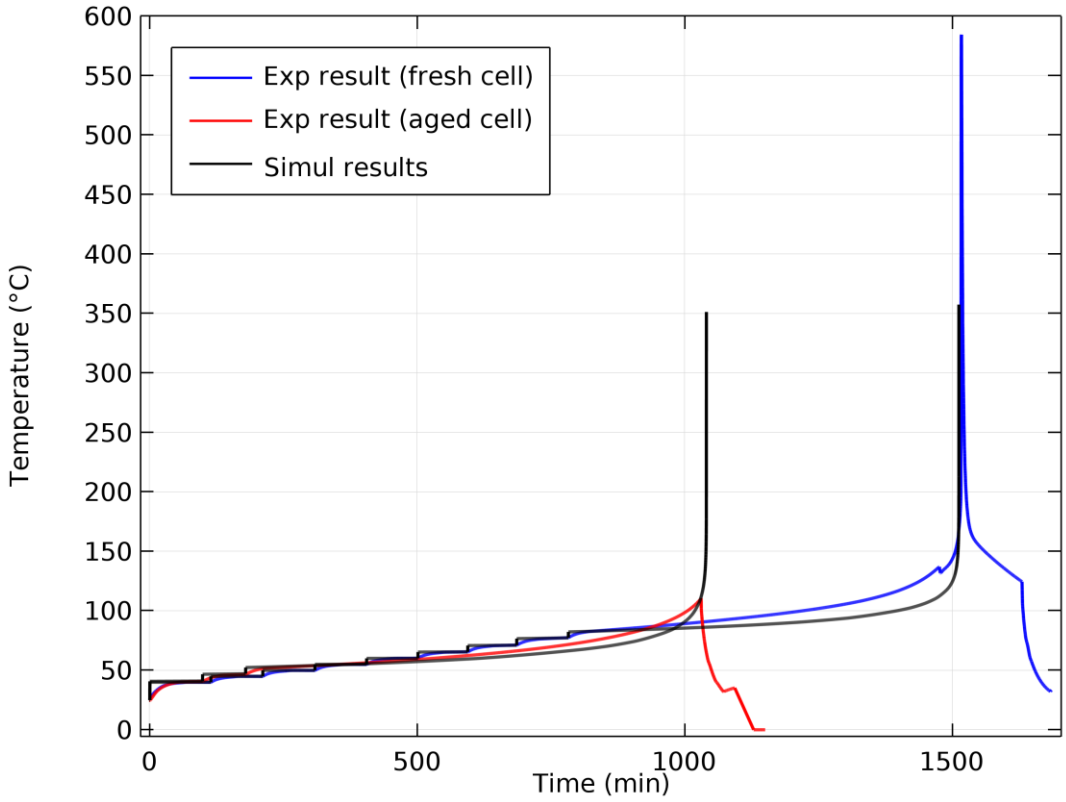

Figure 16: simulation of ARC test result of the cell before (blue curve) and after aging at -20 °C (red curve), the experimental results are presented in black

We can see in this figure that the simulated curve matches quite well with the experimental curve of the ARC test. However, a deviation can be noted in particular between 1000 and 1500 min. Indeed, according to the simulation result, the simulated average temperature is lower in this time interval. This is probably associated with the differences between the degradation kinetics of the reactions involved in the model and the complete cell. Besides, this can also be related to other factors such as the measurement uncertainty of the ARC test or to some overestimated/underestimated parameters in the model.

The model is used under conditions different from those under which the model was established: the TR reactions were characterized using DSC tests performed from 2 to 15°C/min. however, with the ARC test before the runaway zone, the temperature rise is variable but typically about 0.1°C/min which could explain the shift observed in Figure 16.

We proceeded similarly to validate the TR model for the aged INR18650-32E cell. The figure shows the average surface temperature of the aged INR18650-32E cell with cyclic aging at -20 °C (red curve) and the temperature simulated using the model (black curve). The result of the fresh cell is also presented in the same graph to show the impact induced by aging at low temperature on the cell thermal behavior and the robustness of the proposed model.

Some imperfections of the model have been noted in this part. Better results with less error between experimental and simulation should have been obtained with SOTA models described

in the literature (based on numerical fit). But our choice was to make a model based on experimental preliminary DSC investigations and degradation reactions consistent with the commercial cell composition and chemistry and based on a mass balance. Therefore, it seems reasonable that the prediction results are not perfectly correlated with the experimental results but the proposed model is more robust than SOTA models.

Moreover, even if the materials used in the experimental DSC study were collected from the commercial cell at a state of charge close to that of the cell tested in ARC, the composition of analyzed samples may be different; especially the electrolyte which may contain unknown additives.

Moreover, the kinetic parameters of the chemical reactions, notably the activation energy and the frequency factor may sometimes be highly sensitive and difficult to adjust, especially since the reactions are intrinsically linked and some are closely correlated.

3.3 Oven test

The thermal runaway model developed and validated for an ARC test will be used in this section to simulate the thermal behavior of the INR18650-32E cell in a different abusive condition. An oven test is simulated to evaluate the influence of the cell surface temperature on the triggering of thermal runaway.

Then, equation (78) and (79) and the heat dissipation rate from the cell to the outside is considered as follows:

$$\boldsymbol{Q_{diss} = h\,\frac{A}{V}(T - Ts)} \qquad (80)$$

Where A and V are respectively the total area and volume of the INR18650-32E cell, h is the heat exchange coefficient of the cell (W K^{-1} m^{-2}), Ts is the cell surface temperature.

This study is performed for fresh and aged INR18650-32E cells to qualify the impact of the plated lithium/electrolyte reaction on the cell safety behavior during this type of abusive test.

The thermal behavior of the cell was tested for different values of the oven temperature. It was assumed that the temperature at the surface of the cell corresponds to the temperature of the oven. Thus, the cell surface temperature is an input parameter in this model. The initial temperature of the cell was fixed at 25°C.

Firstly, the simulation results of the fresh and aged cells are compared in Figure 17 with two different surface temperatures 90 °C and 120 °C. The heat exchange coefficient h of the cells was fixed to 10 W K^{-1} m^{-2}.

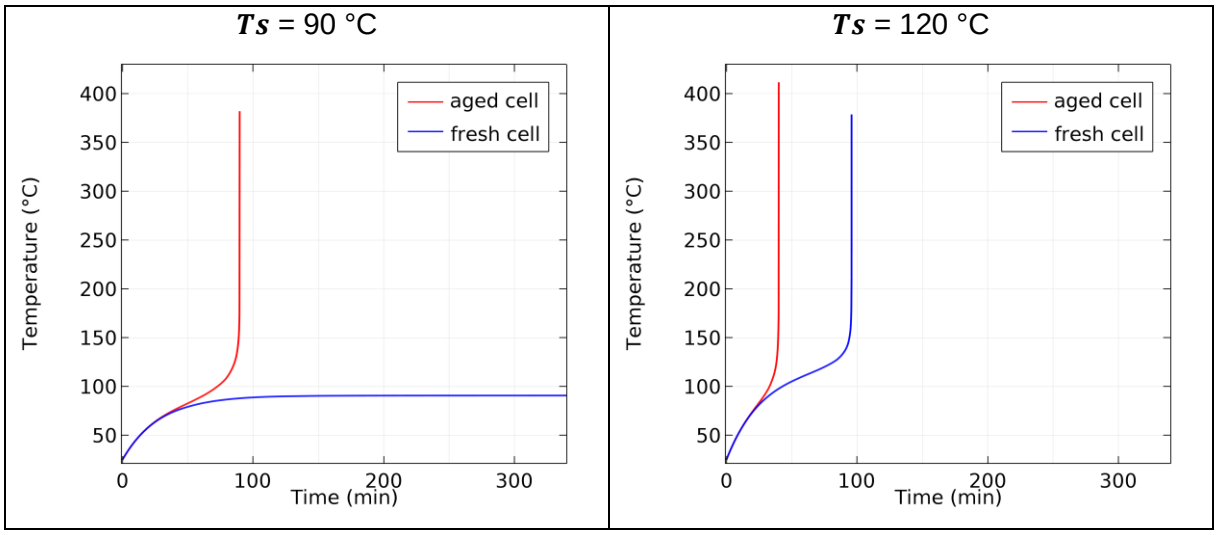

Figure 17: Influence of Li plating on the safety behavior of the INR18650-32E cell during oven test

When Ts = 90 °C, the fresh cell does not go into TR, however at Ts = 120 °C a TR is detected at around 100 min. The behavior of the aged cell is different. A thermal runaway is detected with the two temperatures with some shift.

This result is consistent with that obtained with the ARC test (see Figure 16). Compared to the fresh cell, the aged cell is thermally unstable at low temperature and goes into TR earlier. When the surface temperature is 90°C and considering a perfect heat transfer inside the cell, this is sufficient to activate the reaction between the plated lithium and the electrolyte (T_{onset} < 90 °C see chapter III). This confirms that the TR in aged cells is triggered by the plated lithium/electrolyte reaction.

The fresh cell appears safe at 90 °C, the SEI breakdown is probably activated at this temperature but the heat that is released is not sufficient to trigger the other exothermic reactions. At 120 °C, the aged and fresh cells go into TR at respectively t≈40 min and t≈100 min. It is detected faster with the aged cell due to the reactivity of lithium plating.

Moreover, the influence of the heat exchange coefficient with the outside was tested to simulate the impact of the heating and cooling rate on the safety behavior of the aged and fresh cells for Ts = 90 °C and Ts = 120 °C. Two different heat exchange conditions are tested (2 and 20 W K^{-1} m^{-2}) as illustrated in Figure 18.

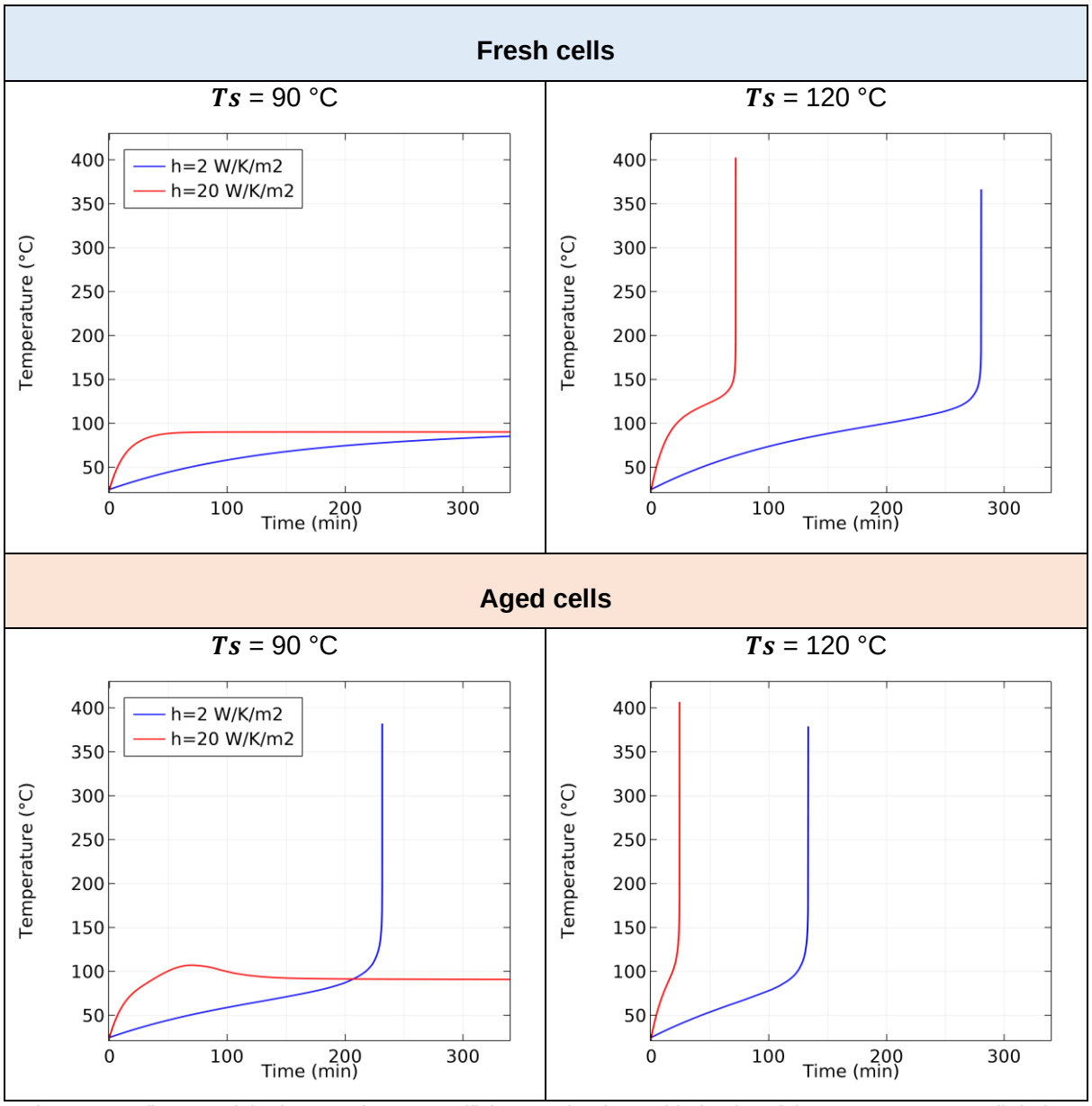

Figure 18: Influence of the heat exchange coefficient on the thermal behavior of the INR18650-32E cell during oven test

For the fresh cell, with Ts = 90 °C the effect of the heat exchange coefficient is not observed because of the thermal stability of the cell at this temperature. However, when Ts = 120 °C and a heat exchange coefficient of 2 W K^{-1} m^{-2}, the cell takes more than 250 min to reach 150 °C while the thermal runaway is triggered before 100min if h = 20 W K^{-1} m^{-2}. The lower the heat exchange coefficient, the more the thermal runaway is retarded.

The influence of the heat exchange coefficient on the surface temperature is more pronounced with the aged cells at 90 °C as we can see in Figure 18. Using a heat exchange coefficient of 20 W K^{-1} m^{-2} the thermal runaway of the aged cell is inhibited. The temperature rise is faster in this case compared to 2 W K^{-1} m^{-2}, it exceeds slightly 100 °C and then decreases until reaching a plateau. No remarkable effect when Ts = 120 °C.

These simulation results have allowed us to highlight the existence of a critical temperature not to be exceeded to avoid the TR of the INR18650-32E. The influence of lithium plating on the safety behavior of the cell is validated.

4 Conclusions

The modeling of TR during the thesis was focused on physical modeling at the cell scale for Li-ion technology. In particular, the analysis was done on the INR18650-32E cell before and after cyclic aging at -20 °C at a high state of charge. The model was calibrated and validated for the NCA/Graphite chemistry using DSC analysis. We were able to separately quantify the heat released by the main TR reactions for the negative and positive electrode materials. The TR chain of reactions and a species balance was proposed respecting the equilibrium of the INR18650-32E cell materials.

The experimental observations before and after cyclic aging at -20 °C were confirmed by the simulation results. Notably, the reaction between the plated lithium and the electrolyte was calibrated and integrated for the first time in this model. More intense released heat at low temperature caused by the plated Li/electrolyte solvent at the electrode scale was simulated. The impact of this reaction on the safety behavior of the cell after aging was validated against ARC test results for the INR18650-32E cell.

Some limitations of the model were underlined. First, the parameterization of the thermal degradation model for the electrode material would require more accuracy, especially on the kinetic parameters (Ea and A). The use of the Kissinger method looks very robust. However, the appropriate quantity of material used in DSC is still difficult to control (evaporation of the electrolyte) and some reactions are still difficult to dissociate Moreover, the status of some parts of the proposed chain of reaction may still be discussed (for example, Kriston in 2019 identified a selected a variant on its chain of reaction).

At the cell level, the ISC between electrodes after the separator melting, and the cell venting (external amount of oxygen) have not been considered in this work. This is a perspective for future research investigation.

5 References

[1] D. Ren *et al.*, « Model-based thermal runaway prediction of lithium-ion batteries from kinetics analysis of cell components », *Appl. Energy*, vol. 228, p. 633-644, Oct. 2018, doi: 10.1016/j.apenergy.2018.06.126.

[2] J. Šesták, G. Berggren, « Study of the kinetics of the mechanism of solid-state reactions at increasing temperatures », *Thermochim. Acta*, vol. 3, nº 1, p. 1-12, Oct. 1971, doi: 10.1016/0040-6031(71)85051-7.

[3] N. Koga, H. Tanaka, « Accommodation of the actual solid-state process in the kinetic model function », *J. Therm. Anal.*, vol. 41, nº 2, p. 455-469, Feb. 1994, doi: 10.1007/BF02549327.

[4] D. D. MacNeil, J. R. Dahn, « Test of Reaction Kinetics Using Both Differential Scanning and Accelerating Rate Calorimetries As Applied to the Reaction of LixCoO2 in Non-aqueous Electrolyte », *J. Phys. Chem. A*, vol. 105, nº 18, p. 4430-4439, May. 2001, doi: 10.1021/jp001187j.

[5] H. E. Kissinger, « Variation of peak temperature with heating rate in differential thermal analysis », *J. Res. Natl. Bur. Stand.*, vol. 57, nº 4, p. 217, Oct. 1956, doi: 10.6028/jres.057.026.

[6] N. O. of D. and Informatics, « WebBook of Cheminstry, NIST ». https://webbook.nist.gov/chemistry/.

[7] N. Tanaka, W. G. Bessler, « Numerical investigation of kinetic mechanism for runaway thermo-electrochemistry in lithium-ion cells », *Solid State Ion.*, vol. 262, p. 70-73, Sept. 2014, doi: 10.1016/j.ssi.2013.10.009.

[8] J. Thomas, E. Petersen, J. Darst, E. Darcy, D. Finegan, « Consequence Analysis of Li-Ion Battery Thermal Runaway Events with Chemical Equilibrium Analysis », Nov. 2018.

[9] K. S. Gavritchev, G. A. Sharpataya, A. A. Smagin, E. N. Malyi, V. A. Matyukha, « Calorimetric study of thermal decomposition of lithium hexafluorophosphate », *J. Therm. Anal. Calorim.*, vol. 73, nº 1, p. 71-83, July 2003, doi: 10.1023/A:1025125306291.

[10] R. Spotnitz, J. Franklin, « Abuse behavior of high-power, lithium-ion cells », *J. Power Sources*, vol. 113, p. 81-100, Jan. 2003, doi: 10.1016/S0378-7753(02)00488-3.

[11] A. W. Golubkov *et al.*, « Thermal runaway of commercial 18650 Li-ion batteries with LFP and NCA cathodes – impact of state of charge and overcharge », *RSC Adv.*, vol. 5, nº 70, p. 57171-57186, Jun. 2015, doi: 10.1039/C5RA05897J.

[12] A. Kriston, I. Adanouj, V. Ruiz, A. Pfrang, « Quantification and simulation of thermal decomposition reactions of Li-ion battery materials by simultaneous thermal analysis coupled with gas analysis », *J. Power Sources*, vol. 435, p. 226774, Sept. 2019, doi: 10.1016/j.jpowsour.2019.226774.

[13] R. C. Shurtz, J. C. Hewson, « Review—Materials Science Predictions of Thermal Runaway in Layered Metal-Oxide Cathodes: A Review of Thermodynamics », *J. Electrochem. Soc.*, vol. 167, nº 9, p. 090543, May 2020, doi: 10.1149/1945-7111/ab8fd9.

[14] J. L. Tebbe, T. F. Fuerst, C. B. Musgrave, « Mechanism of hydrofluoric acid formation in ethylene carbonate electrolytes with fluorine salt additives », *J. Power Sources*, vol. 297, p. 427-435, Nov. 2015, doi: 10.1016/j.jpowsour.2015.07.104.

[15] S. Solchenbach, M. Metzger, M. Egawa, H. Beyer, H. A. Gasteiger, « Quantification of PF5 and POF3 from Side Reactions of LiPF6 in Li-Ion Batteries », *J. Electrochem. Soc.*, vol. 165, nº 13, p. A3022, Sept. 2018, doi: 10.1149/2.0481813jes.

[16] S. E. Sloop, J. K. Pugh, S. Wang, J. B. Kerr, K. Kinoshita, « Chemical Reactivity of PF 5 and LiPF6 in Ethylene Carbonate/Dimethyl Carbonate Solutions », *Electrochem. Solid-State Lett.*, vol. 4, nº 4, p. A42, Feb. 2001, doi: 10.1149/1.1353158.

[17] G. Gachot *et al.*, « Gas Chromatography/Mass Spectrometry As a Suitable Tool for the Li-Ion Battery Electrolyte Degradation Mechanisms Study », *Anal. Chem.*, vol. 83, nº 2, p. 478-485, Jan. 2011, doi: 10.1021/ac101948u.

[18] A. W. Golubkov *et al.*, « Thermal-runaway experiments on consumer Li-ion batteries with metal-oxide and olivin-type cathodes », *RSC Adv*, vol. 4, nº 7, p. 3633-3642, 2014, doi: 10.1039/C3RA45748F.

Conclusion and perspectives

The first objective of this thesis was the understanding of the thermal runaway phenomenon considered the main incident that can affect the technology of Li-ion batteries; not only for cells with a high health statute (fresh cell) but also after aging at low temperature. The second objective was to develop a predictive physical model at the cell level, including the thermal degradation reactions for fresh and aged cells. To achieve these objectives, we have worked with an experimental methodology by analyzing the thermal stability of each component and their interactions; combined with a modeling development.

The safety behavior of the INR18650-32E cell materials (active materials: graphite at the negative electrode and $LiNi_{0,8}Co_{0.15}Al_{0.05}O_2$ at the positive electrode, electrolyte), before and after aging, was investigated by combining DSC analysis with different characterization techniques (XRD, XPS, TOF-SIMS, and NMR). The experiments were performed under almost the same conditions. DSC analyses were conducted with materials from the same cell and by adding the cell electrolyte with similar proportions to the INR18650-32E cell, which is rarely taken into account in the literature and crucial to obtaining representative results.

Because of its negative effect on cell safety behavior, we have focused on lithium plating formation. The characterization and quantification of plated lithium on the aged negative electrode were possible by combing NMR analysis with an original quantification methodology. Roughly, 10 % of the total cycled lithium in the INR18650-32E cell was transformed to plated lithium after aging at -20 °C by cycling according to the IEC 62660-1 standard, i.e., 8 mg/g of the active material of the negative electrode, 2 mg/g of the cell or 32 mg/Ah.

The thermal runaway reactions of the cell components are highly correlated. Most of these reactions were analyzed separately by testing multiple samples and configurations (different materials present or missing).

The main heat sources during a thermal runaway scenario were identified and discussed:
The SEI breakdown and the LiC_6/electrolyte reaction initiate the thermal degradation of the fresh charged NCA/Gr system.
After aging, the reactivity between plated Li and electrolyte solvents releases more heat between 50 °C and 200 °C, accelerating the chain of the thermal runaway reactions and the onset temperature of the charged NCA/Gr system degradation decreases consequently. Besides, the oxygen released from the NCA-based electrode appeared as the key element that controls the thermal runaway of the charged NCA/Gr system before and after aging. This is due to its high reactivity with both electrolyte and LiC_6. Studied separately, these reactions

seem to be powerful compared to other thermal runaway reactions that generated the major part of the heat between 200 °C and 250 °C.
In a real thermal runaway scenario, the oxygen/electrolyte and oxygen/LiC_6 reactions may occur simultaneously, however, the direct contact between the positive electrode and the electrolyte makes the oxygen/electrolyte reaction predominant (as long as the electrolyte is available) compared to the one with intercalated lithium on the graphite side.

The modeling part of this thesis was focused on thermal runaway physical modeling at the cell scale for the safety behavior of the INR18650-32E cell at a high state of charge. The model was calibrated and validated for the NCA/Graphite chemistry using the experimental results. The main thermal runaway reactions between 50 °C and 400 °C were considered. For the first time, the reaction between the plated lithium and the electrolyte was calibrated and integrated into this model. Besides, a species balance was implemented in the model according to the equilibrium of the material inside the INR18650-32E cell.
The experimental observations before and after aging by cycling at -20 °C were confirmed by the simulation results. More intense released heat at low temperature caused by the plated Li/electrolyte solvent at the electrode scale was simulated. The impact of this reaction on the safety behavior of the cell after aging was validated against accelerating rate calorimeter (ARC) test results for the INR18650-32E cell.
Some limitations of the model were underlined. First, the parameterization of the thermal degradation model for the electrode material would require more accuracy, especially on the kinetic parameters (Ea_x and A_x) and some reactions are still difficult to dissociate. Moreover, the degradation reaction scheme can be enhanced by adding other thermal runaway reactions. The accuracy of the model could be improved as a consequence.
At the cell level, the internal short circuit (ISC) between electrodes and the cell venting (external amount of oxygen) has not been considered in this work. This is a perspective for future research investigation.

The main point highlighted in this thesis is that: the trio "electrolyte + negative electrode + positive electrode" is highly energetic than dissociated reactants. Therefore, we could better control the thermal runaway consequences on Li-ion batteries by mainly using more stable positive electrode material (since it is the main source of oxygen in the Li-ion battery technology) and more thermally stable electrolytes.

Some perspectives can be proposed to improve the current model. The coupling of the current thermal runaway model with an electrochemical model for the prediction of thermal runaway during an internal/external short circuit can be envisaged. The model upscaling is also required to anticipate the propagation of the thermal runaway at the battery pack level.

The analysis of the generated gases during the main thermal runaway reactions as well as the other products of the reactions should be useful to consolidate the experimental results and to better understand the degradation mechanism of materials during the thermal runaway.

Furthermore, the same experimental methodology developed in this thesis could be applied to other cell chemistries to study the thermal behavior of the materials used in the latest generation batteries using Si/C and Si electrodes, or the 4a/4b (all solid) generation based on lithium metal.

Résumé

Les batteries Li-ion sont aujourd'hui intégrées dans de nombreux objets de notre quotidien (la mobilité électrique, l'électronique portable et le stationnaire). Les fabricants d'accumulateurs et de système batterie Li-ion ont besoin d'outils facilitant la conception de leurs produits en prenant en compte à la fois les aspects « performances », « vieillissement » et « sécurité ». L'accroissement des performances (densité d'énergie, densité de puissance, durée de vie) des accumulateurs ne peut pas se faire au détriment de la sécurité, et ce, tout au long de la durée de vie dans l'application ciblée.

Le comportement en conditions anormales (dites abusives) des batteries lithium-ion (LIBs) fait l'objet d'une attention particulière compte tenu du déploiement massif de la technologie et des accidents et défaillances recensés ces dernières années. Un outil de simulation prédictif décrivant le comportement d'un accumulateur placé dans des conditions abusives doit permettre d'accélérer le processus de développement et de limiter les processus « Essai-Erreur » qui constituent la référence méthodologique actuelle. L'emballement thermique d'une cellule et la propagation de l'emballement entre cellules sont considérés comme un problème de sécurité majeur.

Dans le cadre des travaux de cette thèse, une étude expérimentale et de modélisation a été menée sur une cellule Ni rich/Graphite avant et après vieillissement à -20 °C dont l'objectif est de développer un modèle multi-échelle de prédiction d'emballement thermique prenant en compte le vieillissement.

La méthodologie proposée est basée sur une analyse de la dégradation thermique des différents composants de la cellule séparément de manière à identifier, et caractériser (enthalpies de réactions, cinétiques de réaction) les différentes réactions exothermiques et d'identifier le « schéma réactionnel » de l'emballement thermique d'une cellule complète. Pour cela, des analyses par calorimétrie différentielle à balayage (DSC) entre 30 °C et 400 °C à différentes vitesses de chauffe ont été réalisées suivant un plan d'expérience adapté et ajusté au fil de l'étude. Les analyses ont été multipliées sous différents états de charge (SOC), avec différentes chimies d'électrolyte avant et après deux périodes de vieillissement différentes. Ce travail expérimental a été complété, par des analyses de caractérisation des matériaux de la batterie par RMN, DRX, XPS et TOF-SIMS.

En se basant sur les résultats expérimentaux, un modèle prédictif d'emballement a été développé à l'échelle des matériaux et de la cellule commerciale complète en intégrant un bilan molaire des espèces et en tenant compte pour la première fois de l'impact du dépôt surfacique de lithium sur l'électrode négative de l'accumulateur.

Abstract

Nowadays, Li-ion batteries are integrated into many objects of our daily life (electric mobility, portable electronics, and stationary). Li-ion battery and battery system manufacturers need tools to facilitate the design of their products by taking into account "performance", "aging" and "safety" aspects. Increasing the performance (energy density, power density, lifetime) of batteries cannot be done without increasing safety, and this during the whole lifetime of the targeted application.

The behavior of lithium-ion batteries (LIBs) under abnormal conditions (called abusive conditions) is the subject of particular attention given the massive deployment of the technology and the accidents and failures recorded in recent years. A predictive simulation tool describing the behavior of a battery placed in abusive conditions is needed to accelerate the development process and to limit the " Test-Error " processes which are the current methodological reference. The thermal runaway of a cell and the propagation of the runaway between cells are considered major safety issues.

In this thesis, an experimental and modeling study has been carried out on a rich Ni/Graphite cell before and after aging at -20 °C. The objective is to develop a multi-scale thermal runaway prediction model taking into account the aging process.

The proposed methodology is based on an analysis of the thermal degradation of the different components of the cell separately to identify and characterize (reaction enthalpies, reaction kinetics) the different exothermic reactions and to identify the "reaction scheme" of the thermal runaway of a complete cell. For this purpose, analyses by differential scanning calorimetry (DSC) between 30 °C and 400 °C at different heating rates were performed according to an adapted experimental plan and adjusted during the study. The analyses were multiplied under different states of charge (SOC), with different electrolyte chemistries before and after two different aging periods. This experimental work was completed by characterization analyses of the battery materials by NMR, XRD, XPS, and TOF-SIMS.

Based on the experimental results, a predictive runaway model has been developed at the material and full commercial cell scale by integrating a molar balance of species and taking into account for the first time the impact of the lithium surface deposition on the negative electrode of the battery.